Synthetic Realizations of Structural Plasticity in Intermetallics: A Guide to Defusing and Inciting Structural Complexity

By

Brandon J. Kilduff

A dissertation submitted in partial fulfillment of the requirements for the degree of

Doctor of Philosophy

(Chemistry)

at the

University of Wisconsin – Madison

2016

Date of final oral examination: 5/31/2016

This dissertation is approved by the following members of the Final Oral Committe:

Daniel C. Fredrickson, Professor, Chemistry

Judith M. Burstyn, Professor, Chemistry

Song Jin, Professor, Chemistry

Mark D. Ediger, Professor, Chemistry

Clark R. Landis, Professor, Chemistry

Abstract

The ability to optimize atomic arrangements with respect to a property requires a fundamental understanding of the driving forces which stabilize their formation. Intermetallics, or crystalline structures composed solely of metallic elements, represent a class of compounds where this comprehension has yet to be fully achieved. Although elemental metals typically form simple structures which can be described in terms of sphere packings, compounds formed by their combination vary in complexity from ordered variants of these simple sphere packings, to structures whose description requires unit cells composed of tens of thousands of atoms or even the invocation of a higher dimensional space. Determining which of a myriad of competing interactions stabilizes these complex atomic arrangements relative to much simpler alternatives remains a challenge. One conceptual framework which has provided a foothold from which to explore the driving forces leading to the formation of complex intermetallics is *structural plasticity*: that many complex intermetallics can be understood as intergrowths or variations of one or more structural motifs characteristic of simpler structures that have become deformed in order to resolve some inherent stress.

This thesis explores the idea of structural plasticity in intermetallics through a sustained dialogue between theoretical analysis and synthetic exploration. The concept of structural plasticity is used to describe complex intermetallics as deformations of simpler structural relatives – providing clues as to which theoretical toolkits would best illuminate the stresses driving structural complexity in each system. The theoretical analyses employed are designed to provide clear, chemically intuitive insights which can

be used to guide synthetic explorations aimed at rationally modifying the structural motifs observed. Results of the subsequent syntheses are then analyzed and used to re-evaluate our understanding of the system – often suggesting additional theoretical or synthetic avenues to be explored. This process is exemplified herein through its application to understand two model systems – the formation of $TiAl_3$-/$PtHg_4$-type intergrowth features in the complex V_8Ga_{41} type and the insertion of interfaces into $CaCu_5$-type derivatives.

We begin by exploring the development of two theoretical techniques used to investigate the forces which drive the formation of complexity in our model systems – the reversed approximation Molecular Orbital (raMO) analysis and Chemical Pressure analysis, which are used to examine the role of electron count and atomic size effects, respectively, in dictating the structural motifs observed in intermetallics. Next, CP analysis is performed on a series of transition metal (T) – Gallides, suggesting that the $TiAl_3$-/$PtHg_4$-type intergrowth features in V_8Ga_{41} are a mechanism to accommodate T atoms whose atomic size it incompatible with the $TiAl_3$ or $PtHg_4$ types. This insight suggests synthetic avenues leading to the expression of more $TiAl_3$-type features in systems which typically form the V_8Ga_{41}-type through doping onto the Ga lattice – resulting in the previously unreported $TiAl_3$-type variant $Mo_2Cu_xGa_{6-x}$ ($x \approx 0.9$). The structure and stoichiometry of this phase led us to suspect that the optimization of electron count played a pivotal role in stabilizing the structures $TiAl_3$-type features. Ensuing raMO analysis identified previously unrecognized Ga supported isolobal T – T σ bonding interactions present in $TiAl_3$-type structures which allows the T atoms to use all 9 of their s, p, and d orbitals to obtain 18-electron configurations; thereby explaining the observed 14 electron/T atom electron count for which $TiAl_3$-type is observed to be stable and suggesting ways to favor T atom clustering or isolation in matrices of main group elements.

Subsequently, we the briefly turn our attention from T – Gallides to explore the structural plasticity of the $CaCu_5$-type $CaPd_5$ structure. A combination of CP analysis and GGA-DFT variable pressure calculations on the structure and other $CaCu_5$-type derivatives indicated that the reported $CaCu_5$-type $CaPd_5$ structure's inefficient use of space leaves it susceptible to phase transitions at an exceptionally mild applied physical pressure. Attempts to synthesize $CaPd_5$ as a precursor for high pressure experiments resulted in the incommensurately modulated $CaPd_{5.22}$ structure. As demonstrated by CP analysis on a commensurate approximant, the structure replaces kagome nets in the $CaCu_5$ type with an undulating hexagonal net of Pd atoms, whose periodicity is incommensurate with that of the remaining $CaCu_5$-type slabs, as a way to relieve intense negative pressures on the Ca atoms in the $CaCu_5$-type $CaPd_5$. CP analysis also suggested that the driving force behind the incommensurability lies within CP quadrupoles expressed by the Pd atoms in the hexagonal net – revealing synthetic methods that may be used to rationally modify its modulation vector through high pressure synthesis.

This thesis ends by exploring a synthetic outcome which was not predicted by theoretical analysis which led us to re-examine the role of heteroatomic interactions in T – Gallides. We examine the serendipitous discovery of the Ta_4Ga_5-type formed by Ta_4Ga_5, $Ta_{4-x}MoxGa_5$, and Nb_4Ga_5. As demonstrated by raMO analysis, its complex structure displays microscopic segregation into regions of T – T and Ga – Ga contacts as a way to allow the nodal properties of the Ga orbitals to preferentially stabilize T – T bonding interactions over anti-bonding ones. In its entirety, this thesis demonstrates the ability of structural plasticity to facilitate a dialogue between chemical theory and synthetic exploration – providing chemists with insight into how the expression of simple or complex structural features in intermetallics can be influenced.

Acknowledgements

I am indebted to more individuals than I could possibly list for helping to provide me the opportunity to pursue a doctoral degree and for offering their support during my time at the University of Wisconsin-Madison. As to avoiding this section equaling the length of the following thesis, I will forgo any attempt to make these acknowledgements comprehensive. However, I would like to take this chance to recognize several individuals who have had a large influence on my ability to succeed in my career thus far.

I'll begin by thanking the multiple mentors, in a variety of academic settings, who helped prepare me for the endeavor of a graduate degree. Prof. Mir Wais Hosseini, thank you for affording me my first chance to do research in your group at L'Université de Strasbourg. Perhaps of all the mentors I have had, I owe the largest thanks to my research advisor and graduate student mentor in Prof. Hosseini's group, Dr. Stéphane Baudron and Dr. Dmitry Pogozhev. I am extremely appreciative of the extraordinary time and effort on both of your parts in helping me develop from an underperforming undergraduate who had difficulty understanding instructions, into a researcher who can feel ownership of his successes and failures in the lab. It would be difficult for me to exaggerate how formative my time working with both of you was. Dmitry, our coffee/cigarette breaks discussing the where to find the cheapest airfare to this day serve as a reminder to me that sometimes a 5 minute break would be more productive than 5 minutes of more work.

Prof. John Turner, thank you for allowing me to continue my growth working with the students in your lab at the University of Sussex. Thank you to my graduate mentor during my time in the Turner group, Dr. Tara Williams, who with only one day's notice and in her last summer of graduate school took

the time to teach me the air-free synthetic techniques, of which I had no prior knowledge, I needed to work with her compounds. Your guidance, and what can only be described as superhuman patience, as I stumbled my way through learning how to use the equipment in your lab helped give me the confidence to attempt difficult research procedures that I would have previously thought were beyond my skillset. Thank you also to my office mates and other members of the Turner group, Dr. Kayla Milner, Dr. Jason Woodford and Dr. Daniel Lester, who all donated their time to help me understand the chemistry I was working on. Dan, thank you for introducing me to Friday Pub Lunch, which I have successfully brought with me to the two following research groups in this section. Also, I still have in my possession the Aqua cassette tapes we would non-ironically listen to while working in lab.

In the final of my pre-graduate research experiences, I would like to everybody with whom I worked in Prof. Benjamin Lear's lab at the Pennsylvania State University. Ben, the freedom you afforded me to tackle whatever lab problem I felt was most interesting, and confidence you showed in me to assemble the resources I would need, is what convinced me to pursue a graduate degree. I would like to thank you and my lab mates during my time in the Lear group, Dr. Angela Birschoff, Dr. Juyeong Kim, Josh Wrubel, and particularly my office mates Dr. Andrea Giordano and Dr. Katie Haas, for making the lab a welcoming, supportive, and fun place to do research. It made me look forward to showing up to work every day.

Part of what has made the Chemistry Department at the University of Wisconsin-Madison a top research program is the incredible faculty, staff, and students it has been able to attract. It is a shame that as I leave, the current political climate in Wisconsin threatens the ability of the department to continue to do so. However, during my time here I have had the benefit of working with some of the best the University of Wisconsin-Madison has to offer. To my research advisor, Prof. Danny Fredrickson, thank

you for accepting me into your research group and offering your support during the trials and tribulations of graduate school. Working with you and the research group that you've assembled has shaped how I approach scientific dilemmas, and made me cognizant of both my strengths and weaknesses as I move forward with my scientific career. I am grateful for the future that working in your lab has afforded me and am excited to see where your research directions take you. I would also like to thank all of the members of the Fredrickson Group (current and former) with whom I've had the pleasure of working for their patience and support: Dr. Rie Fredrickson, Dr. Tim Stacey, Dr. Veronica Berns, Dr. Amelia Hadler, Kale Engelkemier, Yiming Guo, Vincent Yannello, Anastasiya Vinokur, Katerina Hilleke, Gordon Peterson, Leland Martin, Hillary Mitchel Warden, Nicholas Harris, Arthur White, Alexandra Tamerius, and Dan Kikuchi. Detailing the significant interactions I've had with all of you would be a thesis in itself. It seems needless to say, but I would like to say it anyway, that the varied expertise and experiences that you've all brought to our research group have had a profound impact on the direction my work and life has taken during my time here. It is hard for me to imagine a better group of people to call my lab mates (and friends) during my graduate degree - as is demonstrated by all the memories we share both in and outside of the chemistry building. I would like to thank in particular Kale Engelkemier and Yiming Guo, who both joined the research group at the same time I did. I can earnestly say that I would not have been as successful in my graduate career had I not had both of you providing assistance the entirety of the way.

To the staff with whom I've interacted in the UW Chemistry machine shop (Matt Martin and Steve Myers), electrical shop (Bill Goebel), glass shop (Tracy Drier) and X-ray Diffraction labs (Dr. Ilia Guzei), thank you for donating all of your expertise as I struggled to design experiments and keep our lab equipment running. Also, thank you to Philip Gopon and Prof. John Fournelle in the UW-Madison

Geology's SEM lab for all of their help in preparing samples for and performing SEM and EDS analysis. I always looked forward to any chance that I had to come talk with you guys.

Lastly, to address some of the people who I have not been a part of my life in a research capacity during my time here, but have been pivotal to my success. Ambar Rana, Julia Nault, Travis Sunderland, and Julia Wildt, having all of you around during my graduate degree has made the city of Madison, WI feel like home. To my friends not here in Madison with whom I'm in constant contact, Brandon Lusk, Justin and Jason Owlett, Ben and Jordan Sawyer, Kyle Borden, and Luke Trynovich, your general indifference as to whether or not I obtained a PhD has been a needed reminder that what I do does not define the entirety of who I am - thank you. Floriana Foarta, thank you for your love, support and calm understanding over the past five years. I can always count on you to listen when I need it, and tell me that I'm being unreasonable when necessary Finally, to my brother, Nathan Kilduff, and parents, James and Judy Kilduff, thank you for the unwavering support you've given me throughout my entire life. I wouldn't even have had the opportunity meet any of the aforementioned people had it not been for the remarkable sacrifices you made and effort you expended to ensure that I had a chance to succeed. I will be forever grateful

In conclusion to this lengthy acknowledgements section, I must remark that it is difficult for me to believe that I could possibly be as fortunate in finding such a high caliber of mentors and friends in the next stage of my life, as I have been up until now.

Table of Contents

Abstract i

Acknowledgements iv

Table of Contents viii

List of Figures xvi

List of Tables xxiiii

1 Introduction 1

1.1 The Challenges and Rewards of Structural Control in Intermetallics 1

1.2 Building Complexity from Simple Structural Fragments 3

1.3 Higher Dimensional Avenues to Structural Complexity 15

1.4 Outline of this Thesis 23

1.5 References 26

2 Progress in Visualizing Atomic Size Effects with DFT-Chemical Pressure Analysis: From Isolated Atoms to Trends in AB_5 Intermetallics 29

2.1 Abstract 29

2.2 Introduction 31

2.3 Computational Procedures 34

2.4 Grid Unwarping near Atomic Centers 35

2.5	Grid Unwarping between Atoms	41
2.6	Hirshfeld-inspired Contact Volumes	45
2.7	Stability Trends in AB_5 Intermetallics	53
2.8	Conclusion	62
2.9	Acknowledgements	63
2.10	References	64

3	**Isolobal Analogies in Intermetallics: The Reversed Approximation MO Approach and Applications to $CrGa_4$ and Ir_3Ge_7-type Phases**	69
3.1	Abstract	69
3.2	Introduction	70
3.3	Technical Procedures	74
3.4	The Reversed Approximation MO Approach	75
3.4.1	The raMO Procedure	75
3.4.2	Quantitative Analysis of raMO Results	81
3.5	$CrGa_4$ as an 18 Electron Compound	82
3.6	Electron Counting in the Ir_3Ge_7-Type	87
3.7	Project DOS of raMO Functions	95
3.8	raMO Analysis and Electron Count Ranges	98
3.9	Conclusions	100
3.10	Acknowledgements	103

3.11 References 103

4 Defusing Complexity in Intermetallics: How Covalently Shared Electron Pairs Stabilize the FCC Variant $Mo_2Cu_xGa_{6-x}$ ($x \approx 0.9$) 107

4.1 Abstract 107

4.2 Introduction 108

4.3 Experimental Section 110

4.3.1 Synthesis 110

4.3.2 Single Crystal X-ray Diffraction Analysis 111

4.3.3 Powder X-ray Diffraction Analysis 112

4.3.4 Energy Dispersive X-ray Spectroscopy 113

4.3.5 DFT-Calibrated Hückel Calculations 114

4.4 Results and Discussion 115

4.4.1 The Crystal Structure of $Mo_2Cu_{0.9}Ga_{5.1}$ 115

4.4.2 Electronic Psuedogaps in $Mo_2Cu_xGa_{6-x}$ and $TiAl_3$-type Phases 117

4.4.3 Localized Bonding Scheme from a Reversed Approximation Molecular Orbital Analysis 119

4.4.4 Comparison to Previous Bonding Schemes Proposed for the $TiAl_3$ Structure Type 126

4.5 Conclusions 127

4.6 Acknowledgements 129

4.7 References 130

5 Chemical Pressure-Driven Incommensurability in $CaPd_5$: Clues to High Pressure Chemistry Offered by Complex Intermetallics 134

5.1 Abstract 134

5.2 Introduction 136

5.3 Experimental Section 139

5.3.1 Synthesis 139

5.3.2 Single Crystal X-Ray Diffraction Analysis 140

5.3.3 Powder X-Ray Diffraction Analysis 140

5.3.4 Energy Dispersive X-Ray Spectroscopy 142

5.3.5 Electronic Structure Investigations into the Stability of $CaCu_5$-type Phases under Pressure 142

5.3.6 Determination of Atomic Charges and Free Ion Electron Density Profiles 143

5.3.7 DFT-Chemical Pressure Calculations 144

5.4 Stability of the $CaCu_5$-Type under Pressure 145

5.5 The Incommensurate Structure of $CaPd_{5+x}$ 149

5.5.1 Synthetic Results and Preliminary Crystal Examination 149

5.5.2 The Average Structure 152

5.5.3 The Modulated Structure of $CaPd_{5+x}$ ($x \approx 0.22$) 154

5.6 Chemical Pressure Relief in $CaPd_{5+q/2}$ 163

5.7 Conclusions 168

5.8 Acknowledgements 170

5.9 References 171

6 Homoatomic Clustering T_4Ga_5 (T = Ta, Nb, Ta/Mo): A Story of Reluctant Intermetallics Crystallizing in a Binary Structure Type **176**

6.1 Abstract 176

6.2 Introduction 177

6.3 Experimental Section 179

6.3.1 Synthesis 179

6.3.2 Single Crystal X-ray Diffraction Analysis 180

6.3.3 Powder X-ray Diffraction Analysis 181

6.3.4 Energy Dispersive X-ray Spectroscopy 181

6.3.5 Electron Probe Microanalysis 182

6.3.6 Electronic Structure Calculations 184

6.4 Results and Discussion 185

6.4.1 Synthesis and Identification of Ta_4Ga_5-type Phases 185

6.4.2 Structural Description of the Ta_4Ga_5 type 187

6.4.3 Visualizing Elemental Domains within the Ta_4Ga_5 Structure 189

6.4.4 The Electronic Structure of Ta_4Ga_5 193

6.4.5 Reversed Approximation MO Analysis of Ta_4Ga_5 197

6.5 Conclusions 203

6.6 Acknowledgements 206

6.7 References 206

A Supporting Information for Chapter 2

A.1 Detailed Technical Procedures

A.2 Structural Parameters

A.3 Discussion of the Prevalence of Highly Positive CP Features in the Atomic Core Regions That Are Orientated Between Internuclear Vectors, Rather Than Along Them

A.4 Voxel Volume Calculation in Distorted Grid

A.5 References

B Supplemental Information for Chapter 3

B.1 Distinction Between the NBO and raMO Analysis

B.2 Computation Details

C Supplemental Information for Chapter 4

C.1 Crystallographic Tables

C.2 Details of Cu Atom Assignment

C.3 Powder X-Ray Diffraction

C.4 Computational Details and Optimized Geometries

C.5 DFT-Calibrated Hückel Parameters

C.6 Comparison of GGA-DFT and DFT-Calibrated Hückel DOS Distributions

D Supplemental Information for Chapter 5

D.1 Crystallographic Tables for the Average Structures of $CaPd_{5+q/2}$

D.2 Powder X-Ray Diffraction Pattern of $CaPd_{5+q/2}$

D.3 Crystallographic Information Tables for the (3+1)D Model of $CaPd_{5+q/2}$

D.4 Observed Fourier Electron Map Cross Sections Centered on Atomic Positions in $CaPd_{5+q/2}$

D.5 Interatomic Distances in $CaPd_{5+q/2}$

D.6 Discussions of Pd1 and Pd2 Atomic Displacement Parameters

D.7 Discussion of the Relationship Between the q Vector and Stoichiometry

D.8 Computational Details and Optimized Geometries for Chemical Pressure Calculations

D.9 Examination of the Role of Ionic Charge in the Integrated Chemical Pressure Scheme

D.10 Computational Details and Optimized Geometries for Variable Pressure Calculations

D.11 Energy vs Volume Curves and Vinet Equations of State Parameters

E Supplemental Information for Chapter 6

E.1 Crystallographic Information

E.2 GGA-DFT Optimized Geometries

E.3 DFT-Calibrated Hückel Parameters

E.4 Comparison of GGA-DFT and DFT-Calibrated Hückel DOS Curves for Nb_4Ga_5

E.5 Additional Results from the raMO Analysis of Ta_4Ga_5

List of Figures

Chapter 1

1.1	Crystals Formed by Binary and Ternary Combinations of Ta, Al, and Cu	2
1.2	Crystal Structures of Ga Rich Early and Mid-row Transition Metal - Gallides	4
1.3	$TiAl_3$-/$PtHg_4$-Type Intergrowth Features in the Crystal Structure of V_8Ga_{41}	5
1.4	Electronic DOS Curves for Observed and Hypothetical $TiAl_3$-, $PtHg_4$-, and V_8Ga_{41}-Type Gallides	7
1.5	Chemical Pressure Schemes of the $TiAl_3$-Type $NbGa_3$ and $PtHg_4$-Type $CrGa_4$ Structures	8
1.6	Chemical Pressure Scheme of V's Coordination Environment in V_8Ga_{41}	10
1.7	Crystal Structure of $Mo_2Cu_{0.9}Ga_{5.1}$	12
1.8	raMO reconstructions of a Single Nb Atom's s, p, and d Orbitals in $NbGa_3$	13
1.9	Summary of the Synthetic and Theoretical Results Stemming from the Exploration of Structural Plasticity in V_8Ga_{41}	14
1.10	Structure and Chemical Pressure Scheme of the $CaCu_5$-Type $CaPd_5$ Structure	15
1.11	Chemical Pressure-Driven Structural Plasticity in the Formation of Ca_2Ag_7	16

1.12	The Pressure Dependence for the GGA-DFT Reaction Enthalpy for the Decomposition of $CaCu_5$-Type Phases into a Ca_2Ag_7-Type Superstructure, with an Elemental Transition Metal Side Product	18
1.13	The Average Structure of $CaPd_{5+x}$ Determined from the Main Reflections of Its Diffraction Pattern	19
1.14	The Distorted Hexagonal Net Created by the Pd Atoms Whose Interatomic Spacing Along *y* is Incommensurate with That of the $CaCu_5$-Type Slabs in $CaPd_{5+x}$	20
1.15	Chemical pressure (CP) as a Driving Force for the Incommensurate Spacing of the Atoms in the Layers Between $CaCu_5$-Type Slabs in $CaPd_{5+x}$.	21
1.16	Summary of the Synthetic and Theoretical Results Stemming from the Exploration of Structural Plasticity in V_8Ga_{41}	23

Chapter 2

2.0	Schematic Illustration of Chemical Pressure in an AB_5 Compound of the $AuBe_5$ Structure Type	30
2.1	Examples of Structure Types Whose Stability Ranges are Empirically Connected to Atomic Size	35
2.2	DFT-Chemical Pressure (CP) Maps for Individual Atoms Isolated in Large Unit Cells	39
2.3	Cross Sections for the DFT-CP Maps of a Variety of Intermetallic Phases	44
2.4	Comparison of the Integrated DFT-CP Anisotropies and Contact Volumes for $CaPd_2$	48
2.5	Comparison of DFT-CP Anisotropy Schemes Calculated $CaAu_5$	55
2.6	Effect of the Use of Hirshfeld-Inspired Contact Volumes on the Integrated DFT-CP Results for the $AuBe_5$-Type $CaAu_5$ Structure	57
2.7	DFT-CP Analysis of the AB_5 Structure Types $CaCu_5$ and $AuBe_5$	59

Chapter 3

3.0	Schematic Illustration of the Bonding in Os_3Sn_7 as Revealed by the raMO Approach	70
3.1	Compounds Whose Bonding Will Be Investigated Using the Reverse Approximation Molecular Orbital (raMO) method in Chapter 3	74
3.2	The raMO Procedure Illustrated with the Analysis of a π-Bond in 1,3-Butadiene	77
3.3	raMO Reconstruction of the Bonding and Antibonding Functions of a π-Bond Using the Unoccupied MOs of 1,3-Butadiene	80
3.4	raMO Analysis Revealing $CrGa_4$ to be an 18 Electron Compound	83
3.5	Comparison of the GGA-DFT DOS Distribution Calculated for $CrGa_4$ with Energies of the Cr 3d-Based Functions Obtained from a raMO Analysis of the Occupied Bands of a DFT-Calibrated Hückel Calculation on $CrGa_4$	85
3.6	raMO Analysis of the Ir_3Ge_7-Type Os_3Sn_7, Using the 5d, 6s, and 6p Orbitals of a Single Os atom as Target Eigenstates	89
3.7	raMOs Obtained from the Occupied Crystal Orbitals of Os_3Sn_7, Using the Molecular Orbitals of an Os Dimer as Target Eigenstates	92
3.8	A Second Iteration of raMO Analysis on the Remainder Functions of Os_3Sn_7	94
3.9	llustration of the Use of raMO Functions in DOS Analysis	96
3.10	Comparison of the raMOs for the Transition Metal Dimers in the Ir_3Ge_7-Type Phases Os_3Sn_7 and Ir_3Sn_7	98
3.11	Summary of the Use of the raMO Analysis to Iteratively Reduce the Full Electronic Structure of an Intermetallic Phase into a Series of Subsystems Described by Model MO Diagrams	100

Chapter 4

4.0	Schematic Illustration of the Ga Supported Isolobal Mo – Mo σ-Bonding in $Mo_2Cu_{0.9}Ga_{5.1}$ as Revealed by raMO Analysis	108
4.1	The Crystal Structure of $Mo_2Cu_{0.9}Ga_{5.1}$	117
4.2	DFT-Calibrated Hückel DOS Distributions of $TiAl_3$-Type $NbGa_3$, a Hypothetical $MoGa_3$ Phase in the $TiAl_3$-Type, and an Ordered Model of $Mo_2Cu_{0.9}Ga_{5.1}$	118
4.3	raMO Reconstructions of a Single Nb Atom's s, p, and d Orbitals in $NbGa_3$	120
4.4	Covalently Shared Electron Pairs Along Nb-Nb Contacts in $NbGa_3$	122
4.5	Reconstructions of σ and σ^* Orbitals for a Pair of T Atoms in a Series of Structures Based on the $TiAl_3$ Type	124
4.6	Summary of the Electron Counting Scheme Obtained for 14-Electron $TiAl_3$-Type Phases, as Exemplified by $NbGa_3$	125

Chapter 5

5.0	Illustration of the Chemical Pressures (CP) Quadrupoles in $CaPd_{5.22}$ Which Incite the Incommensurate Modulations in Its Structure	135
5.1	The Crystal Structure and Chemical Pressure (CP) Scheme of $CaPd_5$ in the $CaCu_5$ Structure Type	137
5.2	Ca_2Ag_7 (Yb_2Ag_7 Type) Viewed as the Product of a Chemical Pressure (CP)-Driven Transition Away from a Hypothetical $CaCu_5$-Type $CaAg_5$ Phase	139
5.3	The Pressure Dependence for the GGA-DFT Reaction Enthalpy for the Decomposition of $CaCu_5$-Type Phases into a Ca_2Ag_7-Type Superstructure, with an Elemental Transition Metal Side Product	147
5.4	Satellite Reflections in the Diffraction Patterns of Single Crystals of $CaPd_{5+x}$, Indicating the Presence of Incommensurate Modulations	150

5.5	The Average Structure of $CaPd_{5+x}$ Determined from the Main Reflections of Its Diffraction Pattern	153
5.6	Modulation of the Atomic Positions in the Interface Layers Between $CaCu_5$-Type Slabs in $CaPd_{5+x}$	156
5.7	Atomistic Modelling of the (3+1)D Electron Density Features in the Layers Separating $CaCu_5$-Type Slabs in $CaPd_{5+x}$	158
5.8	The Distorted Hexagonal Net Created by the Pd Atoms Whose Interatomic Spacing Along *y* is Incommensurate with That of the $CaCu_5$-Type Slabs in $CaPd_{5+x}$	162
5.9	DFT-Chemical Pressure (CP) Analysis of the Transition Between a $CaCu_5$-Type $CaPd_5$ Structure and a Commensurate Approximant to $CaPd_{5+q/2}$	165
5.10	Chemical Pressure (CP) as a Driving Force for the Incommensurate Spacing of the Atoms in the Layers Between $CaCu_5$-Type Slabs in $CaPd_{5+x}$	167

Chapter 6

6.0	Schematic Illustration of the Ga Supported T – T Bonding in Ta_4Ga_5 as Revealed by raMO Analysis	177
6.1	Structural Features of the Binary Structure Type Adopted by Ta_4Ga_5 and Nb_4Ga_5, Illustrated by Its Hierarchical Relationship to the $MnAlCu_2$ (Heusler) Type	179
6.2	Powder X-Ray Diffraction Pattern of Ta_4Ga_5	183
6.3	The Primitive Cubic Substructure of the Ta_4Ga_5 Structure Type	188
6.4	The Full Crystal Structure of Ta_4Ga_5, Viewed in Terms of the Filling of a Primitive Cubic Host Substructure	189
6.5	Coordination Environments for the Seven Symmetry-Distinct Ta Sites in Ta_4Ga_5	191

6.6	Coordination Environments of the Ga Sites in Ta_4Ga_5, Which Exhibit Clustering of the Ta Neighbors into Rings and Partial Cages	191
6.7	Geometrically Constructed Surface Separating the Ta_4Ga_5 Structure into Ta and Ga Domains	192
6.8	Comparison of the DOS distributions for Ta_4Ga_5 using GGA-DFT and DFT-Calibrated Simple Hückel Models	194
6.9	Crystal Orbital Hamilton Population (COHP) Curves for the Homoatomic and Heteroatomic Interactions in Ta_4Ga_5	195
6.10	raMO Reconstructions of the Ta4 Site's Valence s, p, and d Orbitals	199
6.11	raMO Functions Generated from the Occupied Crystal Orbitals of Ta_4Ga_5 Using the Valence Orbitals of an Atom on the Ta2 Site as Target Eigenstates	201
6.12	raMO Functions Generated Using the Valence Atomic Orbitals of the Ga1 (left) and Ga2 (right) Sites in Ta_4Ga_5 as Target Eigenstates	201
6.13	Illustration of Preferential support given by bridging Ga atoms to Ta-Ta bonding orbitals over their Ta-Ta antibonding counterparts	202

Appendix A

A.1	Positive Chemical Pressure is for a Series of Solid State Structures	218
A.2	The Difference Between the Local Potential Surfaces of Elemental Silicon from the Expanded Unit Cell volume to the Contracted Unit Cell Volume, Corrected for Distortion Using CPmap	219
A.3	The DFT-CP Anisotropies Calculated for Elemental Silicon	220

Appendix C

C.1	Powder X-Ray Diffraction Pattern for $Mo_2Cu_{0.9}Ga_{5.1}$	236

C.2 The Powder Diffraction Patterns for $Mo_2Cu_{0.5}Ga_{5.5}$, $Mo_2Cu_1Ga_5$, and $Mo_2Cu_{1.5}Ga_{4.5}$ Loading Composition 237

C.3 Electronic DOS Curves Calculated for $NbGa_3$, a Hypothetical $TiAl_3$-Type $MoGa_3$ Phase, and an Ordered Model of Mo_2CuGa_5 with GGA-DFT and Best-Fit Hückel Model 243

Appendix D

D.1 The Powder X-Ray Diffraction Pattern of $CaPd_{5+q/2}$ Shown with the Calculated Diffraction Peaks from the Average $CaPd_{5+q/2}$ Structure and the Reported $CaCu_5$-Type $CaPd_5$ Structure 246

D.2 The Functions Modelling the Atomic Positions of Ca1, Pd2, and Pd3 Overlaid on Cross Sections of the Observed Fourier Electron Density Maps 250

D.3 The Functions Modelling the Atomic Positions of Pd3, Pd4, and Pd5 Overlaid on Cross Sections of the Observed Fourier Electron Density Maps 251

D.4 The Functions Modelling the Atomic Positions of Pd6 Overlaid on Cross Sections of the Observed Fourier Electron Density Maps 252

D.5 Interatomic Distances Extracted from the (3+1D) Model of $CaPd_{5+q/2}$ as a Function of the x_4-Intercept for Each of the Symmetry-Inequivalent Atomic Domains 253

D.6 A Plot of $U_{equivalent}$ Versus x_4 Centered on x_{40} for the Atoms Pd1 and Pd2. 254

D.7 A cross section of the electron density at $x_3 = 0$ summed between $0.0 \leq x_1 \leq 0.5$ Used to Demonstrate the Derivation of $CaPd_{5+x}$'s Stoichiometry from the Modulation Vector 256

D.8 The Role Played by Ionic Charge in the Integrated CP Schemes of the Compounds (Real and Hypothetical) Presented in Chapter 5 265

D.9 Energy Versus Volume Curves for $CaCu_5$, Ca_2Cu_7, Cu, $CaPd_5$, Ca_2Pd_7, and Pd Calculated Using the PAW GGA Potentials Provided with the Vienna Ab Initio Simulation Package (VASP) 274

Appendix E

E.1	Electronic DOS Curves Calculated for Nb_4Ga_5 with GGA-DFT and a Best-Fit Hückel Model	293
E.2	raMOs Resulting from the Use of Valence Atomic Orbitals of an Atom on Ta_4Ga_5's Ta1 Site as Target Functions	294
E.3	raMO Analysis of the Ta2 Site of Ta_4Ga_5	294
E.4	raMO Analysis of the Ta3 Site of Ta_4Ga_5	295
E.5	raMO Analysis of the Ta4 Site of Ta_4Ga_5	295
E.6	raMO Analysis of the Ta5 Site of Ta_4Ga_5	295
E.7	raMO Analysis of the Ta6 Site of Ta_4Ga_5	296
E.8	raMO Analysis of the Ta7 Site of Ta_4Ga_5	296
E.9	raMO Analysis of the Ga1 Site of Ta_4Ga_5	296
E.10	raMO Analysis of the Ga2 Site of Ta_4Ga_5	296
E.11	raMO Analysis of the Ga3 Site of Ta_4Ga_5	297
E.12	raMO Analysis of the Ga4 Site of Ta_4Ga_5	297
E.13	raMO Analysis of the Ga5 Site of Ta_4Ga_5	297
E.14	raMO Analysis of the Ga6 Site of Ta_4Ga_5	297
E.15	raMO Analysis of the Ga7 Site of Ta_4Ga_5	298
E.16	raMO Analysis of the Ga8 Site of Ta_4Ga_5	298
E.17	raMO Analysis of the Ga9 Site of Ta_4Ga_5	298

List of Tables

Chapter 4

4.1 Crystallographic Information for $Mo_2Cu_{0.9}Ga_{5.1}$ 112

Chapter 5

5.1 Crystallographic Information for $CaPd_{5.219}$ 141

Chapter 6

6.1 Crystal Data for $Ta_{3.86}Mo_{0.14}Ga_5$, Ta_4Ga_5 and Nb_4Ga_5 182

6.2 Ta_4Ga_5 Atomic Coordinates and Displacement Parameters 183

Appendix A

A.1 Computational Parameters and Total Energies 211

A.2 Unit Cell Parameters for DFT-Optimized Structures 212

A.3 Atomic Coordinates for all Single-Atom Calculations 212

A.4 Atomic Coordinates for ABINIT-Optimized $SrAg_5$ Structure 212

A.5 Atomic Coordinates for ABINIT-Optimized La_5Sn_3 Structure 213

A.6 Atomic Coordinates for ABINIT-Optimized $NbGa_3$ Structure 213

A.7 Atomic Coordinates for VASP-Optimized Ni_3C Structure 214

A.8 Atomic Coordinates for ABINIT-Optimized $CaCu_5$ structure ($CaCu_5$-Type) 214

A.9 Atomic Coordinates for ABINIT-Optimized $CaCu_5$ structure ($AuBe_5$-Type) 215

A.10 Atomic Coordinates for ABINIT-Optimized $CaAu_5$ structure ($CaCu_5$-Type) 215

A.11 Atomic Coordinates for ABINIT-Optimized $CaAu_5$ structure ($AuBe_5$-Type) 216

Appendix B

B.1 Details of LDA-DFT Calculations on Structures Serving as Basis for Parameterization of Hückel Models 227

B.2 DFT-Optimized Geometry of $CrGa_4$ 227

B.3 DFT-Optimized Geometry of Os_3Sn_7 228

B.4 DFT-Optimized Geometry of Ir_3Sn_7 229

B.5 DFT-Calibrated Hückel Parameters 230

Appendix C

C.1 $Mo_2Cu_{0.9}Ga_{5.1}$ Atomic Coordinates and Displacement Parameters 231

C.2 $Mo_2Cu_{0.9}Ga_{5.1}$ Anisotropic Atomic Displacement Parameters 231

C.3 Selected Interatomic Distances for $Mo_2Cu_{0.9}Ga_{5.1}$ 232

C.4 Crystallographic Information of Several Cu Substitution Patterns 235

C.5 Details of GGA-DFT Calculations on Structures Serving as Basis for Parameterization of Hückel Models 238

C.6 DFT-Optimized Geometry of $NbGa_3$ 239

C.7 DFT-Optimized Geometry of $MoGa_3$ 239

C.8 DFT-Optimized Geometry of Mo_2CuGa_5 240

C.9 DFT-Optimized Geometry of Mo_2CuGa_5 with Cu Substituted on Selection of Ga1 Positions 240

C.10 DFT-Optimized Geometry of Mo_2CuGa_5 with Cu Substituted on Selection of Ga2 positions 241

C.11 DFT-Calibrated Hückel Parameters 242

Appendix D

D.1 Refined Atomic Coordinates for the Average $CaPd_{5+q/2}$ Structure 245

D.2 Refined Atomic Displacement Parameters for the Average $CaPd_{5+q/2}$ Structure 245

D.3 Refined Atomic Coordinates for $CaPd_{5+q/2}$ 247

D.4 Refined Atomic Displacement Parameters for $CaPd_{5+q/2}$ 247

D.5 Modulation Parameters for $CaPd_{5+q/2}$ 248

D.6 Details of LDA-DFT Calculations on Structures Serving as a Basis for Chemical Pressure Calculations 259

D.7 LDA-DFT Optimized Cell Parameters 260

D.8 LDA-DFT Optimized Atomic Positions for the $CaCu_5$-type CaT_5 Structure (T=Cu, Ag, or Pd) 260

D.9 LDA-DFT-Optimized Atomic Positions for the Commensurate Approximant of $CaPd_{5+q/2}$ ($q \approx 0.44$) 261

D.10 LDA-DFT-Optimized Atomic Positions of a Hypothetical Ca_2Ag_7-Type Ca_2Pd_7 Phase 262

D.11 LDA-DFT-Optimized Atomic Positions of Ca_2Ag_7 263

D.12 LDA-DFT-Optimized Atomic Positions of a Hypothetical Ca_2Ag_7-Type Ca_2Cu_7 Phase 264

D.13	Computational Parameters and Total Energies of Structures Serving as a Basis for Variable Pressure and Bader Charge Analysis with VASP	268
D.14	GGA-DFT-Optimized Unit Cell Parameters	269
D.15	GGA-DFT-Optimized Atomic Positions for Elemental T (T=Pd or Cu)	269
D.16	GGA-DFT-Optimized Atomic Positions for the $CaCu_5$-type CaT_5 Structure (T=Cu, Ag, or Pd)	270
D.17	GGA-DFT-Optimized Atomic Positions for the Commensurate Approximant of $CaPd_{5+q/2}$	270
D.18	GGA-DFT-Optimized Atomic Positions of a Hypothetical Yb_2Ag_7-Type Ca_2Pd_7 Phase	271
D.19	GGA-DFT-Optimized Atomic Positions of Ca_2Ag_7	272
D.20	GGA-DFT-Optimized Atomic Positions a Hypothetical Yb_2Ag_7-type of Ca_2Cu_7 Phase	273
D.21	Vinet Equation of State Parameters	275

Appendix E

E.1	Ta_4Ga_5 Atomic Coordinates and Displacement Parameters	277
E.2	Ta_4Ga_5 Anisotropic Parameters	278
E.3	Selected Interatomic Distances Ta_4Ga_5	278
E.4	Nb_4Ga_5 Atomic Coordinates and Atomic Displacement Parameters	280
E.5	Nb_4Ga_5 Anisotropic Atomic Displacement Parameters	281
E.6	Selected Interatomic Distances for Nb_4Ga_5	281
E.7	GGA-DFT-Optimized Geometry of Ta_4Ga_5	284
E.8	GGA-DFT-Optimized Geometry of Nb_4Ga_5	288
E.9	DFT-Calibrated Hückel Parameters	292

Chapter 1

Introduction

1.1. The Challenges and Rewards of Structural Control in Intermetallics

The ability to optimize atomic arrangments with respect to a property (such as catalytic activity, physical durability or biological activity) requires an understanding of the driving forces which stabilize its formation. Whether it be tuning the reactivity of a transition metal catalyst through small adjustments to the scaffolding ligand architecture,[1] adjusting the properties of a polymer through alterations to its monomer building blocks,[2] or designing small molecules specifically targeted to the structure of a biologically active site,[3,4] many fields of chemistry have demonstrated the practical benefit of obtaining a fundamental understanding of structure. Unfortunately, for one class of compounds known as intermetallics, (crystalline structures composed solely of metallic elements) this marriage of structural understanding and control remains particularly difficult.

One challenge faced by chemists and materials scientists working toward rationally modifying intermetallic structures is the task of identifying and understanding their overwhelming structural diversity. The juxtaposition of simplicity and complexity can even be observed within a single phase diagram, such as that of Ta and Al.[5] Whereas elemental Ta and Al crystallize in simple bcc[6] and fcc[7] packings respectively, the intermetallics that they form display a much wider variety of structural motifs (Figure 1.1). Thermodynamically stable products in their phase diagram range from the colored fcc variant $TaAl_3$ with 8 atoms in its unit cell,[8] to the α-Mn-type $Ta_{17}Al_{12}$ structure with 58 atoms/unit cell,[9]

culminating with the defect bcc (gray)/ α-Mn-type (blue) intergrowth structure of $Ta_{39}Al_{69}$ with 432 atoms in its basic repeating unit.[10] The addition of Cu to the mix induces further complexity, resulting for example in $Ta_{39.1}Cu_{5.4}Al_{55.4}$ whose massive unit cell is comprised of 23,134 atoms.[11,12] When structures reach this level of complexity, simply characterizing and describing their atomic arrangements (in some cases requiring the invocation of a higher dimensional space) is an arduous undertaking. Determining the source of their stability relative to simpler alternatives is even more difficult.

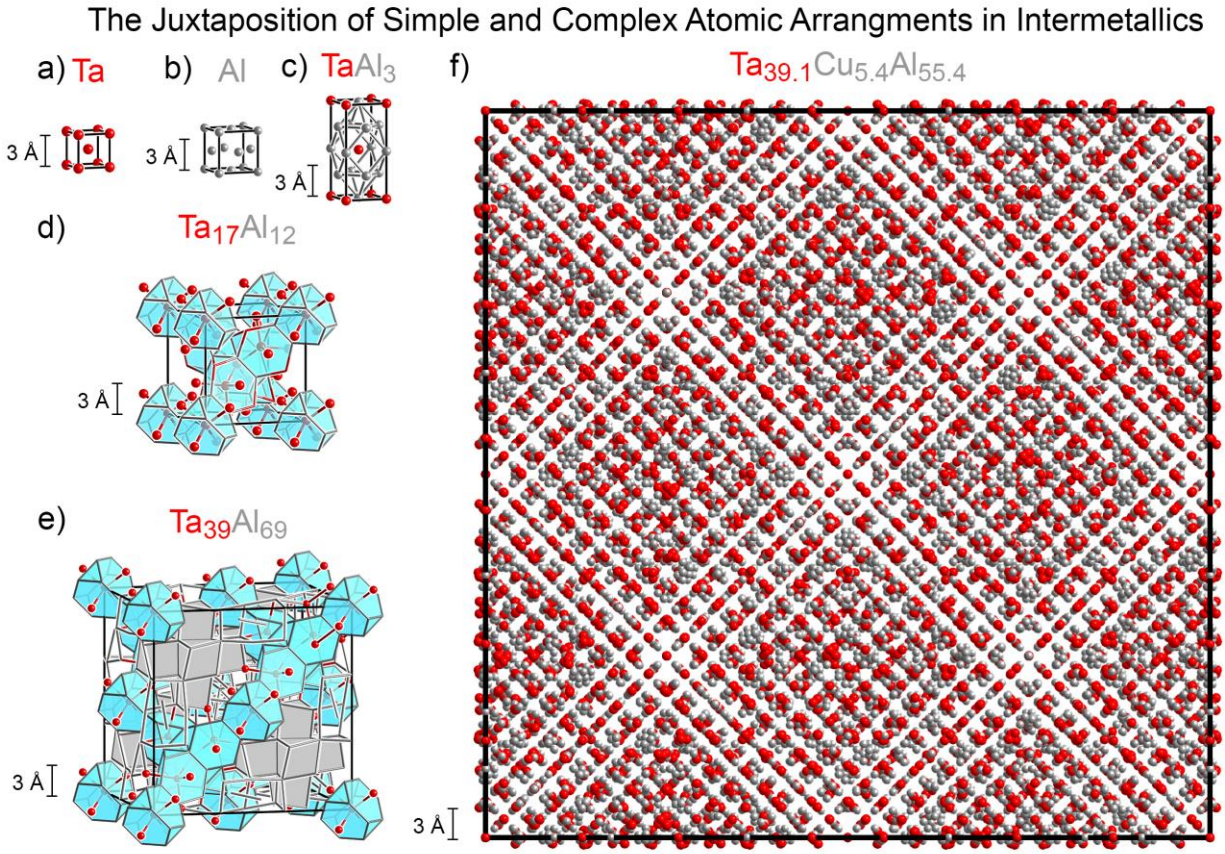

Figure 1.1. The crystals formed by binary and ternary combinations of Ta, Al, and Cu drawn at a common scale. (a) Ta forms a bcc lattice and (b) Al forms an fcc lattice. Binary combinations of the two form simple lattices such as (c) the $TiAl_3$-type $TaAl_3$ structure which is a coloring of the fcc lattice. Their binary structures can also be much more complex as in (d) the α-Mn-type $Ta_{17}Al_{12}$, shown as a network of blue Friauf polyhedra, or (e) the complex $Ta_{39}Al_{69}$ structure which manifests as intergrowth of a network the same blue Friauf polyhedra as in $Ta_{17}Al_{12}$ and a defect bcc lattice shown in gray. The addition of a small amount of copper can induce even more complexity resulting in (f) the daunting structure of $Ta_{39.1}Cu_{5.4}Al_{55.4}$ whose monstrous unit cell contains 23,124 atoms.

Despite the challenges, the possible rewards from illuminating these driving forces are enticing. A deeper understanding of the bonding at work in intermetallics may allow solid state chemists to optimize their structures for specific applications – such as inciting complexity to illicit the phonon glass electron crystal behavior which is desirable in thermoelectric materials.[13] Alternatively, one may wish to suppress superstructure formation while tuning the electronic structure of a compound for properties such as superconductivity[14] or magnetism.[15] Lastly, even more subtle structural control may desired, such as the ability to insert defect interfaces along specific crystallographic planes for applications such as hydrogen storage[16] or to obtain anisotropic transport properties.[17] Indeed, a wealth of properties lay underutilized in intermetallics due to the challenge of optimizing their structures.

1.2. Building Complexity from Simple Structural Fragments

Over the course of this thesis, we will explore one poor soul's approach to elucidating the driving forces that govern the formation of intermetallics through a combination of synthetic exploration and theoretical analysis. We will see examples of several mechanisms that work to stabilize intermetallics compounds –ranging from steric relief through superstructure formation in $CaCu_5$-type derivatives, to Ga supported isolobal transition metal – transition metal (T – T) bonds in T – Gallides. One conceptual framework that will be relied upon throughout the entirety of this work, and has proven quite powerful, is the idea of *structural plasticity* – or that complex intermetallics can be understood as intergrowths or variations of one or more structural motifs characteristic of much simpler structures that have become deformed in order to resolve some inherent stress. We have already hints of this concept in the structural description of $Ta_{39}Al_{69}$, wherein we saw that its complex structure can be understood as an intergrowth of

a defect bcc lattice shown in gray and a diamond network of Friauf polyhedra reminiscent of *α*-Mn represented in blue (Figure 1.1d). For the majority of this work, we will focus on two other model systems which were chosen because their structural chemistry lends itself to this concept: the V_8Ga_{41} type and $CaCu_5$-type variants.

The position of the V_8Ga_{41}-type structure in phase space provides clues to how we can understand its structure. Early T – Gallides form the simple $TiAl_3$-type structure (Figure 1.2, left).[18-20] It can be described as a colored fcc variant, where each T atom (red) is surrounded by a cuboctahedron of Ga atoms (blue). The cuboctahedra arrange themselves to form a body centered cell, such that a T atom lies on the corner and at (½, ½, ½) of the unit, resulting in layers of $T@Ga_{12}$ cuboctahedra perpendicular to *c*, which are shifted relative to each other by (½, ½, 0). Mid-row T – Gallides form the $PtHg_4$-type structure (Figure 1.2, right).[21,22] In this structure the Ga atoms form a primitive cubic network (gray), with Cr atoms (red)

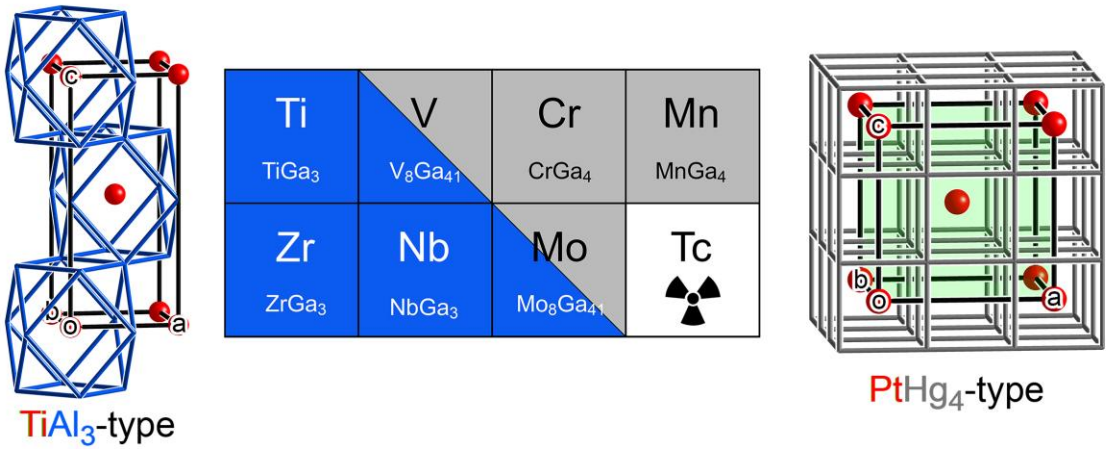

Figure 1.2. The structures of early to mid-row transition metal (T) – Gallides. Early T – Gallides (blue) form the $TiAl_3$ type whose colored fcc lattice can be described as a T atom (red) surrounded by a cuboctahedron (blue) of Ga atoms. Mid-row T atoms from the $PtHg_4$ type which can be understood as a primitive cubic lattice (gray) of Ga atoms in which ¼ of the cubes have been stuffed with a T atom (red), such that each T stuffed Ga cube shared a vertex with four others. At the slanted blue/gray between the domains of stability for compounds adopting the $PtHg_4$- and $TiAl_3$-types, we find the considerably more complex V_8Ga_{41}-type structure.

occupying vertex sharing cubes, resulting in a body centered cell. At the slanted boundary between the domains of stability for compounds adopting the $PtHg_4$- and $TiAl_3$-types, we find the considerably more complex V_8Ga_{41}-type structure which forms for combinations of V and Mo with Ga.[23,24]

The complexity of the V_8Ga_{41} type is in stark contrast with the simplicity of its neighbors. However, a close examination of the structure reveals its relation to the phases formed by other these neighbors (Figure 1.3). Tracing out the Ga – Ga contacts, one begins to perceive a simple cubic lattice (gray) embedded with a cube of T atoms (green) similar to that of the $PtHg_4$ type. In this case, however, the cube of T atoms is not body centered, but rather filled with a cuboctahedron - reminiscent of the $TiAl_3$ type (blue). In this way, the V_8Ga_{41}-type structure can be understood as a structural intermediate between the $TiAl_3$- and $PtHg_4$-types in which features of the two simpler structures are intergrown.

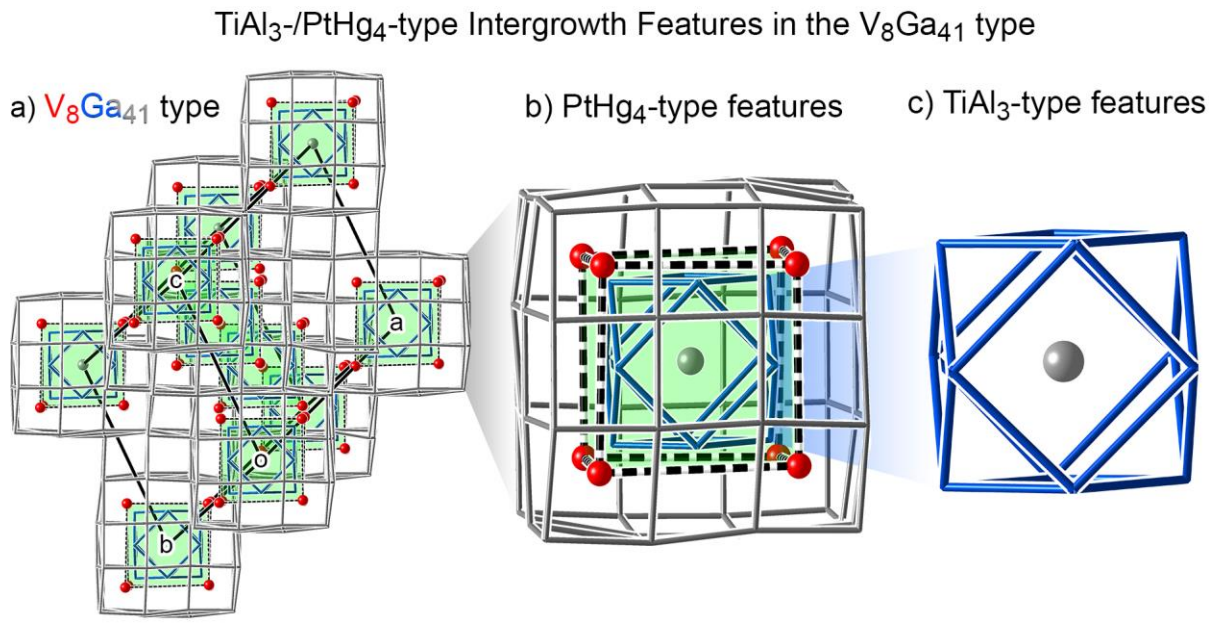

Figure 1.3. (a) The crystal structure of V_8Ga_{41}. It can be understood as a primitive cubic lattice of Ga with inclusions of (b) cubes of V atoms which are reminiscent of the $PtHg_4$ type. Rather than displaying a body centered packing, this cube of V is filled with a (c) cuboctahedron of Ga which is similar to that seen in the $TiAl_3$-type structure, albeit this time centered by Ga rather than a T atom.

Here we see the power of the concept of structural plasticity. Identifying the V_8Ga_{41}-type as an intergrowth of two simpler structure types reveals an approach to understanding its stability without tackling its unwieldy structure directly. Rather beginning with the question, "Why is the complex V_8Ga_{41} type stable," we can ask the question, "What stress in the $TiAl_3$ and $PtHg_4$ types is relieved by their intergrowth to form the V_8Ga_{41}?" An answer to this question can be found through a dialogue between theory and synthetic exploration, wherein we will use theoretical analysis to develop a hypothesis as to the driving force behind the formation of complex structures which will suggest synthetic avenues to explore. In return, the synthetic results either validate the hypotheses or point to other stabilizing interactions that need to be accounted for by theory. We begin this iterative cycle by inquiring what stabilizes the V_8Ga_{41} type.

Often the matching of a pseudogap in the electronic density of states (DOS) distributions with the Fermi energy (E_F) of a structure is indicative that its valence electron concentration has been optimized for the geometrical features it displays. Although, we do see this pseudogap/E_F matching in the electronic DOS curves of the $TiAl_3$-type $NbGa_3$, the $PtHg_4$-type $CrGa_4$, and the V_8Ga_{41} structures (Figure 1.4), suggesting an optimized electronic structure plays a role in stabilizing these structures (as we will explore further in Chapters 2 and 3), it fails to explain all of the observed trends in these T – Gallides. An isoelectronic substitution of Nb with V in the $TiAl_3$-type $NbGa_3$ fails to form $TiAl_3$-type VGa_3 despite the fact that GGA-DFT calculations indicate is E_F would also align with a pseudogap in its electron DOS distribution (Figure 1.4a). Instead, a VGa_3 sample would phase segregate into V_8Ga_{41} and V_2Ga_5. The same can be stated for the isoelectronic substitution of Cr for Mo to form a $PtHg_4$-type $MoGa_4$ structure

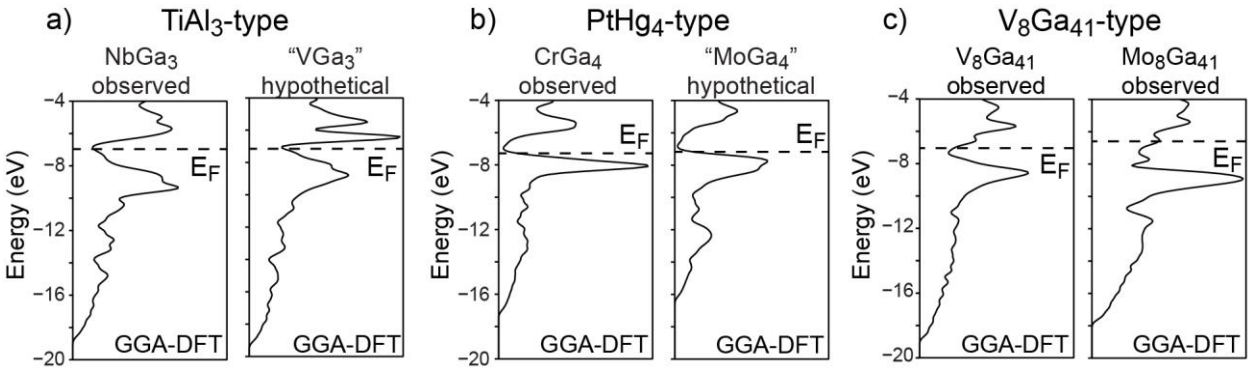

Figure 1.4. Electronic DOS curves for some observed and hypothetical $TiAl_3$-, $PtHg_4$-, and V_8Ga_{41}-type structures. (a) Both the observed $TiAl_3$-type $NbGa_3$ and unobserved $TiAl_3$-type VGa_3 structure display deep pseudogap matching their Fermi energies in their DOS, suggested their structures are optimized for their electron count. The same can be said for (b) the observed $PtHg_4$-type $CrGa_4$ and unobserved $MoGa_4$. What then prevents a $TiAl_3$-type VGa_3 or $PtHg_4$-type $MoGa_4$ from forming? (c) Even more curiously, the DOS curves the observed V_8Ga_{41}-type structure which forms for combinations of V and Mo with Ga appears to be stable invariant of whether their Fermi energies lie in a pseudogap or not.

(Figure 1.4b). Furthermore, although the E_F of V_8Ga_{41} lies within a pseudogap in its DOS, this isn't true for the V_8Ga_{41}-type Mo_8Ga_{41}, whose E_F is placed well above the pseudogap in its DOS (Figure 1.4c). We therefore turn our attention to another factor which determines the stability of intermetallics: atomic size effects.

The multiple electron counts at which the V_8Ga_{41}-type is stable, and the similar metallic radii of V and Mo (1.36 Å and 1.39 Å, respectively), suggest that atomic size plays a role in the formation of the V_8Ga_{41} type. In order to elucidate the role of atomic size effects, we turn to DFT-Chemical Pressure (CP) analysis which translates the output of DFT calculations into a map interatomic pressures. We will discuss the details of CP analysis in Chapter 3 – at this point, however, will we simply see how these CP schemes can be used to understand the compromises made by these close packed structures as they attempt to optimize the interatomic interactions of all of their constituent atoms simultaneously.

Figure 1.5 presents the output of CP analysis on the observed $TiAl_3$-type $NbGa_3$ phase. The positions of the Nb (red) and Ga atoms (gray) are represented by transparent spheres. Within these spheres, white and black CP lobes can be seen to point along interatomic contacts. Black, negative pressure lobes point along the Ga – Ga contacts with components along *c*, indicating that it would be energetically beneficial for these distances to contract. The degree to which this contraction is favorable is represented by the distance between the center of the atomic position and the surface of the lobe along any direction. The contraction of these contacts is prevented by the white, positive chemical pressure lobes between the Nb atoms and all of their Ga contacts and along the Ga – Ga contacts in the *ab* plane – all of these interatomic contacts are too short and would be stabilized by elongation.

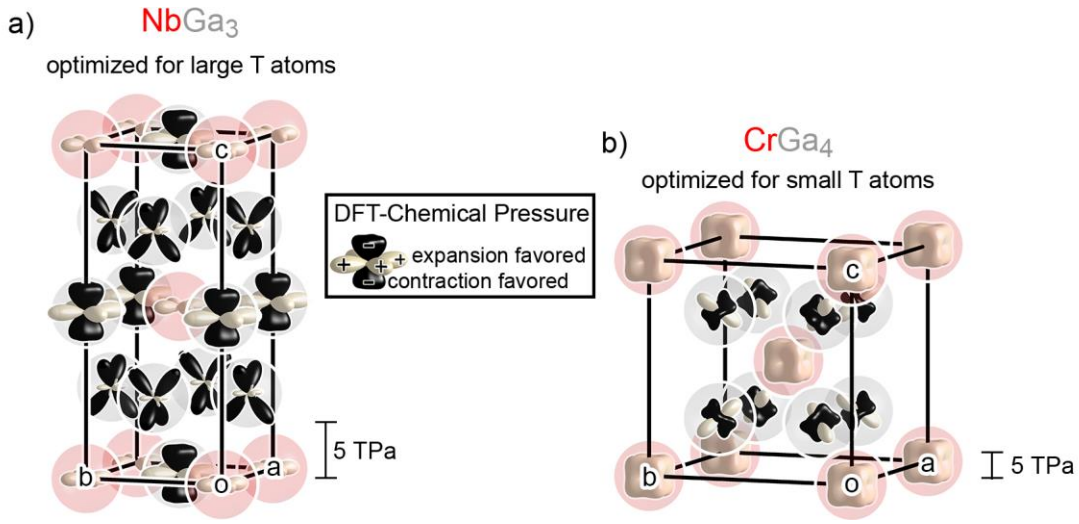

Figure 1.5. Chemical Pressure (CP) schemes for (a) the $TiAl_3$-type $NbGa_3$ and (b) the $PtHg_4$-type $CrGa_4$. White lobes represent directions along which expansion would be favorable (positive pressure), whereas black lobes represent directions where the contacts are too elongated (negative pressure). From these schemes we can see that placing a smaller T atom in the $NbGa_3$ would allow the cuboctahedron to contract, which simultaneous relieves negative Ga – Ga pressures and exacerbates positive Ga – Ga pressures. By decreasing the T atom coordination environment from 12 in the $TiAl_3$-type to 8, the $PtHg_4$-type $CrGa_4$ structure prevents any Ga – Ga positive pressures – however its cube T atom coordination environment would experience large negative Ga – Ga pressures if larger T atoms were accommodated.

From the CP scheme of $NbGa_3$, we can draw some conclusions about the T atoms for which the $TiAl_3$ type should be stable. With the 12 coordinate T atom environment offered by the Ga atoms, the $TiAl_3$-type structure appears to be ideal for large T atoms. Although some of Ga atoms express negative pressures along their Ga – Ga contacts, attempts to relieve them by allowing the Ga coordination environment to contract around a smaller T atom would have the destabilizing consequence of increasing positive CP along other Ga – Ga contacts. One way to avoid exacerbating the positive Ga - Ga CPs while simultaneously relieving the negative Ga – Ga CPs is to remove Ga atoms from T atom's coordination environment as the size of T atom decreases.

Indeed, the CP scheme of the $PtHg_4$-type $CrGa_4$ indicates that this is the exact mechanism it used to accommodate the relatively smaller Cr atom into its structure. The 8 coordinate T atom environment in the $CrGa_4$ displays negative CPs along all of its Ga – Ga contacts. Preventing the Ga – Ga contacts from contracting are the positive pressures between the Cr and Ga atoms. The conclusion drawn from the CP scheme of $CrGa_4$ is the opposite of that gleaned from the CP analysis of $NbGa_3$ – the $PtHg_4$ type structure is optimized for small T atoms. Whereas replacing Cr with a smaller atom would relieve both positive and negative CPs in the structure, a larger T atom would only serve to further push the Ga atoms further apart weakening their interactions with each other.

Equipped with a better understanding of the role of the atomic size in the $TiAl_3$ and $PtHg_4$ types, we can now begin to understand the role of the $TiAl_3$-/$PtHg_4$-type intergrowth features in V_8Ga_{41}. The CP schemes of $NbGa_3$ and $CrGa_4$ suggest that the metallic radii of V and Mo (1.34 Å and 1.39 Å), which lie neatly between that of Nb (1.46 Å) and Cr (1.28 Å) make them incompatible with the 12- and 8-coordinate T atom environments in the $TiAl_3$- and $PtHg_4$-types, respectively. The $TiAl_3$-/$PtHg_4$-type

intergrowth features in V_8Ga_{41}-type provide an intermediate 10-coordinate T atom environment (Figure 1.6).

The CP distribution around the 10-coordinate V atom in V_8Ga_{41} appears to have succeeded in resolving the difficulties of introducing a smaller or larger T atom into the $NbGa_3$ or $CrGa_4$, respectively. All of the Ga atoms have negative pressure lobes pointing along their Ga – Ga contacts, indicating that by removing 2 atoms from the T atoms coordination environment relative to the $TiAl_3$ type, the structure has succeeded in circumventing the introduction of new positive Ga – Ga pressures while accommodating the smaller V atom. On the other hand, the 2 extra Ga atoms in the V atoms coordination environment relative to $PtHg_4$ type allow the structure to optimize its Ga – Ga contacts without exacerbating positive V – Ga pressures.

The CP analysis of these early to mid-row T – Gallides demonstrates the concept of structural

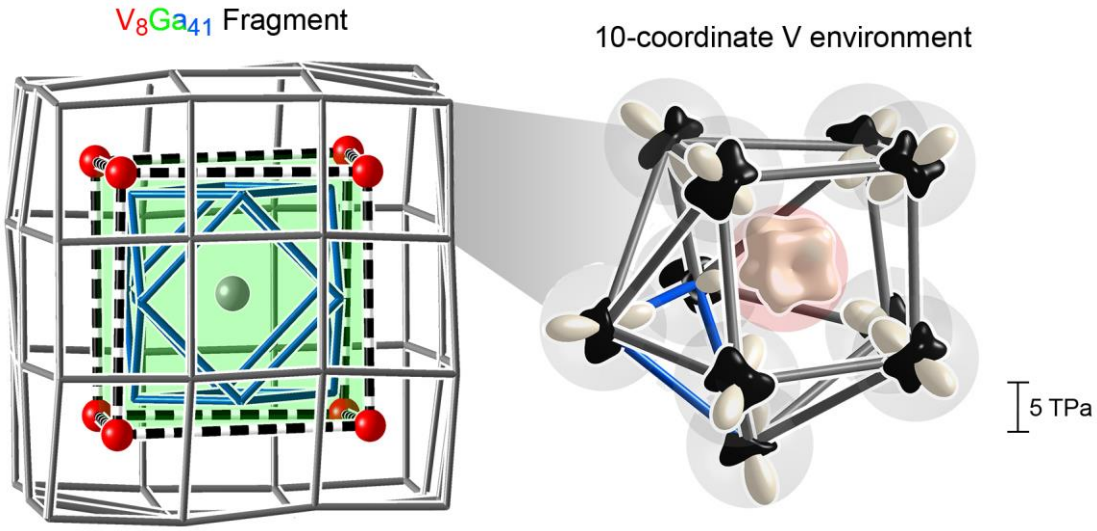

Figure 1.6. A Chemical Pressure scheme for one of the V coordination environments in the V_8Ga_{41}-type structure. The $TiAl_3$-/$PtHg_4$-type intergrowth in V_8Ga_{41} provides a 10-coordinate T atom environment, intermediate between those offered in the $TiAl_3$ or $PtHg_4$ types. The CP scheme reveals that the V_8Ga_{41} type has succeeded in putting more Ga atoms in the V coordination environment relative to the $PtHg_4$ type without substantially exacerbating T – Ga positive CPs or creating Ga – Ga positive CPs.

plasticity at work in the structure of V_8Ga_{41}. This complex structure can be understood as a $TiAl_3$-/$PtHg_4$-intergrowth which forms to relieve the stress induced by placing an overly small or overly large T atom into the $TiAl_3$ or $PtHg_4$ type, respectively. It also provides clear guidelines by which we can test this understanding through synthetic exploration. Doping small amounts of relatively larger atoms onto the T atom sites, or relatively smaller atoms onto the Ga sites in the V_8Ga_{41} should stabilize larger coordination environments – resulting in the expression of more $TiAl_3$-type features. Alternatively, placing relatively smaller atoms onto the T atoms sites, or larger onto the Ga sites should result in more $PtHg_4$-type features.

Following this theoretical guidance provided by Chemical Pressure analysis, we added small amounts of Cu, whose smaller metallic radii relative to Ga was expected to drive the formation of $TiAl_3$-type features, to combinations of Mo and Ga. This synthetic exploration resulted in the $TiAl_3$-variant $Mo_2Cu_xGa_{6-x}$ ($x \approx 0.9$), herein referred to as $Mo_2Cu_{0.9}Ga_{5.1}$ (Figure 1.7). Its structure can be derived from that of a hypothetical $TiAl_3$-type $MoGa_3$ by randomly substituting Cu onto approximately 45% of the Ga atom positions in every other Ga square net along *c*. The Mo and Ga atoms then relax in the neighboring layers – with the Ga atoms collapsing slightly toward the Cu substituted layer while the Mo atoms retreat away. Not only do the $TiAl_3$-type features in $Mo_2Cu_{0.9}Ga_{5.1}$ agree with our interpretation of the CP analysis, but they also suggests further sources of stability for $TiAl_3$ type structures that should be explored by theoretical analysis.

The composition and structure of $Mo_2Cu_{0.9}Ga_{5.1}$ hints that the atomic size is not solely responsible for stabilizing this $TiAl_3$ variant. The Cu/Ga ratio in this structure leads to a valence electron concentration of 14.1 electrons/T atom – suspiciously similar to that of $NbGa_3$ (14 e^-/T atom). Indeed, electronic structure calculations reveal that the E_F of both structures align with deep pseudogaps in their DOS

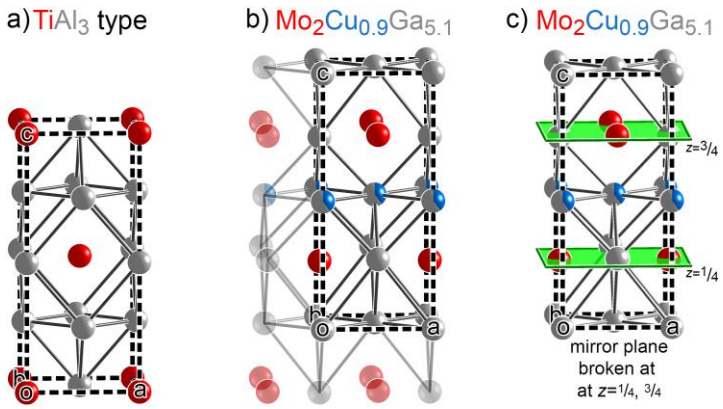

Figure 1.7. The crystal structure of $Mo_2Cu_{0.9}Ga_{5.1}$, a ternary variant of the $TiAl_3$ structure type. (a) The $TiAl_3$ structure type. (b) An expanded view of the $Mo_2Cu_{0.9}Ga_{5.1}$ structure illustrating its relationship to the $TiAl_3$ type. The Ga atoms, originally at z = 3/4 are mixed with approximately 45% Cu. This substitution breaks the body centering of the $TiAl_3$-type cell leading to the primitive unit cell of $Mo_2Cu_{0.9}Ga_{5.1}$ shown. (c) One unit cell of the $Mo_2Cu_{0.9}Ga_{5.1}$ structure.

distributions, suggesting that ~14 e^-/T atom represents a magic electron count for the $TiAl_3$ type. The large contributions from the T atom d orbitals around the E_F suggest that the $TiAl_3$ type's stability may be tied to an optimization of the T atoms bonding. Using the reversed approximation Molecular Orbital (raMO) method, discussed in detail in Chapter 2, we investigate the role of the T atom orbitals in the bonding of $NbGa_3$ and an idealized version of $Mo_2Cu_{0.9}Ga_{5.1}$, in Chapter 4 (Figure 1.8).

The raMO method uses the occupied crystal orbitals of an intermetallic compound as a basis set to reproduce target eigenfuctions which are chosen to illustrate a clear, chemically intuitive bonding picture. Beginning with the binary $TiAl_3$-type $NbGa_3$ for simplicity, we use a Nb atom's s, p, and d atomic orbitals as the target eigenfuctions in order to better understand their role in the placement of the structure's pseudogap. Surprisingly, despite the structure's valence of electron concentration of only14 e^-/T atom, we are able to reproduce all of the Nb atom's 9 s, p, and d orbitals from the occupied crystal orbitals, indicating that the Nb atom is able to obtain an 18-electron closed shell configuration. Linear

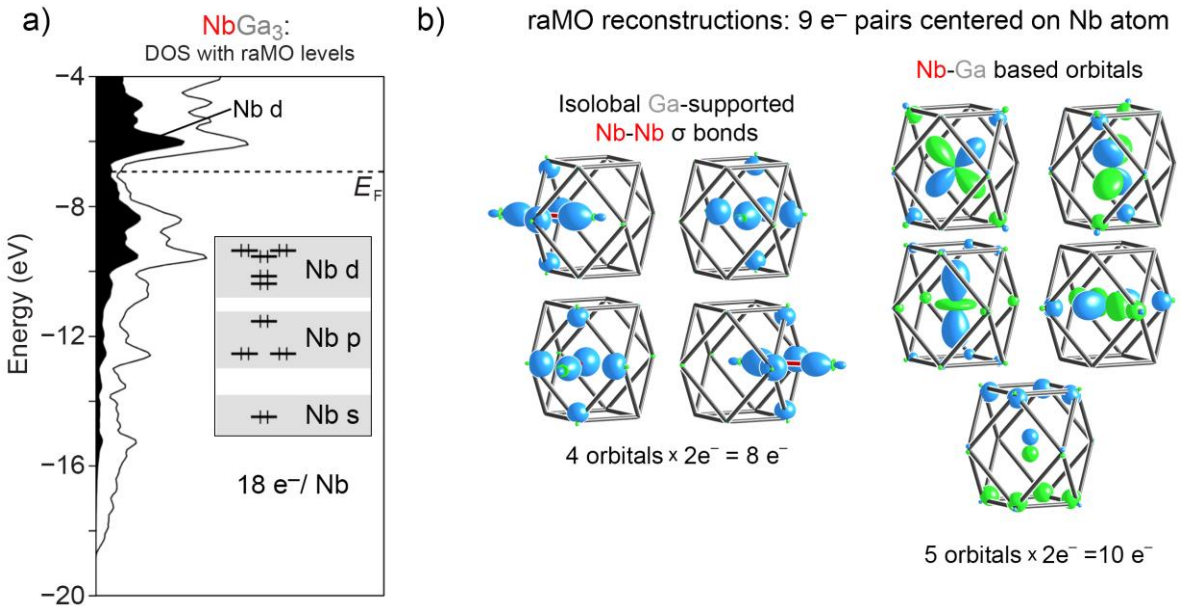

Figure 1.8. The raMO reconstructions of a single Nb atom's s, p, and d orbitals in $NbGa_3$. (a) Energies of the raMO levels drawn alongside the DOS distribution of the phase. (b) raMO reconstructions of the Nb s, p, and d orbitals, with four d orbitals and one p orbital involved in Nb – Ga bonding and four sp^2d hybrids involved in Ga supported Nb – Nb bonding for a total of 18 electrons.

combinations to create sp^2d hybrid orbitals from the raMOs reveal that this electronic configuration is reached in part through the use of four Ga supported Nb – Nb bonding interactions which have the same nodal symmetry as traditional σ bonds. The recognition of this bonding mechanism at work in $NbGa_3$, and in Mo_2CuGa_5, adds them to a growing list of T – E (E = main group metal), including the $PtHg_4$-type $CrGa_4$ as discussed in Chapter 2, whose stability can be traced to the ability of the T atom to fill all of its s, p, and d orbital through T – E, and isolobal T – T bonding interactions. Further synthetic investigation is warranted to explore if the formation of T atom clusters or isolation of T atoms in E matrices can be controlled by adjusting the electron count of the E lattice.

The discovery and bonding analysis of the $Mo_2Cu_{0.9}Ga_{5.1}$ represents one full cycle of the iterative theoretical/experimental approach which the concept of structural plasticity facilitates (Figure 1.9). The

Chemical Pressure analysis of the $TiAl_3$-type $NbGa_3$, $PtHg_4$-type $CrGa_4$, and V_8Ga_{41}-type V_8Ga_{41} revealed that the complex V_8Ga_{41} type can be understood simply as an intergrowth of $TiAl_3$- and $PtHg_4$-type features, which forms a mechanism to simultaneously optimize the atomic size requirements of V or Mo and Ga. This understanding revealed a clear synthetic pathway to expressing $TiAl_3$-type features in the Mo – Ga phase diagram by doping smaller atoms onto the Ga sublattice, which was realized through the formation of the $TiAl_3$-type variant $Mo_2Cu_{0.9}Ga_{5.1}$. By defusing the complexity of the V_8Ga_{41}, we were able to identify previously unrecognized bonding schemes at work in $NbGa_3$ and other $TiAl_3$ structures. In the other model system studied in this thesis, we will see these same conversations can be used to induce complexity in order to realize the same goal.

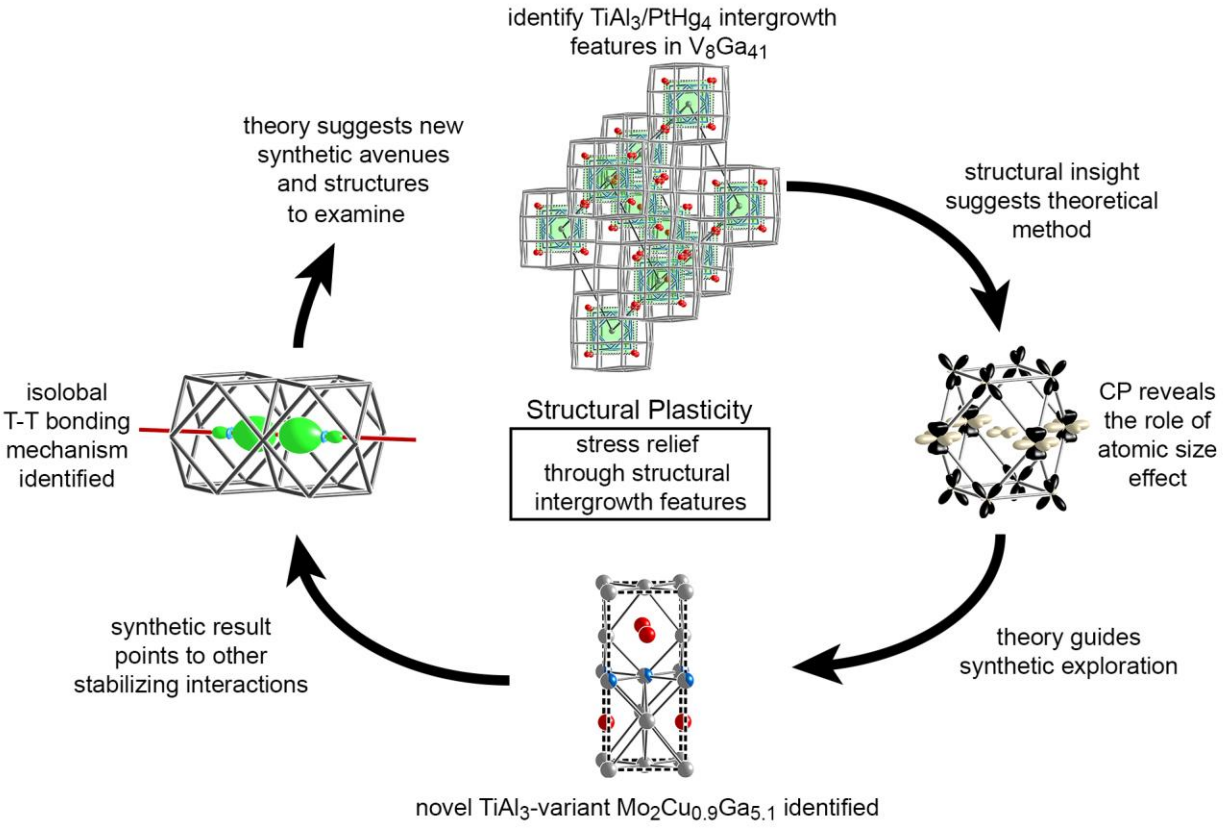

Figure 1.9. A schematic illustration of the dialogue between theoretical analysis and synthetic exploration revolving around the structural plasticity observed in the formation of the complex V_8Ga_{41}-type structure.

1.3. Higher Dimensional Avenues to Structural Complexity

The $CaCu_5$-type $CaPd_5$ structure[25] has been key to developing the idea of structural plasticity. Its structure has been shown to be the progenitor of an entire family tree of intermetallics structures whose branches range from moderately complex superstructures formed by inserting defect planes into the $CaCu_5$ type,[26,27] to Tsai-type quasicrystal approximants.[28,29] As in the V_8Ga_{41} type, the use of Chemical Pressure (CP) analysis has shown that the formation of these $CaCu_5$ derivatives is driven by the desire to relieve internal pressures which are inherent to the $CaCu_5$-type $CaPd_5$ structure.

The $CaCu_5$-type $CaPd_5$ can be understood as alternating layers of Pd kagome (blue) and Ca stuffed honeycomb (green) nets (Figure 1.10). Its CP scheme exhibits large, black negative pressures lobes on each Ca atom which are directed into the void spaces in the kagome nets above and below. Contraction of the structure to relief these negative pressures it prevented by the white, positive CP lobes along the Pd – Pd contacts and between the Ca and Pd atoms elsewhere. Analysis of this CP scheme leads to the overall conclusion that Ca atom is too small for its coordination environment.

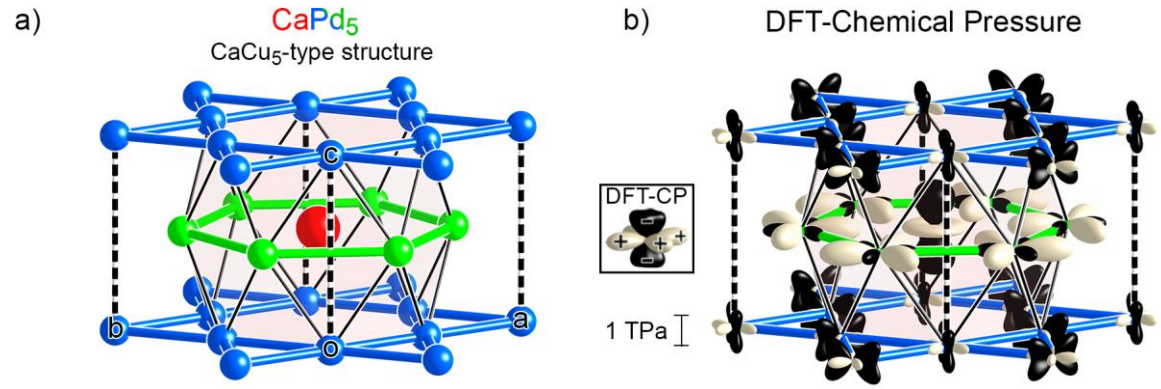

Figure 1.10. The structure and chemical pressure (CP) scheme of $CaPd_5$ in the $CaCu_5$ structure type. (a) The structure can be described as a layering of kagome (blue) and Ca-stuffed honeycomb (green) nets of Pd atoms. (b) The CP scheme of the $CaCu_5$-type $CaPd_5$ structure. Large negative pressure on the Ca atom point into the voids in the layers above and below, indicating an inefficient use of space.

When Pd is replaced with a larger T atom, these negative pressures become so intense as to drive structural transformations. One example is seen in the Ca – Ag system, where the large negative pressures in a hypothetical $CaCu_5$-type $CaAg_5$ are avoided by deleting every other kagome net and shifting the remaining $CaCu_5$-type slabs relative to each other, forming the Ca_2Ag_7 structure (Figure 1.11).[25,29,30] In the Ca – Cd system, these same forces drive the formation of $Ca_{14}Cd_{51}$ and the Tsai-type quasicrystal approximant $CaCd_6$.[28,29,31] The success in explaining the stability of these structures as Chemically Pressure-driven deformations of the $CaCu_5$ type structure led us to pose another question: is it possible to induce these same deformations with an applied physical pressure?

We therefore set out to identify synthetic targets for high pressure experiments in order to better understand the relationship between Chemical Pressure and applied physical pressure in intermetallics. We began by recognizing the parallels between Chemical Pressure and physical pressure induced phase

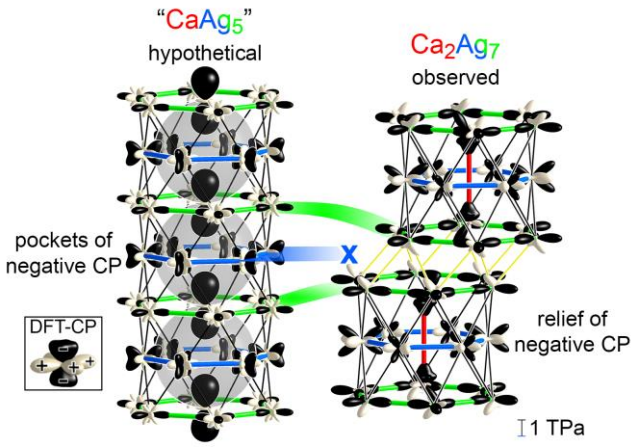

Figure 1.11. Structural plasticity at work in the Ca – Ag system. Ca_2Ag_7 can be understood as a deformation of the hypothetical $CaCu_5$-type $CaAg_5$ structure, which has deleted alternating kagome nets and shifted the remaining $CaCu_5$-type slabs relative to each other in order to avoid negative pressures on the Ca atoms.

transitions. In both instances, the system reacts to an energetic penalty for inefficient atomic packing. In CP induced transitions, the energetic cost is due to the inability of the structure to optimize all of its atomic contacts simultaneously within the confines of a simple structure – lower symmetry superstructures form as a mechanism providing more freedom to optimize these contacts. In high pressure experiments, the penalty of an inefficient packing comes from the positive PV term of the systems free energy. As the pressure is elevated, denser packings become increasingly favored in an effort to minimize the magnitude of this destabilizing term. It thereby follows that structures with pockets of negative CP indicating an inefficient use of space, such as that seen in the $CaCu_5$ type, should be particularly susceptible to phase transitions induced by applied physical pressure.

Since we have seen the transition of the $CaCu_5$ type to the Ca_2Ag_7 type can be induced by Chemical Pressure in the Ca – Ag phase diagram, we employed DFT calculations to estimate at what applied pressure (if any) we might expect the transition to be favorable in other systems. For example, under an externally applied pressure the negative regions of CP in the $CaCu_5$ may be enough of a destabilizing factor as to drive the formation of Ca_2Cu_7 which displays a much more even distribution of CPs throughout its atomic arrangement (expelling elemental Cu as a side product). Indeed, DFT calculation suggest that although this transition in unfavorable at room pressure by more than 60 meV per atom, at 113 GPa it becomes favorable, and the ΔH_{rxn} becomes steadily more negative as the pressure increases (Figure 1.12a).

We note here that from these calculations we don't expect to observe that the formation of Ca_2Cu_7 would be observed from a high pressure experiment on $CaCu_5$. It is more likely that a higher density polymorph of $CaCu_5$, or two $CaCu_{5+x}$ and $CaCu_{5-x}$ phases would manifest at a pressure below the applied pressure predicted to drive the stability of Ca_2Cu_7 and Cu relative to $CaCu_5$. However it does demonstrate

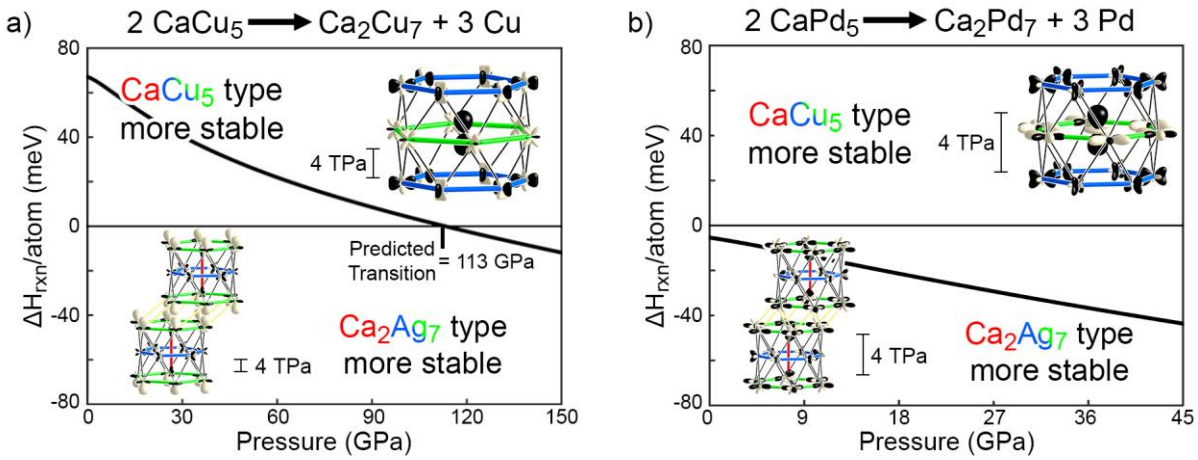

Figure 1.12. The pressure dependence for the GGA-DFT reaction enthalpy for the decomposition of $CaCu_5$-type phases into a denser Ca_2Ag_7-type superstructure, with an elemental transition metal side product. Results are shown for the (a) Ca-Cu and (b) Ca-Pd systems. The CP plots of reported $CaCu_5$- and hypothetical Ca_2Ag_7-type products are plotted. In both cases the reaction is increasingly favored at higher P, in-line with its more efficient atomic packing. Curiously, this reaction is predicted to be favorable for the reported $CaCu_5$-type $CaPd_5$ at ambient pressure, identifying it as a good candidate for high pressure studies.

that an pressure-induced phase transition should be obtainable at pressures accessible with a diamond anvil cell.

As Pd has an intermediate metallic radius between that of Cu (for which the $CaCu_5$ is stable) and Ag (for which Ca_2Ag_7-type is stable), we anticipate that applied pressure at which the reported $CaCu_5$-type $CaPd_5$ becomes unstable relative to Ca_2Ag_7-type Ca_2Pd_7 structure and elemental Pd will be less than that of $CaCu_5$. Surprisingly, GGA DFT predicts that the decomposition of the reported $CaPd_5$ structure into Ca_2Pd_7 and Pd is slightly favored at ambient pressure, becoming increasingly more favorable at high pressure. We, of course, consider this result with a healthy amount of skepticism. These calculations assume a temperature of 0 K; $CaPd_5$ may be stabilized by entropic effects at higher temperatures. It does,

however, identify $CaPd_5$ as an ideal candidate for high pressure experiments aimed at synthetically probing the connection between CP and pressure-induced phase transitions.

Our attempts to synthesize the reported $CaCu_5$-type $CaPd_5$ structure as a precursor for high pressure experiments led us instead to a new realm of CP-driven complexity. The diffraction pattern of crystals obtained from the synthesis aimed at $CaPd_5$, displayed satellite reflections indicating that a higher dimensional space would be required to accurately describe the structure's atomic positions. Beginning with the average structure solution (obtained by only integrating over main reflections and ignoring the satellite diffraction peaks) we are able to determine the 3D symmetry of the structure and obtain clues as to the source of the satellite peaks.

The average structure of this incommensurately modulated $CaPd_5$ structure has *Cmcm* symmetry and can be derived from the $CaCu_5$-type $CaPd_5$ structure. Similar to the Ca_2Ag_7 type, every other kagome net of Pd has been deleted and the remaining $CaCu_5$ slabs have been shifted relative to each other (Figure 1.13). The average structure of $CaPd_5$ differs from Ca_2Ag_7 in that the deleted kagome nets have been

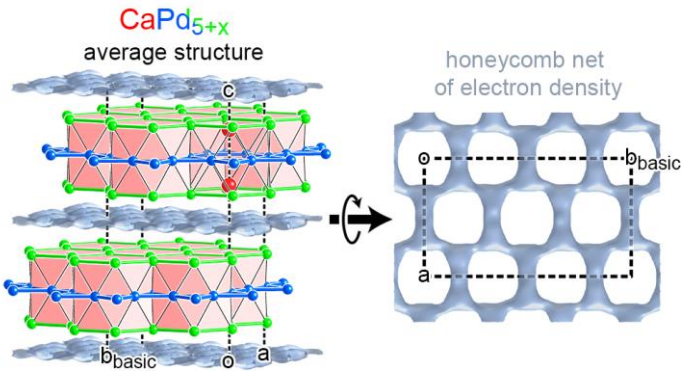

Figure 1.13. The average structure of $CaPd_{5+x}$ determined from the main reflections of its diffraction pattern. This structure is based on $CaCu_5$-type slabs stacked along *c* separated by honeycomb nets of diffuse electron density at $z = 0$ and $1/2$. The diffuse nets of electron density suggest that the ordering of the atoms in this layer are the source of the satellite reflections in the diffraction pattern, which can be resolved into well-defined peaks by moving to a (3+1)D superspace model.

replaced with diffuse honeycomb layers of electron density – suggesting that atomic positions of this layer are the source of the satellite peaks in the diffraction pattern.

By expanding our structural solution into (3+1)D space the diffuse honeycomb net of electron density is resolved into well-defined Pd positions in an undulating hexagonal net which traces out the honeycomb layer of diffuse electron density from the average structure (Figure 1.14a). The periodicity of this hexagonal Pd net is incommensurate with that of the $CaCu_5$-type slabs in the layers above and below. This mismatch of periodicity allows the structure to accommodate more Pd atoms in this hexagonal net than a commensurate structure would permit, resulting in a stoichiometry of approximately $CaPd_{5.22}$.

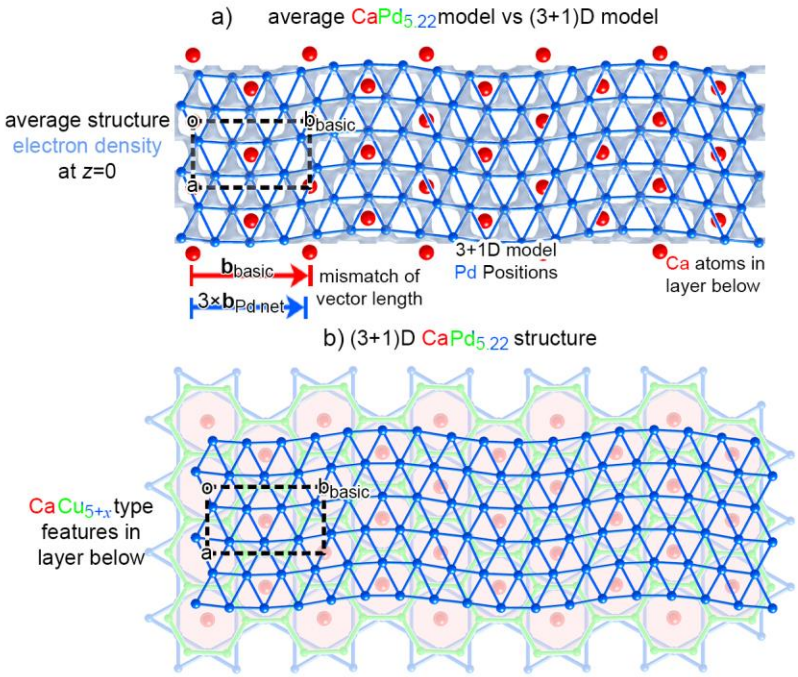

Figure 1.14. The distorted hexagonal net created by the Pd1/Pd2 atoms whose interatomic spacing along *y* is incommensurate with that of the $CaCu_5$-type slabs. (a) The positions of the Pd atoms (blue) at $z = 0$ in the (3+1)D model of $CaPd_{5+x}$ overlaid on the diffuse electron density features found in the average structure . Ca atoms (red) are shown from the $CaCu_5$-type slab from the layer below. (b) The placement of the Pd1/Pd2 atoms relative to the atoms of the $CaCu_5$-type slab below it (faded).

The structural features exhibited by the structure of $CaPd_{5.22}$ are poised to resolve the intense negative pressures identified in the $CaCu_5$-type $CaPd_5$ structure. CP analysis of a commensurate approximant of $CaPd_{5.22}$ where the hexagonal Pd net has been held commensurate with $CaCu_5$-type slabs reveals that that the substitution of kagome layers for hexagonal ones relieves the negative CPs observed on the Ca atoms in the $CaCu_5$-type $CaPd_5$ structure. The analysis also provides clues as to the driving force leading to the incommensurability of the hexagonal Pd net. Large negative pressure lobes can be seen pointing along Pd – Pd contacts in Pd net, with positive pressure pointing along orthogonal directions, suggesting that the addition of Pd atoms can relieve these negative pressures without inducing significant positive pressures.

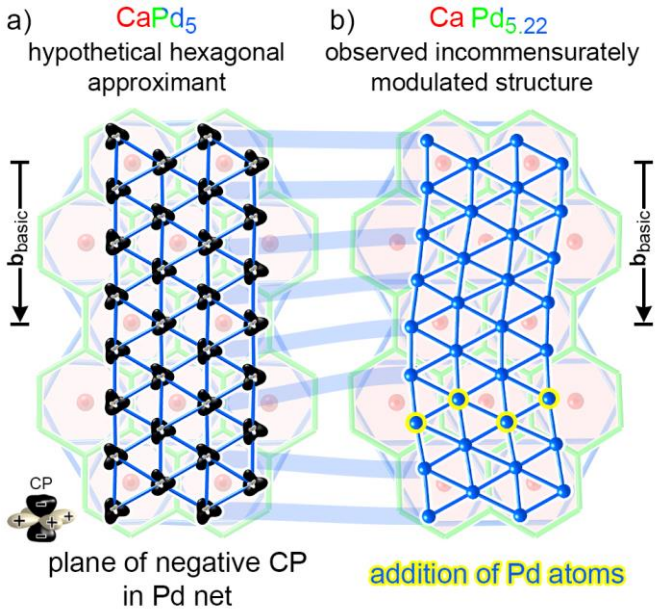

Figure 1.15. Chemical pressure (CP) as a driving force for the incommensurate spacing of the atoms in the layers between $CaCu_5$-type slabs in $CaPd_{5.22}$. (a) DFT-CPs for the Pd1/Pd2 atoms in the commensurate approximant of $CaPd_{5.22}$, in which the spacing of Pd atoms along *y* in this layer is 1/3 the length of the basic unit cell. Pd-Pd contacts within this layer are marked with negative pressures, favoring contraction of the structure. (b) In the refined incommensurate structures, shorter Pd-Pd contacts are obtained by decreasing the spacing of the Pd1/Pd2 atoms along *y*. Light blue bars trace corresponding Pd positions between the panels, illustrating how additional atoms have arisen in the incommensurate layer.

The discovery and characterization of the incommensurately modulated $CaPd_{5.22}$ is yet another example of structural plasiticity at work in intermetallics that is explored in this thesis. Whereas in V_8Ga_{41} we saw its $TiAl_3$-/$PtHg_4$-intergrowth features served to relieve stress in the $TiAl_3$ and $PtHg_4$ types, in $CaPd_{5.22}$ the relief of stress comes from the replacement of kagome nets in the $CaCu_5$-type with incommensurately modulated hexagonal nets. Even though the mechanism of their relief differs, both system demonstrate the utility of seeking to understand complex structures as deformations of simpler structures – affording a foothold from which to begin our analysis. In this example that foothold was the $CaCu_5$-type $CaPd_5$ phase. Theoretical analysis of its simple structure identified that it may be susceptible to the same CP-driven deformations seen in more complex phase diagrams through the application of a mild external pressure, and even anticipated (although not entirely predicted) the structural features that would result. The complex structural chemistry that emerged from the synthetic exploration that followed revealed a new driving force for incommensurability in intermetallics, (as we will see later) suggesting further synthetic avenues to explore.

The open dialogue between chemical theory and synthetic exploration realized in this work represents a sizeable step forward in the ability of experiment and theory to synergistically explore new phase space. We will see in Chapters 6, however, that this communication does falter at times, wherein entirely new realms of complexity are uncovered by synthetic exploration which force us to reconsider what we know about the bonding in a system. But the concept of structural plasticity in its current form has demonstrated its ability to equip solid state chemists with an intuition about how to guide structural modifications in intermetallics, and continues to provide a common ground on which theory and synthesis can work together to guide progress.

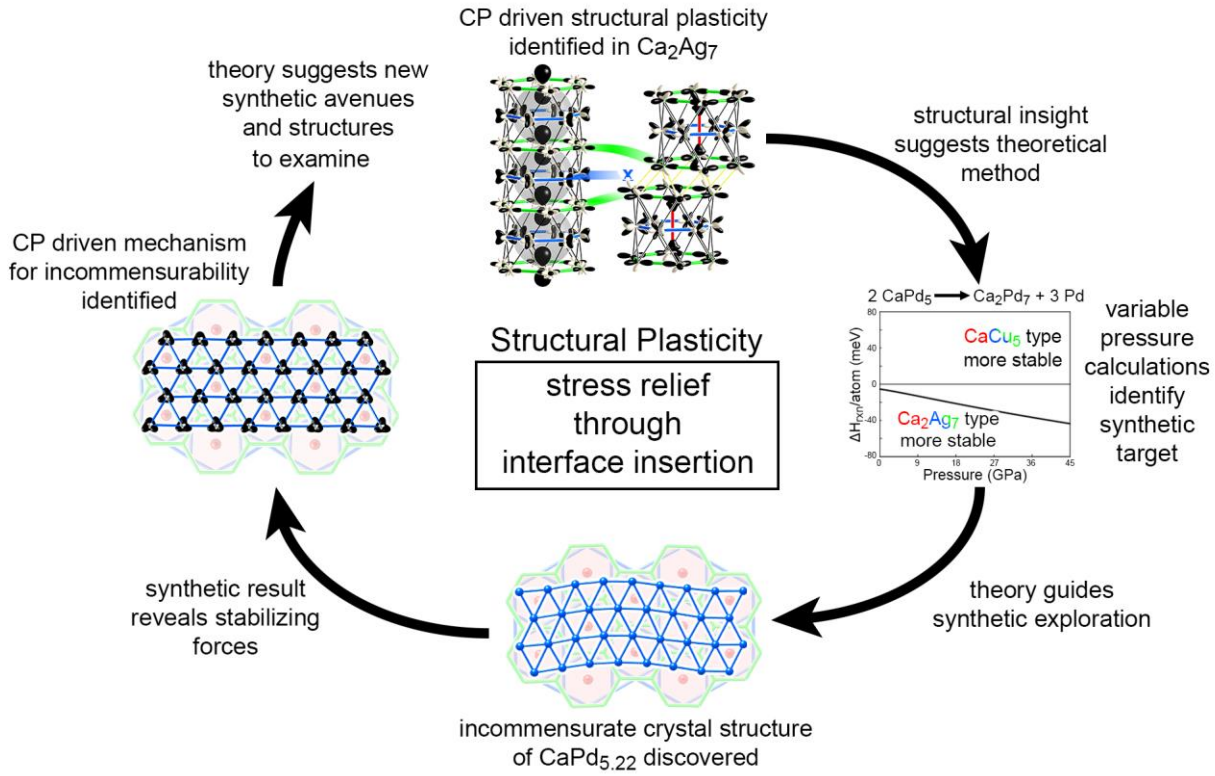

Figure 1.16. A schematic illustration of the dialogue between theory and synthetic exploration revolving around the structural plasticity demonstrated in the formation of complex Ca-late transition metal intermetallic compounds.

1.4. Outline of Thesis

In this thesis, we continue to develop concept of structural plasticity in order to understand the forces driving formation of the complex structures observed for intermetallic compounds and demonstrate its ability to provide insight which allows one to anticipate structural modifications driven by chemical substitutions. The approach presented here involves a sustained dialogue between theoretical analysis and synthetic exploration. We will begin by examining the development of two theoretical methods which serve as the foundations by which we understand the structural plasticity of intermetallic compounds.

Chapter 2 discusses the refinement of DFT-Chemical Pressure (CP) analysis. We see here how the difficulties of extracting information about the role of atomic size from the output of DFT calculations are overcome. Intense chemical pressures which appear as artifacts around atomic core regions due to misalignment of sampling grids in the CP procedure are accounted for and corrected through a grid unwarping procedure. The chapter also introduces a new criterion by which atomic contacts are defined in the CP method using the free ion electron density profile at each point in space. This work then shows how these improvements resolve remaining questions about the CP analysis of the $MgCu_2$ and the $AuBe_5$ type. It ends by comparing the two common structures types for AB_5 intermetallics, the $AuBe_5$ and $CaCu_5$ types, and showing that the CP analysis clearly illustrates the radius ratio arguments which have been previously invoked to explain their relative stabilities.

We then move from examining the role of atomic size to illustrating the importance of electron count in the stability of intermetallics through the development of the reversed approximation Molecular Orbital (raMO) analysis in Chapter 3. This chapter establishes a technique in which the usual approach of using linear combinations of simple functions to approximate true wave functions is reversed, and instead the occupied crystal orbitals of a compound are used as the basis set to reproduce target eigenfunctions chosen to illustrate a clear, chemically intuitive interpretation of the bonding. It begins by illustrating the basics of raMO analysis on the familiar 1,3-butadiene model. The raMO method is then applied to the bonding analysis of the $PtHg_4$-type $CrGa_4$. It is revealed that the deep pseudogap at the Fermi energy in $CrGa_4$'s electronic density of states, and at least in part it's stability, can be traced to the ability of the Cr atom to involve all of its s, p, and d orbitals in bonding to achieve an 18 electron configuration. It concludes with an iterative application of the raMO method to the Ir_3Ge_7-type Os_3Sn_7 structure, where it is shown that the same 18 electron configuration is being obtained by the Os atom in this structure.

However, in this structure, Sn supported Os-Os bonding interactions are present which have same nodal symmetry as σ or π bonds. The stability associated with the ability of T atoms to obtain 18 electron configurations in these T – E (E = main group element) intermetallics becomes a reoccurring theme which we revisit in subsequent chapters.

Having established the theoretical foundations which will be used to investigate the structural plasticity in intermetallics, Chapter 4 presents our first experimental explorations of structural plasticity. The addition of Cu in to mixtures of Mo-Ga is shown to defuse the complexity of the V_8Ga_{41} – type Mo_8Ga_{41} structure, resulting in the $TiAl_3$-type variant $Mo_2Cu_xGa_{6-x}(x \approx 0.9)$. Starting with simpler $TiAl_3$-type $NbGa_3$ structure and expanding to an idealized version of $Mo_2Cu_xGa_{6-x}$, the raMO method introduced in Chapter 3 is used to explore the role of electron count in stabilizing these $TiAl_3$-type and $TiAl_3$-type variant structures. It is found that the pseudogap, and consequently the stability, of both structures can be traced to the ability of the T atoms to fill their s, p, and d orbtials, achieving an 18 electron configurations, through a combination of T – Ga and Ga – supported T –T bonding interactions, explaining the valence electron concentrations at which $TiAl_3$-type structures are observed.

Chapter 5 turns our attention briefly away from T – Gallides to explore another dialogue between theory and experiment which resulted in an incommensurately modulated $CaCu_5$-type variant. Inspired by previous CP studies on $CaPd_5$, we carried out variable pressure calculations to test the structure's susceptibility to a phase transition, finding that only a modest application of external pressure should be needed. Attempts to synthesize the $CaCu_5$-type $CaPd_5$ as a precursor to high pressure studies instead resulted in the incommensurately modulated $CaPd_{5.22}$ structure. CP analysis of a commensurate approximant of $CaPd_{5.22}$ reveal that its structure relieves the negative CP on the Ca atoms present in the

previously $CaCu_5$-type $CaPd_5$ structure and illuminate the driving force behind the compound's incommensurability.

Chapters 4 and 5 present two instances where dialogues between theory and experiment were established and allowed the structural features of new compounds to be anticipated and understood. In Chapter 6 we see instances where synthetic explorations revealed new realms of structural complexity that we hadn't expected. We report the synthesis and structure determination of theTa_4Ga_5-type phases Ta_4Ga_5, $Ta_{4-x}Mo_xGa_5$ and Nb_4Ga_5. In contrast with the usual assumption that intermetallics form due to the stabilizing interactions of heteroatomic contacts, their structures display microscopic segregation into domains of T – T and Ga – Ga contacts. Bonding analysis using the raMO method shows that this segregation into homoatomic domains allows Ga atoms to preferentially stabilize Ta – Ta bonding interactions over anti-bonding ones. Due to the sheer volume of data required to adequately report the details of new crystal structures and electronic structure calculations, appendices with this information are offered for Chapters 2-6 at the end this thesis.

1.5. References

(1) Rousseau, G.; Breit, B. *Angew. Chem. Int. Ed.* **2011**, *50*, 2450-2494.

(2) Hemavathi, B.; Ahipa, T. N.; Pai, R. K. *Eur. Polym. J.* **2015**, *72*, 309-340.

(3) Abdelazeem, A. H.; Khan, S. I.; White, S. W.; Sufka, K. J.; McCurdy, C. R. *Biorg. Med. Chem.* **2015**, *23*, 3248-3259.

(4) Bertaccini, E. J. *Pharmaceuticals* **2010**, *3*, 2178-2196.

(5) Subramanian, P. R.; Miracle, D. B.; Mazdiyasni, S. *Metall. Mater. Trans. A* **1990**, *21*, 539-545.

(6) Edwards, J. W.; Speiser, R.; Johnston, H. L. *J. Appl. Phys.* **1951**, *22*, 424-428.

(7) Copper, A. S. *Acta Crystallogr.* **1962**, *15*, 578-582.

(8) Sridharan, S.; Nowotny, H. N. *Z. Metallkd.* **1983**, *74*, 468-472.

(9) Raman, A. *Aluminum* **1965**, *41*, 318-319.

(10) Mahne, S.; Harbrecht, B. *J. Alloys Compd.* **1994**, *203*, 271-279.

(11) Weber, T.; Dshemuchadse, J.; Kobas, M.; Conrad, M.; Harbrecht, B.; Steurer, W. *Acta Crystallogr., Sect. B: Struct. Sci.* **2009**, *65*, 308-317.

(12) Conrad, M.; Harbrecht, B.; Weber, T.; Jung, D. Y.; Steurer, W. *Acta Crystallogr., Sect. B: Struct. Sci.* **2009**, *65*, 318-325.

(13) Beekman, M.; Morelli, D. T.; Nolas, G. S. *Nat. Mater.* **2015**, *14*, 1182-1185.

(14) Xie, W.; Seibel, E. M.; Cava, R. J. *Inorg. Chem.* **2016**, *55*, 3203-3205.

(15) Balamurugan, B.; Das, B.; Zhang, W. Y.; Skomski, R.; Sellmyer, D. J. *J. Phys.: Condens. Matter* **2014**, *26*, 064204.

(16) Okada, M.; Kuriiwa, T.; Kamegawa, A.; Takamura, H. *Mater. Sci. Eng., A* **2002**, *329-331*, 305-312.

(17) Tamegai, T.; Uozato, K.; Ghosh, A. K.; Tokunaga, M. *Int. J. Mod. Phys. B* **2004**, *19*, 369-374.

(18) Brauer, G. *Z. Anorg. Allg. Chem.* **1939**, *242*, 1-22.

(19) Meissner, H. G.; Schubert, K. *Z. Metallkd.* **1965**, *56*, 475-484.

(20) Wallbaum, H. J. *Z. Metallkd.* **1942**, *34*, 118-119.

(21) Bauer, E.; Nowotny, H.; Stempfl, A. *Monatsh. Chem.* **1953**, *84*, 692-700.

(22) Meissner, H.-G.; Schubert, K. *Z. Metallkd.* **1965**, *56*, 523-530.

(23) Bezinge, A.; Yvon, K.; Decroux, M.; Muller, J. *J. Less-Common Met.* **1984**, *99*, L27-L31.

(24) Girgis, K.; Petter, W.; Pupp, G. *Acta Crystallogr., Sect. B: Struct. Crystallogr. Cryst. Chem.* **1975**, *31*, 113-116.

(25) Mejbar, J.; Notin, M. *Scr. Metall. Mater.* **1990**, *24*, 1697-1700.

(26) Fredrickson, D. C. *J. Am. Chem. Soc.* **2011**, *133*, 10070-10073.

(27) Fredrickson, D. C. *J. Am. Chem. Soc.* **2012**, *134*, 5991-5999.

(28) Berns, V. M.; Fredrickson, D. C. *Inorg. Chem.* **2013**, *52*, 12875-12877.

(29) Berns, V. M.; Fredrickson, D. C. *Inorg. Chem.* **2014**, *53*, 10762-10771.

(30) Snyder, G. J.; Simon, A. *J. Alloys Compd.* **1995**, *223*, 65-69.

(31) Bruzzone, G. *Gazz. Chim. Ital.* **1972**, *102*, 234-242.

Chapter 2.

Progress in Visualizing Atomic Size Effects with DFT-Chemical Pressure Analysis: From Isolated Atoms to Trends in AB_5 Intermetallics

This chapter has been published Berns, V. M.; Engelkemier, J.; Guo, Y.; Kilduff, B. J.; Fredrickson, D. C. *J. Chem. Theory Comput.* **2014**, *10*, 3380-3392. The specific analyses detailed in this chapter were the work of Berns, but all authors made contributions to the general theoretical developments.

2.1. Abstract

The notion of atomic size poses an important challenge to chemical theory: empirical evidence has long established that atoms have spatial requirements, which are summarized in tables of covalent, ionic, metallic, and van der Waals radii. Considerations based on these radii play a central role in the design and interpretation of experiments, but few methods are available to directly support arguments based on atomic size using electronic structure methods. Recently, we described an approach to elucidating atomic size effects using theoretical calculations: the DFT-Chemical Pressure analysis, which visualizes the local pressures arising in crystal structures from the interactions of atomic size and electronic effects. Using this approach, a variety of structural phenomena in intermetallic phases have already been understood in terms that provide guidance to new synthetic experiments. However, the applicability of the DFT-CP method to the broad range of the structures encountered in the solid state is limited by two issues: (1) the difficulty of interpreting the intense pressure features that appear in atomic core regions, and (2) the need to divide

space among pairs of interacting atoms in a meaningful way. In this Article, we describe general solutions to these issues. In addressing the first issue, we explore the CP analysis of a test case in which no core pressures would be expected to arise: isolated atoms in large boxes. Our calculations reveal that intense core pressures do indeed arise in these virtually pressure-less model systems, and allow us to trace the issue to the shifts in the voxel positions relative to atomic centers upon expanding and contracting the unit cell. A compensatory grid unwarping procedure is introduced to remedy this artifact. The second issue revolves around the difficulty of interpreting the pressure map in terms of interatomic interactions in a way that respects the size differences of the atoms and avoids artificial geometrical constraints. In approaching this challenge, we have developed a scheme for allocating the grid pressures to contacts inspired by the Hirshfeld charge analysis. Here, each voxel is allocated to the contact between the two atoms whose free atom electron densities show the largest values at that position. In this way, the differing sizes of atoms are naturally included in the division of space without resorting to empirical radii. The use of the improved DFT-CP method is illustrated through analyses of the applicability of radius ratio arguments to Laves phase structures and the structural preferences of AB_5 intermetallics between the $CaCu_5$ and $AuBe_5$ structure types.

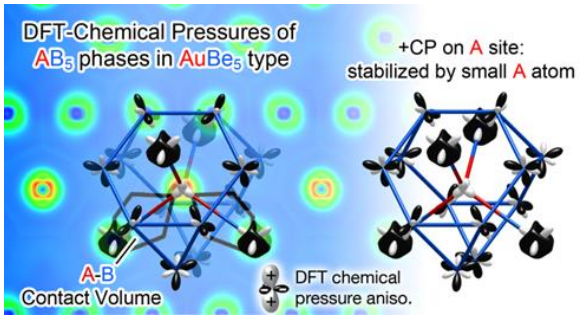

Figure 2.0. Schematic illustration of chemical pressure in an AB_5 compound of the $AuBe_5$ structure type. On the left, we see a 2-dimensional chemical pressure map, overlayed with key contact volumes. This new division of space enables analysis of the $AuBe_5$ structure type, which is shown to be stabilized by a small atom on the A site.

2.2. Introduction

While chemistry has long since stripped itself of the mysticism of the alchemists, its deep roots in experimental observation have led to a number of useful empirical concepts that have their own sort of poetry and allure, such as the chemical bond, electronegativity, and acidity. One goal of modern theoretical chemistry is the mapping of these notions to aspects of a compound's electronic structure, in ways that are both theoretically rigorous yet honor the richness of their historical uses and connotations. Atomic size is perhaps one of the most problematic of these empirical ideas. Experience with molecular and solid state structures suggests that atoms have measurable sizes,[1-3] yet the Schrödinger equation contains no terms involving atomic radii or explicit penalties for atoms encroaching upon each other. Indeed, the gradual and asymptotic decay of wavefunctions away from a system's nuclei is far from conducive to the construction of clear-cut boundaries defining the space occupied by individual atoms.[4] Given the importance of atomic size arguments throughout chemistry, theoretical tools which overcome these challenges could be extremely beneficial to deepening the roles theory can play in the design of experiments.

For inorganic solid state materials, the need for such theoretical methods for analyzing atomic size effects is particularly pressing, as can be seen in a quick survey of the recent literature. Atomic sizes or radius ratios are frequently invoked in discussions of the factors stabilizing particular crystal structures,[5-16] and in the interpretation of physical properties in terms of the presence of rattling atoms or interstitial spaces for guest atoms.[17,18] Furthermore, the empirical concept of chemical pressure, in which elemental substitutions create local stresses in a crystal structure, has been used as a framework for understanding relationships between composition and properties.[19-28]

While energy terms corresponding to atomic size effects are difficult to extract from an electronic

structure calculation, we have recently found that their impact on stability can be productively inferred from a quantum mechanical adaptation of the chemical pressure concept just mentioned.[29-32] The basis of this method is the recognition that the size requirements of atoms are most apparent when interatomic repulsion at one contact in a structure impedes bonding at other contacts. As the repulsion and bonding interactions cannot be optimized simultaneously, local stresses are expected to result which, unlike the atomic sizes themselves, can be evaluated naturally using quantum mechanics through such concepts as the stress density.[33-38]

The DFT-CP analysis offers a way to examine these local pressures using the results of standard electronic structure calculations. The method uses the density and potential grids determined in the course of a DFT calculation to create maps of the pressure within crystal structures, which reveal points of frustration within those structures. This approach has been particularly fruitful in the study of the structural chemistry of intermetallic phases, where it has offered explanations for such phenomena as the creation of complex structures through the insertion of planar interfaces into simpler ones,[30,32] the formation of local icosahedral order in quasicrystal approximants,[39,40] and the ability of some $AuCu_3$-type lattices to accommodate guest atoms.[41]

Over the course of these and other applications, we have found that there are still several issues limiting the range of applicability of the DFT-CP analysis: (1) the proper treatment of the intense pressures that are calculated to occur near the core regions of an atom, and (2) the best scheme to interpret the pressure maps in terms of interatomic interactions.

In this Article, we will describe improved solutions to both of these challenges. Beginning with the CP calculations on individual atoms isolated in large unit cells, we will show that the introduction of an unwarping procedure to correct for the drift of the voxel positions relative to the nuclei upon expanding

and contracting the unit cell can significantly reduce the severe pressures in the atomic core regions obtained in the original procedure. Including this step in the generation of CP-maps allows for more subtle CP features to come to the foreground, and eliminates the need for our earlier isotropic core averaging technique.

After describing this improved method for the construction of CP maps, we will then move to issues with their interpretation. As the CP distributions generally involve positive pressures near the core regions and negative pressures in the interstitial regions, evaluating the net pressure along a contact involves an averaging process over the voxels associated with that contact. The overall results are strongly tied to the scheme used in assigning these voxels to contacts. In our previous applications, we have found that assuming that a voxel's pressure is determined by the contact between its two closest atoms often provided intuitive results. However, this purely geometrical construction does not always assign differing spheres of influence to atoms of vastly different sizes. In this Article, we present a more sophisticated approach inspired by the Hirshfeld method for calculating atomic charges,[42] in which the electron density distributions of free atoms are used in determining which atoms will have the largest influence on a voxel's pressure.

In introducing these methodological improvements, we will make reference to structural trends in intermetallics that have been attributed to atomic size effects (Figure 2.1): the role of radius ratios in the Laves phases, and the transition from the $CaCu_5$ type to the $AuBe_5$ type for AB_5 intermetallics with increasingly small A atoms.[43] Through the use of the updated DFT-CP method, the latter structural trend will become simply explained as a CP-driven transition in line with the pressure-distance paradox.[4,44] We anticipate that these results could provide a foundation for analyses of the origins of a series of complex intermetallic phases built from the intergrowth of the $AuBe_5$ and $MgCu_2$ types, at compositions near which

a $CaCu_5$-type phase might be expected, such as $YbCu_{4.5}$ with its giant 7,448-atom monoclinic unit cell.[45-48]

2.3. Computational procedures

Electronic structure calculations for the geometrical optimization of crystal structures and the output of electron densities, kinetic energy densities, and components of the Kohn-Sham potentials were carried out with the ABINIT program.[49,50] All calculations employed the density functional theory (DFT) with the local density approximation (LDA) of Goedecker, Teter, and Hutter,[51] and the HGH atomic pseudo-potentials.[52] Further details, including the energy cut-offs, number of k-points used in the calculations, and the optimized atomic coordinates of the intermetallic structures discussed in this Article, are given in the Supporting Information.

The output of the ABINIT calculations was used for the generation of CP maps through the scheme described below. The resulting CP maps were visualized with the program VESTA 3.[53] The projections of the CP maps onto spherical harmonics were plotted with Matlab. Software for the calculation and integration of CP maps using the method described in this paper is available at our research group website (http://www.chem.wisc.edu/~danny).

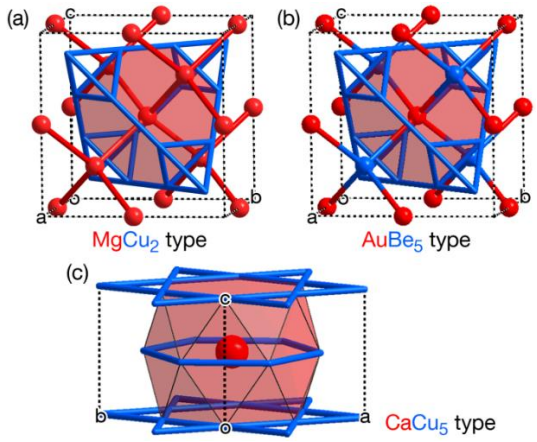

Figure 2.1. Structure types discussed in this Article whose stability ranges are empirically connected to atomic size: (a) The $MgCu_2$ (cubic Laves phase) type. (b) The $AuBe_5$ type. (c) The $CaCu_5$ type.

In the determination of Hirshfeld-inspired contact volumes, free atom electron densities were taken either from the ABINIT website, or calculated using the Atomic Pseudopotentials Engine (APE).[54]

2.4. Grid unwarping near atomic centers

The basis of the DFT-CP method lies in the ability of the DFT total energy to be at least partially represented as an integral over a spatially resolved energy density:

$$E_{DFT} = \iiint_{unit\ cell} \rho_{energy}(\vec{r})dV + E_{remainder} \qquad (2.1)$$

where $E_{remainder}$ contains energetic contributions that are not easily traced to specific points in space, such as the Ewald energy and nonlocal components of the potential energy. Using the output of the ABINIT program, such an energy density function can be constructed in the form of discrete points on a grid, i.e.

$$E_{DFT} \approx \sum_{n}^{N_{voxels}} \rho_{energy}(\vec{r}_n)V_{voxel} + E_{remainder} = \sum_{n}^{N_{voxels}} E_n + E_{remainder} \qquad (2.2)$$

where N_{voxels} and V_{voxel} are respectively the number of voxels in the structure's unit cell and the volume of each individual voxel.

When we recall that pressure and total energy are related as $P = -\partial E/\partial V$, a straightforward approach to constructing pressure maps emerges. We can simply generate energy grids for a structure at volumes that are slightly contracted and expanded relative to the geometry of interest, and use the resulting energy difference at each voxel as the basis for the calculation of voxel pressures:

$$P_n = -\partial E_n / \partial V \tag{2.3}$$

The representation of the total energy as a sum over an energy grid then gives way to the net pressure experienced by a phase being expressed as the average over a pressure grid:

$$P = -\frac{\partial E_{DFT}}{\partial V_{cell}} = -\sum_{n}^{N_{voxels}} \frac{\partial E_n}{N_{voxels}\partial V_{voxel}} - \frac{\partial E_{remainder}}{\partial V_{cell}}$$

$$= \frac{1}{N_{voxels}} \sum_{n}^{N_{voxels}} P_n - P_{remainder} \tag{2.4}$$

In our applications of this procedure, we have found that a rather consistent result is obtained over a wide range of solid state compounds: the pressure maps are marked by intense pressures (of several TPa) near the core regions of the atoms, with much shallower features in the interstitial portions of the structure. The extreme magnitudes of these core pressures mean that success in the interpretation of the pressure map is strongly dependent on how the cores are divided among interatomic interactions.

A key question here is whether the strong pressures in the core regions represent the interactions between atoms, or are instead an artifact of the pseudopotential models for the atoms or the procedure for the generation of the pressure maps. A simple way to answer this question is to consider a case in which interatomic interactions should be absent: isolated atoms. In Figure 2.2a, we show cross-sections of CP

maps calculated for individual atoms placed in large unit cells, for which the interatomic distances are sufficiently long (10 Å) that each atom should exhibit virtually no influence on its neighbors. Maps are shown for a variety of elements, but common features are present: the atomic position at the center of the map is clearly decorated with intense oscillating pressure features emanating from the atomic cores. Depending on the diffuseness of the valence electron wavefunctions, the scales of these features vary over a significant range: from 0.07 atomic units for the valence-only Ca pseudopotential, to 120 atomic units for the semi-core Ga pseudopotential. In all but the shallowest pseudopotentials, pressures of more than 1 atomic unit are attained. When we recall that 1 atomic unit of pressure is equal to 96,000 GPa, it is apparent that they represent pressure responses that are incommensurately large relative to the minuteness of the perturbations on these systems induced by a small expansion or contraction of the unit cell.

Why should such strong pressures arise in the absence of interatomic interactions? An assumption of the above formulation of the DFT-CP approach is that upon changing a unit cell's volume, the features of the potentials and electron density expand or contract along with the voxel grid.[30] In this way, the pressure calculated for a specific voxel (P_n) is then related to the difference in energies calculated for that voxel in slightly expanded and contracted structures:

$$P_n^{DFT-CP} \approx -\frac{E_n^+ - E_n^-}{V_{voxel}^+ - V_{voxel}^-} \tag{2.5}$$

This may be expected to apply well to the regions in the interstitial spaces, where atoms are most responsive to changes in their surroundings. Near the atomic cores, however, where electrons cling tightly to the nuclei, such an assumption is harder to justify. In the cores, the depths of the atomic pseudopotentials are such that variations in the cell volume would represent only minor changes. The electron density would not be expected to migrate along with an expanded or contracted voxel grid.

It would seem that a more careful consideration is needed for the high electron densities of the core regions. The pressure response at these points in space might be better approximated by assuming that a volume element of fixed size and position relative to the associated atomic core should be sampled for the expanded and contracted structure.

This can be accomplished by supplementing the original DFT-CP methodology with an unwarping procedure. Consider energy density distributions calculated for the equilibrium geometry of a crystal structure, a slightly expanded structure, and a contracted structure, which we can represent respectively as $\rho^{o}_{energy}(\vec{r})$, $\rho^{+}_{energy}(\vec{r})$, and $\rho^{-}_{energy}(\vec{r})$. If we then write the pressure of voxel n in terms of its relationship to its nearby atom j ($\vec{r}_n = \Delta\vec{r}^{\,o}_n + \vec{r}^{\,o}_{atom\ j}$), then the pressure at that point, assuming that the energy density does not dilate with the voxel grid, can be calculated as

$$P_n \approx -\frac{\left\{\rho^{+}_{energy}\left(\Delta\vec{r}^{\,o}_n + \vec{r}^{\,+}_{atom\ j}\right) - \rho^{-}_{energy}\left(\Delta\vec{r}^{\,o}_n + \vec{r}^{\,-}_{atom\ j}\right)\right\}V^{o}_{voxel}}{V^{+}_{voxel} - V^{-}_{voxel}} \tag{2.6}$$

Calculating pressures in this way is complicated by the fact that the energy densities obtained over the course of a CP calculation are expressed in terms of the discrete points of a voxel grid. The vectors $\Delta\vec{r}^{\,o}_n + \vec{r}^{\,+}_{atom\ j}$ and $\Delta\vec{r}^{\,o}_n + \vec{r}^{\,-}_{atom\ j}$ then often will lie in between grid points, and the energy densities at those points cannot be determined exactly. Trilinear interpolation, however, can be used to obtain an estimate based on the values for the surrounding voxels. The magnitude of the errors is then related to the fineness of voxel grid spacing relative to the complexity of the electron density function.

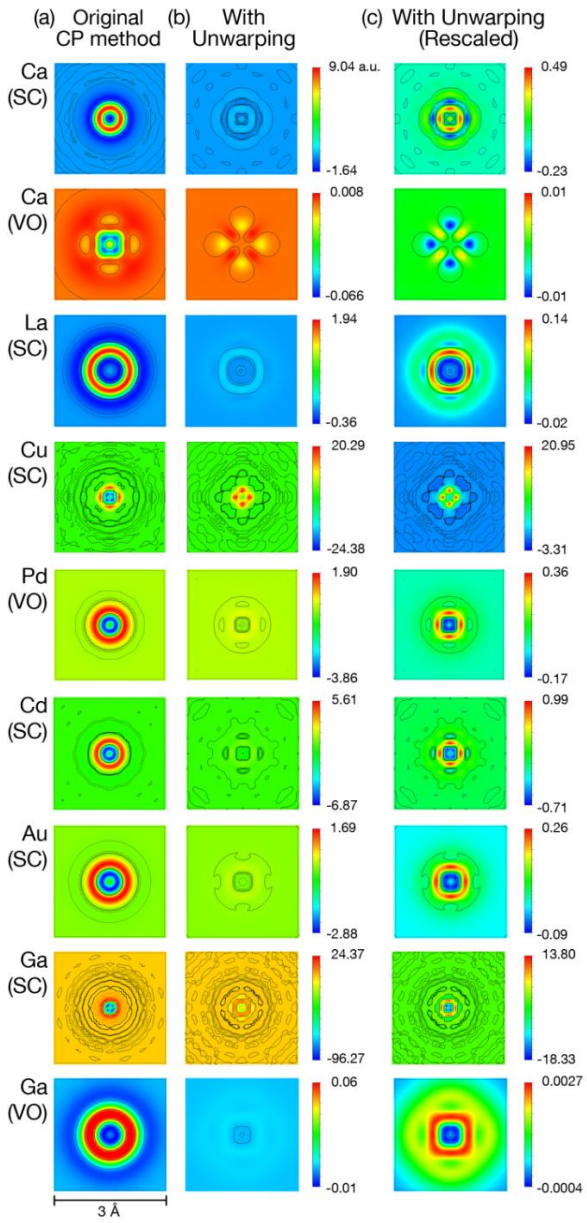

Figure 2.2. DFT-Chemical Pressure (CP) maps for individual atoms isolated in large unit cells (cell edges of 10 Å). (a) Cross sections through the nuclear positions using the original DFT-CP scheme. (b) The corresponding CP maps calculated using the process for unwarping the energy grids near the atomic cores, plotted using the same color map as in (a). (c) The unwarped maps with the color map adjusted to a narrower range. Note that the unwarping procedure significantly reduces the strong core-like features around the atomic position (which should be essentially absent in these calculations on virtually isolated atoms). SC and VO refer to the semicore and valence-only versions of the atomic pseudopotentials, respectively, where applicable. Black contours trace isosurface levels at increments of 0.05 between -0.1 and 0.1 a.u.

This methodology is implemented in our current version of the program *CPmap*. The voxel energies for the expanded and contracted structure are first calculated according to Equation 2.2. The voxels are then associated with specific atomic cores, which can be done by specifying cutoff radii, using a Voronoi scheme,[55] a more complicated division of space as offered by Bader's QTAIM,[56] or, as we will describe in more detail below, a Hirshfeld-type weighting.[42] The voxel centers in the expanded ($\vec{r}_n^{+}$) and contracted ($\vec{r}_n^{-}$) structures are then shifted to their corresponding positions relative to their atom's nuclear position as in the equilibrium volume structure ($\vec{r}_n = \Delta\vec{r}_n^{o} + \vec{r}_{atom\ j}^{o}$). Finally, the pressures at the voxel positions are calculated according to equation 2.6.

As the shifts in the voxel positions represent a different sampling of the same energy density maps, this interpolation leads to only small changes to the total energy obtained by integrating over the voxel grid (ca. 0.05%). Any small residual pressure resulting from differences in the interpolation error for the expanded and contracted structures is added homogeneously to the pressure map.

In Figures 2.2b-c, we illustrate the effect of applying this fixed core correction procedure to atoms isolated in boxes. Figure 2.2b shows cross-sections of the pressure maps for the atoms drawn with the same color map as in Figure 2.2a. The correction leads to a substantial change in the pressure distribution. The original, strongly oscillating ripples of pressure are now replaced with flatter maps and less isotropic features. Figure 2.2c focuses on narrower pressure ranges to allow the more subtle features of these maps to be visible. Here, it can be seen that the variations are in many cases more associated with the corners and faces of the unit cell than with the distance to the atomic core.

2.5. Grid unwarping between atoms

Atoms in more realistic environments should also benefit from this type of core treatment. Figure 2.3a shows two-dimensional slices of CP maps calculated for a diverse array of intermetallic compounds. For most examples using the original method, the maps show the most intense pressures as nearly perfect circles around the atomic positions. These core regions are set against what appears to be a shallow, nearly homogeneous negative background pressure. As such features are reminiscent of our uncorrected treatment of the atoms-in-boxes of Figure 2.2a, it seems likely that implementing grid interpolations here should lead to more meaningful CP maps.

For voxels near the cores of any given atom, the path to applying the above procedure is clear: the voxels can be assigned to their nearby atom, and then treated according to Equation 2.6. The situation becomes less clear for voxels deeper in the interstitial spaces between the atomic cores, where the energy density features might be expected to migrate to various degrees with the voxel grid as the structure is expanded and contracted. How should the unwarping process be applied to these regions?

A voxel's position in the equilibrium grid can be represented in terms of its placement relative to any of the atoms in the structure:

$$\vec{r}_n = \Delta\vec{r}^{\,o}_{n,atom\ 1} + \vec{r}^{\,o}_{atom\ 1} = \Delta\vec{r}^{\,o}_{n,atom\ 2} + \vec{r}^{\,o}_{atom\ 2} = \cdots \qquad (2.7)$$

As we move to the expanded or contracted volumes, the various atoms will shift to different positions, so that the various equalities of Eq. 6.7 cannot be satisfied simultaneously if we keep the $\Delta\vec{r}^{\,o}_{n,atom\ j}$ vectors constant. Instead, we will need to decide to what degree each of the $\Delta\vec{r}^{\,o}_{n,atom\ j}$ terms will be weighted in the determination of the $\vec{r}_n^{+}$ and $\vec{r}_n^{-}$ vectors.

One approach to determining these weights can be found in the Hirshfeld method for the extraction

of atomic charges from electronic structure calculations.[42] In the Hirshfeld approach, one begins with a hypothetical case in which the electron density of a compound is simply a superposition of free atom electron densities centered at the nuclear positions of a structure. The relative contributions from these free atom densities at a given point in space is then translated into relative weights for the apportioning of the true electron density between the atoms in the calculation of charges. The free atom electron densities thus serve as a measure of the distance dependence of each atom's influence.

In a similar way, the Hirshfeld method for the atoms surrounding a voxel can be used in assigning weights to each of the equalities in Equation 2. 7. We first define a Hirshfeld weight for the influence of atom *j* on the position of voxel *n*:

$$w_{j,n} = \frac{\rho^{FA}_{atom\ j}(\vec{r}^{\,o}_n)}{\sum_k^{all\ atoms} \rho^{FA}_{atom\ k}(\vec{r}^{\,o}_n)} \tag{2.8}$$

where $\rho^{FA}_{atom\ k}(\vec{r}^{\,o}_n)$ gives the electron density at the position of voxel *n* calculated for a free atom of the proper element centered at the nuclear coordinates of atom *k*.

Having defined these weightings, we can then use them in determining how much a voxel should maintain its position relative to each of the atomic centers as the cell is expanded and contracted for the calculation of CP maps:

$$\vec{r}^{\,+}_n = \sum_j^{all\ atoms} w_{j,n}(\Delta\vec{r}^{\,o}_{n,j} + \vec{r}^{\,+}_{atom\ j}) \tag{2.9a}$$

$$\vec{r}^{\,-}_n = \sum_j^{all\ atoms} w_{j,n}(\Delta\vec{r}^{\,o}_{n,j} + \vec{r}^{\,-}_{atom\ j}) \tag{2.9b}$$

For voxels near an atomic core, the weight for that atom will dominate these averages, and the original atom-centered interpolation of the previous section is obtained.

In performing this distortion of the voxel grid around the atom centers, the grid points are no longer uniformly distributed, and the voxel volumes become varied throughout the structure. The calculation of the voxel pressures then becomes slightly modified from equation 6.6:

$$P_n \approx -\frac{\rho^{+}_{energy}(\vec{r}^{+}_n)V^{+}_{voxel,n} - \rho^{-}_{energy}(\vec{r}^{-}_n)V^{-}_{voxel,n}}{V^{+}_{voxel} - V^{-}_{voxel}} \tag{2.10}$$

where the numerator involves the volumes of the specific voxel *n* in the expanded and contracted structures, and the denominator uses the average voxel volumes for the two structures. A discussion of the determination of the voxel volumes in the distorted grid is provided in the Supporting Information.

Turning on the unwarping procedure (Figures 2.3b and c) significantly reduces the magnitudes of the pressures of the core regions, allowing more subtle features in the interatomic regions to come more to the foreground. Also, in some cases, particularly La_5Sn_3 and $CaAu_5$, the spherical character of the core regions has diminished, making the centers of the atoms appear more responsive to their surroundings. This is more consistent with the philosophy of pseudopotentials which aims to treat explicitly only those electrons that are perceptibly affected by interatomic interactions as part of the valence set.

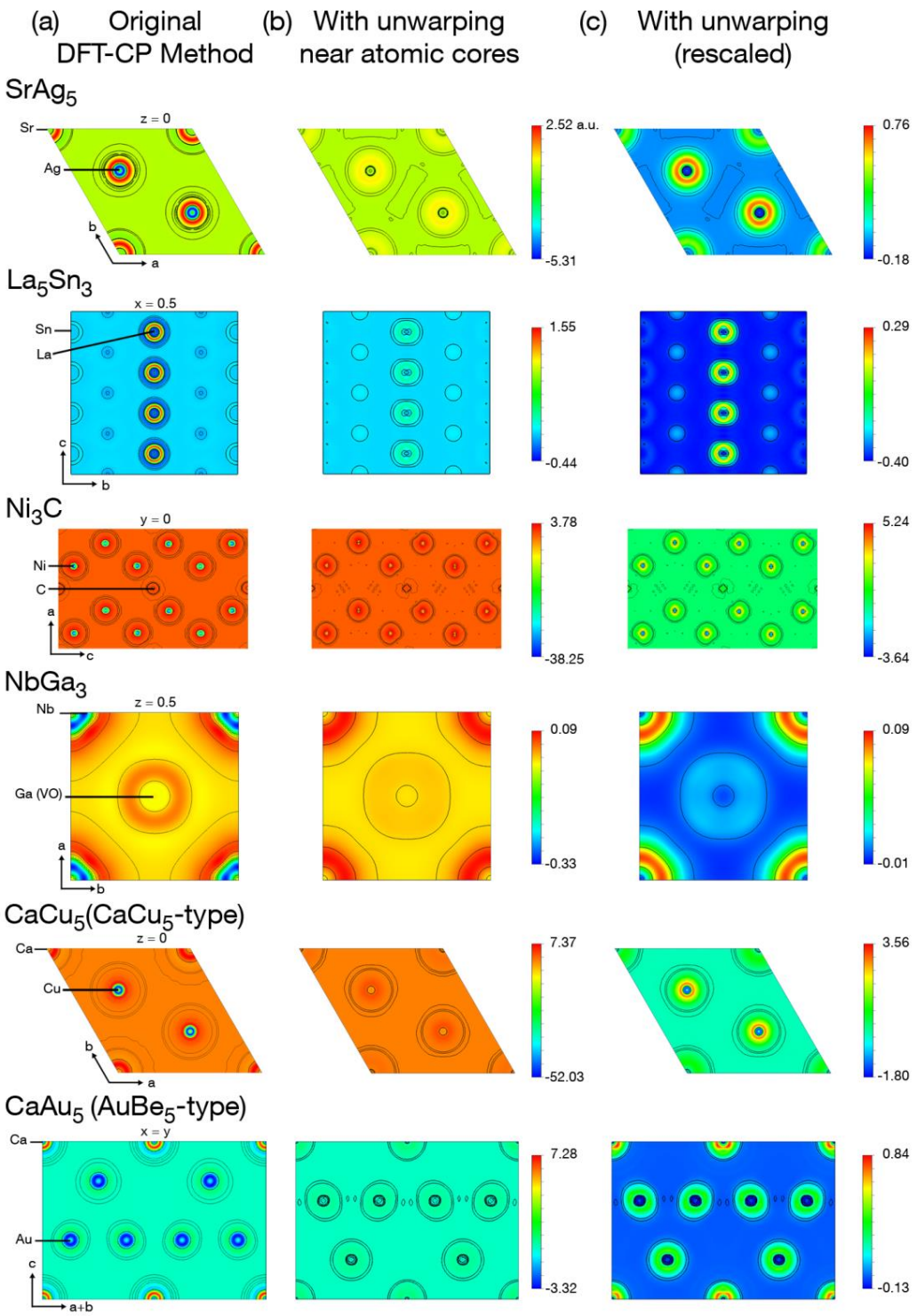

Figure 2.3. Cross sections for the DFT-CP maps of a variety of intermetallic phases calculated (a) before and (b) after the unwarping of the energy grids using the same color map, and (c) the unwarped maps plotted with more appropriately tailored color maps.

2.6. Hirshfeld-inspired contact volumes

In the previous section, we saw how the features of a CP map could be substantially clarified by introducing a step in which corresponding grid points of the expanded and contracted unit cells are shifted to the same position in space relative to an atom assigned to it. By implementing this procedure, the severe isotropic pressures appearing around the atomic cores are reduced, allowing more subtle features to come to the foreground. Even with this improvement, however, the CP distributions still largely consist of positive regions around the atomic centers that are immersed in a shallower negative background pressure. In examining the overall pressures at particular interatomic contacts, we will then need to examine the net effect of these core-like and interstitial pressures through the integration of the pressure map within domains assigned to individual contacts.

In performing such an integration, the pressure between a pair of atoms will be given by

$$P_{jk}^{contact} = \sum_{n}^{N_{voxels}} w_{jk,n} P_n \tag{2.11}$$

where $w_{jk,n}$ is the fraction of the pressure at voxel n that is attributed to the interaction between atom j and atom k. The central challenge in carrying out the integrations in a meaningful way is then the determination of the proper weighting scheme, the set of $w_{jk,n}$'s. In our recent applications of the DFT-CP method, we derived our choice of weights from an assumption that a voxel's pressure is determined by the interaction of its two nearest atoms, i.e.

$$w_{jk,n} = \begin{Bmatrix} 1, if\ atoms\ j\ and\ k\ are\ two\ closest\ to\ voxel\ n \\ \frac{1}{m}, if\ m\ contacts\ are\ tied\ in\ above\ criterion \\ 0, if\ j\ or\ k\ are\ not\ two\ atoms\ closest\ to\ voxel\ n \end{Bmatrix} \tag{2.12}$$

This scheme is advantageous in its simplicity. However, as it is entirely based on geometrical constructions, it neglects the differing ranges of influence of different atom types, and should be considered as only a first step toward a more realistic division of space between contacts.

Over the course of our ongoing exploration of intermetallic phases using the DFT-CP method, we have found that for one large and important class of compounds, the Laves phases and their variants, refinements to the weighting scheme are particularly vital. In these AB_2 compounds (see Figure 1.1a for one example), the A positions (usually occupied by a relatively electropositive element) form a diamond network, a hexagonal diamond network, or an intergrowth of the two. The B atoms occupy the interstitial spaces of the A diamondoid framework, and form truncated tetrahedra (TT) around the A atoms. The resulting coordination environment around the A sites is known as a Friauf polyhedron, consisting of a TT of B atoms with A atoms sitting above the hexagonal faces of the TT.

The geometrical features of the Friauf polyhedron make it a challenging test case for the division of space among interatomic contacts. The A-A and A-B distances exhibit a ratio of 1.0445 (for the high symmetry $MgCu_2$-type case), with the longer A-A lengths being consistent with the trend that the A sites are generally occupied by the larger atom type. However, using the distance-based criterion described above, the voxels inside the Friauf polyhedron will be assigned to the pairs of atoms to which they are closest. As the A-B interatomic distances are shorter than the A-A ones, these will tend to absorb more voxels, despite the A atoms being larger.

This dominance of the A-B contacts in the voxel assignments has interesting consequences for the integrated CP schemes. In Figure 1.4a, we show the results for the $MgCu_2$-type phase $CaPd_2$,[57,58] using the projection scheme described previously. Here, the distribution of voxel pressures around each atom is represented by radial surfaces around its nuclear position. The distance of a point on the surface from the

nucleus is proportional to the sums of the voxel pressures along that direction, while the color of the surface gives the sign of the pressure. Lobes in black point along directions where the pressure is negative, i.e. contraction would be favorable, while portions of the surfaces in white correspond to positive pressures, where the structure would prefer to expand.

For the Friauf polyhedron of $CaPd_2$ using the original geometrical construction of contact volumes, the white and black features are divided largely by element type. The Ca atoms appear as black tetrapods, with large negative pressure lobes pointing along the Ca-Ca contacts (red). These forces calling for the contraction of the lattice are counteracted by white, positive pressure lobes along the Pd-Pd contacts (blue), with the Ca-Pd contacts appearing to be relatively satisfied. This result is encouraging in the sense that the heteroatomic interactions, the usual driving force for the formation of a binary phase from its elements, are well-optimized.

However, inspection of the contact distances uncovers some counterintuitive aspects of this picture. Note that in the Ca-Ca/Pd-Ca distance ratio of 1.0445, the Ca-Ca contacts are only slightly longer than the Ca-Pd ones, despite the metallic radius of Ca being significantly larger than that of Pd (1.97 vs. 1.37 Å[59]). As a consequence, the Ca-Ca distance is much shorter than the sum of the metallic radii (3.32[57] vs. 3.94 Å[59]). This distance is still within the ranges observed for Ca-Ca interactions in the Inorganic Crystal Structure Database,[60,61] but would hardly be the occasion for large negative pressures demanding even closer Ca-Ca contacts. If anything, a positive pressure pushing toward distances more in-line with twice the metallic radius would be expected.

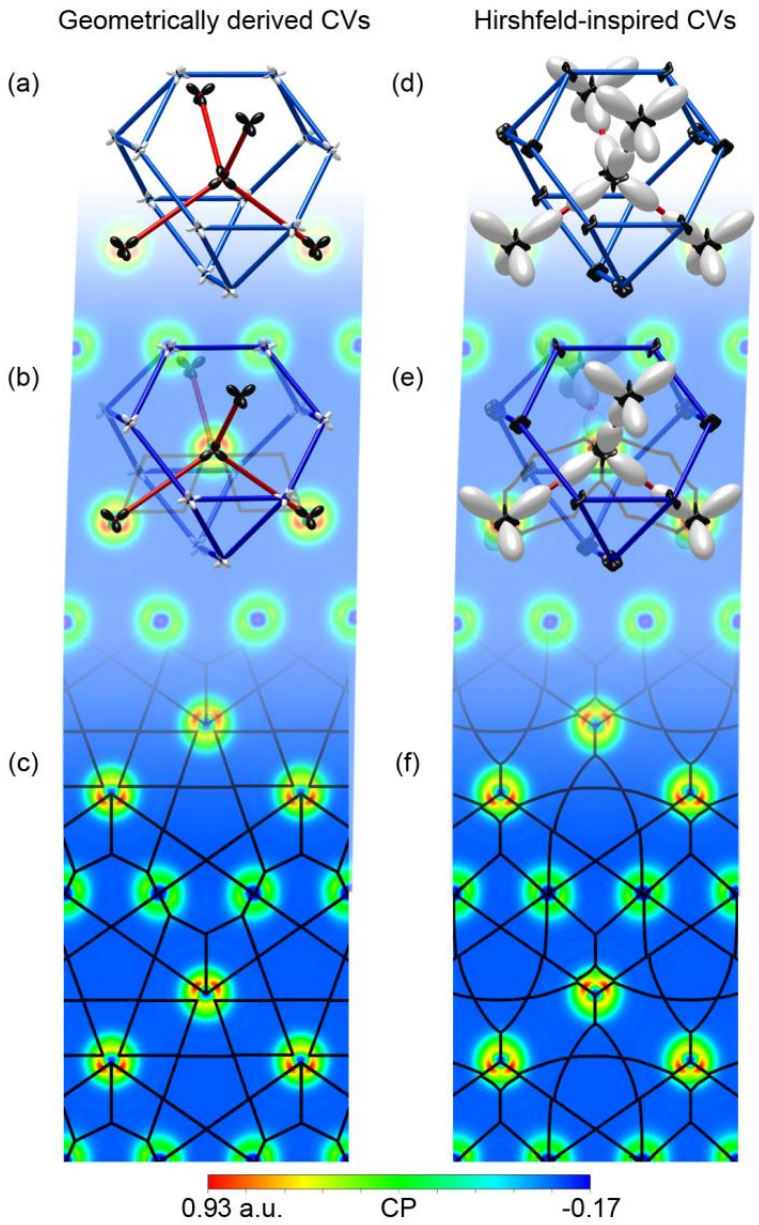

Figure 2.4. Comparison of integrated DFT-CP anisotropies and contact volumes for $CaPd_2$. (a) The DFT-CP distribution calculated for $CaPd_2$ using the original contact volume (CV) scheme. (b) The DFT-CP distribution plotted together with a cross section of the original DFT-CP map. (c) The DFT-CP cross-section shown separately with the contact volume borders indicated. (d)-(e) The corresponding images generated using the Hirshfeld-inspired contact volume scheme (see text). In (a) and (d), the pressure distribution around each atom is represented by a radial plot, with the radial distance indicating the magnitude of the sum of voxel pressures along that direction. The sign of the pressure is indicated with color: black for negative (evoking the image of a black hole acting on the structure), white for positive.

A look at the volumes assigned to each contact in our integration provides an explanation for the appearance of these negative Ca-Ca pressures. In Figures 2.4b,c, we present a cross section of the DFT-CP map for $CaPd_2$ taken through one of the Ca-Ca contacts, with the boundaries between contact volumes drawn in black. The contact volume of the Ca-Ca interaction appears here as a diamond between the two atoms. A brief glance reveals why negative pressures are assigned to this contact: whereas positive pressure features occur around both the Ca atoms of the contact, only the tips of the narrow corners of the contact volume reach into these regions. Instead, the contact volume contains mainly the negative pressure interstitial space between the Ca atoms. The core regions themselves are dominated by Ca-Pd contact volumes.

In other words, the Ca-Pd distances are short enough relative to the Ca-Ca ones that the distance criterion grants them most of the Ca core voxels. As a result, only small positive pressure components are allocated to the Ca-Ca contacts, and negative pressures thus dominate despite the short Ca-Ca distances.

Now that we see the origin of the Ca-Ca negative pressures, a way to correct the CP picture becomes apparent: the Ca-Ca contact volumes should be expanded into the Ca core regions to better reflect the larger size of the Ca atoms relative to Pd atoms. To do this, a change in the weighting scheme of equation 2.12 is needed that takes into account the differing electronic structures of Ca and Pd atoms.

As for our grid-interpolation scheme above, the Hirshfeld approach can be adapted to this task, the essential change being that we are now assigning points in space to pairs of atoms rather than individual atoms. The influence of a contact on a point in space will depend on the sizes of the free atom electron densities for the two atoms at that point. A way of quantifying this is to consider the weights in equation 2.11 as being proportional to the products of the free atom (FA) electron densities for the atoms of the contact:

$$w_{jk,n} \propto \rho^{FA}_{atom\ j}(\vec{r}_n) \cdot \rho^{FA}_{atom\ k}(\vec{r}_n) \tag{2.13}$$

In this way, every voxel would be shared among multiple contacts, with weights that are proportional to the overlaps between the FA electron densities for each contact.

In experimenting with such integration schemes, we have found that following through with this Hirshfeld-based approach in its entirety leads to some issues with interpretation: it is difficult to see which points in space are influencing which contacts. Instead, it is more practical to keep the division of space into discrete contact volumes as in equation 2.12, but using the products of FA electron densities as a guide to their construction. The corresponding weighting is then:

$$w_{jk,n} = \begin{cases} 1, if\ \rho^{FA}_{atom\,1}(\vec{r}_n)\rho^{FA}_{atom\,2}(\vec{r}_n)\ is\ largest\ for\ j,k\ pair \\ \frac{1}{m}, if\ m\ contacts\ are\ tied\ in\ above\ criterion \\ 0, if\ \rho^{FA}_{atom\,1}(\vec{r}_n)\rho^{FA}_{atom\,2}(\vec{r}_n)\ \ not\ largest\ for\ j,k\ pair \end{cases} \qquad (2.14)$$

The result of using this Hirshfeld-inspired scheme is shown in Figures 4d-e. The Ca-Ca contact volume (Figure 2.4e) now reaches much deeper into the Ca cores so that a corner lies on each Ca nuclear position. The angle at each of these corners has also expanded to encompass more of the core's volume. In fact, the core is now entirely divided between the four Ca-Ca contacts arranged in a tetrahedron around the central Ca atom.

At first glance, the new contact volume boundaries do not appear to align with the prominent features of the Ca core regions. In the cross-section of Figure 2.4f, each Ca atom exhibits a pair of red bulges corresponding to high positive pressures. Their directional character would lead us to think that they are associated with particular interatomic interactions. However they are almost perfectly bisected by the borders of the CVs, rather than being centered within a specific CV. A deeper investigation of these features resolves this apparent discrepancy. As is illustrated in the Supporting Information, we have found that the

highest pressures within the core regions tend to accumulate in the spaces lying between important interatomic interactions, rather than along them. The source of this is a negative pressure contribution arising from the overlap of the local pseudopotentials along the interatomic vector. The core regions not aligned with these vectors then tend to be the spaces where the positive core pressures are most prominent.

The increased contribution from the Ca cores to the Ca-Ca contact volumes has a profound effect on the integrated CP distributions (Figure 2.4d). The Ca-Ca contacts now exhibit intense positive pressures that seem appropriate to the relatively short Ca-Ca distances. These positive pressures are balanced by the negative pressure lobes oriented along the Ca-Pd interactions. The Pd-Pd contacts, meanwhile, are largely devoid of CP features, indicating that the distances here are nearly optimal.

In comparing Figures 1.4a and 1.4d, it is somewhat surprising that they represent the same original CP map, and differ only in the integration scheme used. In what ways are they connected? To see their relationship to each other, it is helpful to note that the Ca-Ca contacts pass through hexagons of Pd atoms. The integrated pressures in this region of the structure will depend on the relative sizes and shapes of Ca-Ca, Ca-Pd, and Pd-Pd contact volumes. In the original scheme, the size of the Pd atoms is overestimated relative to the Ca ones, which leads to the Ca-Pd and Pd-Pd volumes dominating the positive cores of the Ca and Pd atoms. The result is positive pressures along the Pd-Pd interactions and only small negative pressures along the Ca-Pd ones.

In moving to the Hirshfeld-inspired scheme, the Ca-Ca volumes are increased at the expense of the Ca-Pd and Pd-Pd volumes. The contact volumes involving Ca then pick up more of the positive core pressures, leading to large positive pressures between the Ca atoms, the removal of positive pressures from the Pd-Pd interactions, and only smaller changes to the Ca-Pd interactions (which lose core contributions from the Ca but gain them from the Pd).

The better treatment of atomic sizes is not the only reason for which the revised CP scheme is attractive: it also corresponds closely with expectations based on the sphere-packing view of the Laves phases. Consider a $MgCu_2$-type AB_2 structure constructed from hard spheres with radius r_A for the A atoms and r_B for the B atoms. The high symmetry of the structure means that the distances are entirely determined by the length of the cubic unit cell edge, and no other degrees of freedom exist for adjusting the structure to accommodate the values of r_A and r_B. If the B atoms are in contact with each other at an interatomic distance of 2 r_B, then the surfaces of the A atoms touch each other when the r_A/r_B radius ratio is $(3/2)^{1/2}$ = 1.225. However, the surfaces of the A atoms would not touch those of the B atoms until $r_A/r_B = (11/2)^{1/2}$-1 = 1.345. As such, bringing the A and B spheres in contact would require allowing the A atoms to slightly interpenetrate each other.

We can now compare these radius ratios for that of the metallic radii for $CaPd_2$, r_{Ca}/r_{Pd} = 1.97 Å/1.37 Å = 1.44. For this ratio, having sphere surfaces touch at the Pd-Pd or Ca-Pd contacts would require the Ca spheres to overlap. In this situation, positive pressures could be expected to arise between the Ca atoms as the structure strives to achieve closer contacts along the Pd-Pd and Ca-Pd interactions. This picture agrees well with the CP scheme of Figures 2.4d-f. We anticipate that the revised CP scheme obtainable for Laves phases will offer opportunities to examine the driving forces for the creation of complex structures through the fragmentation of these simpler structures,[62-70] and will improve our ability to discern the reasons for the intergrowth of Ca-Cd and Cd-Cu interactions in the Bergman-type quasicrystal approximant $Ca_{10}Cu_2Cd_{27}$.

It is important to mention, however, that this result is dependent on the use of a semicore Ca pseudopotential in which not only the Ca 4s but also 3p and 3s electrons are considered as part of the valence set. Using a "valence-only" Ca pseudopotential with just the 4s electrons treated explicitly leads to a CP

scheme similar to Figure 4a regardless of what map generation and integration procedures are applied. We believe that this can be attributed to the relatively high ionicity expected for the $CaPd_2$ phase. Indeed a Bader charge analysis using the *BADER* program[71-73] of our valence-only electron density for this phase gives a charge on the Ca atoms of +1.7, indicating that only 0.3 electrons lie near the Ca cores. With so few valence electrons present on Ca atoms, it is understandable that the explicit inclusion of semicore electrons would be necessary to model the atom's responses to its surroundings. From this, we arrive at a recommendation that semicore potentials be used in cases where atoms are expected to be highly cationic.

Using the improved method including Hirshfeld-inspired contact volumes and interpolation within atomic cells, we have also been able to reproduce the conclusions of our earlier studies examining the stability of the complex Ca_2Ag_7 and $Ca_{36}Sn_{23}$ structures relative to simpler structural alternatives. In the remainder of this Article, we will describe a different application of the DFT-CP method: determining the role of atomic size in the relative stabilities of competing structure types. Our focus will be on the structural preferences of AB_5 structures for $CaCu_5$- or $AuBe_5$-type structures, for which atomic size has been considered a key factor.

2.7. Stability trends in AB_5 intermetallics

In the previous sections of this paper, we described improvements to the DFT-CP method, and showed how they offer a CP scheme for the Laves phase $CaPd_2$ that is in close accord with radius ratio considerations. Using the same implementation of the CP concept, it is also possible to explain the stability trends for another intermetallic structure type that is closely related to the Laves phases: the $AuBe_5$ type. This AB_5 structure type can be derived from the AB_2 $MgCu_2$-type by replacing every other A atom

in the structure with a B atom, i.e. $A_2B_4 \rightarrow ABB_4 = AB_5$ (Figure 2.1b). For AB_5 intermetallics with A being an alkaline earth or lanthanide and B being a late transition metal, the $AuBe_5$ type appears to be in competition with the more common $CaCu_5$ type. The factor determining the relative stabilities of these two structure types appears to be the relative sizes of A and B atoms,[43] an effect that should be amenable to CP analysis.

Let's begin by examining the DFT-CP distribution for a representative of the $AuBe_5$ type: $CaAu_5$.[74] In Figure 2.5, we present CP anisotropy surfaces for this structure calculated with the range of procedures discussed in the previous section. First, in Figure 2.5a, we show the result using the original methodology without interpolation within atomic cells and using a geometrical construction for the contact volumes. In Figures 1.5b-c, we turn on either the interpolation procedure or the Hirshfeld-inspired determination of contact volumes (CVs). Finally, in Figure 2.5d, we use the fully improved method, with both the interpolation and new contact volumes.

Using the original DFT-CP scheme, the integrated CP distribution closely resembles that obtained in this way for the Laves phase $CaPd_2$ (Figure 2.4a), despite having replaced four Ca-Ca contacts with Ca-transition metal ones. Negative pressure lobes (black) point through the faces of the truncated tetrahedron just as in $CaPd_2$, while the edges of the truncated tetrahedron itself are decorated with positive pressure lobes. The Ca atom, overall, has large negative pressure indicating that it would benefit from contraction of the lattice, which is prevented by positive pressures within the Au truncated tetrahedra. As such,

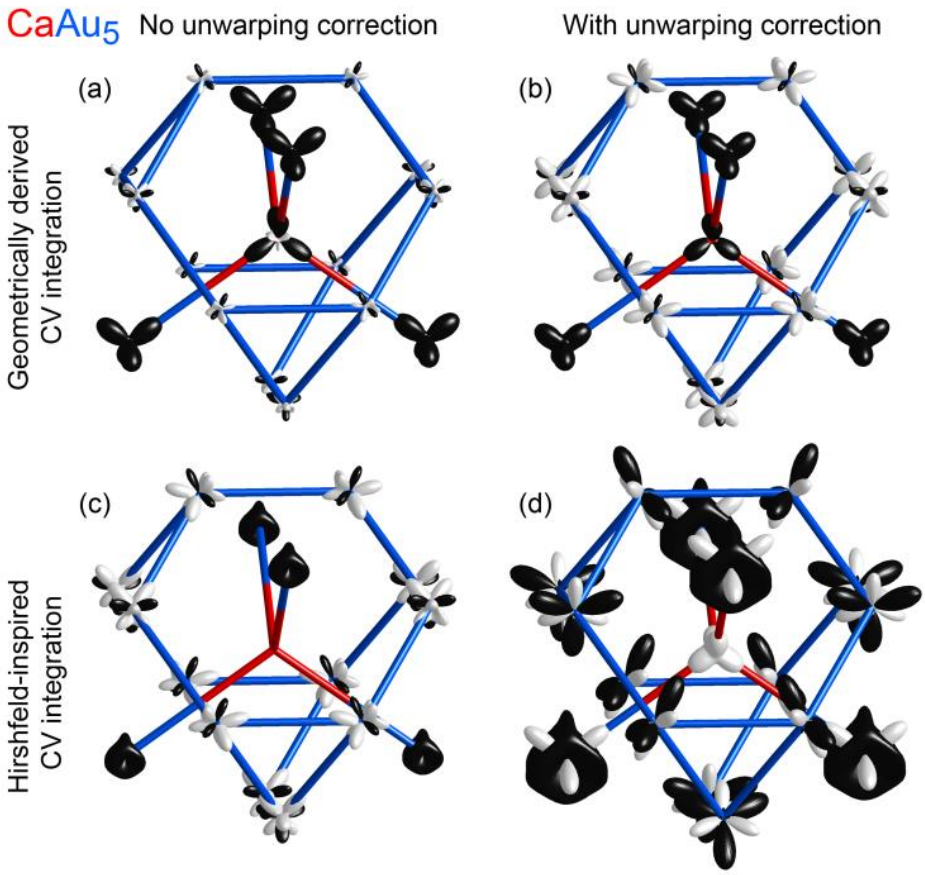

Figure 2.5. Comparison of DFT-CP anisotropy schemes calculated for $CaAu_5$ using (a) the original methodology, (b) the improved map generation (with the unwarping procedure applied) but original geometrically constructed contact volumes, (c) the original map generation but the Hirshfeld-inspired contact volume determination, and (d) the improved methods for the both the creation of maps and contact volumes. See the caption to Figure 1.4 for plotting contentions.

this scheme predicts that the structure would be stabilized by replacing the Ca with a larger atom—which of course runs counter to the empirical trend of the $AuBe_5$ type being observed for small A atoms.

Turning on either the interpolation near atomic cores (Figure 2.5b) or the Hirshfeld-inspired CVs (Figure2.5c), introduces qualitative changes to the CP distributions on the $Ca@Au_4$ tetrahedron, but leaves the positive pressures between the Au atoms of the truncated tetrahedron largely intact. The most dramatic change occurs upon turning on both features of the improved DFT-CP method simultaneously

(Figure 2.5d). Here, positive CP lobes point along all of the Ca-Au contacts, while negative CP is reserved for the Au-Au interactions with the longest interatomic distances. Unlike that of the original DFT-CP scheme, the final integrated result is in close agreement with experimental trends: the positive pressures surrounding the Ca atoms indicate that the stability of this structure will be largely dependent on having a relatively small atom at this position.

In comparing Figures 2.5b and 2.5d, it is evident that the use of Hirshfeld-inspired CVs plays a significant role in obtaining positive pressures on the Ca sites. As for $CaPd_2$, a comparison of the CVs generated with the original and Hirshfeld-inspired schemes is helpful in seeing how these differences arise (Figure 2.6). On moving from the $MgCu_2$ type to the $AuBe_5$ type, the relative interatomic distances are left unchanged. Because of this, the Ca-Ca geometrically derived CV in $CaPd_2$ (Figure 2.4b) is identical to the corresponding one in $CaAu_5$ (Figure2.6b), although now it corresponds to a Ca-Au CV. In the slice through the structure of Figure 2.6, this CV appears as a diamond-shaped polygon. Only the narrow corners of this polygon cross into the positive core regions of the Ca and Au atoms, leading to a net negative pressure for the contact.

As we switch to the Hirshfeld-inspired scheme, the larger size of the Ca atoms relative to Au will lead to the growth of the Ca-Au CVs at the expense of the Au-Au ones. Because the Ca is surrounded by Au atoms, in the shapes of the CVs near the Ca center are essentially unchanged. However, on the Au atoms, there is a marked expansion of the Ca-Au CVs into regions previously occupied by Au-Au ones (Figures 2.6c,f). The Au-Ca CVs then acquire more of the positive core pressures on the Au atoms, leading to the overall positive CPs between the Ca atom and its neighbors.

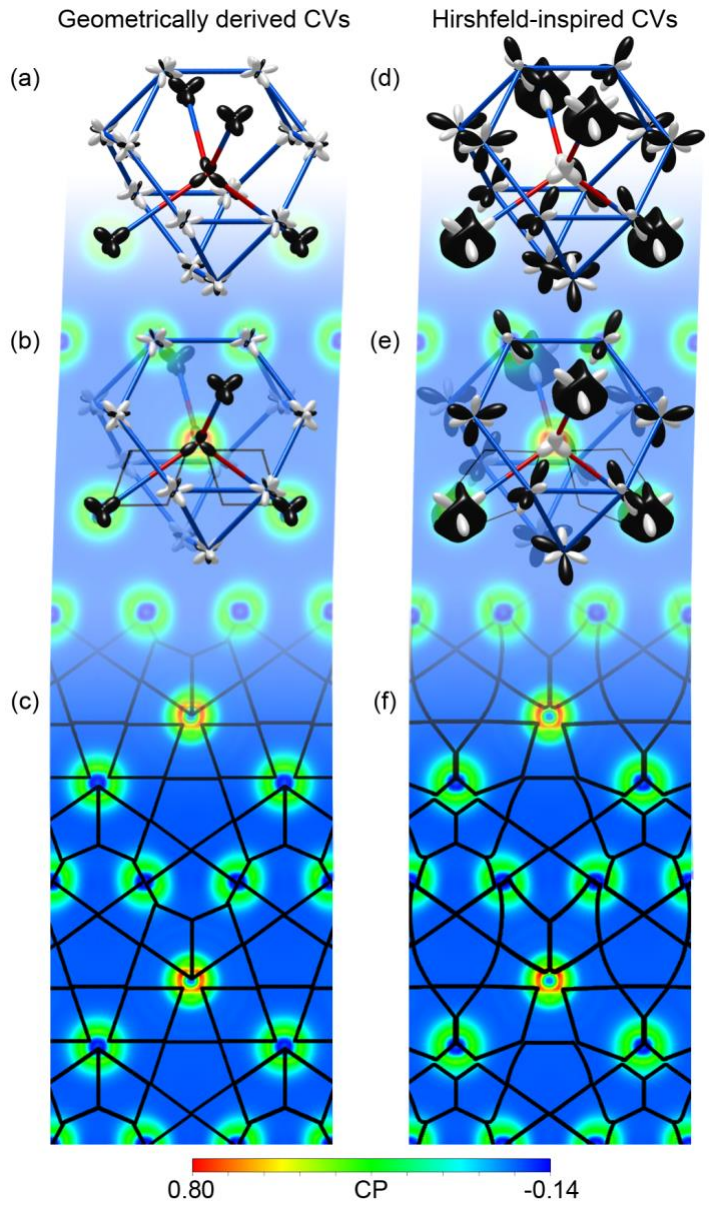

Figure 2.6. Effect of the use of Hirshfeld-inspired contact volumes (CVs) on the integrated DFT-CP results for $CaAu_5$ ($AuBe_5$ type). (a) Atomic DFT-CP anisotropy surfaces calculated for $CaAu_5$ using the original geometrical definition of CVs. (b) The DFT-CP anisotropy surfaces drawn in the context of a cross section of the DFT-CP map with two Ca-Au CVs in the original scheme indicated. (c) The same cross section of the CP map as in (b) with additional CV borders drawn. (d)-(f) The corresponding plots obtained using the Hirshfeld-inspired CV scheme. Note that the CV borders are determined only to the resolution of voxel grid used in the CP calculation. The smooth curves drawn should thus be considered as approximate. See the caption to Figure 2.4 for an explanation of plotting conventions for the DFT-CP anisotropies.

As we mentioned earlier, the positive pressures calculated for the Ca atom with the revised CP scheme (Figure 2.5d) suggest that the $AuBe_5$ type would be stabilized by the replacement of relatively small atoms on this site. Whether a $AuBe_5$ phase forms, however, is not just a factor of the favorability of that single phase, but will depend also on the free energy of the $AuBe_5$-type compound relative to those with alternative structures (or multi-phase mixtures of compounds with an average A:B ratio of 1:5). For AB_5 intermetallics formed between an electropositive metal such as an alkaline earth or lanthanide (for the A sites) and a late transition metal (for the B sites), the $AuBe_5$ type has a fierce competitor: the $CaCu_5$ type (Figure 2.1c). What does the improved DFT-CP approach predict about the relative virtues of these two structure types?

In Figure 2.7, we present a comparison of the CP schemes calculated for the $CaCu_5$- and $AuBe_5$-type structures for two different compounds: $CaCu_5$ and $CaAu_5$, which are experimentally known to prefer the former and latter structure type, respectively (green boxes).[74,75] The plots shown focus on the coordination environment of the Ca atoms (A site) as the relative size of the atom here has been perceived as a key factor in determining which structure type is adopted. In the $CaCu_5$-type structures, this Ca environment consists of an 18-coordinate hexagonal polyhedron built from the layering of honeycomb and kagome sheets of Cu/Au atoms. For the $AuBe_5$-type structures, the Ca coordination environment is the same Friauf polyhedron of Cu/Au atoms that we saw earlier in Figures 2.5 and 2.6.

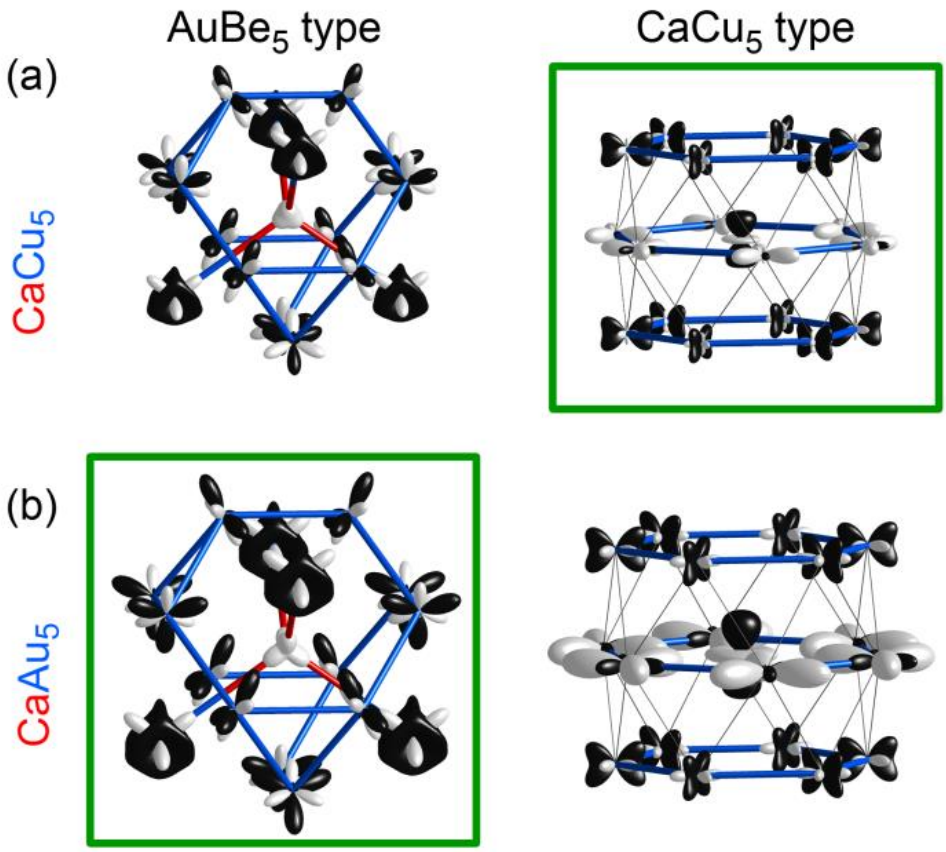

Figure 2.7. DFT-CP analysis of the AB_5 structure types $CaCu_5$ and $AuBe_5$. (a) $CaCu_5$ in the $AuBe_5$ and $CaCu_5$ types. (b) $CaAu_5$ in the same two structure types. Plotting conventions are given in the caption to Figure 4.

A comparison of the results for $CaCu_5$ and $CaAu_5$ reveals that, while differences occur in the sizes of the various lobes, the qualitative features of the CP plots are very similar between the phases of the same structure types. For both $CaCu_5$-type compounds, the Ca atom's CP surface has the shape of a d_{z2} orbital, with negative lobes pointing up and down, and a torus of positive pressure running around the middle. This shape can be interpreted as the Ca atom desiring shorter contacts to the Cu/Au atoms in the layers above and below it, but longer contacts to those in the same plane. Overall, the pressures on the Ca sites are negative (–389 GPa on $CaCu_5$ and –21 in $CaAu_5$), indicating that the combined effect of the 12 overly long contacts to the Cu/Au atoms above and below, outweighs the 6 overly short contacts in the plane.

The net negative CP for the Ca could be relieved by the placement of a larger atom on this site, leading to the prediction that the stability of the phase is enhanced for larger A atoms.

In both of the $AuBe_5$-type phases, on the other hand, the Ca sites are subject to positive pressures, indicative of a desire for the expansion of the lattice. This driving force of enlarging the unit cell is resisted largely by the presence of negative pressure lobes between the Cu/Au atoms of the truncated tetrahedron and the Cu/Au atoms on the diamondoid network, which like the Ca atoms lie in Friauf polyhedra. Due to the symmetry of the structure, the interatomic distances between the atoms in the Friauf polyhedra and their surroundings are the same, regardless of whether the position is occupied by a Ca atom or a Cu/Au one. As such, the structure would be best served by placing an atom on the Ca site with a size more similar to a Cu/Au atom, i.e. a smaller atom.

From these considerations, we can conclude that the $CaCu_5$ and $AuBe_5$ structure types are indeed tailored for a larger and smaller atom on the A atom positions, respectively. Let's now examine how the CP results for the experimentally observed phases compare with the hypothetical ones. As a first step, we need to calibrate ourselves in terms of the significance of the sizes of the CP features in Figure 2.7a. The CP lobes for the two $CaCu_5$ phases in panel a are drawn to scale, as are the two $CaAu_5$ phases in panel b. Between the panels a and b, it is not practical to show the plots at the same scale: Cu with its highly localized 3d electrons generally shows inherently larger pressures numerically than Au, regardless of the structure. Instead panels a and b are scaled so that the relative features of the $CaCu_5$- and $AuBe_5$-type structures are maximally comparable.

A good place to begin is a comparison of the two $AuBe_5$-type phases. As we noted earlier, the CP features are very similar between $CaCu_5$ and $CaAu_5$ in this structure type. However, a close examination of the Ca CP anisotropy surfaces for the two compounds reveals an important difference: in $CaAu_5$ the

positive pressures around the Ca are largely focused along the diamondoid network. The contacts between the Ca and the truncated tetrahedron are more satisfied, and in fact represent the interactions in the structure that are most optimized. Upon replacing the Au atoms with smaller Cu ones to create a $AuBe_5$-type $CaCu_5$ phase, we obtain a different situation. The smaller size of Cu translates into a larger relative size for the Ca, and now the positive pressures around the Ca are more uniformly distributed.

By contrast, the replacement for Au with the smaller Cu atoms to make the $CaCu_5$-type $CaCu_5$ phase leads to a tighter coordination environment around the Ca. As a result, the size of the Ca CP features decreases in the $CaCu_5$ type during this substitution, relative to those of the $AuBe_5$-type phase of the same composition.

These observations are in-line with the trend that moving from $CaAu_5$ to $CaCu_5$ increases the favorability of the $CaCu_5$ type relative to the $AuBe_5$ type. What is more difficult to determine is where the crossing point between the two structure types should occur. This difficulty, in fact, reflects one of the limitations of the use of the DFT-CP method in comparing very different crystal structures. Chemical pressures represent derivatives of the total energy with respect to structural perturbations, and not the magnitudes of the total energy itself. For structures that are closely related, such as a superstructure and the basic structure that it is derived from, the CPs are charting similar energy vs. distance curves for interatomic interactions. As such, minimizing the CPs can be seen as a qualitative surrogate for the minimization of the total energy. For more distantly related structures, such as the $CaCu_5$ and $AuBe_5$ types, the energy vs. distance relationships may be expected to be quite different. We should then seek complementary methods, such as the crystal orbital Hamilton population,[76] to measure the magnitudes of the bond strengths to go along with the derivatives provided by the DFT-CP analysis.

2.8. Conclusions

The concept of chemical pressure offers a means to track the effects of atomic size on the electronic structure. In this Article, we have described advances in the generation of chemical pressure maps for solid state structures using the output of DFT calculations and the interpretation of these maps in terms of interatomic interactions. For the calculation of CP maps, we introduced a correction for the incompressibility of atomic cores in which voxel positions between structures of different sizes are interpolated to the same position relative to the atom with which they are associated. The result is the large reduction of the isotropic core pressures (by factors of up to 15) that have proven so challenging to analyze in previous applications of the DFT-CP approach.

We also introduced an improved scheme for assigning voxels to interatomic contacts for the integration of interatomic pressures: the use of Hirshfeld-inspired contact volumes. In this approach, the relative sizes of the free atom electron densities centered at the atomic positions within a crystal structure are used to evaluate their relative degrees of influence on the pressure at a given voxel. The voxel is then assigned to the interaction between the pair of atoms whose influence is greatest on it. Through the use of the free atom electron density profiles, the differing size of the atoms becomes naturally incorporated into the construction of contact volumes, unlike our earlier geometrical procedure. This formalism is also easily generalized: the radial electron density of the free atom could easily be replaced in the input to the CP programs with other relevant profile functions, such as the local energy component of the atomic pseudopotentials.

The utility of the improved DFT-CP approach was illustrated using several structures whose stability ranges have been associated with atomic size effects: the $MgCu_2$ (cubic Laves phase), $AuBe_5$, and $CaCu_5$ structure types. For the $MgCu_2$-type $CaPd_2$, the CP scheme obtained exhibited parallel features with the

sphere-packing view of the Laves phases, and thus affirms the efforts of several researchers to apply and adapt radius ratio type analyses to this large family of compounds.[2,77-79] In the case of competition between the $AuBe_5$ and $CaCu_5$ types for AB_5 structures, our analyses confirmed the role of atomic size in stabilizing one phase over the other. A moderately sized A atom is predicted to experience positive pressures in the $AuBe_5$ type, and negative pressures in the $CaCu_5$ type. Relatively large A atoms are then expected to prefer the $CaCu_5$-type, while smaller A atoms would prefer the $AuBe_5$ type.

We have already found that these advances in the DFT-CP method have made its use much more straightforward for a wide variety of intermetallic systems, and are looking forward to exploring its capabilities through further applications. Motivated by the insights the method has provided regarding the factors influencing the stabilities of the Laves phases and the AB_5 structure types, we are particularly excited to see what it might reveal concerning the complex intergrowth structures of the $AuBe_5$ and $MgCu_2$ structure types in lanthanide-copper systems, some with thousands of atoms per unit cell.[45-48]

2.9. Acknowledgements

We gratefully acknowledge the financial support of the National Science Foundation through grant DMR-1207409. This research involved calculations using computer resources supported by National Science Foundation Grant CHE-0840494.

2.10. References

(1) Bondi, A. *J. Phys. Chem.* **1964**, *68*, 441-451.

(2) Simon, A. *Angew. Chem. Int. Ed.* **1983**, *22*, 95-113.

(3) van der Waals, J. D. *Nobel Lectures, Physics 1901-1921*; Elsevier Publishing Company: New York, 1967.

(4) Müller, U. *Inorganic structural chemistry*; 2nd ed.; Wiley: Chichester, England ; Hoboken, NJ, 2007.

(5) Levy, O.; Jahnátek, M.; Chepulskii, R. V.; Hart, G. L. W.; Curtarolo, S. *J. Am. Chem. Soc.* **2010**, *133*, 158-163.

(6) Wang, H.; Wang, F.; Jones, K.; Miller, G. J. *Inorg. Chem.* **2011**, *50*, 12714-12723.

(7) Wendorff, M.; Röhr, C. *Z. Anorg. Allg. Chem.* **2011**, *637*, 1013-1023.

(8) Deringer, V. L.; Goerens, C.; Esters, M.; Dronskowski, R.; Fokwa, B. P. T. *Inorg. Chem.* **2012**, *51*, 5677-5685.

(9) Lin, Q.; Smetana, V.; Miller, G. J.; Corbett, J. D. *Inorg. Chem.* **2012**, *51*, 8882-8889.

(10) Osters, O.; Nilges, T.; Schöneich, M.; Schmidt, P.; Rothballer, J.; Pielnhofer, F.; Weihrich, R. *Inorg. Chem.* **2012**, *51*, 8119-8127.

(11) Samal, S. L.; Lin, Q.; Corbett, J. D. *Inorg. Chem.* **2012**, *51*, 9395-9402.

(12) Smetana, V.; Miller, G. J.; Corbett, J. D. *Inorg. Chem.* **2012**, *51*, 7711-7721.

(13) Crivello, J.-C.; Breidi, A.; Joubert, J.-M. *Inorg. Chem.* **2013**, *52*, 3674-3686.

(14) Khatun, M.; Stoyko, S. S.; Mar, A. *Inorg. Chem.* **2013**, *52*, 3148-3158.

(15) Samal, S. L.; Gulo, F.; Corbett, J. D. *Inorg. Chem.* **2013**, *52*, 2697-2704.

(16) Pöttgen, R. *Z. Anorg. Allg. Chem.* **2014**.

(17) Emami, H.; Souques, R.; Crivello, J.-C.; Cuevas, F. *J. Solid State Chem.* **2013**, *198*, 475-484.

(18) Shoko, E.; Kearley, G. J.; Peterson, V. K.; Mutka, H.; Koza, M. M.; Yamaura, J.-i.; Hiroi, Z.; Thorogood, G. J. *arXiv ePrints* **2013**.

(19) Yzambart, G.; Bellec, N.; Nasser, G.; Jeannin, O.; Roisnel, T.; Fourmigué, M.; Auban-Senzier, P.; Íñiguez, J.; Canadell, E.; Lorcy, D. *J. Am. Chem. Soc.* **2012**, *134*, 17138-17148.

(20) Sung, N. H.; Roh, C. J.; Kang, B. Y.; Cho, B. K. *J. Appl. Phys.* **2012**, *111*, 07-117.

(21) Huang, W.-Y.; Yoshimura, F.; Ueda, K.; Shimomura, Y.; Sheu, H.-S.; Chan, T.-S.; Chiang, C.-Y.; Zhou, W.; Liu, R.-S. *Chem. Mater.* **2014**, Article ASAP.

(22) Lue, C. S.; Wong, S. F.; Huang, J. Y.; Hsieh, H. L.; Liao, H. Y.; Ramachandran, B.; Kuo, Y. K. *J. Appl. Phys.* **2013**, *113*, 013710.

(23) Nam, G.; Jeon, J.; Kim, Y.; Kang, S. K.; Ahn, K.; You, T.-S. *J. Solid State Chem.* **2013**, *205*, 10-20.

(24) Wang, P. L.; Kolodiazhnyi, T.; Yao, J.; Mozharivskyj, Y. *J. Am. Chem. Soc.* **2012**, *134*, 1426-1429.

(25) Zhao, H. J.; Ren, W.; Chen, X. M.; Bellaiche, L. *J. Phys.: Condens. Matter* **2013**, *25*, 385604.

(26) Ishida, S.; Nakajima, M.; Liang, T.; Kihou, K.; Lee, C.-H.; Iyo, A.; Eisaki, H.; Kakeshita, T.; Tomioka, Y.; Ito, T.; Uchida, S.-i. *J. Am. Chem. Soc.* **2013**, *135*, 3158-3163.

(27) Lehr, G. J.; Morelli, D. T.; Jin, H.; Heremans, J. P. *J. Appl. Phys.* **2013**, *114*, 223712.

(28) Demirel, S.; Avci, S.; Altin, E.; Altin, S.; Yakinci, M. E. *Ceram. Int.* **2014**, *40*, 5217-5222.

(29) Fredrickson, D. C. *J. Am. Chem. Soc.* **2011**, *133*, 10070-10073.

(30) Fredrickson, D. C. *J. Am. Chem. Soc.* **2012**, *134*, 5991-5999.

(31) Stacey, T. E.; Fredrickson, D. C. *Dalton Trans.* **2012**, *41*, 7801-7813.

(32) Engelkemier, J.; Berns, V. M.; Fredrickson, D. C. *J. Chem. Theory Comput.* **2013**, *9*, 3170-3180.

(33) Nielsen, O. H.; Martin, R. M. *Phys. Rev. B* **1985**, *32*, 3780-3791.

(34) Godfrey, M. J. *Phys. Rev. B* **1988**, *37*, 10176-10183.

(35) Ziesche, P.; Gräfenstein, J.; Nielsen, O. H. *Phys. Rev. B* **1988**, *37*, 8167-8178.

(36) Filippetti, A.; Fiorentini, V. *Phys. Rev. B* **2000**, *61*, 8433-8442.

(37) Treglia, G. In *Stress and strain in epitaxy; theoretical concepts, measurements, and applications*; Elsevier Science B.V.: 2001, p 119-150.

(38) Rogers, C. L.; Rappe, A. M. *Phys. Rev. B* **2002**, *65*, 224117/224111-224117/224118.

(39) Hadler, A. B.; Harris, N. A.; Fredrickson, D. C. *J. Am. Chem. Soc.* **2013**, *135*, 17369-17378.

(40) Berns, V. M.; Fredrickson, D. C. *Inorg. Chem.* **2013**.

(41) Fulfer, B. W.; McAlpin, J. D.; Engelkemier, J.; McCandless, G. T.; Prestigiacomo, J.; Stadler, S.; Fredrickson, D. C.; Chan, J. Y. *Chem. Mater.* **2014**, *26*, 1170-1179.

(42) Hirshfeld, F. L. *Theoret. Chim. Acta* **1977**, *44*, 129-138.

(43) Buschow, K. H. J.; Van Der Goot, A. S.; Birkhan, J. *J. Less Common Met.* **1969**, *19*, 433-436.

(44) Kleber, W. *Krist. Technik* **1967**, *2*, 13-14.

(45) Cerný, R.; François, M.; Yvon, K.; Jaccard, D.; Walker, E.; Petrícek, V.; Císarová, I.; Nissen, H. U.; Wessicken, R. *J. Phys.: Condens. Matter* **1996**, *8*, 4485.

(46) Černý, R.; Guénée, L.; Wessicken, R. *J. Solid State Chem.* **2003**, *174*, 125-131.

(47) Giovannini, M.; Pasero, R.; De Negri, S.; Saccone, A. *Intermetallics* **2008**, *16*, 399-405.

(48) Gottlieb-Schönmeyer, S.; Brühne, S.; Ritter, F.; Assmus, W.; Balanetskyy, S.; Feuerbacher, M.; Weber, T.; Steurer, W. *Intermetallics* **2009**, *17*, 6-10.

(49) Gonze, X.; Rignanese, G.-m.; Verstraete, M.; Beuken, J.-m.; Pouillon, Y.; Caracas, R.; Raty, J.-y.; Olevano, V.; Bruneval, F.; Reining, L.; Godby, R.; Onida, G.; Hamann, D. R.; Allan, D. C. *Z. Kristallogr.* **2005**, *220*, 558-562.

(50) Gonze, X.; Amadon, B.; Anglade, P.-M.; Beuken, J.-M.; Bottin, F.; Boulanger, P.; Bruneval, F.; Caliste, D.; Caracas, R.; Côté, M.; Deutsch, T.; Genovese, L.; Ghosez, P.; Giantomassi, M.; Goedecker, S.; Hamann, D. R.; Hermet, P.; Jollet, F.; Jomard, G.; Leroux, S.; Mancini, M.; Mazevet, S.; Oliveira, M. J. T.; Onida, G.; Pouillon, Y.; Rangel, T.; Rignanese, G.-M.; Sangalli, D.; Shaltaf, R.; Torrent, M.; Verstraete, M. J.; Zerah, G.; Zwanziger, J. W. *Comput. Phys. Commun.* **2009**, *180*, 2582-2615.

(51) Goedecker, S.; Teter, M.; Hutter, J. *Phys. Rev. B* **1996**, *54*, 1703-1710.

(52) Hartwigsen, C.; Goedecker, S.; Hutter, J. *Phys. Rev. B* **1998**, *58*, 3641-3662.

(53) Momma, K.; Izumi, F. *J. Appl. Crystallogr.* **2011**, *44*, 1272-1276.

(54) Oliveira, M. J. T.; Nogueira, F. *Comput. Phys. Commun.* **2008**, *178*, 524-534.

(55) Okabe, A.; Sugihara, K.; Chiu, S. N. *Spatial tessellations : concepts and applications of Voronoi diagrams*; 2nd ed.; Wiley: Chichester ; New York, 2000.

(56) Bader, R. F. W. *Atoms in molecules: a quantum theory*; Oxford University Press: Oxford, England, 1994.

(57) Wood, E. A.; Compton, V. B. *Acta Crystallogr.* **1958**, *11*, 429-433.

(58) Palenzona, A.; Manfrinetti, P. *J. Less Common Met.* **1982**, *85*, 307-312.

(59) Greenwood, N.; Earnshaw, A. In *Chemistry of the Elements*; 2 ed.; Butterworth-Heinemann: Oxford, UK, 1997.

(60) Bergerhoff, G.; Brown, I. D. In *Crystallographic Databases*; Allen, F. H., Bergerhoff, Sievers, R., Eds.; International Union of Crystallography: Chester, 1987.

(61) Belsky, A.; Hellenbrandt, M.; Karen, V. L.; Luksch, P. *Acta Crystallogr. B* **2002**, *58*, 364-369.

(62) Samson, S. *Nature* **1962**, *195*, 259-262.

(63) Samson, S. *Acta Crystallogr.* **1965**, *220*, 401-413.

(64) Samson, S. *Acta Crystallogr.* **1967**, *23*, 586-600.

(65) Andersson, S. *Acta Crystallogr. B* **1980**, *36*, 2513-2516.

(66) Cenzual, K.; Parthé, E.; Waterstrat, R. M. *Acta Crystallogr. C* **1986**, *42*, 261-266.

(67) Yang, Q.-B.; Andersson, S.; Stenberg, L. *Acta Crystallogr. B* **1987**, *43*, 14-16.

(68) Fredrickson, D. C.; Lee, S.; Hoffmann, R. *Angew. Chem., Int. Ed.* **2007**, *46*, 1958-1976.

(69) Berns, V. M.; Stacey, T. E.; Sapiro, M.; Fredrickson, D. C. *Eur. J. Inorg. Chem.* **2011**, *2011*, 3936-3949.

(70) Stacey, T. E.; Fredrickson, D. C. *Inorg. Chem.* **2013**.

(71) Henkelman, G. A., A.; Jónsson, H. *Comput. Mater. Sci.* **2006**, *36*, 254-360.

(72) Sanville, E.; Kenny, S. D.; Smith, R.; Henkelman, G. *J. Comput. Chem.* **2007**, *28*, 899-908.

(73) Tang, W.; Sanville, E.; Henkelman, G. *J. Phys. Condens. Matter* **2009**, *21*, 084204/084201-084204/084207.

(74) Raub, C. J.; Hamilton, D. C. *J. Less-Common Metals* **1964**, *6*, 486-488.

(75) Haucke, W. *Z. Anorg. Allg. Chem.* **1940**, *244*, 17-22.

(76) Dronskowski, R.; Bloechl, P. E. *J. Phys. Chem.* **1993**, *97*, 8617-8624.

(77) Dwight, A. E. *Trans. Am. Soc. Met.* **1961**, *53*, 479-500.

(78) Joseph, R. R.; Gschneidner, K. A., Jr. *Scr. Met.* **1968**, *2*, 631-634.

(79) Pearson, W. B. *Acta Crystallogr., Sect. B* **1968**, *24*, 7-9.

Chapter 3

Isolobal Analogies in Intermetallics: The Reversed Approximation MO Approach and Applications to $CrGa_4$ and Ir_3Ge_7-type Phases

This chapter has been published: Yannello, V.J.; Kilduff, B.J.; Fredrickson, D.C. *Inorg. Chem.* **2014**, 53, 2730-2741. The specific analyses performed in this chapter were the work of Yannello, but all authors contributed to the general theoretical development.

3.1. Abstract

Intermetallic phases offer a wealth of unique and unexplained structural features, which pose exciting challenges for the development of new bonding concepts. In this Article, we present a straightforward approach to rapidly building bonding descriptions of such compounds: the reversed approximation Molecular Orbital (raMO) method. In this approach, we reverse the usual technique of using linear combinations of simple functions to approximate true wavefunctions, and employ the fully occupied crystal orbitals of a compound as a basis set for the determination of the eigenfunctions of a simple, chemically transparent model Hamiltonian. The solutions fall into two sets: (1) a series of functions representing the best-possible approximations to the model system's eigenstates constructible from the occupied crystal orbitals, and (2) a second series of functions that are orthogonal to the bonding picture represented by the model Hamiltonian. The electronic structure of a compound is thus quickly resolved into a series of orthogonal bonding subsystems. We first demonstrate the raMO analysis on a familiar

molecule, 1,3-butadiene, and then move to illustrating its use in discovering new bonding phenomena through applications to three intermetallic phases: the $PtHg_4$-type $CrGa_4$, and the Ir_3Ge_7-type compounds Os_3Sn_7 and Ir_3Sn_7. For $CrGa_4$, a density of states (DOS) minimum coinciding with its Fermi energy is traced to 18-electron configurations on the Cr atoms. For the Os_3Sn_7 and Ir_3Sn_7, 18-electron configurations also underlie DOS pseudogaps. This time, however, the 18-electron counts involve multicenter interactions isolobal with classical Ir-Ir or Os-Os covalent bonds, as well as Sn-Sn single bonds serving as electron reservoirs. Our results are based on DFT-calibrated Hückel calculations, but in principle the raMO analysis can be implemented in any method employing one-electron wavefunctions.

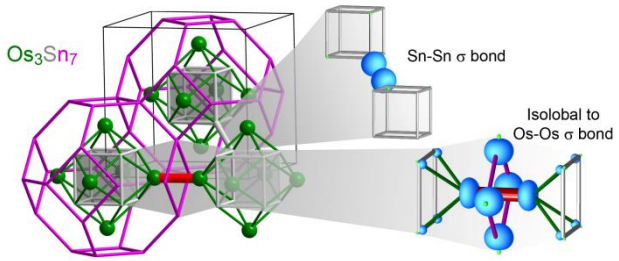

Figure 3.0. A straightforward approach is presented to building bonding descriptions of intermetallics: the reversed approximation Molecular Orbital (raMO) method. Here, we reverse the usual basis set approximation of computations to employ a compound's occupied crystal orbitals as a basis set for determining the eigenfunctions of a simple, chemically transparent model Hamiltonian. We demonstrate the raMO analysis on a familiar molecule, 1,3-butadiene, and then illustrate its use in discovering new bonding phenomena in intermetallic phases.

3.2. Introduction

From the dense atomic packing and large coordination numbers present in intermetallic phases, one might expect that their chemical bonding may be more akin with that of simple metals and alloys than that of molecular systems. And yet, there are alluring hints that the same language of orbital interactions that

has been transformative for molecular chemistry may be used (though in a hitherto unknown dialect) in these compounds. Most important of these clues is perhaps the correlation of phase stability with the presence of a band gap or pseudogap near the Fermi energy (E_F) separating filled and empty electronic levels.[1-23] Much as the size of a HOMO-LUMO gap in a molecule is an indicator of its stability and reactivity, the width and depth of an intermetallic's gap at the E_F largely governs its formation and potential physical properties, such as electrical conductivity, magnetic phenomena, and thermoelectric effects.[24] The connection with molecular systems is strengthened by the realization that these electronic features are reproducible with simple orbital-based models, such as the simple and extended Hückel methods.[25-26] However, distilling the results of these calculations into bonding schemes with utility for materials design remains a challenge.

The greatest progress in explaining the presence of pseudogaps in terms of chemical bonding has been made in certain limiting cases of intermetallics. The Zintl phases, such as NaTl, represent the extremes of bond polarity in compounds formed between metallic elements.[27-33] For these compounds, closed shell electron configurations are obtained on the atoms via formal electron transfer from the electropositive element to the electronegative one, and the covalent sharing of electrons. Electron counts corresponding to the filling of these closed-shells are often correlated with pseudogaps at the Fermi energy (E_F). At another extreme are phases well-described by the nearly-free electron model, where delocalization of the electrons is so complete that they are only weakly perturbed by the ion cores they surround. For these compounds, pseudogaps can be traced to the intersection of the Fermi surface with the Brillouin zone boundary.[1-3]

The predominance of pseudogaps is no less pronounced for other intermetallics, but rationales for explaining and predicting their positions in the electronic density of states (DOS) distributions are still needed. For example, gap/pseudogap formation in transition metal (T)-main group (E) phases is commonly attributed to interactions between the T d and the E p or sp orbitals,[6-10] but still unknown is how these interactions conspire with the crystal structures to place gaps at specific electron counts. Recently, there have been hints of a more detailed bonding scheme from theoretical work on the half-Heusler phases and other derivatives of the fluorite structure type.[14-18] For each of these compounds, pseudogaps at the E_F can be connected to the filling of molecular orbital (MO) diagrams centered on the T atoms that are nearly isolobal to those of molecular 18-electron complexes.

This success suggested to us that the isolobal analogy might elucidate the preferred electron counts of other intermetallic structures, and offer general electron counting rules for this family of compounds. In this Article, we present a theoretical method examining the electronic structures of intermetallics in terms of such analogies to simple MO schemes: the *reversed approximation Molecular Orbital* (raMO) analysis. Our approach here is motivated by ways in which vast improvements in computational power and methodology have changed the nature of the approximations needed for chemical theory. The original approximations employed in MO calculations, such as the representation of the full wavefunction with a linear combination of atomic orbitals (LCAO) basis set, served to simplify the process of solving the electronic structure of a molecule. Now that computational power is no longer a limiting factor in many cases, the challenge has shifted toward interpreting the wealth of information provided by a calculation in terms of a chemically meaningful picture. In other words, *interpretative* rather than *numerical* approximations are becoming increasingly needed. This issue is particularly pressing for intermetallics, where few bonding models are available to serve as a cipher for the decoding of computational output.

In the raMO approach, we reverse the usual basis set approximation of MO calculations to fill this need: we use the fully occupied wavefunctions of a system as an approximate basis set for the solution of a simple chemical problem, such as the interactions between ligand σ-orbitals and a transition metal atom. Solving the Schrödinger equation for this model system in this basis then results in two sets of functions: (1) those with non-zero eigenvalues that provide the approximation to the true eigenstates of the model system possible from linear-combinations of the full compound's occupied orbitals, and (2) those with eigenvalues of zero, which are orthogonal to the bonding picture represented by the model system. In this way the molecular or crystal orbitals of a compound can be transformed into orthogonal bonding systems.

Formally, the raMO analysis is a procedure for the creation of localized molecular orbitals[34] or Wannier functions.[35-39] Its distinctness among other types of Wannier analyses lies in its goal of forging isolobal analogies.[40] Rather than seeking out linear combinations of occupied wavefunctions with specific spatial properties (e.g. maximal localization), the raMO analysis maps these wavefunctions onto simple, familiar molecular orbital diagrams.[41] In its apportioning of electrons to recognizable bonding systems, the method is more closely aligned with the powerful Natural Bond Orbital (NBO) analysis,[42] but is specifically designed to handle the delocalized character of metals.[43]

Over a series of examples in this Article (Figure 3.1), we will see that the raMO approach allows for the rapid deconstructions of the electronic structures of intermetallics into chemically familiar bonding schemes. In this way, the method offers a means of addressing the ever-widening gap between the discovery of new structural phenomena in inorganic materials, and their explanation in terms of experimentally-useful bonding concepts.

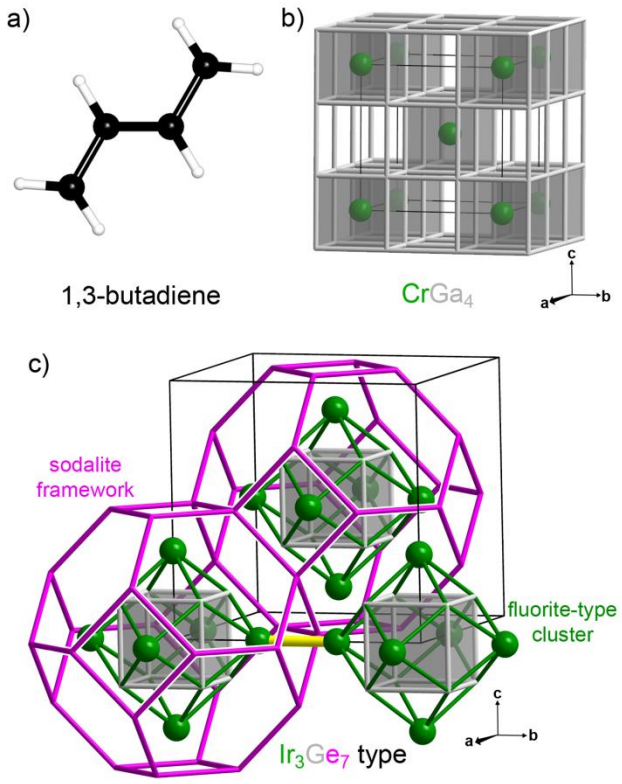

Figure 3.1. Compounds whose bonding will be investigated using the reverse approximation Molecular Orbital (raMO) method in this Article. (a) 1,3-butadiene. (b) The $PtHg_4$-type phase $CrGa_4$. (c) The Ir_3Ge_7 type.

3.3. Technical Procedures

To provide a basis for the parameterization of simple Hückel models for the compounds discussed in this work, the DFT band energies and electronic DOS distributions were calculated for the crystal structures of benzene (as a representative of conjugated hydrocarbons, including 1,3-butadiene),[44] $CrGa_4$,[45] Os_3Sn_7,[46] and Ir_3Sn_7[47] using the Vienna Ab Initio Simulation Package (VASP).[48-49] All calculations were performed in the high precision mode, using the LDA ultrasoft pseudopotentials[50] provided with the package. Further details such as the energy-cutoffs and k-point grids used are given in the Supporting Information.

The output of each VASP calculation was then used as a reference for the refinement of Hückel parameters using the program eHtuner,[51] with the actual Hückel calculations being carried out with YAeHMOP.[52] The optimized Hückel parameters are tabulated in the Supporting Information, along with the root-mean-squared deviations between the band energies of the Hückel models and those calculated with VASP (typically < 0.25 eV).

Once the Hückel parameterization for each compound was complete, a Hückel calculation was carried out using a 2×2×2 supercell, so that the majority of the special k-points of the primitive cell became mapped to the Γ-point. The Hamiltonian matrix for the Γ point of this supercell was then printed, and imported into MATLAB for processing as described below.

3.4. The Reversed Approximation MO Approach

3.4.1. The raMO Procedure

As with most other modern theoretical methods for analyzing bonding, our goal is to interpret the solutions of the Schrödinger equation,

$$\hat{H}\left|\psi_j\right\rangle = E_j\left|\psi_j\right\rangle \qquad (3.1),$$

in terms of familiar chemical interactions. For intermetallic phases, the wavefunctions that result from, say, a DFT calculation, are numerous and complicated. Often they spread across the whole lattice of the crystal, and are organized in k-space rather than by their properties in physical space. In this section, we will describe the raMO approach for extracting simple MO interaction schemes from these complex electronic structures. To demonstrate the steps of the procedure, we will make use of a well-understood

molecular system, 1,3-butadiene (Figure 3.1a), considering the question of how independent the π-bonds in its Lewis structure are from each other.

We begin with the assumption that in the full set of interacting orbitals for a system, a subset interacts in a fashion that is analogous to a well-understood molecular system. For this subsystem, we have a simplified Schrödinger equation:

$$\hat{H}^{\circ}\left|\psi_k^{\circ}\right\rangle = E_k^{\circ}\left|\psi_k^{\circ}\right\rangle \qquad (3.2)$$

where $\hat{H}^{\circ}$ is the Hamiltonian operator within this subspace, and its eigenstates are given by $|\psi_k^{\circ}>$. In the case of 1,3-butadiene, we might consider one of the two π-bonds drawn in the standard Lewis structure (Figure 3.2), each of which is individually more simple than the full conjugated π-system: the eigenfunctions resulting from the π-interaction between two C 2p orbitals are just an in-phase π-bonding orbital and an out-of-phase π* orbital (Figure 3.2a).

We now look to the question of how well the $|\psi_k^{\circ}>$ states are represented by linear combinations of the occupied eigenstates of the full system, i.e. to what degree the following equation satisfied:

$$\left|\psi_k^{\circ}\right\rangle \approx \sum_{\substack{j=occupied\\states}} c_j\left|\psi_j\right\rangle \qquad (3.3)$$

The degree to which such expressions are fulfilled measures the validity of proposed analogies between a model MO diagram and the electronics of the full compound. The form of the expression bears a resemblance to the equation representing the linear combination of atomic orbitals (LCAO) approximation, as both use a limited basis set to reconstruct a target function. In the case of LCAO, one

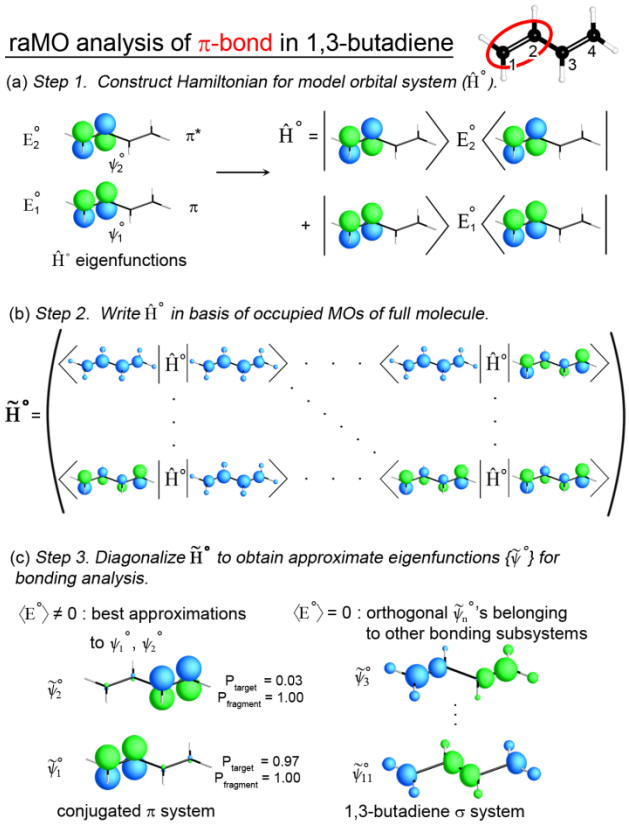

Figure 3.2. The raMO procedure illustrated with the analysis of a π-bond in 1,3-butadiene. (a) Step 1: the eigenfunctions of a simplified orbital system are used to construct a model Hamiltonian operator, Ĥ°. (b) Step 2: This Ĥ° operator is expressed in terms of matrix elements between the occupied MOs of the full molecule, to give the **H̃°** matrix. (c) Step 3: Diagonalization of the **H̃°** matrix yields of orthonormal set of linear combinations of the occupied MOs which divides naturally into two classes. Those with non-zero expectation values, <E°>, of Ĥ° represent the best possible approximations to the original eigenfunctions of the model, while those with <E°>=0 belong to separate bonding subsystems in the compound.

determines the best approximation of the true ground state wavefunction by minimizing the energy with respect to the atomic orbital coefficients.

Here, we perform a similar procedure to obtain the best approximations to the model orbitals from the full wavefunctions. We first write out the model Hamiltonian in terms of its eigenfunctions, recalling that these functions will comprise a complete basis set:[53]

$$\hat{H}^{\circ} = \hat{H}^{\circ} \bullet 1 = \hat{H}^{\circ}(\sum_{k} |\psi_k^{\circ}\rangle\langle\psi_k^{\circ}|) = \sum_{k} |\psi_k^{\circ}\rangle E_k^{\circ}\langle\psi_k^{\circ}| \qquad (3.4)$$

In our example of a 2-center π -bond in 1,3-butadiene, this operator has two terms (Figure 3.2a, right). One term projects the function it acts upon onto a C-C π-bonding orbital with a weight of the energy of this orbital. The other term carries out the analogous projection of the function onto a C-C π* orbital.

Next, we calculate model Hamiltonian matrix elements in the basis of the occupied wavefunctions of the full system:

$$\begin{aligned} \tilde{H}_{ij}^{\circ} &= \langle\psi_i| \sum_{k} |\psi_k^{\circ}\rangle E_k^{\circ}\langle\psi_k^{\circ}| |\psi_j\rangle \\ &= \sum_{k} E_k^{\circ}\langle\psi_i|\psi_k^{\circ}\rangle\langle\psi_k^{\circ}|\psi_j\rangle \end{aligned} \qquad (3.5)$$

Here, the tilde above the matrix element symbol indicates that it is part of an approximate matrix representation of the operator in equation 3.4, built from the incomplete basis set (the occupied wavefunctions). As is illustrated in Figure 3.2b, the construction of this matrix for 1,3-butadiene would involve all of the occupied MOs of both the σ-system and the conjugated π-system. In principle, these MOs could be taken from the results of Hartree-Fock, DFT or other methods employing 1-electron wavefunctions. For simplicity, here we use MOs obtained from a DFT-calibrated simple Hückel calculation.

Once the matrix elements of $\mathbf{\tilde{H}}^{\circ}$ are obtained, the procedure is completed by the diagonalization of the $\mathbf{\tilde{H}}^{\circ}$ matrix to yield eigenvectors and eigenvalues. The eigenvectors form an orthonormal set of functions $\{\tilde{\psi}_k^{\circ}\}$ that are organized by their eigenvalues according to their relationships to a model bonding system. Those with eigenvalues not equal to zero ($\langle\tilde{E}^{\circ}\rangle \neq 0$) represent the optimal fit between the MOs of our simple model system and occupied wavefunctions of the full Hückel calculation. The remaining functions with eigenvalues of zero ($\langle E^{\circ}\rangle = 0$) build up a series of functions that are orthogonal to the

model system. This set consists of linear combinations of the occupied wavefunctions that contribute to other bonding subsystems of the molecule.

The results of this final step for a π-bond in 1,3-butadiene illustrate the information obtainable from this procedure (Figure 3.2c). Two eigenvectors with $\langle E \tilde{}^{\circ} \rangle \neq 0$ are obtained, $\tilde{\psi}_1^{\circ}$ and $\tilde{\psi}_2^{\circ}$. The first represents the best approximation to the π-bonding orbital between carbon atoms 1 and 2 (C1 and C2) possible from the occupied levels, while the second shows the best attempt at reconstructing an π* orbital between those atoms. Not surprisingly, given the strong π bonding present in this molecule, the π-bonding orbital is well-reconstructed in $\tilde{\psi}_1^{\circ}$, while very little of the true π* orbital appears in $\tilde{\psi}_2^{\circ}$.

More insight can be obtained into the bonding in the 1,3-butadiene π-system by looking more closely at the forms of these functions. $\tilde{\psi}_1^{\circ}$ is predominantly based on a π-bond between C1 and C2, but small contributions can also be seen on C3 and C4. These appear as a miniature C3-C4 π* orbital, with bonding overlap occurring between C2 and C3 at the center of the molecule. This function altogether then represents a C1-C2 π-bond that is donating electron density to the π* orbital of the C3-C4 interaction, in a Lewis acid/base fashion. The $\tilde{\psi}_2^{\circ}$ function can be interpreted in a similar fashion, but this time we see that the C1-C2 π* function that we intended to create through the raMO analysis exists only by virtue of its receiving electron density through its bonding overlap with a C3-C4 π-bond.

The large mismatch in relative contributions between the π-bonding and π-antibonding components of these functions indicates that to a large extent the bonding in the π-system can be viewed as a perturbation on separate C1-C2 and C3-C4 π-bonds. The conjugation we associate with this system then appears from this localized view in the partial donation of their electron pairs into the π* orbitals of their neighbor, a view which converges with the donor-acceptor picture for conjugation that emerges from a

NBO analysis.[42] This is, in fact, just another way of viewing the full MOs of the 1,3-butadiene π-system: in adding and subtracting $\tilde{\psi}_1^\circ$ and $\tilde{\psi}_2^\circ$ we can recover the molecule's occupied π MOs.

The remaining eigenvectors of the $\mathbf{H}^{\tilde{}\circ}$ matrix have eigenvalues of zero and form as series of functions that have no overlap with the π and π* orbitals of our model MO diagram. Nine of these functions are obtained (Figure 3.2c, right), which represent the bonding orbitals of the σ-framework of the molecule.

So far, we have only considered the occupied MOs of the 1,3-butadiene. In predicting the reactivity of a molecule, one should also consider the low-lying unoccupied MOs as well. This can be accomplished in the raMO framework by using the unoccupied 1-electron wavefunctions as a basis for the eigenfunctions of the model Hamiltonian operator. The results of this process for a π-bond in 1,3-butadiene is shown in Figure 3.3. In this case, the reverse of the situation in Figure 3.2c is obtained: the π* function on each the terminal pair of C-atoms is destabilized by an antibonding interaction with the π-bonding function on the neighboring pair.

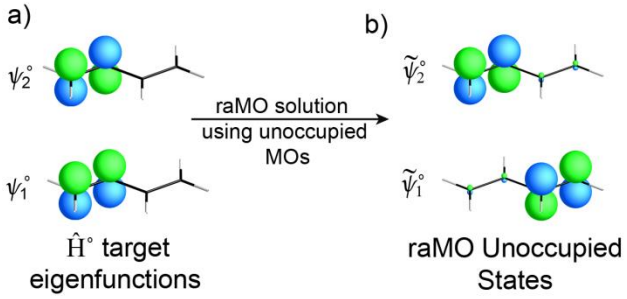

Figure 3.3. raMO reconstruction of the bonding and antibonding functions of a π-bond using the unoccupied MOs of 1,3-butadiene. (a) The target eigenfunctions. (b) The best-approximants to the target eigenfunctions built from the unoccupied MOs.

Using the example of 1,3-butadiene, we have seen the potential for the raMO analysis to quickly dissect the electronic structure of a compound. By starting with a simple test of the degree of π-bonding between two carbon atoms, we immediately obtained the conjugated π-system (in a localized form), and the orthogonal σ-system. While this largely reiterates familiar themes in the bonding of organic molecules, we will see soon how similarly intuitive bonding schemes can be constructed for much more complicated chemical systems, namely intermetallic phases.

3.4.2. Quantitative Analysis of raMO Results

In our raMO analysis of the π-system of 1,3-butadiene, we found that for either of the localized π-bonds in the standard Lewis structure there is some occupation of both the bonding and anti-bonding orbitals. As we move to less familiar systems, it will be helpful to have ways of quantifying the relative occupations of such bonding/antibonding pairs. One tool for doing this is to calculate the projection of the target eigenfunction onto its corresponding raMO approximant: $\langle \tilde{\psi}_n^\circ | \psi_n^\circ \rangle$. In particular, the square of this projection, is simply the probability that an electron in the raMO function would be found in the target eigenstate if it were interrogated with the proper measurement. We term this probability as $P_{target} = \left| \langle \tilde{\psi}_n^\circ | \psi_n^\circ \rangle \right|^2$, which serves as a measure of how well the target eigenstate is represented in the occupied wavefunctions of the system.

The P_{target} values of π-bonding and antibonding target eigenstates are given alongside their raMO approximants in Figure 3.2. The P_{target} value for the π-bonding function is 0.97, which indicates a 97% probability of finding that π-bond occupied. The corresponding probability for the π-antibonding function is only 3%, which agrees well with the 3.65% value obtained from an earlier NBO analysis.[42]

In the periodic structures that we will be discussing in the remainder of the Article, it will become impractical to show the raMO functions in the context of the full crystal structure. Instead, we will focus on local features of interest for our discussion of bonding. For this reason, it is useful to introduce another quantity, $P_{fragment}$, which gives the probability of finding an electron in a raMO function in the fragment of the structure portrayed in the figure. In the case of 1,3-butadiene, the full molecule is shown for all of the raMOs in Figure 3.2. As such, $P_{fragment} = 1$ throughout. For the other structures in this paper, the $P_{fragment}$ values will provide a measure of how much the electron density of a raMO function spills out of the region displayed.

3.5. $CrGa_4$ as an 18 Electron Compound

Having illustrated how the raMO method works using a well-understood molecular system, we are now in a position to see what it can tell us about the more elusive interactions underlying the stability of intermetallic phases. Let's begin with a simple example for which theoretical calculations indicate that electron count plays a central role: the $PtHg_4$-type phase $CrGa_4$ (Figure 3.4). In this compound, the Ga atoms form a primitive cubic array (gray), with the Cr atoms (green) lying at the centers of one quarter of the cubic voids. The $Cr@Ga_8$ cubic polyhedra are arranged so that the full structure can be viewed as a body-centered cubic lattice of these polyhedra linked through vertex-sharing.

This structure's partial-filling of a primitive cubic network of main group atoms by transition metals is mirrored in a number of compounds: the half-Heusler phases and the fluorite-type silicides such as $NiSi_2$. In all of these compounds, a pseudogap appears in the electronic DOS distributions corresponding to 18-electron configurations on the TM atoms.[13-17,54-55] $CrGa_4$ adheres to this special electron count (9×1

+ 3×3 = 18), and its electronic DOS distribution has been calculated to exhibit the expected deep minimum at the Fermi energy (E_F) lying just above a dense series of states based on Cr 3d orbitals.[9] For the other compounds in this family, the favorability of the 18 electron count is traced to the involvement of all of the TM atoms' d, s, and p valence orbitals, as in a molecular transition metal complex. The raMO approach allows us to quickly test this hypothesis for $CrGa_4$.

In this interpretation of the 18-electron count, the occupied orbitals of the system should be expressible as localized functions with a one-to-one correspondence with the TM atoms' d, s, and p orbitals. The corresponding model Hamiltonian operator ($\hat{H}^\circ$) expressing this assumption could then be written using the atomic valence orbitals of a TM atom as $|\psi_k^\circ>$'s (Figure 3.4b). This operator can then

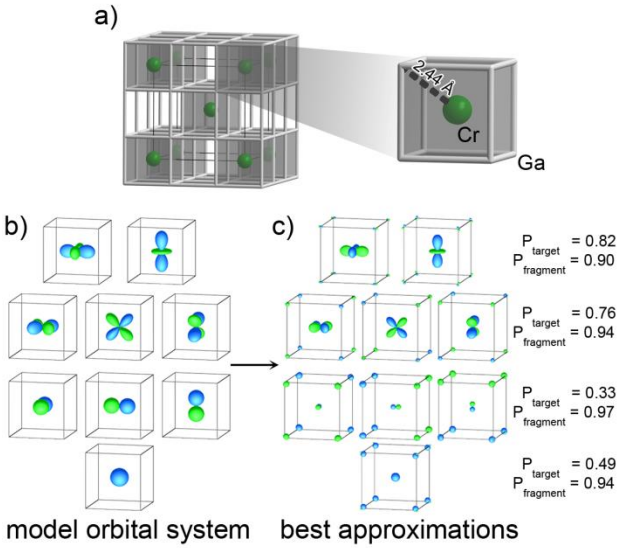

Figure 3.4. raMO analysis reveals $CrGa_4$ to be an 18 electron compound. (a) The crystal structure of $CrGa_4$, with the Cr atoms' cubic coordination by Ga highlighted. Cr: green. Ga: gray. (b) The basis of Cr 4s, 3d and 4p orbitals used as the model MO system for the raMO analysis. (c) The nine reconstructed functions resulting from the raMO analysis, corresponding to Cr-Ga bonding and Cr nonbonding orbitals localized around the original Cr atom. Each function is calculated to have an energy lying below the E_F of the compound. Together they form a complete 18-electron configuration on the Cr atom.

be used, following the procedure outlined in Figure 3.2, to analyze the wavefunctions obtained from a band structure calculation on the $CrGa_4$ crystal structure.

To obtain the wavefunctions for the full structure, we parameterized a simple Hückel model for $CrGa_4$, using our program *eHtuner*,[51] against the band energies and projected DOS curves calculated with GGA-DFT (see the Technical Procedures section for further details). The reasonable correspondence obtained (RMS deviation in the band energies ca. 0.1 eV) allows us to use our Hückel model as a guide to interpreting the DFT results. We then performed a periodic Hückel calculation using a 2×2×2 supercell of the conventional $CrGa_4$ unit cell so that multiple k-points in the Brillouin zone are mapped to the Γ-point.[25-26] The wavefunctions and Hamiltonian matrix for Γ were then outputted, and considered as representative of the interactions of the system.

Upon writing the $\hat{H}^{\circ}$ operator in terms of the basis of occupied wavefunctions (step 2) and diagonalizing the resulting matrix (step 3), nine functions with non-zero eigenvalues are obtained. These are shown in Figure 3.4c, where it can be seen that one function appears for each of the TM s, p and d orbitals. The s- and p-orbital-based functions are augmented by bonding interactions with Ga σ orbitals (appearing in the appropriate symmetry-adapted linear combinations). The t_{2g} 3d orbitals partake in similar Cr-Ga bonding interactions, while the e_g orbitals are essentially nonbonding, with only very minor π-type contributions from the Ga. All of these functions show only small components beyond the first-coordination environment of the central Cr atom ($P_{fragment} \approx 1.0$), indicating that they can be assigned entirely to this Cr site. No interactions between Cr atoms are apparent.

These results support the view that the 18-electron count in the $CrGa_4$ structure is associated with the each of the Cr's valence orbitals being utilized. As this would account for all valence electrons in the phase,

we should be able to build a $\hat{H}^{\circ}$ operator that accounts for full electronic structure of the compound using the s, p and d orbitals of *all* Cr atoms as $|\psi_k^{\circ}>$'s. Carrying out such a raMO analysis leads to no eigenfunctions with eigenvalues of zero, indicating that there are no additional bonding subsystems at work in the compound. From this point of view, we would then expect that the band structure of $CrGa_4$ would be fully interpretable in terms of weakly interacting Cr octadecets.

The features of the electronic density of states (DOS) distribution of $CrGa_4$ can be understood in this way (Figure 3.5). The DOS curve begins at low energies with a somewhat parabolic shape. Such low-energy tails are often interpreted as sp nearly free-electron levels,[56] which is consistent with the large absence of Cr d character (shaded portion of distribution) seen in this region. This sp distribution is interrupted at ca. -8.5 eV by a sharp peak of Cr d-rich states. Above this peak lies the Fermi energy (E_F) in a deep DOS minimum, followed by a dense series of unoccupied levels.

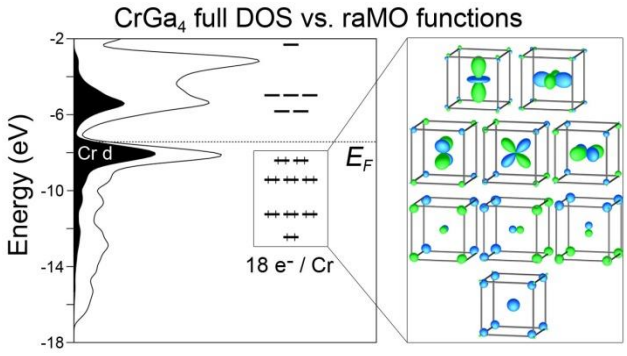

Figure 3.5. Comparison of the GGA-DFT DOS distribution calculated for $CrGa_4$ with energies of the Cr 3d-based functions obtained from a raMO analysis of the occupied bands of a DFT-calibrated Hückel calculation on $CrGa_4$. In the energy level diagram, the levels are drawn above the E_F are derived from a raMO analysis of the unoccupied bands. Contributions to the total DOS from the Cr d are shaded. The DOS curve has been treated with Gaussian broadening to make its general features more apparent.

Alongside the DOS curve, we also plot the energy expectation values calculated for the nine $\tilde{\psi}_n^\circ$'s resulting from the raMO analysis of $CrGa_4$. The four lowest-energy functions correspond to the Cr 4s and 4p orbitals, with significant bonding contributions from sp hybrid orbitals on the surrounding Ga atoms. As these functions are derived primarily from s and p orbitals it is fitting that their energies are aligned with the middle of the low energy DOS features arising from the nearly free electron sp states. The wide energy range of the sp DOS distribution is then viewed as stemming from the broadening of the energies of raMO sp functions upon their inclusion in their context of the full crystal structure.

The remaining five raMO functions are dominated by the original Cr 3d orbitals, which are split in energy according to whether they are Cr-Ga bonding (t_{2g}) or nonbonding (e_g). As is anticipated by their nonbonding character, the e_g functions are coincident in energy with the sharp DOS peak of Cr 3d states. The t_{2g} functions experience stronger interactions with the Ga sp, and as such correspond in energy with the top of a lower energy tail in the Cr 3d DOS contribution which stretches downward into the total DOS curve's sp region.

Filling all of these raMO states brings the HOMO level for this diagram to just under the E_F and DOS minimum of the compound's DOS curve. The pseudogap can thus be seen as consistent with the filling of 18-electron configurations on the Cr atoms. In this way, the raMO method gives an estimate of the lower boundary of the pseudogap region.

So far, however, the raMO approach has not provided any information on where the pseudogap region should end, i.e. where the lowest unoccupied molecular orbital (LUMO) levels for our simple MO model for $CrGa_4$ should lie. To investigate the character of the unfilled levels of the DOS distribution, we can repeat the steps of the raMO analysis (as shown schematically in Figure 3.2), but this time using the

unoccupied crystal orbitals as our basis set. The resulting energy levels appear in Figure 3.4 above the E_F of $CrGa_4$. They coincide closely with the dense block of states in the DOS appearing above the pseudogap. The energy difference between the lowest of these functions (which might be termed the raMO LUMO) and the highest of the original raMO functions (the raMO HOMO) straddles the full compound's DOS pseudogap.

In this section, we have seen how the raMO approach provides a simple means of interpreting the electronic structure of $CrGa_4$. Its DOS pseudogap at the E_F arises from a filling of 18 electron configurations on the Cr atoms. Some of these Cr-based levels experience significant energy broadening through their bonding interactions with the Ga sp. However, in terms of bookkeeping, every electron can be associated with a valence orbital on the Cr.

3.6. Electron Counting in the Ir_3Ge_7-type

Let's now move to more complicated compounds in which a simple assignment of 18 electron configurations is not sufficient for rationalizing the bonding: the Ir_3Ge_7-type phases. This structure is observed for a rather large range of electron counts (17 to 18.67/transition metal atom), which we will sample with Os_3Sn_7 (17.3 electrons/Os) and Ir_3Sn_7 (18.3 electrons/Ir). The higher end of this electron count range is in excess of 18, suggesting the availability of states for accepting electrons beyond transition metal-based bonding and nonbonding orbitals. Meanwhile, the lower range falls short of a complete octadecet for individual transition metal atoms, and one might anticipate covalent sharing of electrons between transition metal atoms as a way of responding to this deficiency. As we will see in this section, both of these pictures are relevant to bonding in the Ir_3Ge_7 type.

We begin with the possibility of Os-Os bonding electron pairs in Os_3Sn_7. Hints of such Os-Os interactions can be seen in the crystal structure of this phase (Figure 3.6a). The structure is based on a body-centered packing of small fragments of the fluorite structure type (as is adopted by the related compounds $CoSi_2$ and $NiSi_2$). Each fragment consists of an empty Sn_8 cube, with an Os atom capping each of its square faces. The fragments are placed in the void spaces of sodalite-type network of Sn atoms (face-sharing truncated octahedra). Through the shared square faces of the Sn sodalite cages (purple), the Os atoms from neighboring fluorite-type clusters meet with a contact distance of 2.97 Å (in our DFT-optimized structure). This distance is long for a conventional Os-Os bond, but is too short to neglect the possibility of interactions between this pair of Os atoms.

The raMO analysis offers an approach to investigate the potential Os-Os bonding at these contacts. Our first step is to consider as a model MO system the 5d, 6s, and 6p orbitals of a single Os atom, and see how well this atomic energy level diagram can be reproduced from the basis of the occupied crystal orbitals of Os_3Sn_7 (Figure 3.6b). Our target eigenfunctions are drawn on the left in the context of the coordination environment of an Os dimer.

Upon performing the raMO analysis, the functions drawn on the right of Figure 3.6b are obtained with non-zero energy eigenvalues. The five 5d orbitals are well-reproduced, suggesting that each Os atom has ten electrons associated with its d orbitals. We will refer to this situation as $5d^{10}$ configuration, while recognizing that traditional electron counting might formally assign some of these electrons to the surrounding ligand atoms. For the 6s and 6p orbitals the pictures are less clear as they are more spread out among the surrounding Sn atoms, as might be expected from the high ionization energy of the Os sp orbitals.

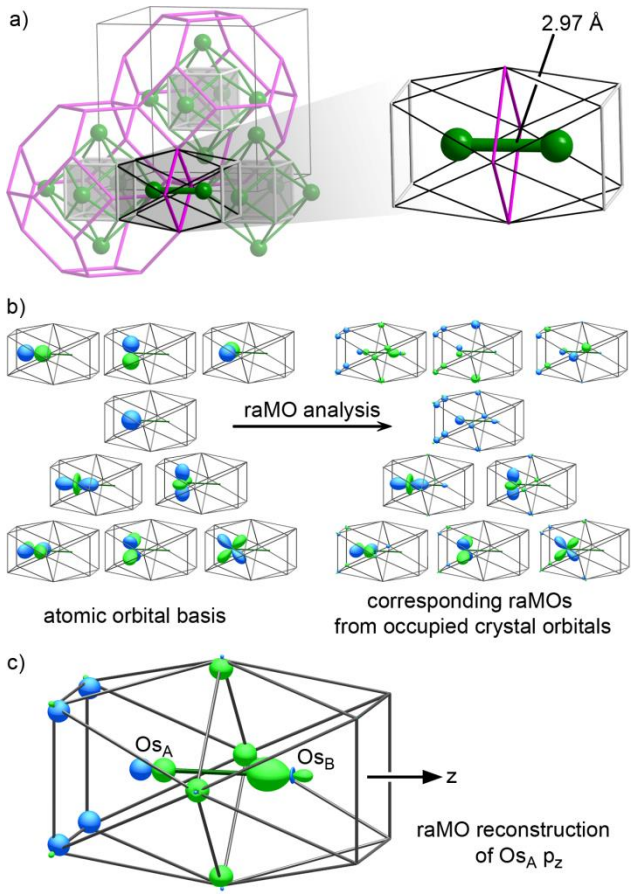

Figure 3.6. raMO analysis of the Ir_3Ge_7-type Os_3Sn_7, using the 5d, 6s, and 6p orbitals of a single Os atom as target eigenstates. (a) The crystal structure of Os_3Sn_7, with one of the Os dimers that link its fluorite-type fragments highlighted. (b) The target eigenstates, and their best approximant raMOs obtained from the occupied crystal orbitals of Os_3Sn_7. (c) Magnified view of the Os-Os σ-bonding function that emerges in the generation of the raMOs.

A close-up of the function resulting from the p-orbital oriented along the Os-Os is particularly informative here (Figure 3.5c). The target Os p orbital (left) appears stabilized by σ-bonding interactions from the surrounding Sn atoms, as well as from the similarly oriented p orbital on the neighboring Os atom. The appearance of an Os-Os bonding interaction in this raMO has profound implications for the electronic structure of the phase. It indicates that the target Os p orbital seldom appears in the

wavefunctions of the system without a bonding contribution from the neighboring Os atom, suggesting that presence of an Os-Os bond.

Based on these results, it would seem that the Os atoms might be better treated as dimers rather than individual atoms. In Figure 3.7, we take this approach, using the MOs for an Os dimer as our target eigenfunctions in the raMO analysis. These eigenfunctions can be naturally grouped according to their symmetry properties into six σ orbitals (Figure 3.7a), eight π orbitals (Figure 3.7b), and four δ orbitals (Figure 3.7c). Within each of these groups, the orbitals are drawn with the bonding combinations at the bottom, non-bonding states near the middle, and anti-bonding orbitals at the top.

On the left sides of the panels of Figure 3.7, we show the raMOs corresponding to each of these functions. For the σ orbitals in Figure 3.7a, most of the target orbitals are well-reproduced, with varying degrees of delocalization over the surrounding Sn atoms. The major exception is the sp-sp σ* orbital (top, left), which shows only vanishing contributions from the Os in its raMO function. The non-occupation of this σ* orbital, while its bonding counterpart is well-reproduced in the raMOs from the occupied orbitals, is strongly suggestive of net Os-Os bonding.

We should note that this is not an Os-Os bond in the classical 2c-2e sense. The bonding orbital involves supporting interactions from the bridging Sn atoms, making this a multicenter interaction. However, this bonding function shares the same nodal properties 2-center Os-Os sigma interaction, and may thus be considered as isolobal to a standard Os-Os bond. The balance of transition metal and main group contributions to these interactions could be expected to change depending on the relative electronegativities of these elements. This factor may explain why earlier analyses using electron localization function (ELF) revealed rather variable results from one Ir_3Ge_7-type compound to another.[8]

In Figure 3.7b, we show the corresponding results for the π-type interactions between the Os atoms. Eight eigenfunctions target functions result from π or π* interactions, oriented either parallel or perpendicular to the plane of the page, between either p or d orbitals (with a small amount of admixture between them). The d-based functions are well-reproduced in the raMOs, as is consistent with a d^{10} configuration on the on the Os atoms.

For the p-orbital-based functions, however, much less Os p character is evident in the raMOs. The p-p π* raMO exhibits very small contributions on the Os_2 pair, which is spread through bonding interactions to the surrounding Sn atoms. The raMO reconstruction of the p-p π bonding target eigenfunction yields larger contributions from the Os_2 pair and its environment, which again are bridged by significant bonding contributions from the bridging Sn atoms. For both, the balance between the Os p and Sn contributions is much more shifted to the Sn, as expected given the lower ionization energies of the Sn s and p orbitals than the Os p orbitals.

How should these results be interpreted? Equal occupation of the p-p π*and p-p π bonding functions would result in a net π-bond order (which here should be interpreted in an isolobal sense rather than in terms of a localized bond between the Os atoms) of zero. However, it is evident from comparing the raMOs that the bonding function is much better represented in the occupied crystal orbitals that its antibonding counterpart. This would suggest a π-bond order somewhere between 0 and 1 for the interactions both in the plane of the page, and perpendicular to the page. As we will see below, the overall electron count for this phase can be well-understood by assigning a bond order of 0.5 for each interaction.

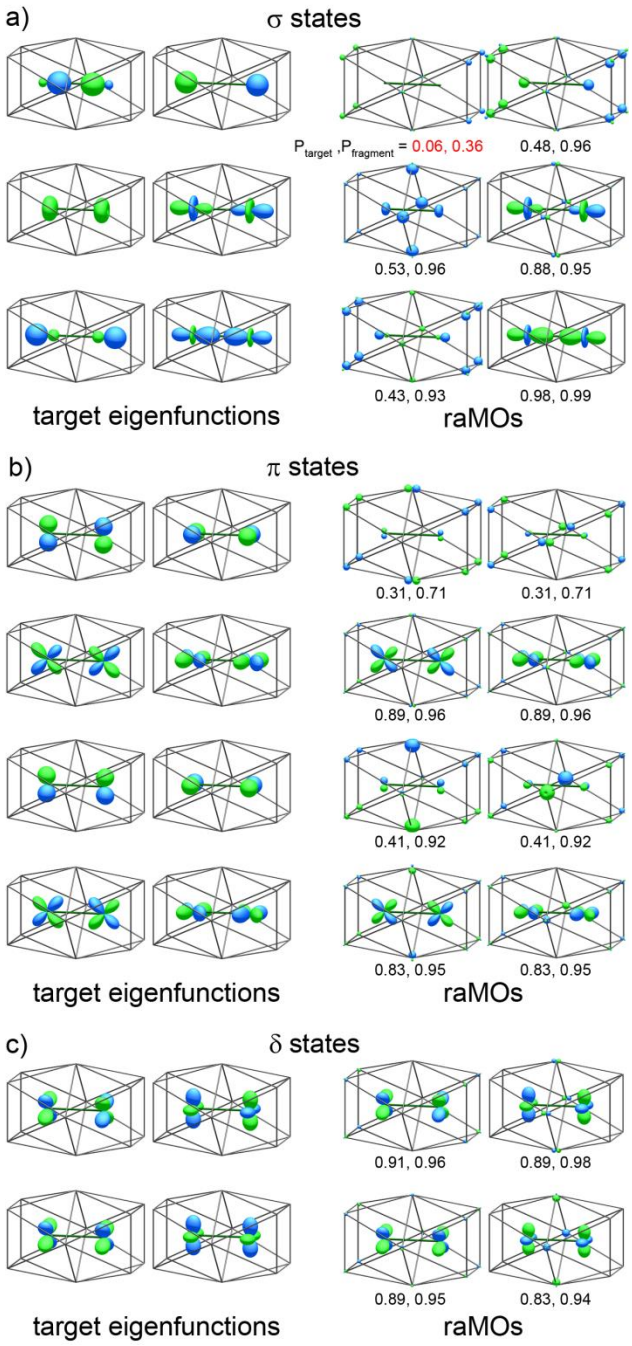

Figure 3.7. raMOs obtained from the occupied crystal orbitals of Os_3Sn_7, using the molecular orbitals of an Os dimer as target eigenstates. (a) raMOs from targets of Os-Os σ-character. (b) Those obtained from targets of π-character. (c) raMOs of δ-character.

The last set of target eignfunctions for the Os_2 dimer are the δ/δ^* orbitals (Figure 3.7c). All four of these functions are well-reproduced in the raMO analysis, as predicted by the d^{10} configuration of the Os atoms.

From this analysis, we are now in a position to assign a formal electron count to the Os centers of Os_3Sn_7. For isolated Os atoms, we would expect 18 electrons/Os to be the optimal count for fully utilizing the bonding potential of each Os atom's s, p, and d valence orbitals. In this case, however, the Os atoms occur in pairs with functions isolobal to a full Os-Os σ bond and two Os-Os ca. half π-bonds. This would suggest that 4 electrons are shared between the Os atoms, and that each Os atoms would only need to bring 16 electrons for a close-shell configuration to be achieved.

If we compare this number to the experimental valence electron count for Os_3Sn_7 of $(3\times8+7\times4)/3 = 17.3$ electrons, it is apparent that there are electrons that are still unaccounted for in our bonding scheme. These electrons can be located by an examination of the remainder raMO functions (with eigenvalues of zero) obtained when the Os_2 dimer MOs are used as target eigenstates. The remainder raMOs (not shown) are focused on the Sn cubes in the fluorite-type fragments, with bonding interactions being apparent at contacts between neighboring cubes along the unit cell diagonal (Figure 3.8a).

To determine the character of these interactions in more detail, we can perform a raMO analysis on the remainder states obtained during our examination of the Os_2 dumbells. Here, we consider the Sn-Sn bonding and antibonding functions built from Sn 5s orbitals as target eigenstates (Figure 3.8b). We then attempt to recover these functions from the remainder raMOs, to see to what extent localized Sn-Sn bonds occur at these contacts.

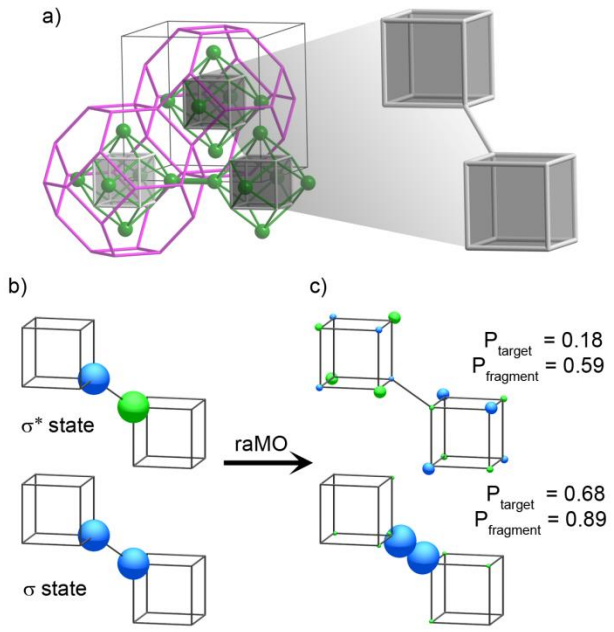

Figure 3.8. A second iteration of raMO analysis on the remainder functions of Os_3Sn_7 (not contributing to the Os_2 pairs) reveals Sn-Sn bonding between (a) neighboring Sn_8 cubes. (b) Target eigenfunctions for σ and σ* orbitals along one of these Sn-Sn contacts. (c) The corresponding raMOs generated from the remainder functions.

The resulting Sn-based raMO functions are plotted in Figure 3.8c. The Sn-Sn bonding raMO appears well localized ($P_{fragment}$ = 0.89, with the remainder of the electron density consisting of tiny contributions scattered throughout the structure). Furthermore, the bonding is enhanced relative to the original target function by s-p hybridization into the contact on both Sn atoms. The form of the raMO then appears to indicate strong Sn-Sn bonding. This conclusion is supported by the raMO approximating the Sn-Sn σ* function: little electron density involving the Sn-Sn contact is apparent here.

Placing a Sn-Sn bond along every bridging contact between the fluorite-type clusters accounts for essentially all of the electron density in the remainder raMOs. With this result in hand, we are now ready to make a full accounting of the valence electrons in Os_3Sn_7. Each Os atom achieves a filled octadecet with 16 electrons, via Os-Os σ and π bonding. Meanwhile, 4 of the 7 Sn atoms in the formula unit lie on the

cubes of the fluorite clusters, and contribute 1 electron each to Sn-Sn bonding. This leads to a total valence electron count for the bonding scheme of $(16\times3 + 4\times1)/3 = 17.33$ electrons, in close agreement with the experimental electron count.

3.7. Projected DOS of raMO Functions

In our calculations thus far, we have worked to map the features of the crystal orbitals of intermetallic phases onto local molecular orbital diagrams. The raMO functions that are created are then fairly localized in space, and orthogonal to each other. This might create the impression that they are essentially non-interacting with each other, but we should remember that they occur in the context of a metallic crystal structure. Some broadening of their energy levels should thus be expected as these are embedded in their structural context, much as the four localized C sp^3/H 1s σ bonds in methane interact to create a_1 and t_2 levels in the full MO diagram.

This broadening of the raMO levels can be tracked using their projected DOS distributions, as is shown in Figure 3.9. We begin in Figures 3.9a,b by presenting the full DFT-calibrated Hückel DOS curve for Os_3Sn_7 calculated with a dense k-point grid alongside the corresponding curve obtained from the 2×2×2 supercell with just the Γ-point. As might be expected the coarse sampling of k-space in the latter gives rise to a spikier curve, but the overall distribution and the broad minimum around the Fermi energy are well-maintained. The supercell thus provides a fairly representative sampling of the interactions within the structure.

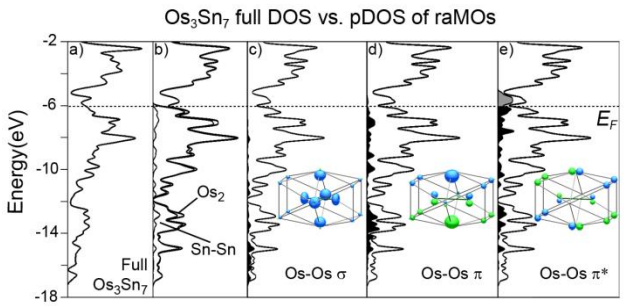

Figure 3.9. The use of raMO functions in DOS analysis. (a) DFT-calibrated Hückel DOS distribution of Os_3Sn_7. (b) The DOS curve for the Γ-point of a 2×2×2 supercell of Os_3Sn_7, with projections for the Os_2 dimer and Sn-Sn σ raMOs. (c)-(e) projected DOS distributions for the Os_2 σ, π, and π* raMOs respectively. Regions shaded in gray in panels c-e above the E_F correspond to projections from raMOs calculated with the valence electron count changed from 17.33 to 18.33 electrons/Os atom.

In Figure 3.9b, we also show projected DOS contributions from the Os_2 dimer and Sn-Sn σ raMOs. Summed together these account for the full DOS distribution up to the E_F. Above the E_F, their projections are zero as these raMOs consist of linear combinations of occupied states. The Os_2 DOS dominates the curve throughout, indicating that even the Sn s-rich states at the bottom of the energy scale are deeply involved in bonding with the Os. The Sn-Sn σ raMOs, on the other hand, are spread diffusely over the energy range, and have little effect on the total DOS curve's shape.

The different bonding types between the Os atoms have slightly more well-defined energy ranges, as may be seen by an examination of the Os_2 σ, π, and π* raMOs separately (shaded in black in Figures 3.9c-e). While the DOS distributions for all three spread across the energy spectrum up to the E_F, the Os_2 σ raMO DOS is particularly concentrated at the lowest end of the DOS distribution, from around -17 to -13 eV. At this point, the Os_2 π appears to take over, until just below the E_F. Near the E_F the π* functions become dominant. The progression from σ to π to π* with increasing energy follows the order expected by analogy to molecular systems.

From the DOS curves in Figures 3.9c-e, it is clear that the orbitals closest to the E_F have a strong π^* character. Removing electrons from the system would thus serve to increase the net π-bonding between the transition metal atoms.

How would increasing the electron count affect the bonding? Analyzing this case requires the consideration of unoccupied crystal orbitals. One approach to doing this would be to generate raMOs from the full set of these unoccupied levels, and analyze their DOS distributions. We have found, however, that the discontinuities between the raMOs calculated from levels above and below the E_F seriously complicate such an analysis. This issue can be eliminated by probing the states above the E_F in a different way: raising the E_F in calculation so that more crystal orbitals are included in the analysis. In this way the same raMO functions are used for the projected DOS calculation both above and below the original E_F.

In Figures 3.9c-e, we have carried out this procedure by including states up across the next DOS peak above the E_F to reach a deep pseudogap at ca. -5.5 eV. Filling the DOS curve to this point corresponds to 18.33 electrons/Os atom, as would be obtained from replacing each of the Os atoms with Ir to form Ir_3Sn_7. The projected DOS for the Os-Os σ, π, and π^* obtained above the E_F in this way is shaded in gray. A glance at these curves reveals that the DOS peak between the 17.33 to 18.33 electrons/Os atom is predominantly Os-Os π^* in character (the remainder consists of small contributions from a variety of functions). Recalling that the region just below the Os_3Sn_7 E_F also exhibited strong projections onto the Os-Os π^* raMOs, we see that the E_F essentially bisects the Os-Os π^* DOS. Adding or removing electrons to the system would thus serve to respectively weaken or strengthen the π bonding along these dimer contacts.

In this section, we have seen how the use of raMO functions can be applied in the DOS analysis of intermetallic phases. By calculating the contributions from individual types of raMO functions, such as

Os-Os σ, π, and π*, the advantages of traditional projected DOS and crystal orbital overlap or Hamiltonian population (COOP and COHP)[57-59] analyses can be combined into a single type of plot.

3.8. raMO Analysis and Electron Count Ranges

Our projected DOS analysis of the Os_3Sn_7 phase indicated that the states just above the E_F are rich in Os-Os π* character. This observation suggests that upon increasing the valence electron count through elemental substitution, the additional electrons would serve to weaken the Os-Os π-bonding without substantially affecting other interactions in the structure.

This prediction can be tested by applying the raMO analysis to an Ir_3Ge_7-type phase based on a later transition metal element, say Ir_3Sn_7. In Figure 3.10, we present the σ, π, π*, and σ* raMOs for one of the Ir_2 dimers in Ir_3Sn_7 alongside those we obtained earlier for Os_3Sn_7. For the majority of the raMO functions, there is a remarkably close correspondence between the structures. The σ and π functions appear to be essentially unchanged upon substituting Os with Ir. Similarly, the σ*orbital is poorly represented in both structures, indicating that the σ bonding remains intact in Ir_3Sn_7.

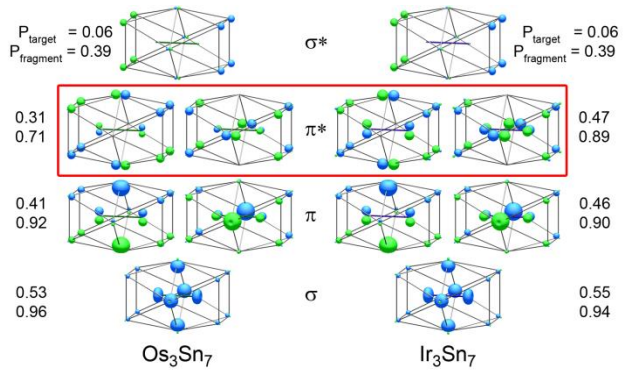

Figure 3.10. Comparison of the raMOs for the transition metal dimers in the Ir_3Ge_7-type phases Os_3Sn_7 and Ir_3Sn_7. The additional valence electrons introduced into the structure by replacing Os with Ir serve to strengthen the presence of the π* component to the interactions, leading to no net π-bonding.

The major change occurs in the π* raMOs, where the coefficients on the transition metals and bridging Sn atoms grow significantly upon moving from Os_3Sn_7 to Ir_3Sn_7. This effect confirms that the additional electrons are accommodated largely by the π* functions of the transition metal dimers. For Ir_3Sn_7, this growth in the π* interactions reaches the point where it is essentially equal in strength to the stabilizing interactions in the π-bonding raMOs. In this phase, then, the π-bonding is virtually removed by the occupation of π* functions, leaving only a σ-bond between the Ir atoms. In the absence of π-bonding between the Ir atoms, our predicted electron count changes. As the Ir pairs share only a single pair of electrons, they would each require 17 electrons to achieve closed-shell octadecets. This change would lead to an ideal count of $(17\times3 + 4\times1)/3 = 18.33$ electrons/Ir, which coincides exactly with that calculated from the compound's stoichiometry.

Our identification of a single σ-bond to the Ir_2 units of Ir_3Sn_7 provides a somewhat firmer basis for our tentative assignment of double bonds at the corresponding dimers in Os_3Sn_7. Replacing each Ir atom with Os, lowers the valence electron count by one, largely through the depopulation of transition metal-transition metal π* states. Going from an Ir_2 dimer to an Os_2 one would then result in removing two electrons. Pulling these electrons from the π* states increases the net bond order along the dimers from 1 to 2.

This comparison suggests a mechanism by which transition metal-transition metal bonds can allow 18-electron configurations to be maintained over a range of electron counts. For a pair of atoms joined by a single σ bond, the removal of electrons can be compensated through the sharing of electrons in π-bonds. An analogous situation occurs in the molecules F_2, O_2, and N_2, which all follow the octet rule despite having different numbers of valence electrons.

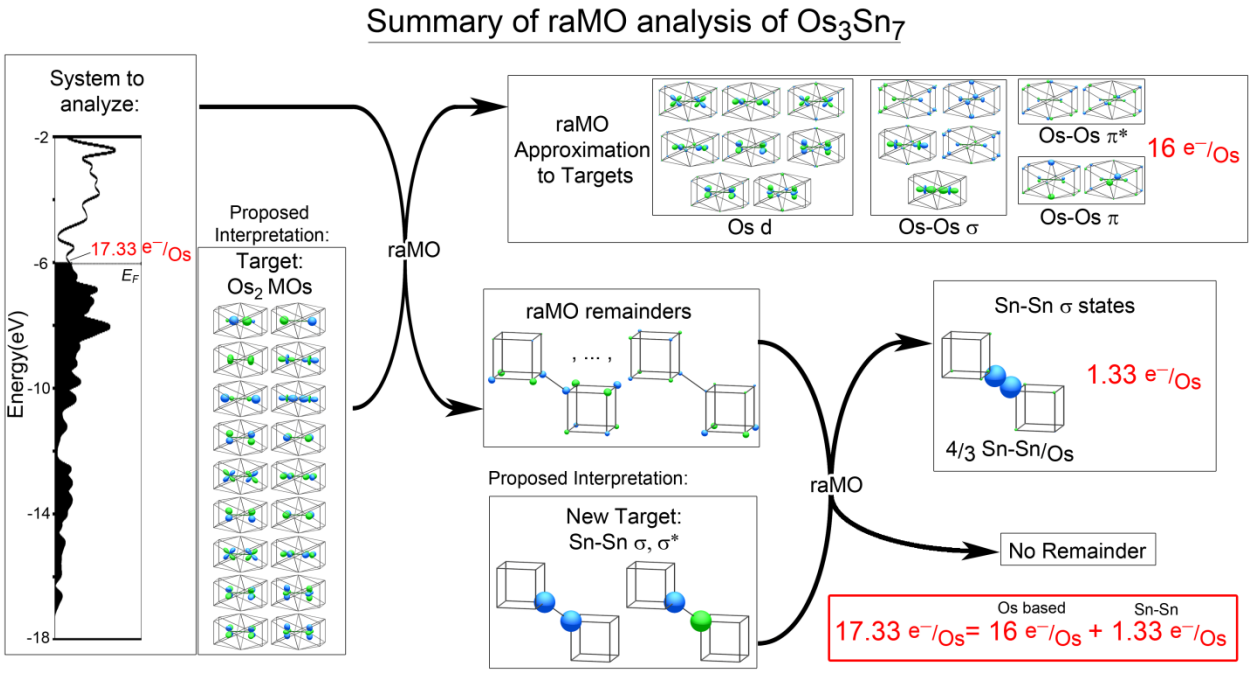

Figure 3.11. Summary of the use of the raMO analysis to iteratively reduce the full electronic structure of an intermetallic phase into a series of subsystems described by model MO diagrams. For Os_3Sn_7, the result is an explanation of the DOS pseudogap near 17.33 electrons/Os as the sum of Os=Os dimers (16 electrons/Os) and Sn-Sn bonds (⅔ Sn-Sn bonds/Os = 1.33 electrons/Os).

3.9. Conclusions

As is so vividly demonstrated by the Zintl-Klemm concept[29] and the orbital interpretations of band structures,[3,25-26] molecular bonding schemes have the potential to bring valuable insights into the structures and properties of solid state inorganic compounds. In this Article, we have presented a method for rapidly testing and generalizing such molecular ideas: the reverse approximation Molecular Orbital (raMO) approach. Underlying the raMO approach is the fact that the full wavefunctions of a system will consist of linear combinations of any localized bonding features that may be present. The localization of these features can be restored through a reversal of the usual basis set approximation of electronic structure

calculations: the full wavefunctions of a compound are considered as being a basis set for the solution of simple molecular orbital problems, such as the interaction between two p orbitals to make a π-bond.

We illustrated the raMO method for a series of examples. 1,3-butadiene served as a test case where the bonding is already well-understood. Here, the raMO approach quickly yielded a donor-acceptor model for the conjugation of the π-system, and the orthogonality of this π-system to the σ framework of the molecule. Increasingly more complicated compounds, beginning with $CrGa_4$ and then moving to Ir_3Ge_7-type phases, could be similarly dissected into localized bonding systems: For $CrGa_4$, the pseudogap at the E_F was traced to virtually independent 18-electron configurations on each of the Cr atoms. For the Ir_3Ge_7-type phases, a similar pseudogap emerges from 18-electron configurations on the transition metal atoms (facilitated by the covalent sharing of electrons between the transition metals), as well as two-center two-electron bonds between main group atoms.

The application to Ir_3Ge_7-type phase Os_3Sn_7 illustrates how the raMO analysis can be used in an iterative fashion to break down the electronics of complex structures (Figure 3.11). Beginning with the full electronic structure, we offer a model for the bonding in the form of target eigenfunctions, in this case the MOs of Os_2 dimers. The raMO procedure then yields best approximants to these MOs which amount to 18-electron configurations on the Os atoms achieved with the help of interactions that are isolobal to Os-Os σ and π bonds. The procedure also yields remainder functions which are orthogonal to the proposed Os_2 dimer-based bonding model. A second raMO cycle using a Sn-Sn bonding model can then be applied to these remainder states, which then captures the remaining electron density. At this point, no remainder steps are left, but one could imagine carrying out longer sequences of raMO analysis for more complicated combinations of bonding.

This type of information is complementary to that provided by other theoretical tools for bonding analysis, such as the crystal orbital overlap and Hamiltonian populations (COOP and COHP),[57-59] and the electron localization function and indicator (ELF and ELI).[60-64] The COOP and COHP analyses quantify the bonding strength between pairs of atoms or orbitals in a structure, and the dependence of these interactions on electron count. Meanwhile, the ELF and ELI analyze the curvature of the Fermi hole to describe the tendency for electrons to form localized pairs within the structure. New features that are offered by the raMO analysis include the abilities to divide the interactions into orthogonal groups, and to partition integer numbers of electrons to each of these bonding subsystems. Such a quantization of electron counts in individual bonding systems has historically been a key step in deriving electron counting rules.

So far, our raMO analyses have been carried out on DFT-calibrated Hückel calculations, which serve as effective atomic orbital-based models that quantitatively reproduce the band energies and density of states curves of DFT calculations on the corresponding compounds. However, the formalism is not limited to this particular semi-empirical method, but in principle could be applied to any first-principles method that employs one-electron wavefunctions. We are looking forward to developing a DFT-implementation of this approach, in which the wavefunctions in the DFT output are used directly as a basis set for solving simple MO diagrams. In this way, the raMO method should be applicable to the wide range of systems, molecular and periodic, for which DFT provides useful descriptions of electronic structure.

3.10. Acknowledgments

We are grateful to Prof. Clark Landis for engaging discussions on the relationships between the raMO and NBO approaches, and also thank Veronica Berns, Joshua Engelkemier, Yiming Guo, and Amelia Hadler in our research group for their applications of the raMO analysis to a variety of intermetallic systems. We gratefully acknowledge the financial support of the Department of Energy Office of Science Early Career Program (DE-SC0003947), through the Office of Basic Energy Sciences (for the development of the raMO methodology), the National Science Foundation (NSF) through grant DMR-1207409 (for the applications of raMO to $CrGa_4$ and the Ir_3Ge_7-type phases), and the Wisconsin Alumni Research Foundation. Computations contributing to this work were performed on computer resources supported by NSF grant CHE-0840494.

3.11. References

(1) Mott, N. F.; Jones, H. *Theory of the Properties of Metals and Alloys*; Clarendon Press: Oxford, 1936.

(2) Mizutani, U.; Kondo, Y.; Nishino, Y.; Inukai, M.; Feuerbacher, M.; Sato, H. *J. Phys.: Condens. Matter* **2010**, *22*, 485501.

(3) Berger, R. F.; Walters, P. L.; Lee, S.; Hoffmann, R. *Chem. Rev.* **2011**, *111*, 4522-4545.

(4) Xu, J.-h.; Freeman, A. *Phys. Rev. B* **1989**, *40*, 11927-11930.

(5) Ravindran, P.; Subramoniam, G.; Asokamani, R. *Phys. Rev. B* **1996**, *53*, 1129-1137.

(6) Wolf, W.; Bihlmayer, G.; Blügel, S. *Phys. Rev. B* **1997**, *55*, 6918-6926.

(7) Imai, Y.; Mukaida, M.; Tsunoda, T. *Intermetallics* **2000**, *8*, 381-390.

(8) Haussermann, U.; Elding-Ponten, M.; Svensson, C.; Lidin, S. *Chem. Eur. J.* **1998**, *4*, 1007-1015.

(9) Häussermann, U.; Viklund, P.; Boström, M.; Norrestam, R.; Simak, S. *Phys. Rev. B* **2001**, *63*.

(10) Imai, Y.; Watanabe, A. *J. Alloys Compd.* **2006**, *417*, 173-179.

(11) Fredrickson, D. C.; Lee, S.; Hoffmann, R. *Inorg. Chem.* **2004**, *43*, 6159-6167.

(12) Fredrickson, D. C.; Lee, S.; Hoffmann, R.; Lin, J. *Inorg. Chem.* **2004**, *43*, 6151-6158.

(13) Tobola, J.; Pierre, J.; Kaprzyk, S.; Skolozdra, R. V.; Kouacou, M. A. *J. Phys.: Condens. Matter* **1998**, *10*, 1013-1032.

(14) Jung, D.; Koo, H. J.; Whangbo, M. H. *J. Mol. Struct.-Theochem.* **2000**, *527*, 113-119.

(15) Kandpal, H. C.; Felser, C.; Seshadri, R. *J. Phys. D: Appl. Phys.* **2006**, *39*, 776-785.

(16) Kohler, J.; Deng, S. Q.; Lee, C.; Whangbo, M. H. *Inorg. Chem.* **2007**, *46*, 1957-1959.

(17) Fredrickson, R. T.; Fredrickson, D. C. *Inorg. Chem.* **2012**, *51*, 10341-10349.

(18) Fredrickson, R. T.; Fredrickson, D. C. *Inorg. Chem.* **2013**, *52*, 3178-3189.

(19) Han, M. K.; Wu, Y. Q.; Kramer, M.; Vatovez, B.; Grandjean, F.; Long, G. J.; Miller, G. J. *Inorg. Chem.* **2006**, *45*, 10503-10519.

(20) Lin, Q.; Corbett, J. D. *J. Am. Chem. Soc.* **2007**, *129*, 6789-6797.

(21) Berns, V. M.; Stacey, T. E.; Sapiro, M.; Fredrickson, D. C. *Eur. J. Inorg. Chem.* **2011**, *2011*, 3936-3949.

(22) Hadler, A. B.; Fredrickson, D. C. *J. Am. Chem. Soc.* **2012**, *134*, 10361-10364.

(23) Stacey, T. E.; Fredrickson, D. C. *Inorg. Chem.* **2012**, *51*, 4250-4264.

(24) Westbrook, J. H.; Fleischer, R. L. *Magnetic, electrical and optical properties, and applications of intermetallic compounds*; Wiley: Chichester, England ; New York, 2000.

(25) Hoffmann, R. *Solids and surfaces: a chemist's view of bonding in extended structures*; VCH Publishers: New York, NY, 1988.

(26) Burdett, J. K. *Chemical bonding in solids*; Oxford University Press: New York, 1995.

(27) Zintl, E. *Angew. Chem.* **1939**, *52*, 1-6.

(28) McNeil, M. B.; Pearson, W. B.; Bennett, L. H.; Watson, R. E. *J. Phys. C: Solid State Phys.* **1973**, *6*, 1-10.

(29) Kauzlarich, S. M. *Chemistry, structure, and bonding of Zintl phases and ions*; VCH: New York, 1996.

(30) Klem, M. T.; Vaughey, J. T.; Harp, J. G.; Corbett, J. D. *Inorg. Chem.* **2001**, *40*, 7020-7026.

(31) Li, B.; Corbett, J. D. *Inorg. Chem.* **2002**, *41*, 3944-3949.

(32) Mudring, A.-V.; Corbett, J. D. *J. Am. Chem. Soc.* **2004**, *126*, 5277-5281.

(33) Saparov, B.; Xia, S.-q.; Bobev, S. *Inorg. Chem.* **2008**, *47*, 11237-11244.

(34) Foster, J. M.; Boys, S. F. *Rev. Mod. Phys.* **1960**, *32*, 300-302.

(35) Wannier, G. H. *Phys. Rev.* **1937**, *52*, 191-197.

(36) Marzari, N.; Mostofi, A. A.; Yates, J. R.; Souza, I.; Vanderbilt, D. *Rev. Mod. Phys.* **2012**, *84*, 1419-1475.

(37) Zurek, E.; Jepsen, O.; Andersen, O. K. *ChemPhysChem* **2005**, *6*, 1934-1942.

(38) Shamp, A.; Hooper, J.; Zurek, E. *Inorg. Chem.* **2012**, *51*, 9333-9342.

(39) Hooper, J.; Zurek, E. *Chem. Eur. J.* **2012**, *18*, 5013-5021.

(40) Hoffmann, R. *Angew. Chem. Int. Ed.* **1982**, *21*, 711-724.

(41) Beautiful examples of mapping crystal orbitals onto simple MO diagrams are given by the work of Zurek and coworkers in their analysis of 3-center 4-electron bonding in H_3- units. See: Shamp, A.; Hooper, J.; Zurek, E. Inorg. Chem. 2012, 51, 9333-9342; Hooper, J.; Zurek, E. Chem. Eur. J. 2012, 18, 5013-5021.

(42) Weinhold, F.; Landis, C. R. *Valency and bonding : a natural bond orbital donor-acceptor perspective*; Cambridge University Press: Cambridge, UK ; New York, 2005.

(43) The technical and prodecural differences between the NBO and raMO analyses are discussed in the Supporting Information.

(44) Cox, E. G. *Rev. Mod. Phys.* **1958**, *30*, 159-162.

(45) Meissner, H.-G.; Schubert, K. *Z. Metallkd.* **1965**, *56*, 523-530.

(46) Künnen, B.; Niepmann, D.; Jeitschko, W. *J. Alloys Compd.* **2000**, *309*, 1-9.

(47) Schlüter, M.; Häussermann, U.; Heying, B.; Pöttgen, R. *J. Solid State Chem.* **2003**, *173*, 418-424.

(48) Kresse, G.; Furthmüller, J. *Phys. Rev. B* **1996**, *54*, 11169-11186.

(49) Kresse, G.; Furthmüller, J. *Comput. Mater. Sci.* **1996**, *6*, 15-50.

(50) Vanderbilt, D. *Phys. Rev. B* **1990**, *41*, 7892-7895.

(51) Stacey, T. E.; Fredrickson, D. C. *Dalton Trans.* **2012**, *41*, 7801-7813.

(52) Landrum, G. A; Glassey, W. YAeHMOP: Yet Another extended Hückel Molecular Orbital Package, Ver. 3. YAeHMOP is freely available at URL: http://sourceforge.net/projects/yaehmop/

(53) Cohen-Tannoudji, C.; Diu, B.; Laloë, F. *Quantum mechanics*; Wiley: New York, 1977; Vol. 1.

(54) Tobola, J.; Pierre, J.; Kaprzyk, S.; Skolozdra, R. V.; Kouacou, M. A. *J. Magn. Magn. Mater.* **1996**, *159*, 192-200.

(55) Tobola, J.; Pierre, J. *J. Alloys Compd.* **2000**, *296*, 243-252.

(56) Pettifor, D. G. *Bonding and structure of molecules and solids*; Oxford University Press: Oxford, 1995.

(57) Hughbanks, T.; Hoffmann, R. *J. Am. Chem. Soc.* **1983**, *105*, 3528-3537.

(58) Hughbanks, T.; Hoffmann, R. *J. Am. Chem. Soc.* **1983**, *105*, 1150-1162.

(59) Dronskowski, R.; Bloechl, P. E. *J. Phys. Chem.* **1993**, *97*, 8617-8624.

(60) Becke, A. D.; Edgecombe, K. E. *J. Chem. Phys.* **1990**, *92*, 5397-5403.

(61) Savin, A.; Becke, A. D.; Flad, J.; Nesper, R.; Preuss, H.; Von Schnering, H. G. *Angew. Chem. Int. Ed.* **1991**, *39*, 409-412.

(62) Savin, A.; Nesper, R.; Wengert, S.; Fassler, T. F. *Angew. Chem. Int. Ed.* **1997**, *36*, 1808-1832.

(63) Kohout, M.; Pernal, K.; Wagner, F. R.; Grin, Y. *Theor. Chem. Acc.* **2004**, *112*, 453-459.

(64) Wagner, F. R.; Bezugly, V.; Kohout, M.; Grin, Y. *Chem. Eur. J.* **2007**, *13*, 5724-5741.

Chapter 4

Defusing Complexity in Intermetallics: How Covalently Shared Electron Pairs Stabilize the FCC Variant $Mo_2Cu_xGa_{6-x}$ ($x = 0.9$)

This chapter has been published: Kilduff, B.J.; Yannello, V.J.; Fredrickson, D.C. *Inorg. Chem.* **2014**, 53, 2730-2741. The synthetic and theoretical work presented in this paper were performed by Kilduff, but all authors contributed to the application of raMO analysis to these $TiAl_3$-type variants.

4.1. Abstract

Simple sphere packings of metallic atoms are generally assumed to exhibit highly delocalized bonding, often visualized in terms of a lattice of metal cations immersed in an electron gas. In this Article, we present a compound that demonstrates how covalently shared electron pairs can, in fact, play a key role in the stability of such structures: $Mo_2Cu_xGa_{6-x}$ ($x \approx 0.9$). $Mo_2Cu_xGa_{6-x}$ adopts a variant of the common TiAl3 structure type, which itself is a binary coloring of the fcc lattice. Electronic structure calculations trace the formation of this compound to a magic electron count of 14 electrons/T atom (T = transition metal) for the $TiAl_3$ type, the Fermi Energy for which coincides with an electronic pseudogap. This count is one electron/T atom lower the electron concentration for a hypothetical $MoGa_3$ phase, making this structure less competitive relative to more complex alternatives. The favorable 14 electron count can be reached, however, through the partial substitution of Ga with Cu. Using DFT-calibrated Hückel calculations and the reversed approximation Molecular Orbital (raMO) method, we show that the favorability of the 14

electron count has a simple structural origin in terms of the 18-*n* rule of T-E intermetallics (E = main group element): the T atoms of the $TiAl_3$ type are arranged into square nets whose edges are bridged by E atoms. The presence of shared electron pairs along these T-T contacts allows for 18 electron configurations to be achieved on the T atoms despite possessing only 18-4 = 14 electrons/T atom. This bonding scheme provides a rationale for the observed stability range of $TiAl_3$-type TE_3 phases of ca. 13 to 14 electrons/T atom, and demonstrates how the concept of the covalent bond can extend even to the most metallic of structure types.

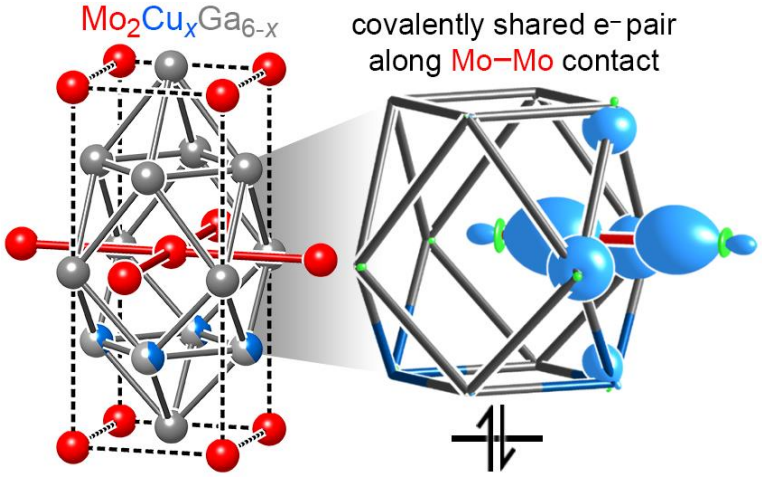

Figure 4.0. Simple metallic structures are generally assumed to exhibit highly delocalized bonding, often visualized in terms of a lattice of metal cations immersed in an electron gas. In this Article, we demonstrate that covalently shared electron pairs, in fact, play a key role in the new fcc variant $Mo_2Cu_{0.9}Ga_{5.1}$. Its stability derives from shared electron pairs along Mo-Mo contacts, which allow for 18 electron configurations on the Mo despite there only being 14 electrons/Mo atom.

4.2. Introduction

Of the three fundamental types of bonding—covalent, ionic, and metallic—the metallic bond has been uniquely difficult to grasp from the chemical point of view. This difficulty is made vivid by the early

attempts to draw resonance structures for simple elemental metals such as Li, wherein frustration quickly arises through the extremely low ratio of electrons to close interatomic contacts (1:7 for bcc alkali metals).[1,2] An intractable number of possible resonance structures is the result. The bonding in such systems has been more satisfyingly viewed in terms of free electrons that are weakly perturbed by the presence of a lattice of cations. While different from the way chemists usually approach bonding (though not entirely incompatible with it),[3,4] this idea has immense power: it forms the basis of the Mott-Jones model for Hume-Rothery phases[5] and motivates the use of plane waves as a basis-set for quantum mechanical calculations on periodic solids.[6,7]

From the successes of the nearly-free electron model over a localized view of bonding in simple metals, it is tempting to consider the concept of the covalently shared electron pair as completely foreign to structures based on fcc, bcc, or hcp atomic packings. In this Article, we present a counter-example to this expectation, with the synthesis, crystal structure, and bonding analysis of the new phase $Mo_2Cu_xGa_{6-x}$ ($x \approx 0.9$), hereafter referred to as $Mo_2Cu_{0.9}Ga_{5.1}$. This phase exhibits a disordered variant of the $HfCuSi_2$ type,[8] which is itself a variant of the $TiAl_3$ type[9] – all of which are colorings of the fcc structure.

The simplicity of the $Mo_2Cu_{0.9}Ga_{5.1}$ structure is in stark contrast to the intriguing intermetallic phase Mo_8Ga_{41} that inspired our investigations into the Mo-Cu-Ga system. Mo_8Ga_{41} crystallizes in the V_8Ga_{41} structure type,[10,11] in which a primitive cubic lattice of Ga atoms serves as a host to guest clusters of transition metal-capped Ga_{12} cuboctahedra.[12] Small variations of the composition of this phase have been found to lead to variations on this host guest theme. In Mo_6Ga_{31}[13] and $Mo_8Ga_{40.88}S_{0.86}$,[14] dimers and columns of such guest clusters were observed embedded in a similar host matrix, and more extensive structural chemistry was revealed in the structure of $V_{11}Cu_9Ga_{46}$ by Lux et al.[15] Based on these

observations, we were interested in how the addition of Cu to the Mo-Ga system could influence these host-guest type arrangements. In the structure of $Mo_2Cu_{0.9}Ga_{5.1}$, the answer appears to be the suppression of structural complexity in favor of more simple atomic packing.

As we will see below, a bonding analysis of $Mo_2Cu_{0.9}Ga_{5.1}$ (and related phases) offers a simple explanation for how Cu substitution in the Mo-Ga system brings these results. DFT calculations reveal that, as in other compounds based on the $TiAl_3$ type,[16-20] this phase exhibits a pronounced electronic pseudogap at the valence electron count of 14 electrons/transition metal (T) atom, indicative of special stability. Using the reversed approximation Molecular Orbital (raMO) method,[21] we trace this pseudogap to the filling of 18 electron configurations on the T atoms, achieved with the help of shared electron pairs along four T-T contacts at each T center. In this way, the phase becomes an example of the recently proposed 18-*n* rule for intermetallics.[22]

Without Cu, a hypothetical $TiAl_3$-type $MoGa_3$ phase would overshoot the preferred 14 electron/T count by one electron/T atom, making this structure less energetically competitive in a Ga-rich melt relative to complex structures such as Mo_8Ga_{41}. Substitution with Cu, however, offers the ability to lower the valence electron count back towards its optimal value. In this way, the existence of $Mo_2Cu_{0.9}Ga_{5.1}$ reveals how covalently-shared electron pairs can stabilize even the most archetypal of metallic structures.

4.3. Experimental Section

4.3.1. Synthesis

Samples of $Mo_2Cu_xGa_{6-x}$ where x = 0.5, 1.0, 1.5, and 2.0 were prepared by combining loose powders of Mo (Strem Chemical, 99.95%) and Cu (Strem Chemicals, 99.9%) with ingots of Ga (Strem Chemical,

99.99%) into Al_2O_3 crucibles in an Ar filled glovebox. The crucibles were then lowered into fused silica tubes, which were transferred to a vacuum line (with precautions taken to avoid exposure to atmospheric O_2), where they were evacuated to ~95 mtorr and sealed with a torch. The sealed tubes were then placed on-end in a muffle furnace and heated from room temperature to 800 °C over 4 h, held at 800 °C for 96 h, and cooled to room temperature over 80 h. A nearly phase pure sample of $Mo_2Cu_{0.9}Ga_{5.1}$ was prepared by arc melting a pellet of composition $Mo_2Cu_{0.75}Ga_{5.25}$ (a slight excess of Ga was used to compensate for the potential loss of Ga during pellet pressing and arc melting), sealing it in an evacuated fused silica tube, and annealing in a muffle furnace using the same heating profile as described above.

4.3.2. Single Crystal X-ray Diffraction Analysis

Single crystal X-ray diffraction analysis was performed on a crystal picked from the sample with loading composition $Mo_2Cu_xGa_{6-x}$ ($x \approx 1.0$), where the phase appeared in the largest yield as indicated from powder X-ray diffraction data. Data were collected on an Oxford Diffraction Xcalibur E diffractometer using graphite monochromatized Mo Kα radiation (λ=0.71073 Å) at ambient temperature. Run list optimization and data were performed using the CrysAlis Pro ver. 171.36.28 software supplied by the manufacturer. The structure was solved with the charge flipping algorithm[23,24] using the program SUPERFLIP.[25] The solution was refined using JANA2006[26] by full matrix least squares on F^2, which yielded (when combined with compositional information from EDS) a structure of composition $Mo_2Cu_{0.9}Ga_{5.1}$. Further information concerning the crystal data are given in Table 1, while details of the refinement are provided in the Supporting Information.

Table 4.1. Crystallographic Information for $Mo_2Cu_{0.9}Ga_{5.1}$

Chemical Formula	$Mo_2Cu_{0.9}Ga_{5.1}$[a]
EDS Composition	$Mo_2Cu_{0.84(9)}Ga_{5.25(22)}$
Space Group	*P*4/*nmm*
a (Å)	3.69830(10)
c (Å)	8.6170(2)
cell volume	117.858(5)
Z	1
Pearson symbol	*tP*8
cryst. dimensions (mm^3)	0.03 × 0.05 × 0.07
crystal color	metallic grey
crystal shape	irregular
data collection temp.	RT
radiation source, λ (Å)	Mo, Kα (0.7107)
absorption coefficient (mm^{-1})	37.606
absorption correction	analytical[28]
min/max transmission	0.203, 0.408
$\theta_{min,}, \theta_{max}$	4.73, 32.42
number of reflections	2340
$R_{int}[I > 3\sigma(I)]$, R_{int}(all)	2.53, 2.55
unique ref. [all, $I > 3\sigma(I)$]	155, 141
number of parameters	12
$R[I > 3\sigma(I)]$, $R_w[I > 3\sigma(I)]$	1.48, 3.93
R(all), R_w(all)	1.75, 4.08
$S[I > 3\sigma(I)]$, S(all)	1.18, 1.20
$\Delta\rho_{max}$, $\Delta\rho_{min}$ ($e^-/Å^3$)	0.72, -0.86

[a]The chemical formula formula was determined as follows: The Mo:(Cu/Ga) ratio was determined from single crystal X-ray diffraction results, while the Cu/Ga ratio (which is difficult to determine from diffraction data due to Cu's and Ga's similar form factors in Mo, Kα radiation) was estimated from SEM-EDS results of the sample from which the single crystal was taken.

4.3.3. Powder X-ray Diffraction Analysis

Samples were ground into fine powders using an agate mortar and pestle, and mounted onto a zero-background plate. Diffraction intensities were collected with a Bruker D8 Advance Powder Diffractometer

using Cu Kα radiation (λ=1.5418 Å) at room temperature. The measurements employed a LYNXEYE detector and an exposure time of 0.6 s per 0.01° for the 2θ range 15° to 90°. The diffraction patterns were analyzed using Match! version 2.2.2 and JANA2006. Loading compositions with x = 0.5, 1.0, and 1.5 displayed peaks agreeing with the calculated $Mo_2Cu_{0.9}Ga_{5.1}$ pattern. The unit cells of $Mo_2Cu_xGa_{6-x}$ for each loading composition were determined from the powder patterns using a least squares refinement implemented in UNITCELL.[27] Shifts in the diffractions peaks between x = 0.5 and 1.5 indicated a contraction of a = 0.007 Å and expansion of c = 0.013 Å for larger values of x, indicating a small phase width for Cu substitution. For x = 0.5, large quantities of Mo_3Ga and $Mo_2Cu_3Ga_5$, as well as a small amount of Mo_8Ga_{41}, could be identified as impurities. At x = 1.0, $Mo_2Cu_xGa_{6-x}$, Mo_3Ga, and $Mo_2Cu_3Ga_5$ were identified in agreement with SEM-EDS analysis. For loading compositions above x = 1.0 an unidentified phase began to form with a peak at $2\theta = 40.38^o$. Powder diffraction patterns are provided in the Supporting Information (Figures B1 and B2).

4.3.4. Energy Dispersive X-ray Spectroscopy

Samples were prepared for elemental analysis using energy dispersive X-ray spectroscopy (EDS) by suspending fragments of the reaction products in nonconductive epoxy in a hollow Al bullet. Once the epoxy had hardened, the surface was polished with diamond lapping film (down to a 0.5 μm grit) until cross sections of the crystals were visible under a light microscope. The samples were then sonicated for ~60 s in isopropanol to remove any surface contamination from polishing, allowed to dry in air, and then coated by evaporation with a 200 Å thick layer of carbon to avoid charging in an electron beam. The $Mo_2Cu_xGa_{6-x}$ samples were examined with a Hitachi S-3100N scanning electron microscope equipped

with an EDS probe (15 kV). 20 to 30 points were measured on each sample. For samples with x = 0.5, 1.0, and 1.5, three phases were identified corresponding to Mo_3Ga, $Mo_2Cu_3Ga_8$, and $Mo_2Cu_xGa_{6-x}$. For x = 2.0 only compositions corresponding to Mo_3Ga and $Mo_2Cu_3Ga_8$ were found. The average composition of $Mo_2Cu_xGa_{6-x}$, excluding carbon, was determined from the Mo L-shell, Ga Kα-, and Cu Kα-shell emission lines. The compositions of the $Mo_2Cu_xGa_{6-x}$ phase were determined to be $Mo_{1.92(3)}Cu_{0.76(9)}Ga_{5.32(23)}$, $Mo_{1.91(3)}Cu_{0.84(9)}Ga_{5.25(22)}$, and $Mo_{1.93(3)}Cu_{0.94(9)}Ga_{5.13(23)}$ for loading compositions with x = 0.5, 1.0, and 1.5 respectively. While the three compositions appear to show a correlation between Cu content and x, the observed variation in composition across the series is within the error bars of the measurements. The homogeneity range of this phase is thus narrower than the precision of the EDS results.

4.3.5. DFT-calibrated Hückel Calculations

To provide a basis for the creation of Hückel models for $Mo_2Cu_{0.9}Ga_{5.1}$ (approximated as Mo_2CuGa_5 to obtain an ordered structure), $NbGa_3$, and a hypothetical $TiAl_3$-type $MoGa_3$ phase, electronic structure calculations were carried out on their structures using the Vienna ab initio Simulation Package (VASP).[29,30] First, the crystal structures were geometrically optimized, and then the DFT band energies and electronic density of states (DOS) distributions of the obtained structures were computed. All VASP calculations were performed in the high-precision mode, using the GGA ultrasoft pseudopotentials[31] provided with the package. 12 × 12 × 5 and 13 × 13 × 5 Γ-centered k-point grids were used for $TiAl_3$-type and Mo_2CuGa_5 structures, respectively (See the supporting information for further details).

Simple Hückel parameters were then refined from the output of the VASP calculations using the program eHtuner,[32] with the Hückel calculations themselves being carried out with a modified version of

YAeHMOP.[33] The optimized Hückel parameters can be found in the Supporting Information, along with the RMS deviations between the band energies of the Hückel models and those calculated with VASP (all < 0.2 eV).

Following the refinement of the Hückel parameters, Hückel DOS curves were calculated, and preparations were made for a reversed approximation Molecular Orbital (raMO) analysis[21] by performing Hückel calculations on 4 × 4 × 2 supercells of the structures, so that several of the special k points of the primitive cells were mapped to the Γ points. The Hamiltonian matrix for the Γ point of each supercell was printed and imported into MATLAB, where the raMO analysis was carried out using a series of in-house functions.

4.4. Results and Discussion

4.4.1. The Crystal Structure of $Mo_2Cu_{0.9}Ga_{5.1}$

During our syntheses in the Mo-Cu-Ga system, we obtained crystals whose diffraction patterns were consistent with a tetragonal cell of dimensions a = 3.70 Å and c = 8.62 Å. These cell dimensions are suggestive of the $TiAl_3$ structure type adopted by a number of 1:3 transition metal (T) gallides.[34-37] A closer look at reciprocal lattice reconstructions of the single crystal diffraction data indicated that the strongest reflections indeed follow the $h+k+l = 2n$ condition expected for the $I4/mmm$ space group of the $TiAl_3$ type. However, weaker reflections were also present violating this systematic absence law, indicating that a superstructure pattern breaking the *I*-centering of the original structure type is present. Inspection of the remaining systematic absences suggested $P4/nmm$ as the highest space group symmetry consistent with

the diffraction pattern. This choice was confirmed in the subsequent steps of the structure solution and refinement, which yielded a structure of composition $Mo_2Cu_{0.9}Ga_{5.1}$.

As expected from these cell parameters, the crystal structure of this phase is closely related to the $TiAl_3$ structure type (Figure 4.1a). The $TiAl_3$ type itself can be simply derived by considering an fcc lattice of Al atoms, doubling the unit cell along *c*, and finally replacing the corner and central Al atoms of the supercell with Ti atoms. In $Mo_2Cu_{0.9}Ga_{5.1}$, Mo and Ga/Cu atoms take positions analogous to those of the Ti and Al in the $TiAl_3$ type, respectively (Figure 4.1b-c). However, the placement of Ga and Cu among the Al-type sites is not uniform. The Cu atoms are largely restricted to the $z = 3/4$ layer of the $TiAl_3$ structure, with the remainder of the Al-type sites are occupied by Ga. Full occupation of the $z = 3/4$ sites with Cu would correspond to the $HfCuSi_2$ structure type, but the X-ray diffraction data indicate that this layer consists of mixed Ga/Cu sites, with the EDS results suggesting that the ratio is approximately 45 Cu : 55 Ga. The placement of Cu onto this site agrees with DFT-calculations; only models with Cu substituted onto the $z = 3/4$ layer resulted in the observed crystal geometry when structurally optimized (see Section S2 of the Supporting Information).

This substitution of a single layer in the unit cell with Cu breaks both the *I*-centering of the original $TiAl_3$ type, and the mirror planes passing through the transition metal atoms perpendicular to the *c*-axis. This change in symmetry leads to a shift in the unit-cell origin by $(0, 1/2, 1/4)$, as shown in Figure 4.1b. The new origin places the Cu-substituted layer prominently in the center of the unit cell along *c*. The lower symmetry of this arrangement means that the Mo and Ga atoms in the planes above and below the Cu substituted layer are no longer held at fixed positions as they were in the $TiAl_3$-type cell. They are now free to move along the *c*-axis in response to the fact that they have Cu/Ga mixed sites on one side of them along

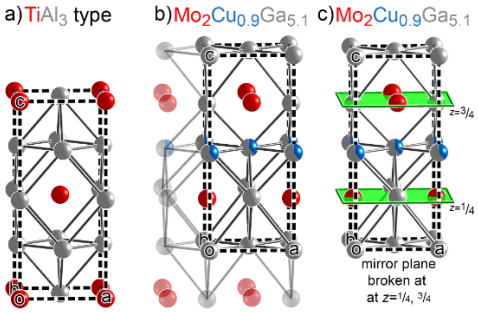

Figure 4.1. The crystal structure of $Mo_2Cu_{0.9}Ga_{5.1}$, a ternary variant of the $TiAl_3$ structure type. (a) The $TiAl_3$ structure type. (b) An expanded view of the $Mo_2Cu_{0.9}Ga_{5.1}$ structure illustrating its relationship to the $TiAl_3$ type. The Ga atoms, originally at z = 3/4 are mixed with approximately 45% Cu. This substitution breaks the body centering of the $TiAl_3$-type cell leading to the primitive unit cell of $Mo_2Cu_{0.9}Ga_{5.1}$ shown. (c) One unit cell of the $Mo_2Cu_{0.9}Ga_{5.1}$ structure.

c, but only Ga atoms on the other. In these motions, the Mo atoms retreat away from the Cu substituted layer while the Ga atoms advance toward the Cu substitution (Figure 4.1c).

4.4.2. Electronic Pseudogaps in $Mo_2Cu_xGa_{6-x}$ and $TiAl_3$-type Phases

The structural analysis above illustrates how the addition of Cu to a Ga-rich Mo-Ga melt leads to the formation of a simple $TiAl_3$-type variant rather than the significantly more complex Mo_8Ga_{41} phase. An important clue to the origins of $Mo_2Cu_{0.9}Ga_{5.1}$ is the observation that while $MoGa_3$ does not exist,[38] a $TiAl_3$-type phase does form when we move from Mo to Nb: $NbGa_3$.[37] This observation can be rationalized by a comparison of the electronic density of states (DOS) distributions calculated for $NbGa_3$ and a hypothetical $TiAl_3$-type $MoGa_3$ phase (Figures 4.2a,b) using a DFT-calibrated Hückel model (see the Experimental Section for details). The Fermi energy (E_F) of the $NbGa_3$ structure sits comfortably in a pseudogap in the structure's electronic DOS distribution, as has been noted previously.[20] This matching of the E_F at the structure's electron count of 14/T atom with a pseudogap is an indication of a favorable

electron count, just as large HOMO-LUMO gaps are correlated with stability in molecules. This expectation is confirmed by an examination of the binary T-E intermetallics listed as crystallizing in the $TiAl_3$ type by the Inorganic Crystal Structure Database (ICSD).[39-41] The vast majority exhibit valence electron counts in the range of 13 to 14 electrons/T atom.

On moving from $NbGa_3$ to the hypothetical $MoGa_3$ structure, the DOS distribution is largely unchanged, with an analogous pseudogap still occurring at 14 electrons/T atom. However, the replacement of Nb with Mo has increased the phase's electron count from 14 to 15 electrons/T atom. As a consequence, the E_F now occurs above the pseudogap (Figure 4.2b). A $TiAl_3$-type $MoGa_3$ phase would thus be in excess of the structure's preferred electron count by 1 electron per atom.

The partial substitution of Ga with Cu offers an opportunity to remedy this electron excess, as Cu atoms have two fewer electrons than Ga ones. Indeed, moving from $MoGa_3$ to Mo_2CuGa_5 (very close to the experimental composition of $Mo_2Cu_{0.9}Ga_{5.1}$) restores the valence electron count to 14 electrons/T atom. Such is confirmed by a calculation on an ordered model of this phase (with Cu and Ga atoms placed

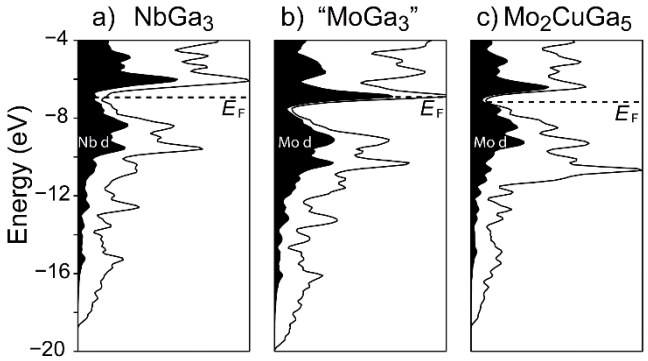

Figure 4.2. The DFT-calibrated Hückel DOS distributions of $TiAl_3$-type $NbGa_3$, a hypothetical $MoGa_3$ phase in the $TiAl_3$-type, and an ordered model of $Mo_2Cu_{0.9}Ga_{5.1}$. The DOS contributions from the Nb and Mo d-states are shaded in black. (See Figure B3 in the Supporting Information for GGA-DFT versions of these curves).

in a checker-board pattern in the z=0.5 layer). For this Mo_2CuGa_5 structure, the E_F lies once again in the DOS pseudogap (Figure 4.2c).

4.4.3. Localized Bonding Scheme from a Reversed Approximation Molecular Orbital Analysis

From this analysis, we see that restoring the valence electron count to 14 electrons/T atom appears to be important to the preference of this Mo-Cu-Ga phase for a $TiAl_3$-type structure. The favorability of this electron count for the $TiAl_3$ type has previously been rationalized with an innovative extension of Wade's rules to the Al sublattice, after which interactions with the T atoms are introduced (see section 3.4 for additional discussion).[19] In this section, we will see how focusing on the T sublattice instead can fold these compounds into a more general electron counting rule for intermetallics, the 18-*n* rule.

The basis of our analysis is the recently developed reversed approximation Molecular Orbital (raMO) approach,[21] which offers a way to directly connect local structural features to preferred electron counts. In this method, the occupied crystal orbitals of a compound are used as a basis set for constructing a local MO diagram for a portion of a structure. For T-E intermetallics, we have found that a powerful MO diagram for this purpose is the 9 bonding and nonbonding levels of an 18-electron transition metal complex, whose MOs are templated by the nine s, p, and d valence atomic orbitals of the T center. Such an MO diagram can be extracted from the wavefunctions of an intermetallic by using the valence atomic orbitals of one of its T atoms as target states, and using the raMO procedure to obtain the best orthogonal approximations to these states that can be constructed from linear combinations of the occupied crystal orbitals.

In Figure 4.3, we show the results of applying this method to $NbGa_3$, using the 4d, 5s, and 5p orbitals of a Nb atom as target eigenstates. In examining the resulting raMO orbitals, we see that for each Nb valence atomic orbital, a corresponding raMO function appears that is centered by that orbital. However, in each case the target orbital is accompanied by in-phase contributions on the surrounding atoms, which indicate the presence of bonding interactions.

Strong σ type interactions between the central Nb atom and its Ga neighbors are common to all of the raMOs. However, the balance in the functions between the Nb and Ga atoms (as is measured by the probability of finding a raMO's electrons on the target orbital, P_{target}) varies depending on whether the orbital is based on a Nb s, p, or d orbital. The low P_{target} values for the Nb s and p reconstructions suggest

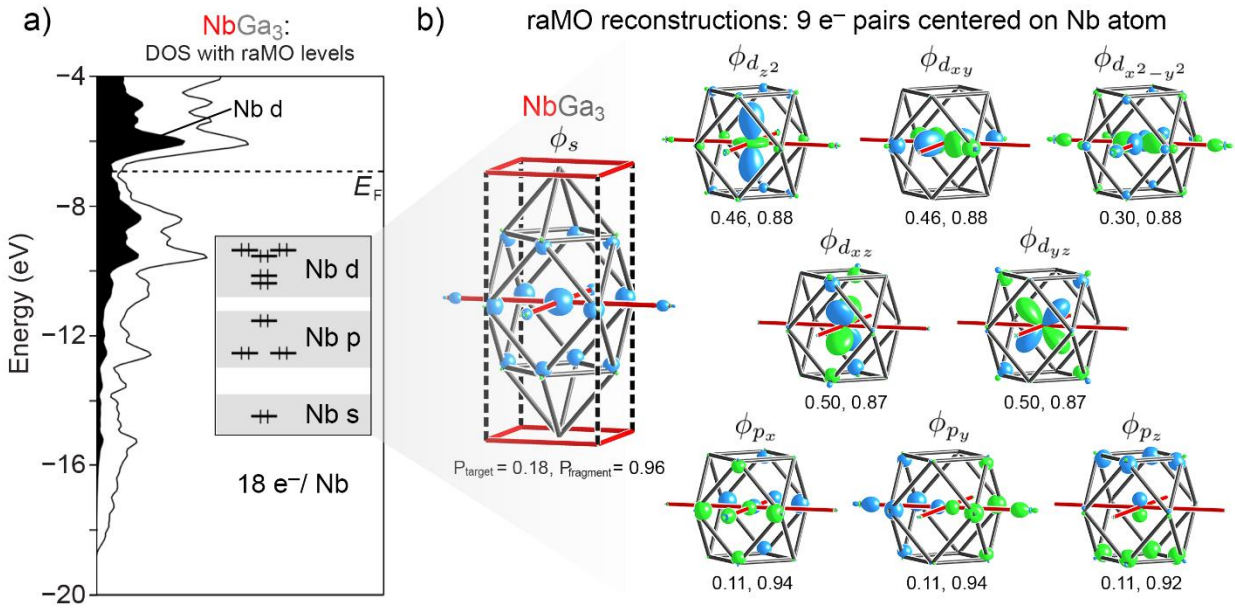

Figure 4.3. The raMO reconstructions of a single Nb atom's s, p, and d orbitals in $NbGa_3$. (a) Energies of the raMO levels drawn alongside the DOS distribution of the phase. (b) The raMO functions. σ contributions can be seen from the atoms Ga and Nb nearest neighbors. The quantities P_{target} and $P_{fragment}$ supply information about the degree of each raMO's localization, by giving the probability of finding a raMO's electrons in, respectively, the target orbital and the structural fragment displayed in the image.

their raMOs are heavily polarized toward the Ga neighbors. The values of P_{target} are notably higher for the Nb d orbitals (≈0.5), indicating that the probability of finding an electron on the Nb atom is larger for these functions. These results are in accord with the relative energies of the Nb s, p, and d: the Nb 4d orbitals being lower in energy contributes more to the Nb-Ga bonding states than the Nb 5s or 5p orbitals.

Some of the raMO functions also exhibit features that are less familiar to molecular chemistry. On the s-, p_x-, p_y-, and $d_{x^2-y^2}$- centered raMO reconstructions, significant in-phase σ-contributions from the neighboring Nb atoms are present (Figure 4.4a). The appearance of bonding overlap at these Nb-Nb contacts is rather unexpected as the Nb-Nb distance of 3.79 Å (in the GGA-DFT optimized structure) is far too long to be considered as a traditional through-space Nb-Nb bond. The appearance of such interactions, despite the long interatomic distances, is made more understandable by turning our attention to the orbital contributions from the Ga atoms around the Nb-Nb contacts. Each Nb-Nb contact is bridged by a square of Ga atoms (corresponding to one of the square faces of the Ga_{12} cuboctahedron of the Nb coordination environment), which provide *σ* bonding lobes to support the overlap between the Nb atoms.

The appearance of four bonding Nb-Nb functions for four Nb-Nb contacts around the central Nb atom suggests the possibility of obtaining more localized functions. In fact, the combination of s, p_x, p_y, and d_{x2-y2} orbitals are exactly the set of orbitals needed for the creation of sp^2d hybrid orbitals on a transition metal center for pointing to the vertices of a square planar complex.[2] In Figure 4.4b, we take the proper linear combinations of these raMOs to create such hybrids. Four localized functions result, each corresponding to a multicenter interaction isolobal to a standard Nb-Nb *σ* bond, and (as they are constructed from linear combinations of occupied functions) are populated by two electrons. The

appearance of such electron pairs at main group-bridged T-T contacts places the $TiAl_3$ type into a growing family of intermetallics that use this mechanism to achieve closed shell electron configurations (examples include $Fe_8Al_{17.4}Si_{7.6}$,[42] $Co_3Al_4Si_2$,[43] $Ca_{10}Pt_7Si_3$,[44] Ir_3Ge_7 type,[21] and the Nowotny chimney ladders[22]).

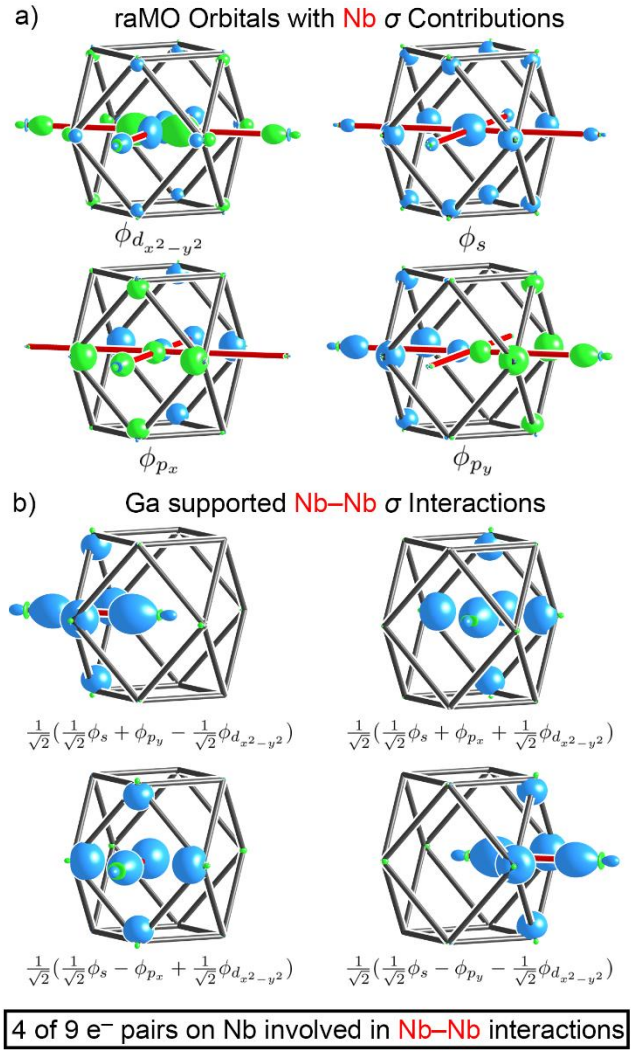

Figure 4.4. Covalently shared electron pairs along Nb-Nb contacts in $NbGa_3$. (a) raMO orbital reconstructions of raMOs exhibiting Nb-Nb bonding. (b) Localized linear combinations of the raMOs in (a) chosen to create the sp^2d hybrid functions on the Nb center.

As in these other phases, the T-T interactions in the $NbGa_3$ play a large role in determining its ideal electron count. Our raMO analysis indicates that there is an electron pair associated with each of the Nb valence orbitals, which suggests that the stability of the phase should be understandable from the point of view of filled 18-electron configurations on the Nb atoms.[45] However, the observed electron count is only 14 electrons/Nb atom, which is 4 electrons/Nb atom short of the number needed for independent Nb atoms. To solve this issue, each Nb atom shares electron pairs with four other Nb atoms. This is a specific instance of an *n*=4 case of the more general 18-*n* rule emerging for T-E intermetallics.

How would moving from $NbGa_3$ to $MoGa_3$, with its extra valence electron, affect this picture? To see this, it is helpful to focus in on one specific T-T σ bond, and examine how it is changed during this substitution. To do this we use a T-T σ bonding and antibonding pair of functions (Figure 4.5a) as target eigenstates for a new raMO analysis, and examine how the character and occupation of the resulting σ and σ* functions change on going from $NbGa_3$ to the hypothetical $MoGa_3$ and finally to Mo_2CuGa_5. In Figures 4.5b-d, we compare the resulting raMO functions for the three phases.

Starting as before with $NbGa_3$ (Figure 4.5b), the *σ* bonding orbital is reproduced very well, and brings in supporting character from the bridging Ga atoms. The *σ** contribution, however, shows only a minuscule amount of occupation (P_{target} = 0.05), and the minor features present on the Nb atoms are hybridized away from the Nb-Nb contact in question. By expanding the fragment of the structure displayed to include two more Nb atoms in the chain, we see that in attempting to reconstruct an antibonding function at the Nb-Nb contact, we in fact obtain an out-of-phase combination of bonding functions for the neighboring Nb-Nb contacts along the same chain.

As we move to the hypothetical $MoGa_3$ structure, the bonding picture changes (Figure 4.5c). The Mo-Mo σ raMO appears quite similar to that of $NbGa_3$, however the σ^* combination is now reproduced much better (P_{target} = 0.18), and exhibits less hybridization away from the T-T contact. Additionally, the stabilizing contribution from the neighboring Mo atoms has decreased relative to Nb, suggesting that the σ antibonding interaction has become more localized between the Mo atoms. In effect, the extra valence electron/T atom injected into the system upon replacing Nb with Mo has resulted in an increased population of T-T σ^* states, and thus an overall disruption of bonding between the T atoms.

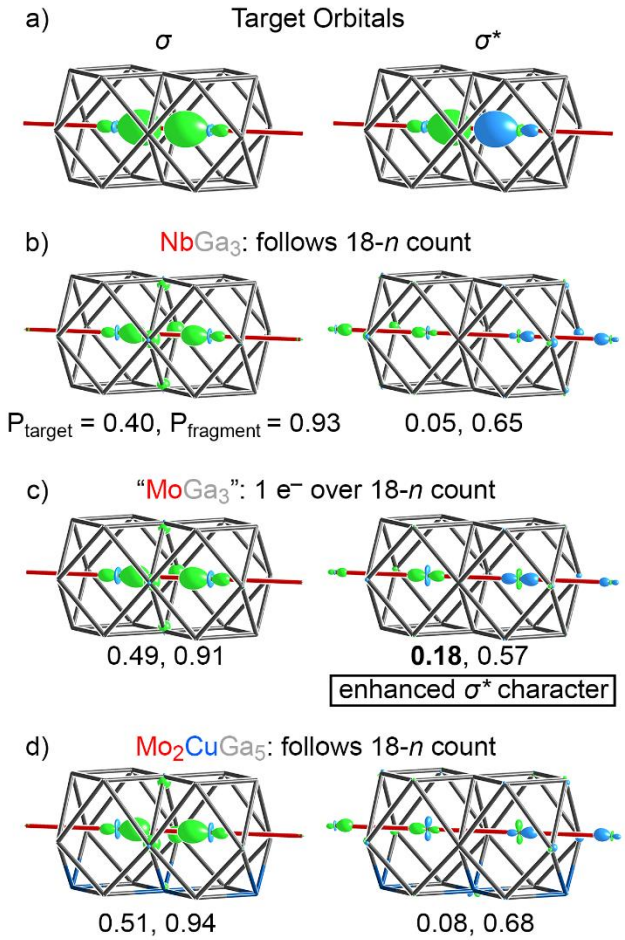

Figure 4.5. Reconstructions of σ and σ^* orbitals for a pair of T atoms in a series of structures based on the $TiAl_3$ type. raMO reconstructions of (a) the target eigenfunctions are shown for (b) $NbGa_3$, (c) a hypothetical $MoGa_3$ phase, and (d) Mo_2CuGa_5.

If adding electrons to the structure reduces the T-T bonding, removing these excess electrons should restore this bonding character. This is exactly what is observed in the raMO reconstructions of Mo_2CuGa_5 (Figure 4.5d). The T-T σ^* antibonding orbital is now once again poorly reproduced and the stabilizing contributions from the neighboring T atoms have regained the magnitude seen in the $NbGa_3$ raMOs. Our raMO analysis of Mo_2CuGa_5 thus confirms our earlier picture of filled 18-electron configurations on the T atoms of the $TiAl_3$-type arising from shared electron pairs in T-T bonds.

In this section, we have seen a simple picture develop for bonding in T-E $TiAl_3$-type phases, as summarized in Figure 4.6. On each T atom, 5 electron pairs (in 4 d orbitals and 1 p orbital) are involved in bonding between the T and its E coordination environment. The 4 additional electron pairs (in functions built from the remaining valence atomic orbitals: s, p_x, p_y, and d_{x2-y2}) are shared in E-supported T-T bonds, one through each of the square faces of the E cuboctahedron in the xy plane. The result is the filling of 18 electron configurations on the T atoms at an electron count of 14/T atom.

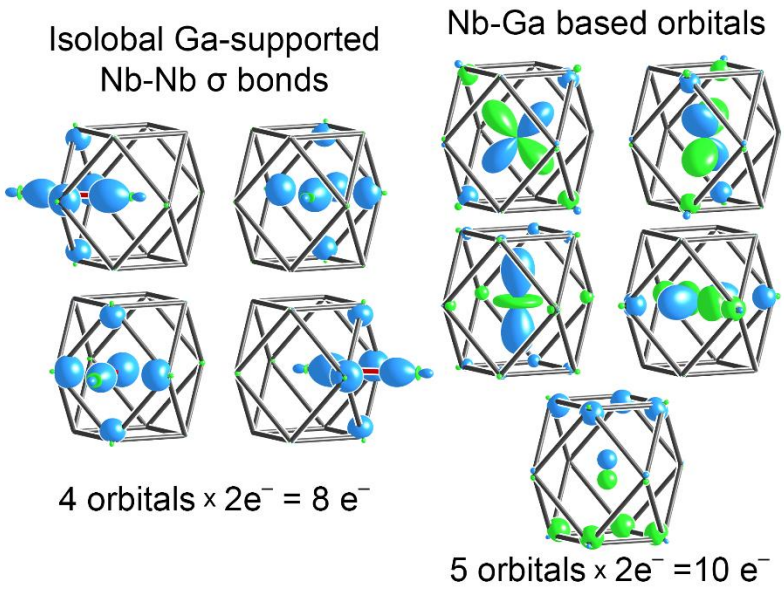

Figure 4.6. A summary of the electron counting scheme obtained for 14-electron $TiAl_3$-type phases, as exemplified by $NbGa_3$.

This prediction of 14 electrons/T atom as a magic electron count for T-E $TiAl_3$-type phases coincides well with the upper limit of the observed range of ca. 13 to 14 electrons/T. How should this scheme be modified for the lower end of the electron count range? Our preliminary calculations suggest that moving to lower electron counts depopulates functions with the nodal character of T-T π^* functions. The removal of electrons relative to the 14 electron count could then be partially accommodated through the creation of net T-T π bonding interactions to supplement the T-T σ interactions already in place.

4.4.4. Comparison to Previous Bonding Schemes Proposed for the $TiAl_3$ Structure Type

How does this bonding model derived from raMO analysis compare with the results of other theoretical studies of $TiAl_3$-type structures? A common feature of most earlier analyses of the $TiAl_3$ type is the prominent role of covalent interactions between the T and E atoms. [17,18,46,47] The raMO functions of Figures 4.3-4.6 confirm this conclusion, as each reconstruction of a T atomic orbital appears with substantial in-phase contributions from neighboring E atoms. This observation extends to the shared electron pairs along the T-T contacts, where the bridging E atoms play a key role in stabilizing the electron pairs.

Another point of comparison is how 14 electrons/T arises as the favorable electron count for the structure. Condron et al. provided a compelling explanation by conceptually building up the electronic structure through orbital considerations.[19] They began by demonstrating, through an extension of the Wade-Mingos rules, that the optimal electron count for the E-sublattice should be 10 electrons/formula unit. Next, they analyzed how the T valence orbitals would interact with the E-sublattice, finding that two d orbitals per T atom (d_{z^2} and $d_{x^2-y^2}$) are available for occupation. These T d orbitals provide room for

the remaining four electrons/formula unit, so that the preferred electron count becomes 14 electrons/T atom.

In our T-centric, raMO-based approach the involvement of the T atom orbitals is different: they serve as templates for the nodal properties of the wave functions, rather than interacting with pre-formed E-based states. Given that we arrive at the same electron count, one might wonder whether these approaches, in the end, reduce to the same overall chemical picture. An important difference can be seen in the role the T $d_{x^2-y^2}$ function plays in the two models. In the E-centered picture, the T $d_{x^2-y^2}$ orbitals each host two electrons, precluding the possibility of their being involved in T-T interactions. In the raMO-derived scheme, however, the T $d_{x^2-y^2}$ orbital appears as one of four T orbitals participating in the formation of the four T-T bonds around each T center. As such, the T $d_{x^2-y^2}$ functions would only be considered as having one rather than two electrons/T atom. In other words, the T-E and E-supported T-T interactions in these systems are sufficiently strong that a somewhat different electronic structure results than is derived assuming strong E-E interactions. As the raMO-based picture is derived from the occupied wave functions of $NbGa_3$ and Mo_2CuGa_5, it appears that its scheme is more representative of the bonding in these gallides.

4.5. Conclusions

In this Article, we have described a new phase, $Mo_2Cu_{0.9}Ga_{5.1}$, which serves as a clear counterexample to the electron gas bonding picture generally assumed for simple metallic lattices. This compound crystallizes in a colored fcc variant structure, in which the Mo atoms and Cu/Ga atoms are distributed to the Ti and Al-positions in a $TiAl_3$-type lattice. The Cu and Ga atoms are then further resolved among the

Al-type positions such that the Cu atoms partially substitute for Ga in half of the square nets of the structure. $Mo_2Cu_{0.9}Ga_{5.1}$ can thus be interpreted as a Cu substituted derivative of the $TiAl_3$-type $MoGa_3$ phase, a hypothetical Mo-analogue of the $TiAl_3$-type phase in the Nb-Ga system.

Through investigations into the bonding in $NbGa_3$ and $Mo_2Cu_{0.9}Ga_{5.1}$ we developed a simple picture for how Cu substitution stabilizes a $TiAl_3$-type phase not found in combinations of Mo and Ga on their own. DFT calculations revealed that these $TiAl_3$-based phases exhibit a pseudogap at the Fermi energy at 14 electrons per T atom. raMO analysis of these results using DFT-calibrated Hückel models traces this pseudogap to the filling of 18 electron configurations on the T atoms, which are achieved despite the electron count of 14 electrons/T atom, via multi-center interactions isolobal to four T-T σ bonds. While $MoGa_3$ in the $TiAl_3$ type deviate from this electron count with 15 electrons/Mo, the partial substitution of Ga with Cu lowers the valence electron concentration (VEC) back to 14, reuniting the E_F with the pseudogap. The $TiAl_3$ type can thus be placed on the growing list of structures whose preferred electron counts can be understood in terms of the 18-*n* rule, which includes 18 electron half Heusler compounds,[48,49] $Fe_8Al_{17.4}Si_{7.6}$,[42] $Co_3Al_4Si_2$,[43] the Ir_3Ge_7 type,[21] and the Nowotny chimney ladders.[22]

A second lesson offered by $Mo_2Cu_{0.9}Ga_{5.1}$ concerns the competition between simple and complex crystal structures in intermetallics. The Ga-rich part of the Mo-Ga phase diagram contains phases with relatively large unit cells, hinting at host-guest relationships. No simple binary structure seems to be available as a more stable alternative. However, the addition of a third element, Cu, serves to enhance the stability of one of these nominally binary structure types by offering extra flexibility to alleviate an unfavorable VEC. Examples of this effect in $TiAl_3$-type aluminides are prevalent: Mo_2CuAl_5,[50] W_2CuAl_5,[51]

$ZrAl_2Si$,[52] and $MoCo_{0.28}Al_{2.72}$[53] are all described as adopting this structure type,[54] whereas the TAl_3 unsubstituted binaries either crystallize in more complex structures[9,55] or do not form.[56]

A parallel story involving sterics was encountered for the phases $Ca_2Cu_2Cd_9$ and Ca_5Cu_2Cd in our earlier exploration of the Ca-Cu-Cd system.[57] These structures are based off of binary structure types not found in any of the binary subsystems of the Ca-Cu-Cd ternary systems – a trend we connected to atomic packing issues. The addition of a third element expanded the palette of available atomic sizes, allowing the packing issues to be resolved. We are looking forward to exploring how other plausible but unobserved binary structures may be stabilized through the addition of some amount of a third element suggested by the theoretical evaluation of the factors limiting their stability. Promising systems for these investigations are binary systems exhibiting only complex structures, where significant bonding issues with simple alternative structures would be easiest to detect.

4.6. Acknowledgments

We thank Dr. John Fournelle for assistance with SEM-EDS measurements. We also gratefully acknowledge financial support from the National Science Foundation (NSF) through Grant DMR-1207409. B.J.K. thanks the NSF for a graduate student fellowship (Grant DGE-1256259). This research involved calculations using computer resources supported by NSF Grant CHE-0840494.

4.7 References

(1) Pauling, L. *Proc. R. Soc. London, Ser. A* **1949**, *196*, 343-362.

(2) Pauling, L. *The Nature of the Chemical Bond*; 3rd ed.; Cornell University Press: Ithaca, New York, 1995.

(3) Anderson, W. P.; Burdett, J. K.; Czech, P. T. *J. Am. Chem. Soc.* **1994**, *116*, 8808-8809.

(4) Berger, R. F.; Walters, P. L.; Lee, S.; Hoffmann, R. *Chem. Rev.* **2011**, *111*, 4522-4545.

(5) Mott, N. F.; Jones, H. *The Theory and Properties of Metals and Alloys*; Oxford University Press: Oxford, England, 1936.

(6) Ashcroft, N. W.; Mermin, N. D. *Solid State Physics*; 1st ed.; Holt, Rinehart and Winston: New York, N. Y., 1976.

(7) Pettifor, D. G. *Bonding and Structure of Molecules and Solids*; 1st ed.; Oxford University Press: New York, NY, 1995.

(8) Andruchiv, L. S.; Lysenko, L. O.; Yarmolyuk, Y. P.; Gladyshevskii, E. I. *Dopov. Akad. Nauk Ukr. RSR* **1975**, *A*, 645-648.

(9) Brauer, G. *Z. Anorg. Allg. Chem.* **1939**, *242*, 1-22.

(10) Yvon, K. *Acta Crystallogr., Sect. B* **1975**, *31*, 117-120.

(11) Girgis, K.; Petter, W.; Pupp, G. *Acta Crystallogr., Sect. B* **1975**, *31*, 113-116.

(12) Häussermann, U.; Viklund, P.; Svensson, C.; Eriksson, S.; Berastegui, P.; Lidin, S. *Angew. Chem. Int. Ed.* **1999**, *38*, 488-492.

(13) Yvon, K. *Acta Crystallogr., Sect. B* **1974**, *30*, 853-861.

(14) Wołcyrz, M.; Andruszkiewicz, R.; Łukaszewicz, K. *Acta Crystallogr., Sect. C* **1989**, *45*, 991-993.

(15) Lux, R.; Kuntze, V.; Hillebrecht, H. *Solid State Sciences* **2012**, *14*, 1445-1453.

(16) Xu, J.-h.; Freeman, A. J. *Physical Review B* **1989**, *40*, 11927-11930.

(17) Hong, T.; Watson-Yang, T. J.; Freeman, A. J.; Oguchi, T.; Xu, J.-h. *Physical Review B* **1990**, *41*, 12462-12467.

(18) Xu, J.-h.; Freeman, A. J. *J. Mater. Res.* **1991**, *6*, 1188-1199.

(19) Condron, C. L.; Miller, G. J.; Strand, J. D.; Bud'ko, S. L.; Canfield, P. C. *Inorg. Chem.* **2003**, *42*, 8371-8376.

(20) Lue, C. S.; Su, T. H.; Xie, B. X.; Cheng, C. *Phys. Rev. B* **2006**, *74*, 094101.

(21) Yannello, V. J.; Kilduff, B. J.; Fredrickson, D. C. *Inorg. Chem.* **2014**, *53*, 2730-2741.

(22) Yannello, V. J.; Fredrickson, D. C. *Inorg. Chem.* **2014**, *53*, 10627-10631.

(23) Oszlányi, G.; Sütő, A. *Acta Crystallogr A* **2004**, *60*, 134-141.

(24) Oszlányi, G.; Sütő, A. *Acta Crystallogr A* **2005**, *61*, 147-152.

(25) Palatinus, L.; Chapuis, G. *J. Appl. Crystallogr.* **2007**, *40*, 786-790.

(26) Petříček, V.; Dušek, M.; Palatinus, L. *Z. Kristallogr.* **2014**, *229*, 345-352.

(27) Holland, T. J. B.; Redfern, S. A. T. *Mineral Mag* **1997**, *61*, 65-77.

(28) Clark, R. C.; Reid, J. S. *Acta Crystallogr. Sect. A: Found. Crystallogr.* **1995**, *51*, 887-897.

(29) Kresse, G.; Furthmüller, J. *Phys. Rev. B: Condens. Matter* **1996**, *54*, 11169-11186.

(30) Kresse, G.; Furthmüller, J. *Comput. Mater. Sci.* **1996**, *6*, 15-50.

(31) Vanderbilt, D. *Physical Review B* **1990**, *41*, 7892-7895.

(32) Stacey, T. E.; Fredrickson, D. C. *Dalton Trans* **2012**, *41*, 7801-7813.

(33) Landrum, G. A.; Glassey, W. V. YAeHMOP: Yet Another extended Huckel Molecular Orbital Package. YAeHMOP is freely available at http://sourceforge.net/projects/yaehmop/. Last accessed: June 11, 2015.

(34) Wallbaum, H. J. *Zeitschrift fuer Metallkunde* **1942**, *34*, 118-119.

(35) Poetzschke, M.; Schubert, K. *Zeitschrift fuer Metallkunde* **1962**, *53*, 474-488.

(36) Poetzschke, M.; Schubert, K. *Zeitschrift fuer Metallkunde* **1962**, *53*, 548-560.

(37) Meissner, H. G.; Schubert, K. *Zeitschrift fuer Metallkunde* **1965**, *56*, 475-484.

(38) Brewer, L.; Lamoreaux, R. H., Mo-Ga Phase Diagram, ASM Phase Diagrams Database, Villars, P., editor-in-chief; Okamoto, H., Cenzual, K., section editors, ASM International: Materials Park, OH, 2006. Last accessed: July 8, 2015.

(39) Bergerhoff, G.; Hundt, R.; Sievers, R.; Brown, I. D. *J. Chem. Inf. Comput. Sci.* **1983**, *23*, 66-69.

(40) Bergerhoff, G.; Brown, I. D. In *Crystallographic Databases*; Allen, F. H., Bergerhoff, Sievers, R., Eds.; International Union of Crystallography: Chester, 1987, p 77-95.

(41) Belsky, A.; Hellenbrandt, M.; Karen, V. L.; Luksch, P. *Acta Crystallogr. B* **2002**, *58*, 364-369.

(42) Fredrickson, R. T.; Fredrickson, D. C. *Inorg. Chem.* **2012**, *51*, 10341-10349.

(43) Fredrickson, R. T.; Fredrickson, D. C. *Inorg. Chem.* **2013**, *52*, 3178-3189.

(44) Fredrickson, D. C.; Doverbratt, I.; Ponou, S.; Lidin, S. *Crystals* **2013**, *3*, 504-516.

(45) Based on the square planar hybridization we have evoked for the Nb center, one might wonder if a 16 electron count (as observed for molecular d8 complexes) might be more appropriate. In those molecular square planar clusters, the out-of-plane T p-orbital remains unfilled due as no bonding interactions occur to offset its high energy. In the case of NbGa3, this p orbital is heavily involved in bonding with the Ga atoms in the planes above and below, as is evident from its raMO function in Figure 4.3.

(46) Lue, C. S.; Su, T. H.; Xie, B. X.; Cheng, C. *Physical Review B* **2006**, *74*.

(47) Kavich, I. V.; Shcherba, I. D. *Metallofizika (Kiev)* **1981**, *3*, 38-42.

(48) Jung, D.; Koo, H. J.; Whangbo, M. H. *J. Mol. Struct.-Theochem.* **2000**, *527*, 113-119.

(49) Kandpal, H. C.; Felser, C.; Seshadri, R. *J. Phys. D: Appl. Phys.* **2006**, *39*, 776-785.

(50) Prevarskii, A. P.; Kuz'ma, Y. B.; Onyshkevich, M. M. *Izvestiya Akademii Nauk SSSR, Metally* **1977**, *4*, 201-203.

(51) Prevarskii, A. P.; Kuz'ma, Y. B. *Izvestiya Akademii Nauk SSSR, Metally* **1983**, *5*, 225-226.

(52) Schob, O.; Nowotny, H. N.; Benesovsky, F. *Monatshefte fuer Chemie* **1961**, *92*, 1218-1226.

(53) Burnasheva, V. V.; Starodub, P. K.; Stroganov, G. B. *Izvestiya Akademii Nauk SSSR, Metally* **1977**, *5*, 235-236.

(54) The structures of these compounds appear to have been assigned from powder X-ray diffraction data, where the superstructures similar to the one we have found for $Mo_2Cu_{0.9}Ga_{5.1}$ would be difficult to detect.

(55) Schuster, J. C.; Ipser, H. *Metall. Trans. A* **1991**, *22*, 1729-1736.

(56) Okamoto, H., Al-W Phase Diagram, ASM Phase Diagrams Database, Villars, P., editor-in-chief; Okamoto, H., Cenzual, K., section editors, ASM International: Materials Park, OH, 2006. Last accessed: July 8, 2015.

(57) Harris, N. A.; Hadler, A. B.; Fredrickson, D. C. *Z. Anorg. Allg. Chem.* **2011**, *637*, 1961-1974.

Chapter 5

Chemical Pressure-Driven Incommensurability in $CaPd_5$: Clues to High Pressure Chemistry Offered by Complex Intermetallics

This chapter has been submitted for publication: Kilduff, B. J.; Fredrickson, D. C. *Inorg. Chem.*

5.1. Abstract

Composition and pressure are two of the key factors that can be controlled during the synthesis and optimization of solid state materials. While they are generally considered to be orthogonal parameters, their distinctness is blurred by the concept of chemical pressure (CP), in which the packing constraints of a crystal structure lead to local pressures acting on its atoms in the absence of an externally applied force. In this Article, we describe the first cycle of an iterative theoretical/experimental investigation into this connection. We begin by using DFT calculations to probe the ability of physical pressure to promote structural transitions in experimentally observed $CaCu_5$-type phases that are driven by CP in other systems at ambient pressure. Our results point to the instability of the reported $CaCu_5$-type $CaPd_5$ phase to such a transition even at ambient pressure, suggesting that new structural chemistry in this system should be obtainable with the application of only modest pressures. Next, we present our attempts to synthesize $CaPd_5$ as a starting material for such high-pressure experiments. Rather than obtaining the expected $CaCu_5$-type phase reported in the literature, we encountered crystals of an incommensurately

modulated variant $CaPd_{5+q/2}$, whose composition is related to its satellite spacing, $\mathbf{q} = q\,\mathbf{b}_{basic}^*$ with $q \approx 0.44$. The structure of this phase was solved and refined in the (3 + 1)D superspace group *Cmcm(0β0)s00*, revealing slabs of the $CaCu_5$ type that are separated by distorted Pd hexagonal nets whose periodicity is incommensurate with original $CaCu_5$-type slabs. DFT-CP analysis on a commensurate model for $CaPd_{5+q/2}$ indicates that the new Pd nets serve to relieve intense negative CPs that the Ca atoms would experience in a $CaCu_5$-type $CaPd_5$ phase, but suffer from a desire to contract relative to the rest of the structure. In this way, both the Pd layer substitution and incommensurability in $CaPd_{5+q/2}$ are anticipated by the CP schemes of simpler model systems, with CP quadrupoles tracing the paths of the favorable atomic motions. The applicability of this approach to materials design is evident in the predictions it makes for how elemental substitution and physical pressure should affect the driving forces for these structural motifs, as might be readily implemented in the exploration of structure-properties relationships in the magnetic phase Zr_2Co_{11}, the previously proposed structural models for which show close parallels to the $CaPd_{5+q/2}$ structure.

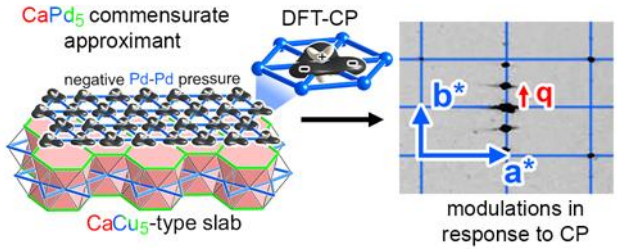

Figure 5.0. We describe the first cycle of an iterative theoretical/experimental investigation into the connection between physical and chemical pressure. Following theoretical calculations suggesting that the $CaCu_5$-type phase $CaPd_5$ should become increasingly susceptible to structural transitions under applied pressures, we set out to synthesize it as a starting material for high pressure experiments. Rather than obtaining the expected $CaCu_5$-type compound, however, we encountered an incommensurately modulated phase whose structural features are anticipated by chemical pressure analysis.

5.2. Introduction

Pressure is an intriguing concept that spans many length scales: just like temperature, it is considered to be a macroscopic physical property of a system that reduces, at the microscopic level, to forces acting between atoms or molecules. And just as we can contemplate the temperature of a single molecule,[1-3] we can consider what pressures an individual atom might experience due to its interactions with its surroundings. This notion of *chemical pressure* (CP) has a long history in discussions of how elemental substitutions influence the physical properties of a material by imparting local strain.[4-14] More recently, this concept has been extended, through the DFT-CP method, to the rationalization of a diverse range of structural phenomena in metallic materials, including the formation of interfaces[15-17] and icosahedral clusters familiar from the structures of quasicrystals.[18-20] These examples illustrate how chemical pressure can provide an intuitive framework for understanding experimental observations. In this Article, we describe how it can also guide experiments with the discovery of incommensurate modulations in the structure of $CaPd_5$.

$CaPd_5$ has played a fundamental role in the development of the concept of structural chemistry driven by CP release. Its simple $CaCu_5$-type structure[21] (Figure 5.1) provides a reference through which the more complicated crystal structures of the Ca-Ag[22] and Ca-Cd[23,24] systems can be interpreted. Its CP scheme exhibits large negative pressures in the spaces above and below the Ca atoms along the high-symmetry axis of the structure (black lobes in Figure 5.1b), indicating that the Ca-Pd contacts along this direction are overly extended. The contraction of the structure to relieve these pressures, however, is prevented by positive pressures elsewhere (white lobes) due to overly short contacts. The overall outcome

is that the Ca atoms appear as two small for their coordination environments in the structure, an issue that would be exacerbated by the replacement of Pd atoms with larger transition metal atoms.

The complex structures of Ca_2Ag_7,[25,26] $Ca_{14}Cd_{51}$,[27] and $CaCd_6$[28,29] can all be understood along these lines. If Ca-Ag or Ca-Cd $CaCu_5$-type phases were to form, the Ca atoms would again experience intense negative pressures as they attempt to fill the overly-large coordination environments provided by the Cd or Ag sublattices. As is shown for one example in Figure 5.2, the observed structures relieve the negative pressures on the Ca through the incorporation of interfaces (Ca_2Ag_7 and $Ca_{14}Cd_{51}$) or disclination defects to create the building blocks of Tsai-type quasicrystals ($CaCd_6$).[15,16,18,20]

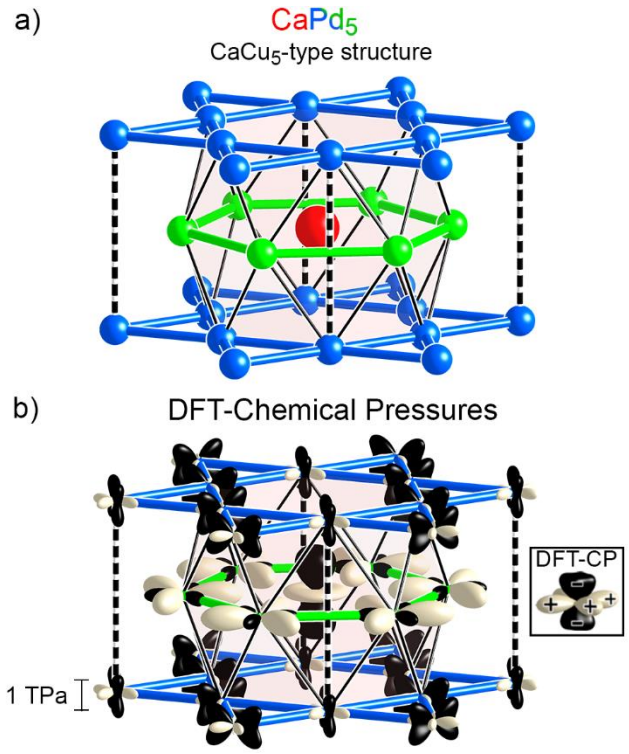

Figure 5.1. The chemical pressure (CP) scheme of $CaPd_5$ in the $CaCu_5$ structure type. (a) The structure can be described as a layering of kagome (blue) and Ca-stuffed honeycomb (green) nets of Pd atoms. (b) CP anisotropy surfaces of the phase, where the sums of the local pressures experienced by each atom are projected onto low-order spherical harmonics. White lobes represent directions along which expansion would be favorable (positive pressure), whereas black lobes represent directions where the contacts are too elongated (negative pressure).

After observing these mechanisms of CP relief in the Ca-Ag and Ca-Cd systems, we began to wonder if similar structural transformations could be induced in the Ca-Pd system. One approach would be to use elemental substitution on the Pd sites to start to stretch the Pd-sublattice relative to the Ca atoms. Another would be to pursue the analogy between chemical and physical pressures, and consider how the application of physical pressure might influence the driving force for collapsing the void spaces around the Ca atoms in the $CaCu_5$ type. Indeed, the presence of the interstitial spaces highlighted by negative features in the CP scheme is highly suggestive of an inefficient atomic packing, which should become increasingly unfavorable under applied pressure.

As we will see below, DFT calculations suggest that physical pressure could indeed drive transitions in $CaPd_5$ similar to those underlying the structures in the Ca-Ag or Ca-Cd system. In fact, the reaction $2CaPd_5 \rightarrow Ca_2Pd_7 + 3Pd$ was calculated to be favorable even at ambient pressure. With this encouragement, we set out to synthesize $CaPd_5$ as the starting material in a high pressure study. In the following sections, we will describe the unexpected results of this seemingly straightforward synthesis, in which an incommensurately modulated variant of $CaPd_5$ emerged. Through the solution and refinement of the incommensurately modulated structure using (3+1)D superspace methods, geometrical details will be revealed that align closely with the expectations derived from the CP scheme of the $CaCu_5$ type, with close similarities to structural models proposed from TEM studies and computational work on Zr_2Co_{11}, a phase of interest for applications as a lanthanide-free permanent magnet.[30-33] The resulting structure highlights both the potential of CP analysis as a guide in materials synthesis, and demonstrates a driving force for the formation of incommensurate modulations in intermetallic phases

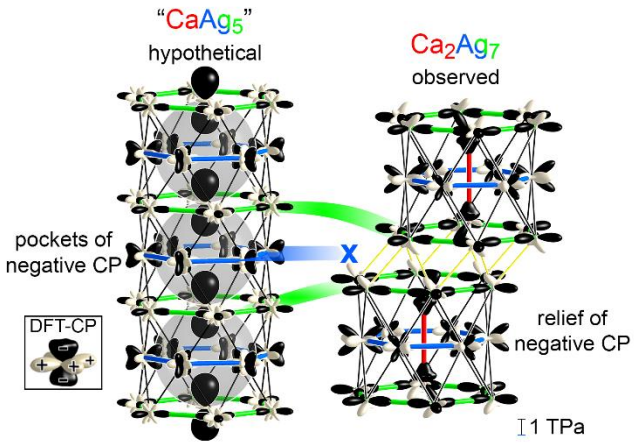

Figure 5.2. Ca_2Ag_7 (Yb_2Ag_7 type) viewed as the product of a chemical pressure (CP)-driven transition away from a hypothetical $CaCu_5$-type $CaAg_5$ phase. The pockets of large negative pressure in the $CaAg_5$ structure (gray spheres) indicate the structure has relatively open atomic packing (compared to other metallic structures), in which space is inefficiently used. The Ca_2Ag_7 structure uses layer deletion and shifts between $CaCu_5$-type slabs to create a more efficient packing, with the large negative CPs of the $CaCu_5$ type being significantly reduced.

5.3. Experimental Section

5.3.1. Synthesis

Samples of $CaPd_{5+x}$ ($x \approx 0.22$) were prepared by loading Ca granules (Alfa Aesar, 99.5%) and Pd powder (filed from a Pd coin) in a 1:5 ratio into a Nb tube in an Ar filled glove box. The Nb tube was arc-sealed under Ar, placed on its side in a vacuum furnace (~10^{-5} torr), heated to 1600°C over 160 min, held at 1600°C for 12 hours, and cooled to room temperature over 320 minutes. The Nb tube was removed from the vacuum furnace, sealed in an evacuated fused silica tube (~100 mtorr), placed in a muffle furnace, heated to 900°C over 4.5 hours, annealed for 3 weeks, and subsequently cooled quickly by quenching in ice water. The Nb tube was opened and large (~250 μm) malleable crystals were harvested from the sides of the Nb tube. Small amounts of a metal, most likely excess Ca, could be seen to oxidize over time when the sample was exposed to air.

5.3.2. Single Crystal X-Ray Diffraction Analysis

Single crystal X-ray diffraction data were collected on an Oxford Diffraction Xcalibur E diffractometer using graphite-monochromatized Mo Kα radiation (λ=0.71069 Å) at ambient temperature. Run list optimization and processing of the frame data were performed using the CrysAlis Pro ver. 171.36.28 software supplied by the manufacturer. The structure was solved with the charge flipping algorithm[34,35] using the program SUPERFLIP.[36] The solution was refined on F^2 with JANA2006.[37] The structural models and electron density isosurfaces were examined using the Diamond 3[38] and VESTA[39,40] programs, respectively. Selected crystal data are given in Table 5.1, while the development and refinement of the model is described in Section 5.4, and the refined structural parameters are listed in the Supporting Information.

5.3.3. Powder X-Ray Diffraction Analysis

The sample was ground using an agate mortar and pestle. However, due to the malleable nature of the crystals only a coarse powder could be obtained. The sample was mounted onto a zero-background diffraction plate and diffraction intensities were collected on a Bruker D8 Advanced Powder Diffractometer using Cu Kα radiation (λ = 1.5418 Å) at room temperature using a LYNXEYE detector with an exposure time of 0.7s per 0.01° over a 2θ range between 15° and 90°. The diffraction pattern was analyzed using Match! version 2.4.7, and is presented and discussed in the Supporting Information.

Table 5.1. Crystallographic Information for $CaPd_{5.219}$

Chemical Formula	$CaPd_{5.219}$
EDS Composition	$Ca_{1.00(3)}Pd_{5.48(5)}$
(3+1)D Superspace Group	*Cmcm(0ß0)s00*
a (Å)	5.1604(11)
b (Å)	9.1488(18)
c (Å)	17.745(3)
q-vector	0.4398(2) $\mathbf{b}_{\mathbf{basic}}^*$
cell volume (Å^3), Z	837.8(3), 8
crystal dimensions (mm^3)	0.02 × 0.02 × 0.09
crystal color, shape	metallic gray, needle
data collection temp.	RT
radiation source, λ (Å)	Mo, K*a* (0.71069)
absorption coefficient (mm^{-1})	22.965
absorption correction	multiscan
θ_{min}, θ_{max}	4.497, 27.057
refinement method	F^2
$R_{int}[I > 3\sigma(I)]$, R_{int}(all)	2.40, 3.09
statistics for main reflections	
unique ref. $[I > 3\sigma(I)$, all]	428, 525
$R[I > 3\sigma(I)]$, $R_w[I > 3\sigma(I)]$	2.45, 6.73
R(all), R_w(all)	2.98, 6.97
statistics for satellites, $m = 1$	
unique ref. $[I > 3\sigma(I)$, all]	423, 829
$R[I > 3\sigma(I)]$, $R_w[I > 3\sigma(I)]$	3.65, 7.62
R(all), R_w(all)	8.01, 9.79
statistics for satellites, $m = 2$	
unique ref. $[I > 3\sigma(I)$, all]	162, 1031
$R[I > 3\sigma(I)]$, $R_w[I > 3\sigma(I)]$	3.71, 7.70
R(all), R_w(all)	20.39, 13.95
statistics for satellites, $m = 3$	
unique ref. $[I > 3\sigma(I)$, all]	83, 821
$R[I > 3\sigma(I)]$, $R_w[I > 3\sigma(I)]$	4.49, 10.56
R(all), R_w(all)	34.12, 21.04
overall refinement	

number of reflections	17521
number of parameters	102
unique ref. [$I > 3\sigma(I)$, all]	1096, 3206
R[$I > 3\sigma(I)$], R_w[$I > 3\sigma(I)$]	2.94, 7.21
R(all), R_w(all)	8.32 9.50
S[$I > 3\sigma(I)$], S(all)	1.75, 1.28
$\Delta\rho_{max}$, $\Delta\rho_{min}$ ($e^-/Å^3$)	2.97, -2.84

5.3.4. Energy Dispersive X-Ray Spectroscopy

Samples were prepared for elemental analysis with energy dispersive X-ray spectroscopy (EDS) by suspending fragments of the reaction products in nonconductive epoxy in a hollow Al bullet. Once the epoxy had hardened, the surface was polished with diamond lapping film (down to a 0.5 μm grit) until cross sections of the crystals were visible under a light microscope. The samples were then sonicated for ~60 s in isopropanol to remove any surface contamination from polishing, allowed to dry in air, and then coated by evaporation with a 200 Å thick layer of carbon to avoid charging in an electron beam. The $CaPd_{5+x}$ crystals were examined with a Hitachi S-3100N scanning electron microscope equipped with an EDS probe (voltage = 15 kV). Back-scattered electron images, collected to detect areas of different compositions, appeared homogeneous, suggesting that only one phase is present. The average composition (excluding carbon) was determined to be $Ca_{1.00(3)}Pd_{5.48(5)}$ by measuring the Ca Kα- and Pd L-shell emission lines of 27 points. No emission lines corresponding to other elements were observed.

5.3.5. Electronic Structure Investigations into the Stability of $CaCu_5$-type Phases under Pressure

The pressure-dependence of the T=0 K reaction enthalpy for the $CaCu_5$-type phases into Ca_2Ag_7-type superstructures (with an elemental transition metal side product) was explored with GGA-DFT

calculations using the Vienna Ab initio Simulation Package (VASP).[41,42] VASP was used to geometrically optimize each structure and then single point total energy calculations were performed for the equilibrium volume for each phase involved in the reactions $2CaCu_5 \rightarrow Ca_2Cu_7 + 3Cu$ and $2CaPd_5 \rightarrow Ca_2Pd_7 + 3Pd$. The cell volumes ($V_{cell}$'s) were then expanded and contracted at intervals of 0.5%, the ion positions and cell dimension were re-optimized at a constant volume, and single point energy calculations were performed. All VASP calculations were performed in the high-precision mode using the projector augmented wave (PAW) potentials[43,44] provided with the package and the generalized gradient approximation (GGA) for the exchange correlation functional, as formulated by Perdew and Wang.[45] Additional details regarding the energy cut offs and k-point grids used can be found in the Supporting Information.

Parameters for the Rose-Vinet equation of state[46] for each phase were then fit against the GGA-DFT total energies with the program Phonopy,[47] utilizing the quasi-harmonic approximation. With these parameters, the energy and applied physical pressure experienced by each structure could be calculated at any given volume, however only volumes lying with the range examined with VASP calculations were used. The pressure-dependence of the reaction enthalpies were then calculated using these functions. Comparisons of the DFT total energies to the best-fit $E(V_{cell})$ equations, and the resulting Vinet parameters are given in the Supporting Information.

5.3.6. Determination of Atomic Charges and Free Ion Electron Density Profiles

For the evaluation of the chemical pressure (CP) schemes of the Ca-Cu and Ca-Pd phases discussed in this Article, one input parameter is the atomic charges on the atomic sites. To determine the appropriate charge of ions, Bader charge analysis[48] was performed with the Bader program using the equilibrium-

volume electron densities from the VASP calculations.[49-51] This information is used in the CP analysis by defining the shape of the free atom/ion radial electron density profiles used in the core unwarping and contact volume determination procedures. After determining the Bader charge for each atomic site, radial electron density profiles were generated using the Atomic Pseudopotential Engine (APE)[52] with the ionic charge varied from 0 to the full Bader charges. Following earlier considerations[53] we explored the dependence of the CP schemes on the ionicity values, and found little sensitivity to this parameter. The results presented in the main text were calculated with the ionicity set to 50% of the Bader charges; additional results are presented in the Supporting Information.

5.3.7. DFT-Chemical Pressure Calculations

DFT-chemical pressure analyses were performed on the $CaCu_5$-type and Yb_2Ag_7-type Ca-Cu and Ca-Pd phases, as well as a commensurate approximant of the observed $CaPd_{5+x}$ structure. The input for the calculation of the CP schemes was the output from LDA-DFT calculations performed with the ABINIT program.[54,55] ABINIT was first used to geometrically optimize the structures, and then single point calculations performed on each phase to obtain the local components of the Kohn-Sham potential, the kinetic energy density, and the electron density for the equilibrium structure, as well as slightly expanded and contracted cells (total volume range≈3.0%). The ABINIT calculations utilized the norm-conserving semicore pseudopotentials of Hartwigsen, Goedecker, and Hutter[56] along with the LDA XC functional of Goedecker, Teter, and Hutter.[57] Further details, including the energy cutoffs and k-point grids used, are given as Supporting Information.

The chemical pressure maps were calculated from the ABINIT output using the CPmap module of our group's Chemical Pressure package, employing the core unwarping procedure.[58] Integration and projection of the CP map were carried out with the binary Hirshfeld-inspired scheme using the CPintegrate module. The pressures surrounding each atom were projected onto real spherical harmonics with $l \leq 5$. The CP schemes were visualized with Figuretool, an in-house Matlab application.

5.4. Stability of the $CaCu_5$-type under Pressure

Our earlier theoretical studies of the $CaCu_5$ type revealed dramatic negative chemical pressures (CPs) surrounding the Ca sites, as is represented with black lobes pointing up and down from the Ca atom in Figure 5.1b. This tension makes the structure susceptible to structural transformations away from this simple arrangement of atoms, as is manifested in the structures of Ca_2Ag_7,[25,26] $Ca_{14}Cd_{51}$,[27] $CaCd_6$,[28,29] and the icosahedral quasicrystal $CaCd_{5.7}$.[59] For other related systems, such as Ca-Pd,[21] Ca-Cu,[60] and Ca-Zn,[61] $CaCu_5$-type phases have been reported without such structural rearrangements. In these cases, the same driving forces are present but are apparently overcome by competing factors. In this section, we will consider how physical pressure could be used to enhance the role that CP plays in these structures.

We begin by noting that the presence of large negative CPs is a sign of inefficient atomic packing: for such concentrations of negative CP to form, open spaces must be made in the structure by the concentration of positive pressures elsewhere. Taken to the extreme, this construction would lead to highly porous structures or open frameworks. The structural transformations, such as the formation of Ca_2Ag_7 from the hypothetical $CaCu_5$-type $CaAg_5$ phase, serve to eliminate these voids so that negative and positive CPs are more uniformly distributed in a more efficient atomic packing.

There are parallels to physical pressure-induced phase transitions here. In both instances, the system reacts to an energetic penalty for inefficient atomic packing. In the case of CP-induced transitions, the energetic cost is due solely to the inability for the structure to optimize all the atomic contacts simultaneously within the confines of a simple structure, with more complex structures providing more freedom. In a high pressure experiment, the penalty has a more explicit form: at elevated pressures the positive PV term of system's free energy grows in importance, leading to denser packings being increasingly favored. In structures with strong negative CP regions, such as the $CaCu_5$ type, the application of pressure should thus enhance the driving force for structural transitions to squeeze out these regions.

These considerations can be given a more concrete form by considering a specific structural progression. For example, the void spaces present in $CaCu_5$ could be relieved by the phase undergoing the decomposition reaction $2CaCu_5 \rightarrow Ca_2Cu_7 + 3Cu$, with Ca_2Cu_7 being the Cu-analog of the CP-driven Ca_2Ag_7 phase (see the CP schemes of Figure 5.3a). At ambient pressure, however, this transition is unfavorable (by more than 60 meV/atom) , which seems in part to result from positive Cu-Cu CPs that would arise at the interfaces between $CaCu_5$-type slabs in a Ca_2Cu_7 phase.

However, the application of physical pressure provides a means of overcoming the Cu-Cu repulsion that inhibits the transition. The negative CPs in Ca_2Cu_7 are much more evenly distributed through the structure than in $CaCu_5$, indicating that space is being filled more efficiently. The resulting higher density of Ca_2Cu_7 (+ an elemental Cu side product) compared to $CaCu_5$ should then lead to its stability being enhanced at high pressures. Indeed, as the pressure is increased, the ΔH_{rxn} begins to steadily drop, until it crosses zero at 113 GPa, a pressure routinely obtainable in diamond anvil cells.[62] At higher pressures, the decomposition of $CaCu_5$ into Ca_2Cu_7 + Cu metal is predicted to be favorable.

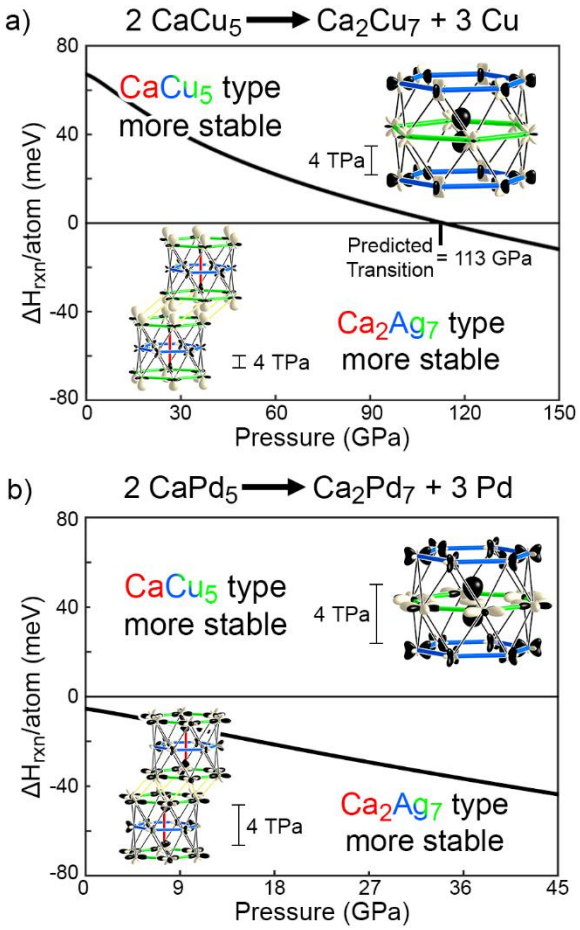

Figure 5.3. The pressure dependence for the GGA-DFT reaction enthalpy for the decomposition of $CaCu_5$-type phases into a Ca_2Ag_7-type superstructure, with an elemental transition metal side product. Results are shown for the (a) Ca-Cu and (b) Ca-Pd systems. Alongside the ΔH_{rxn} vs. P curves, CP plots of reported $CaCu_5$- and hypothetical Ca_2Ag_7-type products are plotted (see the caption to Figure 5.1 for plotting conventions). In both cases, the Ca_2Ag_7-type phase (+Cu or Pd side product) is increasingly favored at higher P, in-line with its more efficient atomic packing. Curiously, this reaction is predicted to be favorable for $CaPd_5$ at ambient pressure, an observation that prompted the experimental investigations described in this Article.

We are careful to note here that this particular transition may not be what is observed in a high pressure experiment. Many other possible phase transformations are possible, such as the formation of another polymorph of $CaCu_5$ or segregation into two $CaCu_{5-x}$ and $CaCu_{5+x}$ phases. Rather, what we have learned

from this calculation is that CP-driven transitions not observed in this system at ambient pressure can be promoted with the use of external applied pressure, and that the upper bound for new structural chemistry to appear for $CaCu_5$ is predicted to be 113 GPa (although this number applies strictly to a temperature of 0 K; entropic effects at higher temperatures could also play a role).

The requirement of 113 GPa of pressure to drive the formation of Ca_2Cu_7 is in stark contrast to the Ca-Ag system, where Ca_2Ag_7 is reported as stable at ambient pressure. As Pd is intermediate in size between Cu and Ag, we may expect the experimentally observed $CaCu_5$-type $CaPd_5$ phase would undergo phase transitions at a lower pressure. The effect of replacing Cu with Pd in the high pressure calculations is striking (Figure 5.3b). The ΔH_{rxn} is now negative at 0 GPa, and becomes more favorable as the pressure is increased. Given the numerous other paths that the structure could follow to relieve the negative CPs around the Ca in $CaPd_5$, this result hints that $CaPd_5$ may be susceptible to a phase transition at a relatively mild applied physical pressure.

$CaPd_5$ seemed to us, then, as an ideal candidate for exploring synthetically how CP analysis could guide experimental investigations of intermetallic compounds under applied pressure. We therefore set out to synthesize $CaPd_5$ for use as a starting material in such experiments. As we will see in the next sections, this seemingly straightforward task led us to the discovery of a new, although not entirely unexpected, incommensurately modulated variant of the $CaCu_5$ type in the Ca-Pd phase diagram.

5.5. The Incommensurate Structure of $CaPd_{5+x}$

5.5.1. Synthetic Results and Preliminary Crystal Examination

Our syntheses targeting $CaPd_5$ yielded large, well-faceted crystals attached to the sides of the Nb tubing used as a reaction vessel. While they were easily dislodged from the tube walls, these light gray crystals with a bright metallic sheen were found to be malleable under further mechanical stress. Due to the malleable nature, powder X-ray diffraction patterns of a ground portion of the samples exhibited wide diffuse peaks, making it difficult to conclusively assign phases to the product. Many of the strongest diffraction peaks matched well those expected for the $CaCu_5$-type $CaPd_5$ structure. However, additional peaks were also present that could not be indexed with any reported phases in the system.

Elemental analysis with energy dispersive X-ray spectroscopy (EDS) revealed an essentially single phase with composition $Ca_{1.00(3)}Pd_{5.48(5)}$, suggesting that these additional diffraction peaks stem from the major phase rather than side products. For this reason, we can tentatively attribute the full powder pattern to a $CaPd_{5+x}$ compound rather than a $CaCu_5$-type phase plus impurities.

Based on these unexpected and problematic features in the powder X-ray diffraction pattern, we turned to single crystal studies to understand the structural chemistry present in our samples. In our initial single crystal X-ray diffraction experiments, we found that many of the strongest reflections for $CaPd_{5+x}$ could be indexed with a hexagonal unit cell whose *a* axis length of 5.21 Å appeared consistent with the $CaCu_5$-type $CaPd_5$ phase previously reported. Surprisingly, though, the *c* axis length obtained was about four times that expected from the literature at 17.75 Å. Another hint that the sample was more complex than a $CaCu_5$-type crystal was that roughly half of the observed reflections were left unindexed with this unit cell assignment.

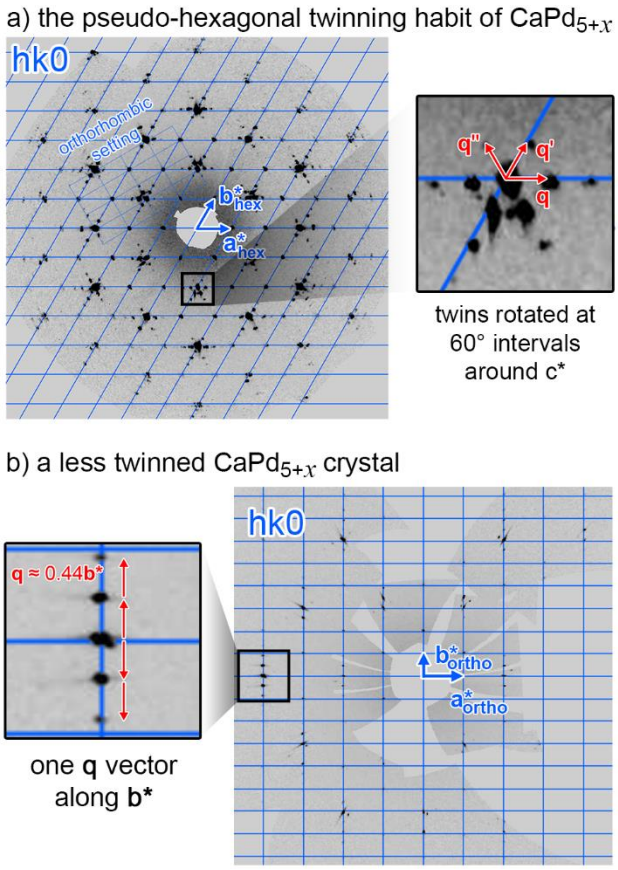

Figure 5.4. Satellite reflections in the diffraction patterns of single crystals of $CaPd_{5+x}$, indicating the presence of incommensurate modulations. (a) Reciprocal lattice reconstruction of the *hk*0 layer of the diffraction data collected for a $CaPd_{5+x}$ crystal. The strongest reflections in this layer can be indexed with a metrically hexagonal reciprocal lattice (solid blue), or with an orthorhombic lattice (lighter blue). Satellites emanate from the main reflections along three directions, labelled **q**, **q'**, and **q''** in the inset, occurring in intervals of 60° around the *c**-axis. (b) The corresponding reciprocal lattice image for a higher-quality crystal. Here, one **q** vector (lying along *b** in the orthorhombic setting) dominates, suggesting that the three q-vectors of the previous crystal result from twinning facilitated by hexagonal pseudo-symmetry.

An examination of reciprocal lattice reconstructions of the diffraction data indicated that these remaining reflections follow a definite pattern, as is shown for the *hk*0 layer in Figure 5.4a. In this image, the hexagonal grid (blue) defined by the $\mathbf{a}_{hex}^*$ and $\mathbf{b}_{hex}^*$ vectors captured the most intense reflections. In addition, clear satellite peaks can be seen to emanate at fixed intervals from many of the indexed reflections

along the $\mathbf{a}_{hex}^*$, $\mathbf{b}_{hex}^*$, and $\mathbf{b}_{hex}^* - \mathbf{a}_{hex}^*$ directions. This distinction between strong reflections lying on a reciprocal lattice and weaker satellites is the hallmark of a modulated crystal.

At first glance, the three different orientations of the satellite sequences would suggest that modulations with several different q-vectors are affecting the structure, labelled as **q**, **q'**, and **q''** in the inset to Figure 5.4a. Closer inspection, however, reveals that these progressions of satellites are essentially independent of each other: no additional reflections resulting from linear combinations of these q-vectors are apparent. Given the hexagonal symmetry of the main reflections (and thus most likely the average structure), it seems likely that this pattern is created by twin domains each with a single q-vector that have been rotated relative to each other by 60° intervals around **c***.

To verify this hypothesis, we screened additional crystals in search of a twin-free specimen of $CaPd_{5+x}$. Our first attempts to cleave larger crystals into smaller fragments succeeded only in destroying the sample's crystallinity due to its malleable nature. After extensive screening of smaller crystals, we eventually found one for which only a single q-vector was needed for indexing the diffraction pattern (Figure 5.4b), confirming the suspected the pseudo-hexagonal twinning habit of the system.

The presence of a single q-vector perpendicular to the high symmetry axis breaks the hexagonal symmetry apparent in the main reflections on their own, lowering the maximum possible symmetry to orthorhombic. Re-indexation of the diffraction pattern to accomodate the orthorhombic crystal system resulted in a *C*-centered cell with a = 5.16 Å, b = 9.13 Å ($\approx\sqrt{3}/2\ a$), c = 17.76 Å. The main reflections exhibited systematic absences consistent with the space group *Cmcm*. The remaining reflections could be indexed with a q-vector of length ~0.44 along b^*. Indexation of the satellites using a supercell would

require lengthening the *b*-axis at least 25-fold; we therefore continued the structure solution under the assumption that the phase was incommensurately modulated, requiring a (3+1)D superspace solution.

5.5.2. The Average Structure

A great deal can be learned about the crystal structure of this modulated $CaPd_{5+x}$ phase by examining its average structure, that is to say carrying out a structure solution from the main reflections alone. After integrating the main reflections, structure solution proceeded smoothly using the charge-flipping algorithm, yielding an electron density map consistent with the orthorhombic space group *Cmcm* we assigned above. The resulting electron density map can be divided into two types of lamellar regions stacked along the *c*-axis. The first type consists of nearly spherical electron density peaks, representing well-defined atomic positions (which were quickly assigned to Ca and Pd by the Jana2006 software). These atoms trace out one-unit-cell-thick slabs of the $CaCu_5$ type (Figure 5.5, left), similar to those that form the basis of the Ca_2Ag_7 structure (Figure 5.2).

In the remaining regions of the structure, the electron density is nearly continuous (Figure 5.5, right), such that specific atomic sites cannot be resolved. The electron density within these layers follows a flat honeycomb distribution, whose thickness is consistent with a monolayer of Pd atoms. Despite the apparent diffuseness of this region, no disorder is apparent in the $CaCu_5$-type slab positions: neighboring slabs, separated by the diffuse layer, are shifted by $\frac{1}{3}\mathbf{b}_{\mathbf{basic}}$ relative to each other.

These features in the average structure of $CaPd_{5+x}$ provide clues as to the nature of the modulated structure. The sharply-defined atomic positions of $CaCu_5$-type slabs suggest that these regions of the structure are largely rigid from basic cell to basic cell in the full crystal structure. The main variations

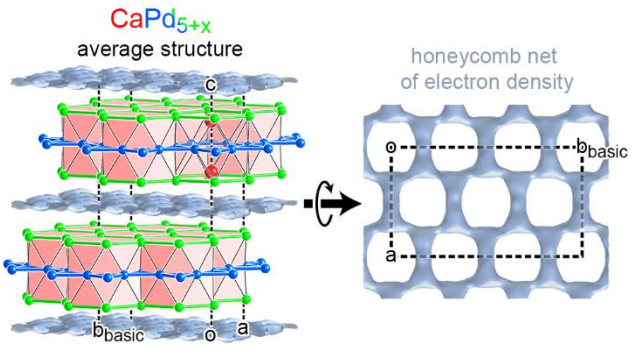

Figure 5.5. The average structure of $CaPd_{5+x}$ determined from the main reflections of its diffraction pattern. This structure is based on $CaCu_5$-type slabs stacked along *c* separated by hexagonal nets of diffuse electron density at $z = 0$ and $1/2$. The ordering of atomic positions within the diffuse electron density features is a likely source of the satellite reflections shown in Figure 5.4. Isosurface level for electron density plots: 8 electrons/Å^3.

created by the modulation are localized instead to the diffuse layer. In the absence of satellite reflections, this region would be modelled through the placement of partially occupied atoms in an attempt to account for the electron density distribution in an atomistic fashion. The presence of strong satellite reflection in the diffraction pattern hints that more order is in fact present in these layers, but with a periodicity incommensurate with that of the $CaCu_5$-type slabs.

Using this average structure model, the features of the powder X-ray diffraction pattern for our bulk $CaPd_{5+x}$ sample can be interpreted (it is not uncommon for the satellite reflections of modulated structures to be undiscernible with laboratory powder X-ray diffractometers). As is shown in Figure D1 of the supporting information, the calculated powder pattern for this model accounts for all major peaks in the experimental pattern, including both those attributable and not attributable to a $CaCu_5$-type phase. Based on our inability to obtain a $CaCu_5$-type $CaPd_5$ in our syntheses, it is possible that previous descriptions of $CaCu_5$-type $CaPd_5$ phase (which were based on powder diffraction experiments) may have in fact referred

to $CaPd_{5+x}$. We still cannot rule out, however, the possibility that a $CaCu_5$-type phase may be preferred under different conditions, say at high temperatures.

5.5.3. The Modulated Structure of $CaPd_{5+x}$ ($x \approx 0.22$)

Now that we have seen how the $CaPd_{5+x}$ structure is derived from slabs of the $CaCu_5$-type separated by atomic layers with an incommensurate periodicity, let's explore how deeper structural detail can be resolved using a (3+1)D structure solution.[63-66] The first step in this process is assigning the (3+1)D superspace group of the structure.[67,68] Here, each of the symmetry operations of the *Cmcm* space group of the average structure become embedded in (3+1)D superspace as operations on the general position (x_1, x_2, x_3, x_4). The key issue to resolve in this mapping is whether each operation has a glide component along the newly introduced dimension, x_4. For example, a mirror plane perpendicular to **a** in the 3D structure, $(x, y, z) \rightarrow (-x, y, z)$, could be included in the (3+1)D superspace group as $(x_1, x_2, x_3, x_4) \rightarrow (-x_1, x_2, x_3, x_4)$ or $(x_1, x_2, x_3, x_4) \rightarrow (-x_1, x_2, x_3, x_4+½)$.

From inspection of the systematic absences, we concluded that only the first operation is associated with an x_4 glide, and that no other reflection conditions outside of those expected for the *Cmcm* space group were present. This analysis yields the (3+1)D superspace group *Cmcm*(*0ß0*)*s00*, where the "(*0ß0*)" symbol specifies that the q-vector is along b^*, and the three characters "s00" give the glide components for the three generating operations, with "s" = ½. This assignment was confirmed by the subsequent steps in the structure refinement.

With this (3+1)D superspace group in-place, we then attempted to convert the diffraction intensities to an electron density map using the charge-flipping algorithm with the Superflip program, a method that

applies to diffraction data indexed with any dimensionality. The charge-flipping iterations converged without issue on a (3+1)D electron density that matched well with the assigned superspace group, and initial atom positions and identities were derived from this map with the peak search function of Jana2006.

In the resulting model, the atomic positions are represented as lines in the (3+1)D superspace whose coordinates along the *x*, *y*, and *z* axes of physical space are functions of the fourth dimension, x_4. The x_4 axis itself, which represents the phase of the modulation function throughout the crystal, is oriented perpendicular to physical space, while the non-modulated axes x_1 and x_3 lie parallel to physical *x* and *z* axes, respectively (Figure 5.6). For the modulated direction, *y*, the (3+1)D crystallographic axis x_2 is tilted out of physical space, such that a lattice translation along x_2 must be accompanied by a shift along x_4 in order to stay in physical space. In this way, translations along *y* in physical space lead to changes in both x_2 and x_4, leading to the physical cross-section sampling different points along x_4.

For atoms not affected by the modulation function, their positions would simply appear as straight lines running parallel to x_4, such that they do not move significantly from their average position between basic cells. Most of the atoms in the $CaCu_5$-type slabs that we identified in the average $CaPd_{5+x}$ structure show only small oscillations away from these straight lines. This weak dependence of their placement in the basic cell on x_4 helps account for the ease with which they were located in the average structure solution. As can be seen from plots of the modulation functions for each of the sites in the Supporting Information, the Fourier electron density associated with these atoms appear as softly undulating columns in the (3+1)D superspace.

The electron density in (3+1)D structure between the $CaCu_5$-type slabs, however, shows very different behavior, as expected from the diffuse features found here for the average structure. As in the

$CaCu_5$-type slab regions, the electron density is concentrated into atomic domains that are stretched into columns running out of physical space (blue isosurfaces in Figure 5.6). Rather than being oriented parallel to the x_4 axis, though, they appear as slanted, with kinks occurring at regular intervals.

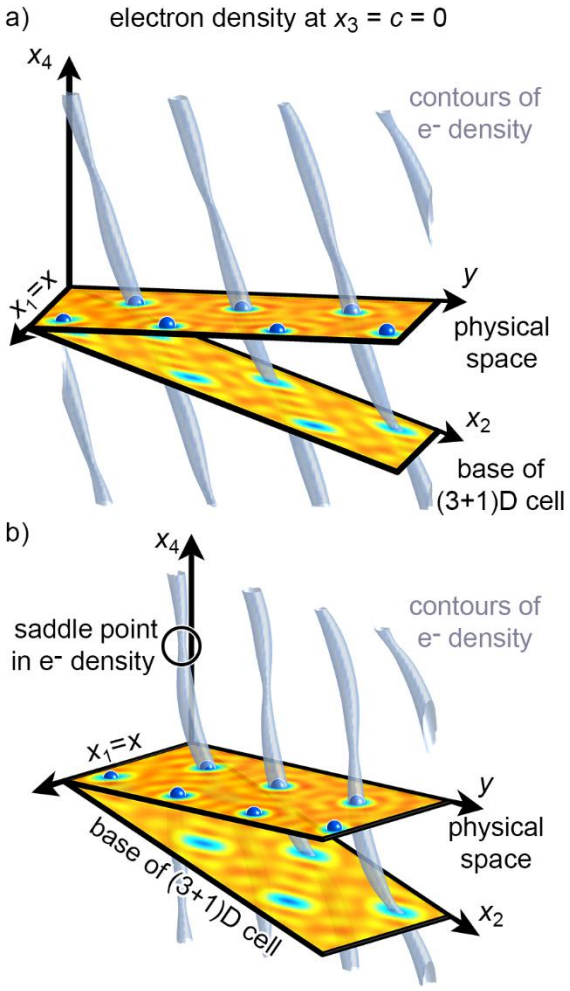

Figure 5.6. Modulation of the atomic positions in the interface layers between $CaCu_5$-type slabs in $CaPd_{5+x}$ (corresponding to the diffuse electron density features in Figure 5.5) shown at two different angles. The electron density of the *x*-*y* plane though these positions in physical space is shown as a cross-section through the (3+1)D superspace density, represented as an electron density isosurface (level = 25 electrons/Å^3). Here, the fourth dimension, x_4, represents the phase of the modulation function, while the tilting of the x_2 axis off of the physical cross-section leads to motions along the physical *y* axis being coupled with shifts in x_4, i.e. the modulation of the structure along *y*. (a) The slant of the atomic domains relative to the x_4 axis indicates that these atoms are incommensurately spaced along *y* relative to the rest of the structure. (b) Additionally, kinks can be perceived in these domains, suggesting that modulations of the atomic position arise from interactions with the remainder of the structure.

The slanting of the atomic domains has a pronounced structural consequence: as the x_4 value for any given domain increases, its x_2 position monotonically decreases. As the physical cross section passes though these domains along the y axis, the placements of the atoms within the basic cells become increasingly shifted to lower values of y. The overall effect is that the periodicity with which these atoms are placed within the physical crystal structure has a shorter repeat vector than that of the $CaCu_5$-type slabs.

Overall, then, this $CaPd_{5+x}$ phase appears to be adopting a composite structure, in which two separate sublattices occur with different periodicities. This situation complicates the structural modeling in that the slanted atomic domains do not have a well- defined average x_2 coordinate; instead their slanted orientation causes them to stretch along the full length of the x_2 axis. One approach to handling such cases is offered by the (3+1)D superspace formalism for composite crystals, in which the two incommensurately spaced sublattices are described with different coordinate systems that are related through a transformation matrix, W.[64,65,69-71]

A simpler method, which proved more effective in this case, is to divide the atomic domains into segments whose centers can be specified using the same coordinate system as the rest of the structure. While the division of a continuous domain into discrete sections would at first seem artificial, the features of the electron density in fact point to natural places to draw boundaries. The kinks visible in Figure 5.6 have lower electron densities than their surroundings along the columns, making them excellent points to place gaps between atomic domains.

This model is illustrated in Figure5. 7 with an x_2-x_4 cross-section (summed over the range $0.0 \leq x_1 \leq 0.5$) through the slanted atomic domains. Here, the contours of the Fourier electron density appear to

create stripes that run downwards from left to right, with bends that correspond to the kinks in Figure 5.6. Within each of stripe, the intervals of $\Delta x_4 = 1$ can be divided into two segments using these kinds as boundaries. To describe the atom's position as a function of x_4 for each of these segments, one could then draw a slanted line within the electron density stripe. In practice, this is done by using crenel functions (square wave functions for the atomic occupation that have a value of 1 for a specific range of x_4 values and are 0 elsewhere), combined with Legendre polynomials to model the positional character in the crenel interval.[72]

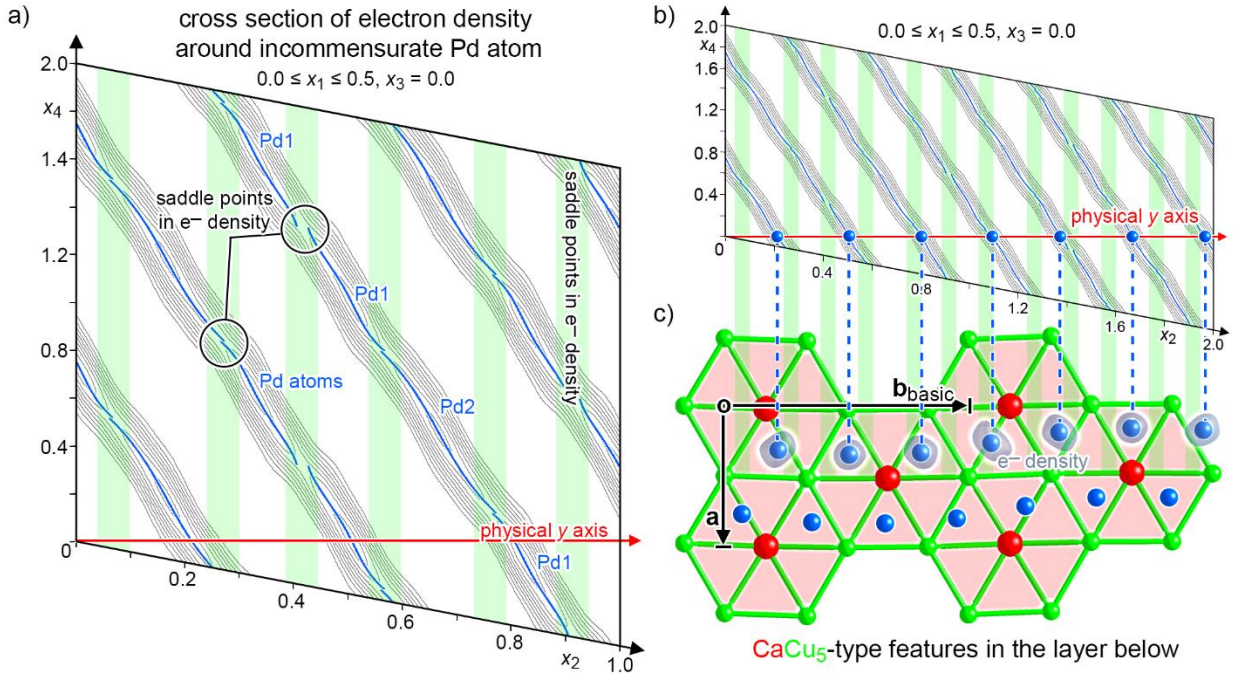

Figure 5.7. Atomistic modelling of the (3+1)D electron density features in the layers separating $CaCu_5$-type slabs in $CaPd_{5+x}$. (a) Contours of the (3+1)D electron density at $x_3 = 0$ summed over the range $0.0 \leq x_1 \leq 0.5$ (similar to the representation in Figure 5.6). The slanted columns of electron density are modelled with two atomic domains, Pd1 and Pd2 (blue curves), which meet with slight discontinuities at the kinks in the columns. (b) The kinks in electron density features correspond to (c) locations where the Pd1/Pd2 atom is placed above a Ca-Pd or Pd-Pd contact in the layer below. An elongation of the electron density for Pd1/Pd2 atoms placed above these edges (shown with electron density isosurfaces) suggests that disorder is used by the structure to avoid these local configurations.

Creating this model requires two separate Pd domains to be included, which we have labeled Pd1 and Pd2. In the refinement of this model, however, it is essential to keep in mind that the Pd1 and Pd2 sites together represent a single atomic site. The transition between them at the kinks should then be made as seamless as possible. By positioning the center of two crenel functions at x_4= 0.25 and ~0.77 (the highest peaks in the strings of electron density), the atomic domains can be constructed to meet each other at the kinks in the electron density at ca. x_4 = 0.0 and 0.5.

When the remaining atoms are treated with harmonic positional modulation functions, and anisotropic atomic displacement parameters are applied to all positions (with the atomic displacement parameters being modulated for Pd1 and Pd2), the refinement of the model converges to R(I>3σ) of 2.94. Most importantly, the agreement of the modelling of the modulation functions with the diffraction data is affirmed by the values of the R(I>3σ) for the satellites, which are 3.65, 3.71, and 4.49 for the first, second and third order satellites, respectively (Table 5.1).

The refined atomic positions of the Pd1 and Pd2 sites are shown with blue curves in Figure 5.7. The functions for the two sites follow well the overall column of electron density in the Fourier map. Small discontinuities arise at the transitions between the Pd1 and Pd2 domains, but such is not entirely unexpected given the kinks in the electron density at these points.

How should these atomic domains, with their discontinuities, be interpreted in terms of 3D space? In Figures 5.7b and 5.7c, we align the physical cross-section though the Pd1/Pd2 domains of the (3+1)D model with the corresponding positions that result in 3D space. Where the physical y-axis crosses one of the Pd1 or Pd2 curves, a Pd atom appears in the 3D structure at that y-coordinate (blue spheres in Figure 5.7c). To help visualize the placement of these atoms in the phase, we also show the layer of atoms from

the $CaCu_5$-type slab below, which appears as a hexagonal net of Ca (red) and Pd (green) atoms. The incommensurate spacing of the Pd1/Pd2 atoms with respect to the $CaCu_5$-type slab is evident in the varying points at which they appear along the slab's hexagonal net. The first Pd1/Pd2 atom on the left lies to the right side of a triangle in the layer below. The next atom, however, lies directly over the center of the second triangle with the same orientation to the right. The third atom is now displaced to the left side of its triangle below. Overall, the spacing of the Pd1/Pd2 atoms is slightly smaller than the edge lengths of the triangle net below.

The different structural contexts encountered by the Pd1/Pd2 atoms offers an explanation for the kinks in their electron density features. Using shaded green lines, we show in Figures 5.7b-c how the kinks in electron density of the (3+1)D model align with the features of the $CaCu_5$-type slab below the Pd1/Pd2 layer. In each case, the green line passes directly through the center of a Ca-Pd or Pd-Pd edge in the $CaCu_5$-type slab below. The electron density kinks and discontinuities in the model at these points suggest that the placement of the Pd atom directly above one of the edges of the hexagonal net below is unfavorable relative to the positions above the triangles of the net, an effect similar to that observed earlier in the incommensurately modulated structure of $Co_3Al_4Si_2$.[73]

In 3D space, this discomfort over the edges is seen in an elongation of the Fourier density surrounding the Pd1/Pd2 positions as the edge is crossed. As is shown with isosurfaces in Figure 5.7c, the electron density around these atoms is fairly spherical when over the triangles of the Ca-Pd layer below. As the Pd1/Pd2 positions approach one of the edges in the layer below, the isosurfaces progressively elongate over the edges. These stretched electron density features suggest some disorder in the Pd1/Pd2 atom's position at these points. As was found previously for $Co_3Al_4Si_2$, this avoidance of the edges appears to

prevent overly close interatomic contacts, a theme that will reemerge in our chemical pressure analysis of this structure in the next section.

To model this disorder crystallographically, we applied modulations to the anisotropic ADPs for the Pd1/Pd2. The use of the ADPs to capture the ambiguity in the atomic positions over the edges helps account for the noticeably larger $U_{\text{equivalent}}$ for the Pd1/Pd2 atoms relative to those of the other Pd sites in the structure (see Figure D6 in the Supporting Information).

Another consequence of the mismatched periodicities can be seen in Figure 5.7c. In a fully commensurate structure, the atoms in the Pd hexagonal net (blue) could sit in the center of every other triangle formed by the Ca-Pd contacts in the layer below, with only a single position along x being needed. Due to the smaller spacing of the Pd1/Pd2 atoms along y, however, they explore a larger variety of positions relative to the layer below. Sometimes they appear above triangles with centers at $x \approx 1/3$ whose tips point up in Figure 5.7c, as seen in the first cell along $\mathbf{b}_{\text{basic}}$. At other times, they appear above triangles with centers at $x \approx 1/6$ (whose tips point down) as in the second basic cell. The Pd net responds with a gentle waving motion propagating along $\mathbf{b}$, allowing the Pd atoms to follow the midpoints between the Pd and Ca atoms in the layer below. These undulations, along with smaller modulations of the nearby atoms in the $CaCu_5$-type slabs, provide another mechanism so that $CaPd_{5+x}$ avoids overly short Ca-Pd and Pd-Pd contacts between the $CaCu_5$-type slabs and the Pd hexagonal net.

The application of superspace crystallography to this structure has thus provided a much more detailed picture of the placement of atoms between the $CaCu_5$-type slabs than was possible from the average structure alone. An interesting question to address now is to what extent this model accounts for the diffuse electron density features found for these interstitial layers in the average structure. In Figure

5.8a, we overlay the Pd1/Pd2 positions from the (3+1)D model on an isosurface of the diffuse electron density we saw in Figure 5.5. For orientation, the Ca atoms from the $CaCu_5$-type slab in the layer below are also included. Here, the Pd positions from the (3+1)D model of $CaPd_{5+x}$ indeed trace out the smeared electron density from the average structure model. From this representation, we also can also see with greater clarity the mismatch between the periodicities of the Pd hexagonal net and the $CaCu_5$-type slabs, with $3\times\mathbf{b}_{Pd1/Pd2}$ falling just short of $\mathbf{b}_{basic}$.

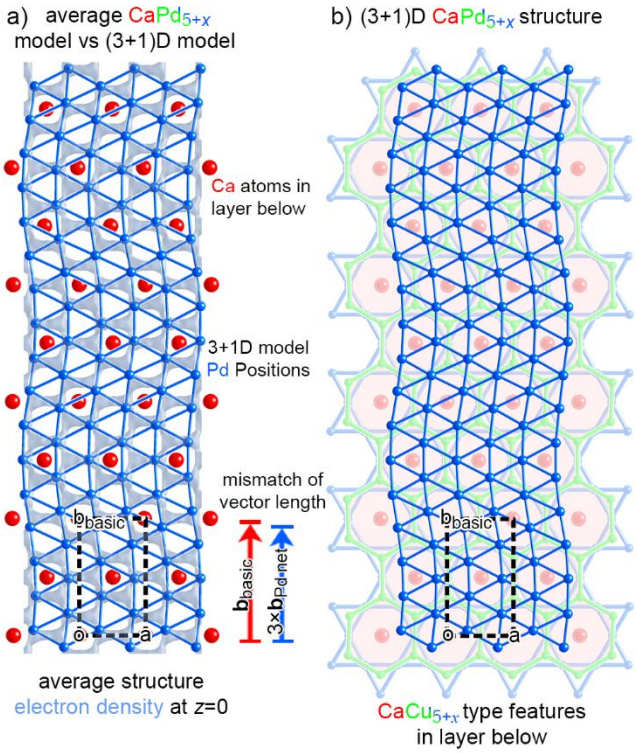

Figure 5.8. The distorted hexagonal net created by the Pd1/Pd2 atoms whose interatomic spacing along *y* is incommensurate with that of the $CaCu_5$-type slabs. (a) The positions of the Pd atoms (blue) at $z = 0$ in the (3+1)D model of $CaPd_{5+x}$ overlaid on the diffuse electron density features found in the average structure (isosurface level = 8 electrons/Å^3). Ca atoms (red) are shown from the $CaCu_5$-type slab from the layer below. (b) The placement of the Pd1/Pd2 atoms relative to the atoms of the $CaCu_5$-type slab below it (faded).

The overall structure of $CaPd_{5+x}$ is summarized in Figure 5.8b, where the Pd1/Pd2 positions together form a hexagonal net whose periodicity along *y* is incommensurate with the $CaCu_5$-type layers that it from each other. The atoms of this hexagonal layer undergo oscillations in their position along **a**, to better fit into the grooves between atoms in these slabs. This pattern bears a remarkable resemblance to models obtained for Zr_2Co_{11}, a promising magnetic material whose structure remains undetermined, from computational structure searches using evolutionary algorithms.[31] $CaPd_{5+x}$ may in fact be analogous to the orthorhombic polymorph of Zr_2Co_{11}, suggesting that similar CP driving forces could be present in the Zr-Co system.

This incommensurate arrangement of $CaPd_{5+x}$ plays a role in the overall composition of the compound. Were the $\mathbf{b}_{Pd1/Pd2}$ period to be exactly one third of $\mathbf{b}_{basic}$, the composition of the phase would be $CaPd_5$. The shorter length of $\mathbf{b}_{Pd1/Pd2}$ means that the layer contains additional Pd relative to the 1:5 stoichiometry, as is consistent the the EDS composition of $Ca_{1.00(3)}Pd_{5.48(5)}$. As is described in the Section S7 of the Supporting Information, the relationship between the $\mathbf{b}_{Pd1/Pd2} : \mathbf{b}_{basic}$ ratio and the composition of the phase can be quantified through geometrical considerations in (3+1)D superspace. The result is that the composition of the compound is given by $CaPd_{5+q/2}$, where *q* is the ratio of the satellite spacing to the main reflection spacing along the $\mathbf{b}^*$ direction in the diffraction pattern. As $\mathbf{q} = 0.44\ \mathbf{b}_{basic}$ for this crystal, the composition of the structure model is $CaPd_{5.22}$.

5.6. Chemical Pressure Relief in $CaPd_{5+q/2}$

Our experimental investigations into the phase $CaPd_5$ were prompted by theoretical predictions that it should exhibit facile pressure-induced phase transitions due to the large negative chemical pressures (CPs)

its Ca atoms would experience in the $CaCu_5$ structure type (Figure 5.9a). The structural results of the previous sections highlight that, in fact, the application of physical pressure is not necessary to see such structural chemistry emerge in the Ca-Pd system: our attempts to synthesize the reported $CaCu_5$-type $CaPd_5$ compound instead yielded an incommensurately modulated variant in which every other kagome layer of the $CaCu_5$ type is replaced with a distorted hexagonal layer whose lattice spacing is mismatched with respect to the rest of the original structure. In this section, we will see how this structural rearrangement relieves the intense CPs expected for a $CaCu_5$-type $CaPd_5$ phase.

As a first step in analyzing the $CaPd_{5+x}$ structure with the CP approach, we must overcome one difficulty. While for DFT calculations on extended solids a periodic structure is essential, the crystal structure of $CaPd_{5+x}$ is aperiodic along one direction in physical space. As such, it becomes necessary to create a periodic approximant to the incommensurate structure. In our above structural analysis of the phase, we noted that the spacing of the Pd atoms in the Pd1/Pd2 net along y is somewhat short of 1/3 $\mathbf{b}_{\mathbf{basic}}$. By making the approximation $3\times\mathbf{b}_{\mathbf{Pd1/Pd2}} = \mathbf{b}_{\mathbf{basic}}$ (and fixing the Pd1 and Pd2 atoms to lie along straight lines along y over the triangular spaces in the Ca-Pd layer below them), a simple hexagonal approximant emerges whose space group is $P\bar{6}2c$ (Figure 5.9b). The composition of this model structure is just $CaPd_5$, and despite its simplicity, we will see that it illustrates both how the Pd1/Pd2 layers provide CP relief to the structure, and the role that incommensurability plays in its stability.

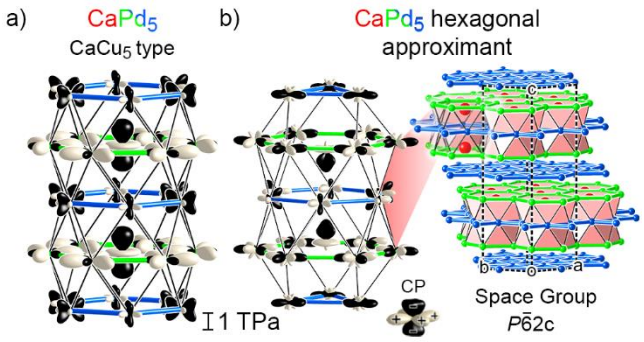

Figure 5.9. DFT-chemical pressure (CP) analysis of the transition between a $CaCu_5$-type $CaPd_5$ structure and a commensurate approximant to $CaPd_{5+q/2}$. (a) CP scheme for a pair of Ca coordination environments in $CaCu_5$-type $CaPd_5$. (b) The corresponding results for the $CaPd_{5+x}$ approximant. Note the significantly smaller CP features on the Ca atoms in the latter structure. For the plotting conventions regarding the CP results, see the caption to Figure 5.1.

With an approximant to the incommensurate $CaPd_{5+x}$ in place, we now compare its CP scheme with that of the previously reported $CaCu_5$-type $CaPd_5$ structure (Figure 5.9). For the $CaCu_5$-type structure, we again see the features which led us to consider $CaPd_5$ as a candidate for high pressure experiments: on the Ca atoms large negative lobes point into hexagonal holes of the Pd kagome nets above and below (Figure 5.9a). Upon going from this $CaCu_5$ type structure to the $CaPd_{5+x}$ approximant, every other Pd kagome net is replaced with a simple hexagonal net derived from the Pd1/Pd2 positions of the incommensurate structure solution. In the process, one of the hexagonal openings above or below each Ca atom is replaced with a Pd triangle, such that the 18-coordinate Ca polyhedron of the original structure now becomes 15-coordinate.

This tightening of the Ca environment has a pronounced effect of the structure's CP scheme (Figure 5.9b): one of the two large negative CP lobes emanating from the Ca up and down along c in the $CaCu_5$ type has been replaced by a small positive bump pointing to newly inserted Pd triangle on one side, whose Ca-Pd distances are significantly shorter than those of the original kagome layer. The other negative CP

lobe on the Ca has become reduced as the Ca has moved out of the plane of the honeycomb layer (green) to achieve shorter distances to the remaining kagome layer. The elongation of the Ca contacts to the honeycomb Pd atoms also soothes the ring of positive CP around the equator of the Ca. This motion also leads to a pairing of the Ca atoms, such that the shortest Ca-Ca contact in the structure goes from 4.40 Å in the $CaCu_5$-type structure to 3.66 Å in the $CaPd_5$ approximant (in the LDA-DFT-optimized structures).

All of these features point to the incorporation of the Pd1/Pd2 layer providing CP relief to the structure. Some tension remains in this approximant structure, however, which points toward the driving force for the incommensurate spacing of the Pd1/Pd2 layer. In Figure 5.10, we highlight the CPs for one such Pd1/Pd2 layer in the commensurate approximant. The major feature on each of these Pd atoms is a black triangular surface lying flat in the plane of the layer. This uniformly negative CP within the layer indicates that its Pd-Pd contacts are overly-long and would benefit from the contraction of the structure. As in the original $CaCu_5$ type, other CP features are present which prevent such a shrinking of the whole structure: in addition the positive CPs within the $CaCu_5$-type slabs, the Pd1/Pd2 atoms exhibit small white lobes pointing to those slabs above and below them. These features give the Pd1/Pd2 CP surface a strong quadrupole component, which we previously correlated with soft phonon modes.[53]

Relief of the negative CPs within the Pd1/Pd2 layers thus requires a structural change that decreases distances within them without substantially squeezing the remainder of the structure. The smaller spacing of the Pd1/Pd2 atoms in the incommensurate refined structure of $CaPd_{5+x}$ achieves this end by selectively adding Pd atoms to the Pd1/Pd2 layer (Figure 5.10b). The Pd contacts within the hexagonal net contract from 3.01 Å and 2.91 Å in the LDA-DFT optimized approximant to an average of 2.81 Å in the experimentally observed structure – a contraction expected to reduce the negative CPs within the layer.

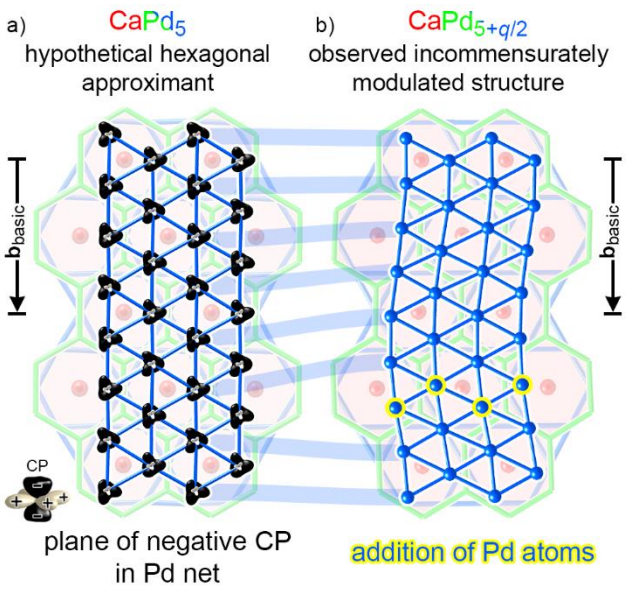

Figure 5.10. Chemical pressure (CP) as a driving force for the incommensurate spacing of the atoms in the layers between $CaCu_5$-type slabs in $CaPd_{5+x}$. (a) DFT-CPs for the Pd1/Pd2 atoms in the commensurate approximant of $CaPd_{5+x}$, in which the spacing of Pd atoms along y in this layer is 1/3 $\mathbf{b}_{basic}$. Pd-Pd contacts within this layer are marked with negative pressures, favoring contraction of the structure. (b) In the refined incommensurate structures, shorter Pd-Pd contacts are obtained by decreasing the spacing of the Pd1/Pd2 atoms along y. Light blue bars trace corresponding Pd positions between the panels, illustrated how additional atoms have arisen in the incommensurate layer.

The insertion of additional Pd1/Pd2 atoms into the interslab layer also appears to address the positive Ca-Pd CPs experienced by these layers. Through a combination of the positional modulations (giving rise to curved appearance of the strands of Pd1/Pd2 atoms along y) and the increase in space between $CaCu_5$-type slabs, the atomic contacts between the Ca atoms and the Pd1/Pd2 atoms expand from 3.02 Å in the LDA-DFT optimized $CaPd_5$ hexagonal approximant to an average distance of 3.13 Å in the experimentally observed $CaPd_{5+q/2}$ structure– which can be expected to relieve the positive pressure shown between these atoms in the CP plot of the approximant $CaPd_5$ structure. The positive CPs between the Pd1/Pd2 atoms and the $CaCu_5$-type slabs also account for the tendency of the Pd1/Pd2 atoms to avoid bridging positions over the Ca-Pd and Pd-Pd edges in these slabs.

In summary, the features of the $CaPd_{5+x}$ structure can be well-understood from the point of view of CP relief. The $CaCu_5$-type structure previously reported for this compound would place large negative pressures between the Ca atoms and the hexagons of the Pd kagome nets above and below them along the *c*-axis. In the commensurate approximant to $CaPd_{5+x}$, the open hexagons of half of the kagome nets are replaced with the triangles of a hexagonal net, tightening the Ca coordination environments. The change solves the local CP issues of the Ca atoms, but leads to a new packing issue in the nascent Pd hexagonal nets: the more even distribution of Pd atoms in these nets compared to the original kagome layers leads to overly-long Pd-Pd contacts and negative CPs. The incommensurate spacing of these Pd atoms relative to the rest of the structure provides the needed shorter Pd-Pd distances within this layer.

5.7. Conclusion

We began this Article with a hypothesis about the relationship between chemical and physical pressure: structural transitions relieving negative chemical pressures (CPs) should be promotable through the application of physical pressure. DFT total energy calculations supported this notion for $CaCu_5$-type phases $CaCu_5$ and $CaPd_5$, whose CP schemes exhibit large negative features around the Ca sites. The enthalpies for transforming these compounds to more complex superstructures were calculated to become increasingly favorable under pressure. The particularly facile nature of the transformation predicted for $CaPd_5$ led us to synthesize it as a precursor for high pressure experiments. The results of these syntheses, however, indicated that even at ambient pressures CP-driven transitions can take place: rather than a simple $CaCu_5$-type phase, we obtained an incommensurately modulated derivative, $CaPd_{5+q/2}$, whose structure, as modelled in (3+1)D superspace, can be closely correlated with the expectations of the CP schemes for the $CaCu_5$ type and a commensurate approximant.

The structural features of $CaPd_{5+x}$ provide experimental validation of the CP approach's ability to anticipate structural transformations on two separate points. First, the CP scheme of the previously reported $CaCu_5$-type $CaPd_5$ phase highlighted that the coordination environments provided by the hexagonal channels of the Pd sublattice are too large for the Ca atoms. The experimentally observed structure counters this by replacing the hexagons of a Pd kagome net at one side of each Ca atom with the triangle or diamond of a Pd hexagonal net. The CP scheme also makes a forecast about the lattice matching between the new Pd layers and the remainder of the structure: in the commensurate case, the more even distribution of the Pd positions in the hexagonal layer compared to the kagome net results in overly-long Pd-Pd distances. This issue is resolved by the $CaPd_{5+q/2}$ structure by giving the new Pd layers their own lattice periodicity with a shortened Pd-Pd spacing. An intriguing question for future research is whether a similar driving force applies to other types of composite structures[74-78] and to what extent it could be used to optimize their structures.

In both of these cases, the tendency toward structural changes can be traced to a common shape in the CP features around key atoms. The Ca atoms and Pd kagome atoms of the $CaCu_5$-type phase, and the Pd1/Pd2 atoms of the commensurate approximant to $CaPd_{5+q/2}$ exhibit CP distributions that resemble d-orbitals. For such CP quadrupoles, atomic motions along the negative CP directions (and perpendicular to positive CP components) are expected to simultaneously soothe positive CPs while satisfying the need for contraction along one direction. This mechanism for CP relief, which we have also shown can correspond to soft phonon modes,[53] suggests exciting research avenues for crystal structure design in intermetallics.

As in other cases of CP-relief, this mechanism for incommensurability in $CaPd_{5+q/2}$ provides predictions for how the structure should response to perturbations introduced through elemental substitution or (as we have seen in Section 3 of this Article) physical pressure. Particularly, the placement of smaller atoms in the Pd interface layer to augment its negative CPs, or the application for pressure to increase the penalty of the poor packing reflected in these negative CPs, would enhance the driving force for shrinking the spacing of the atoms in this layer relative to the rest of the structure. This shorter spacing would lead to the incorporation of more Pd into the structure, which (as indicated by the formula $CaPd_{5+q/2}$) should result in a lengthening of the q-vector for the phase.

The use of high-pressure would be a uniquely direct approach to testing this prediction, as experiments with elemental substitution would be faced with issues of site preferences, the specter of possible phase segregation, and the fact that elemental substitutions invariably change several factors simultaneously (e.g. atomic size, chemical hardness, and electronegativity). Similar approaches could also be taken to using pressure to adjust the structure of the rare earth-free ferromagnet Zr_2Co_{11}, whose predicted structures show structural similarities to those revealed for $CaPd_{5+q/2}$ here, with the goal of developing of structure-properties relationships for this material.

5.8. Acknowledgements

We thank Phillip Gopon and Dr. John Fournelle for assistance with SEM-EDS measurements; Joshua Engelkemier, Yiming Guo, Vincent Yannello, and Katerina Hilleke for insightful conversations regarding CP analysis; and Andrew Shamp for helpful discussions concerning variable pressure calculations. We also gratefully acknowledge financial support from the National Science Foundation (NSF) through Grant

DMR-1508496. B.J.K. thanks the NSF for a graduate student fellowship (Grant DGE-1256259). This research involved calculations using computer resources supported by NSF Grant CHE-0840494.

5.9. References

(1) Vasil'ev, Y. V.; Abzalimov, R. R.; Nasibullaev, S. K.; Drewello, T. *Fullerenes, Nanotubes, Carbon Nanostruct.* **2004**, *12*, 229-234.

(2) Faisal, F. H. M.; Abdurrouf, A.; Miyazaki, K.; Miyaji, G. *Phys. Rev. Lett.* **2007**, *98*, 143001.143001-143004.

(3) Hornberger, K.; Hackermüller, L.; Arndt, M. *Phys. Rev. A: At., Mol., Opt. Phys.* **2005**, *71*, 023601.023601-023610.

(4) Raaen, S.; Parks, R. D. *Solid State Commun.* **1983**, *48*, 199-202.

(5) Millon, E.; Gerardin, R.; Bonazebi, A.; Brice, J. F.; Evrard, O. *Rev. Chim. Miner.* **1987**, *23*, 782-788.

(6) Abbati, I.; DeMichelis, B.; Fasana, A.; Sancrotti, M.; Iandelli, A.; Olcese, G. L.; Eggenhöffner, R. *Solid State Commun.* **1988**, *65*, 743-747.

(7) Nakamura, H.; Wada, H.; Yoshimura, K.; Shiga, M.; Nakamura, Y.; Sakurai, J.; Komura, Y. *J. Phys. F: Met. Phys.* **1988**, *18*, 981-991.

(8) Sampathkumaran, E. V.; Dhar, S. K.; Malik, S. K. *J Phys C Solid State* **1987**, *20*, L53-L56.

(9) Canepa, F.; Eggenhoffner, R. *J. Less-Common Met.* **1990**, *161*, L33-L36.

(10) Canepa, F.; Franceschi, E. A.; Olcese, G. L.; Eggenhoffner, R. *J. Less-Common Met.* **1989**, *154*, 115-120.

(11) Tan, X.; Fabbris, G.; Haskel, D.; Yaroslavtsev, A. A.; Cao, H.; Thompson, C. M.; Kovnir, K.; Menushenkov, A. P.; Chernikov, R. V.; Garlea, V. O.; Shatruk, M. *J. Am. Chem. Soc.* **2016**, *138*, 2724-2731.

(12) Nieva, G.; Lee, B. W.; Guimpel, J.; Iwasaki, H.; Maple, M. P.; Schuller, I. K. *Phys. C (Amsterdam, Neth.)* **1991**, *185-189*, 561-562.

(13) Saini, N. L.; Bianconi, A.; Lanzara, A.; Agrestini, S.; Di Castro, D.; Oyanagi, H. *Int. J. Mod. Phys. B* **2000**, *14*, 2761-2766.

(14) Marezio, M.; Licci, F.; Gauzzi, A. *Phys. C (Amsterdam, Neth.)* **2000**, *337*, 195-199.

(15) Fredrickson, D. C. *J. Am. Chem. Soc.* **2012**, *134*, 5991-5999.

(16) Engelkemier, J.; Berns, V. M.; Fredrickson, D. C. *J. Chem. Theory Comput.* **2013**, *9*, 3170-3180.

(17) Fredrickson, R. T.; Guo, Y.; Fredrickson, D. C. *J. Am. Chem. Soc.* **2016**, *138*, 248-256.

(18) Berns, V. M.; Fredrickson, D. C. *Inorg. Chem.* **2013**, *52*, 12875-12877.

(19) Hadler, A. B.; Harris, N. A.; Fredrickson, D. C. *J. Am. Chem. Soc.* **2013**, *135*, 17369-17378.

(20) Berns, V. M.; Fredrickson, D. C. *Inorg. Chem.* **2014**, *53*, 10762-10771.

(21) Palenzona, A.; Manfrinetti, P. *J Less-Common Met* **1982**, *85*, 307-312.

(22) Baren, M. R. In *Binary Alloy Phase Diagrams*; Massalski, T. B. O., H.; Subramanian, P. R.; Kacprzak, L., Ed.; ASM International: Materials Park, Ohio, 1990, p 20-21.

(23) Bruzzone, G. *Gazz. Chim. Ital.* **1972**, *102*, 234-242.

(24) Subramanian, P. R. In *Binary Alloy Phase Diagrams, 2nd Ed.*; Massalski, T. B., Ed.; ASM International: Materials Park, Ohio, 1990; Vol. 44, p 899-901.

(25) Cordier, G.; Henseleit, R. *Z. Kristallogr.* **1991**, *194*, 146-147.

(26) Snyder, G. J.; Simon, A. *J. Alloys Compd.* **1995**, *223*, 65-69.

(27) McMasters, O. D.; Gschneider, K. A., Jr.; Venteicher, R. F. *Acta Crystallogr., Sect. B Struct. Crystallogr. Cryst. Chem.* **1970**, *26*, 1224-1229.

(28) Larson, A. C.; Cromer, D. T. *Acta Crystallographica Section B Structural Crystallography and Crystal Chemistry* **1971**, *27*, 1875-1879.

(29) Gómez, C. P.; Lidin, S. *Phys. Rev. B: Condens. Matter* **2003**, *68*, 024203.024201-024209.

(30) Ivanova, G. V.; Shchegoleva, N. N.; Gabay, A. M. *J. Alloys Compd.* **2007**, *432*, 135-141.

(31) Zhao, X.; Nguyen, M. C.; Zhang, W. Y.; Wang, C. Z.; Kramer, M. J.; Sellmyer, D. J.; Li, X. Z.; Zhang, F.; Ke, L. Q.; Antropov, V. P.; Ho, K. M. *Phys. Rev. Lett.* **2014**, *112*, 045502.045501-045505.

(32) Li, X. Z.; Zhang, W. Y.; Sellmyer, D. J.; Zhao, X.; Nguyen, M. C.; Wang, C. Z.; Ho, K. M. *J. Alloys Compd.* **2014**, *611*, 167-170.

(33) Demczyk, B. G.; Cheng, S. F. *J. Appl. Crystallogr.* **1991**, *24*, 1023-1026.

(34) Oszlányi, G.; Sütő, A. *Acta Crystallogr. Sect. A: Found. Crystallogr.* **2004**, *60*, 134-141.

(35) Oszlányi, G.; Sütő, A. *Acta Crystallogr. Sect. A: Found. Crystallogr.* **2005**, *61*, 147-152.

(36) Palatinus, L.; Chapuis, G. *J. Appl. Crystallogr.* **2007**, *40*, 786-790.

(37) Petříček, V.; Dušek, M.; Palatinus, L. *Z. Kristallogr.* **2014**, *229*, 345-352.

(38) Bergerhoff, G.; Berndt, M.; Brandenburg, K. *J Res Natl Inst Stan* **1996**, *101*, 221-225.

(39) Momma, K.; Izumi, F. *J. Appl. Crystallogr.* **2011**, *44*, 1272-1276.

(40) Momma, K.; Izumi, F. *J. Appl. Crystallogr.* **2008**, *41*, 653-658.

(41) Kresse, G.; Furthmüller, J. *Phys. Rev. B: Condens. Matter* **1996**, *54*, 11169-11186.

(42) Kresse, G.; Furthmüller, J. *Comput. Mater. Sci.* **1996**, *6*, 15-50.

(43) Blöchl, P. E. *Phys. Rev. B: Condens. Matter* **1994**, *50*, 17953-17979.

(44) Kresse, G.; Joubert, D. *Phys. Rev. B: Condens. Matter* **1999**, *59*, 1758-1775.

(45) Perdew, J. P.; Burke, K.; Wang, Y. *Physical Review B* **1996**, *54*, 16533-16539.

(46) Vinet, P.; Smith, J. R.; Ferrante, J.; Rose, J. H. *Physical Review B* **1987**, *35*, 1945-1953.

(47) Togo, A.; Tanaka, I. *Scripta Mater.* **2015**, *108*, 1-5.

(48) Bader, R. F. W. *Atoms in molecules: a quantum theory*; Oxford University Press: Oxford, England, 1990.

(49) Tang, W.; Sanville, E.; Henkelman, G. *J. Phys.: Condens. Matter* **2009**, *21*, 084204.084201-084207.

(50) Sanville, E.; Kenny, S. D.; Smith, R.; Henkelman, G. *J. Comput. Chem.* **2007**, *28*, 899-908.

(51) Yu, M.; Trinkle, D. R. *J. Chem. Phys.* **2011**, *134*, 064111.064111-064118.

(52) Oliveira, M. J. T.; Nogueira, F. *Comput. Phys. Commun.* **2008**, *178*, 524-534.

(53) Engelkemier, J.; Fredrickson, D. C. *Chem. Mater.* **2016**, ASAP, DOI: 10.1021/acs.chemmater.1026b00917.

(54) Gonze, X.; Amadon, B.; Anglade, P. M.; Beuken, J. M.; Bottin, F.; Boulanger, P.; Bruneval, F.; Caliste, D.; Caracas, R.; Cote, M.; Deutsch, T.; Genovese, L.; Ghosez, P.; Giantomassi, M.; Goedecker, S.; Hamann, D. R.; Hermet, P.; Jollet, F.; Jomard, G.; Leroux, S.; Mancini, M.; Mazevet, S.; Oliveira, M. J. T.; Onida, G.; Pouillon, Y.; Rangel, T.; Rignanese, G. M.; Sangalli, D.; Shaltaf, R.; Torrent, M.; Verstraete, M. J.; Zerah, G.; Zwanziger, J. W. *Comput. Phys. Commun.* **2009**, *180*, 2582-2615.

(55) Gonze, X.; Rignanese, G.-m.; Verstraete, M.; Beuken, J.-m.; Pouillon, Y.; Caracas, R.; Raty, J.-y.; Olevano, V.; Bruneval, F.; Reining, L.; Godby, R.; Onida, G.; Hamann, D. R.; Allan, D. C. *Z. Kristallogr.* **2005**, *220*, 558-562.

(56) Hartwigsen, C.; Goedecker, S.; Hutter, J. *Physical Review B* **1998**, *58*, 3641-3662.

(57) Goedecker, S.; Teter, M.; Hutter, J. *Physical Review B* **1996**, *54*, 1703-1710.

(58) Berns, V. M.; Engelkemier, J.; Guo, Y.; Kilduff, B. J.; Fredrickson, D. C. *J. Chem. Theory Comput.* **2014**, *10*, 3380-3392.

(59) Takakura, H.; Gómez, C. P.; Yamamoto, A.; De Boissieu, M.; Tsai, A. P. *Nature Mater.* **2007**, *6*, 58-63.

(60) Okamoto, H. *J. Phase Equilib.*, *22*, 179-179.

(61) Wasiur-Rahman, S.; Medraj, M. *Intermetallics* **2009**, *17*, 847-864.

(62) Jayaraman, A. *Rev. Sci. Instrum.* **1986**, *57*, 1013-1031.

(63) Janseen, T.; Janner, A.; Looijenga-Vos, A.; de Wolff, P. M. In *International Tables for Crystallography*; Prince, E., Ed.; Kluwer Academic Publishers: 2006; Vol. C, p 970-955.

(64) Janssen, T.; Chapuis, G.; de Boissieu, M. *Aperiodic Crystals*; Oxford University Press, 2007.

(65) van Smaalen, S. *Incommensurate Crystallography*; Oxford University Press, 2007.

(66) Wagner, T.; Schönleber, A. *Acta Crystallogr., Sect. B: Struct. Sci.* **2009**, *65*, 249-268.

(67) Stokes, H. T.; Campbell, B. J.; van Smaalen, S. *Acta Crystallogr., Sect. A: Found. Crystallogr.* **2011**, *67*, 45-55.

(68) van Smaalen, S.; Campbell, B. J.; Stokes, H. T. *Acta Crystallogr., Sect. A: Found. Crystallogr.* **2013**, *69*, 75-90.

(69) Yamamoto, A. *Acta Crystallogr. Sect. A: Found. Crystallogr.* **1993**, *49*, 831-846.

(70) Jobst, A.; van Smaalen, S. *Acta Crystallographica Section B Structural Science* **2002**, *58*, 179-190.

(71) Sun, J.; Lee, S.; Lin, J. *Chem. Asian J.* **2007**, *2*, 1204-1229.

(72) Petříček, V.; Eigner, V.; Dušek, M.; Čejchan, A. *Z. Kristallogr.* **2016**, *231*, 301-312.

(73) Fredrickson, R. T.; Fredrickson, D. C. *Inorg. Chem.* **2013**, *52*, 3178-3189.

(74) Bolotina, N. B.; Tursina, A. I.; Nesterenko, S. N. *J. Struct. Chem.* **2012**, *53*, 15-25.

(75) Samal, S. L.; Lin, Q.; Corbett, J. D. *Inorg. Chem.* **2012**, *51*, 9395-9402.

(76) Piao, S. Y.; Lidin, S. *Philos. Mag.* **2007**, *87*, 2693-2699.

(77) McMahon, M. I. *J. Synchrotron Radiat.* **2005**, *12*, 549-553.

(78) Degtyareva, O.; Gregoryanz, E.; Somayazulu, M.; Dera, P.; Mao, H.-k.; Hemley, R. J. *Nat. Mater.* **2005**, *4*, 152-155.

Chapter 6

Homoatomic Clustering in T_4Ga_5 (T = Ta, Nb, Ta/Mo): A Story of Reluctant Intermetallics Crystallizing in a Binary Structure Type

This chapter has been published: Fredrickson, R. T.; Kilduff, B. J.; Fredrickson, D. C. *Inorg. Chem.* **2015**, 54, 821-831. The identification and characterization of the Ta_4Ga_5-type in the Ta-Ga and Ta-Mo-Ga systems were performed by R. Fredrickson. The synthesis and characterization of the Ta_4Ga_5-type Nb_4Ga_5 and theoretical analyses presented here were performed by Kilduff. All authors contributed to the preparation of the text below.

6.1. Abstract

In the formation of binary compounds, heteroatomic interactions are generally expected to play the leading role in providing stability. In this Article, we present a series of gallides, T_4Ga_5 (T = Ta, Nb, and Ta/Mo), which appear to defy this expectation. Their complex crystal structures represent a new binary structure type, which can be visualized in terms of a host lattice of $T@T_8$ bcc clusters linked through face-capping Ga_2 dumbbells to form a primitive cubic framework. The cubic spaces that result are alternately filled by distorted T pentagonal dodecahedra (sharing atoms with the host lattice) and dimers of bcc fragments, leading to a $\sqrt{2}\times\sqrt{2}\times2$ supercell of the host framework structure. Ga tetrahedra and icosahedral units fill the remaining void spaces. Underlying these structural features is a strong tendency for homoatomic clustering of Ta and Ga, which is evident in all of the coordination polyhedra. Electronic structure calculations using GGA-DFT and DFT-calibrated Hückel models reveal possible origins for this

elemental segregation and the factors stabilizing the structure as a whole. A deep pseudogap is present at the Fermi energy of Ta_4Ga_5 (as well as at that of Nb_4Ga_5), corresponding to the near optimization of Ta-Ta and Ta-Ga interactions. This pseudogap emerges due to the ability of extensive Ta-Ta bonding to provide local 18-electron configurations to the Ta atoms, despite the electron concentration being only 8.75 electrons per Ta atom. Support for these Ta-Ta interactions is provided by Ga bridging atoms, whose valence orbitals' low number of angular nodes confers preferential stabilization to Ta-Ta bonding functions over antibonding ones. The observed spatial separation of the structure into Ta and Ga domains occurs as a consequence of the Ga atoms being pushed toward the periphery of the Ta clusters to play this supporting role.

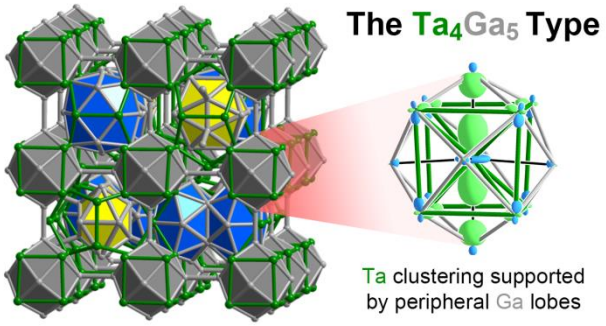

Figure 6.0. Ta_4Ga_5 (and two related phases) crystallizes in a new binary structure type in which a tendency for homoatomic clustering of the Ta and Ga is observed. In fact, heteroatomic interactions appear almost as an afterthought. Electronic structure calculations trace this elemental clustering to the structure's use of extensive Ga-supported Ta-Ta bonding to provide each Ta atom with an 18-electron configuration, despite the electron concentration being only 8.75 electrons per Ta atom in Ta_4Ga_5.

6.2. Introduction

The theme of "like dissolves like" in solubility and intermolecular interactions has some curious extensions into the realm of metallic phases. Certain combinations of metals refuse to be alloyed together to form solid solutions,

and in some cases will form 2-phase liquids in the melt.[1] In intermetallic phases, this theme can be perceived in some of the most complex crystal structures, where large unit cells arise from a segregation of the atoms into domains of differing polarity,[2] packing types,[3-5] or groupings of elements.[6-9] For most of these cases, the driving forces holding the conflicting domains together remain a matter of speculation, but if understood they could offer new avenues to guiding the crystal structures of metallic materials. In this Article, we describe a series of transition metal gallides—Ta_4Ga_5, Nb_4Ga_5, and $Ta_{3.9}Mo_{0.1}Ga_5$—that illustrate one mechanism by which such segregation can occur in intermetallics.

Our first encounter with this series occurred during syntheses in the Mo-Ga system, which were inspired by the host-guest arrangements exhibited by the structures of Mo_6Ga_{31}[10] and the V_8Ga_{41}-type[11,12] phase Mo_8Ga_{41},[13] and the prospect of a larger progression of structures based on these motifs. During these syntheses, we used Ta and Nb tubes as reaction containers, which proved to be less inert than expected. Crystals of $Ta_{4-x}Mo_xGa_5$ and $Nb_{4-x}Mo_xGa_5$ ($x \approx 0.1$) were obtained as side products, which appeared to be related to the Ta_4Ga_5 and Nb_4Ga_5 phases reported in the Ta-Ga and Nb-Ga phase diagrams,[15,16] but whose crystal structures were hitherto unknown.[14,15] In subsequent syntheses in these binary systems, we were able to confirm this relationship by obtaining Ta_4Ga_5 and Nb_4Ga_5 as major phases, and solving their structures using single crystal X-ray diffraction.

As we will see, their structures correspond to a new binary structure type, the Ta_4Ga_5 type, which can be easily visualized in terms of a hierarchical relationship[9,16-18] to the simple Heusler structure type, as exemplified by $MnAlCu_2$ (Figure 6.1).[19,20] In the $MnAlCu_2$ structure, the Cu atoms form a primitive cubic network (gray), with the Mn and Al atoms filling the cubic holes in an alternating fashion (blue and yellow). In the Ta_4Ga_5 type, a similar pattern is encountered with clusters occurring in place of individual atoms: the primitive cubic framework is built from Ta bcc units whose square faces are capped by Ga, while the cubic holes are occupied by pseudo-icosahedral clusters and pairs of bcc fragments.

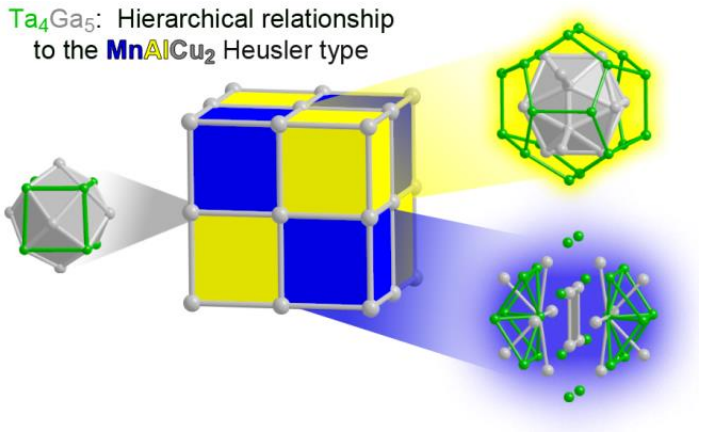

Figure 6.1. Structural features of the new binary structure type adopted by Ta_4Ga_5 and Nb_4Ga_5, illustrated by its hierarchical relationship to the $MnAlCu_2$ (Heusler) type.

Throughout this structure there is a tendency for the T and Ga atoms to coalesce into homoatomic clusters, such as T bcc units, Ga tetrahedra, and Ga icosahedra. This apparent dominance of homoatomic clusters appears to be at odds with the usual expectation that heteroatomic interactions provide the impetus for binary phase formation. Using DFT-calibrated Hückel calculations and the reversed approximation Molecular Orbital (raMO) analysis,[21] we will trace these geometrical features to the dominance of T-T interactions in forming a pseudogap at the Fermi energy, and the role of the Ga atoms in preferentially stabilizing T-T bonding states over T-T antibonding ones. The resulting bonding picture offers a view into how the balance between homoatomic and heteroatomic interactions can influence the shapes of clusters in intermetallic phases.

6.3. Experimental Section

6.3.1. Synthesis

Our first crystal exhibiting the Ta_4Ga_5 type was obtained upon heating Ga (Strem chemicals, 99.99%) and Mo (Strem chemicals, 99.95%) in a 5.0 mm diameter Ta tube (American Elements, 99.9%). The elements were weighed in a molar ratio of Ga:Mo=5:1 in an Ar filled glove box and placed in a Ta tube. The Ta tube was welded

shut using an arc-melting furnace and sealed in an evacuated fused silica ampoule. The sample tube was annealed at 800°C for 120 hours. Attempts to prepare phase pure Ta_4Ga_5 were then made. In the most successful of these syntheses, Ta foil (Sigma Aldrich, >99.9%) and Ga (Strem chemicals, 99.99%) were used as starting materials (following the procedure for transition metal gallide synthesis of Girgis[22]), with a small amount of I_2 added to promote vapor phase diffusion and crystal growth. The elements were weighed in the stoichiometric molar ratio Ta:Ga:I=4:5:0.0001, and placed in a fused silica tube. After being evacuated and sealed, the tube was annealed at 850°C for 700 hours.

Nb_4Ga_5 was similarly first identified as a side reaction of Ga with a Nb reaction container during synthetic explorations using Ga as a flux. Phase pure Nb_4Ga_5 was then synthesized by loading stoichiometric amounts of Nb powder (Strem Chemicals, 99.8%) and Ga shot (Strem Chemicals, 99.99 %) into an alumina crucible in an argon-filled glovebox. The alumina crucibles were then placed in fused silica tubes, which were transferred to a vacuum line (with care taken to avoid exposure to atmospheric oxygen), and sealed under vacuum (~100 mtorr). The tubes were next set vertically in a muffle furnace, heated to 1100 °C in 5.5 h, held at this temperature for 198 h, and cooled to room temperature over 11 h.

6.3.2. Single Crystal X-ray Diffraction Analysis

Single crystal X-ray diffraction data for the original Ta_4Ga_5-type crystal ($Ta_{3.86}Mo_{0.14}Ga_5$) and crystals from the binary Ta_4Ga_5 and Nb_4Ga_5 syntheses were collected at room temperature on a Bruker Quazar SMART APEX2 diffractometer with Mo Kα microfocus source (λ = 0.71073 Å). Unit cell determination and peak integration were performed using the SAINT V8.34A software package supplied by the manufacturer. Scaling and absorption correction were executed with SADABS. The structures were solved with the charge flipping algorithm[23,24] using the program SUPERFLIP,[25] and refined on F^2 using the program JANA2006.[26] The Fourier electron densities and surfaces separating the Ta_4Ga_5 structure into Ta- and Ga-rich domains were visualized with the program

VESTA3.[27] Further details regarding the refinements and structure models are given in Tables 6.1-6.2, and in the Supporting Information.

6.3.3 Powder X-ray Diffraction Analysis

The phase composition of the samples was analyzed using powder X-ray diffraction. Material from each sample was ground to a fine powder and placed on a zero-background plate. Data were measured on a Bruker D8 Advance Powder Diffractometer with Cu Kα radiation (λ=1.5418 Å) at ambient temperature. Diffraction intensities were measured using a LYNXEYE detector with a 2θ range of at least 20° to 80° (increment=0.01°), with exposure times of 0.7 seconds or longer. The diffraction patterns were analyzed using the programs Match! version 2.0.9 and JANA2006.

6.3.4 Energy Dispersive X-ray Spectroscopy

Semi-quantitative determinations of the elemental compositions of the Ta_4Ga_5 and Nb_4Ga_5 phases were performed using Energy Dispersive X-ray Spectroscopy (EDS). The crushed samples were suspended in epoxy and then polished by hand with diamond lapping film down to 0.5 μm grit. A 20 nm thick layer of carbon was evaporated onto the sample to avoid charging due to the non-conductive epoxy. The polished and coated samples were then examined with a Hitachi S-3100N scanning electron microscope equipped with an EDS probe (voltage: 15 keV). Measurement of 23 random points on both Ta_4Ga_5 and Nb_4Ga_5 revealed only one phase to be present, consistent with powder X-ray diffraction results. The averaged composition, excluding carbon from the conductive coating, was determined to be $Ta_{4.04(12)}Ga_{4.96(12)}$ from the Ta *M*-shell and Ga *L*-shell emission lines for Ta_4Ga_5, and $Nb_{4.03(6)}Ga_{4.97(6)}$ from the Nb *L*- and the Ga *Kα*-shell emission lines for Nb_4Ga_5. No other elements were observed.

Table 6.1. Crystal data for $Ta_{3.86}Mo_{0.14}Ga_5$, Ta_4Ga_5 and Nb_4Ga_5.[a]

Chemical formula	$Ta_{3.86}Mo_{0.14}Ga_5$[b]	Ta_4Ga_5	Nb_4Ga_5
EDS/WDS composition	$Ta_{3.92(12)}Mo_{0.12(2)}Ga_{4.97(13)}$[c]	$Ta_{4.04(12)}Ga_{4.96(12)}$[d]	$Nb_{4.02(7)}Ga_{4.98(7)}$[d]
Space group	$P4_2/mnm$ (no. 136)	$P4_2/mnm$ (no. 136)	$P4_2/mnm$ (no. 136)
Unit cell a [Å]	11.78000(10)	11.78880(10)	11.8279(11)
c [Å]	16.9547(2)	16.9818(3)	17.0691(15)
Cell volume	2352.78 (4)	2360.06(5)	2388.0(4)
Z	16	16	16
Pearson symbol	$tP144$[e]	$tP144$[e]	$tP144$
Cryst. dimensions [mm^3]	0.05×0.03×0.01	0.02×0.01×0.005	0.02×0.02×0.01
Crystal color, habit	Metallic black, plate	Metallic black, irregular	Metallic grey, irregular
Data collection temp.	RT	RT	RT
Radiation source, λ [Å]	Mo, Kα [0.7107]	Mo, Kα [0.7107]	Mo, Kα [0.7107]
Absorption coef. [mm^{-1}]	93.351	96.257	29.428
Absorption correction	Multi-scan	Multi-scan	Multi-scan
θ_{min}, θ_{max}	2.11, 33.39	2.1, 33.45	2.09, 32.6
Number of reflections	69406	60353	46270
Unique refl. [I>3σ(I), all]	2349, 2462	2046, 2469	1843, 2374
Refinement method	F^2	F^2	F^2
Rint [I > 3σ(I), all]	4.55, 4.56	4.22, 4.48	5.30, 5.94
Number of parameters	106	106	99
R[I>3σ(I)],Rw[I>3σ(I)]	0.0200, 0.0656	0.0156, 0.0341	0.0172, 0.0386
R(all), Rw(all)	0.0223, 0.0787	0.0244, 0.0377	0.0289, 0.0423
S[I > 3σ(I)], S(all)	2.29, 2.68	1.58, 1.59	1.07, 1.03
$\Delta\rho_{max}$, $\Delta\rho_{min}$(e-/Å^3)	2.44, -3.12	2.30, -2.36	1.71, -1.41

[a]Crystallographic information files containing further details for $Ta_{3.86}Mo_{0.14}Ga_5$, Ta_4Ga_5, and Nb_4Ga_5 can be obtained from the Fachinformationszentrum Karlsruhe (E-mail: crysdata@fiz-karlsruhe.de), upon quoting the depository numbers 428175, 428173, and 428174, respectively. [b]Preliminary structure model. See text for details. [c]WDS composition. [d]EDS composition. [e]The Pearson symbol refers to an idealized disorder free version of the structure, in which the < 2 % occupancies of the Ta8 and Ta9 sites are rounded to zero.

6.3.5. Electron Probe Microanalysis

The determination of the elemental composition of the $(Ta/Mo)_4Ga_5$ phase was performed using electron probe micro analysis (EPMA). To prepare the sample for EPMA measurements, a small amount of the sample material was suspended in epoxy at one end of a short segment of aluminum tubing. The tube was then ground

Table 6.2. Ta_4Ga_5 atomic coordinates and displacement parameters.

Site	Wyckoff Position	*X*	*y*	*Z*	U_{eff}	Occupancy
Ta1	16d	0.495017(17)	0.207012(17)	0.146334(13)	0.00404(6)	1.0
Ta2	8d	0.753450(18)	0.246550(18)	0.101243(17)	0.00383(6)	1.0
Ta3	8d	0.34746(2)	0.14424(2)	0	0.00372(7)	1.0
Ta4	4d	1/2	0	1/4	0.00286(8)	1.0
Ta5	4d	0.38351(2)	0.38351(2)	0	0.00529(8)	1.0
Ta6	8d	0.390805(17)	0.609195(17)	0.258047(17)	0.00460(6)	1.0
Ta7	16d	0.298033(17)	0.011915(17)	0.148626(13)	0.00375(6)	1.0
Ta8[a]	8d	0.3900(11)	0.3900(11)	0.2392(11)	0.010(4)	0.0176(13)[b]
Ta9[a]	4d	0.1171(15)	0.1171(15)	0	0.010(4)	0.0176(15)[b]
Ga1	8d	1/2	0	0.07756(5)	0.0050(2)	1.0
Ga2	8d	0.24883(7)	0.93523(7)	0	0.0079(2)	1.0
Ga3	8d	0.57159(7)	0.21779(7)	0	0.0066(2)	1.0
Ga4	8d	0.11666(5)	0.11666(5)	0.07435(5)	0.00631(17)	0.9824(15)
Ga5	16d	0.17015(5)	0.33378(5)	0.25994(3)	0.00451(14)	1.0
Ga6	8d	0.26136(5)	0.26136(5)	0.12618(5)	0.00490(16)	1.0
Ga7	8d	0.59051(5)	0.40949(5)	0.08795(5)	0.00615(17)	1.0
Ga8	8d	0.40429(5)	0.40429(5)	0.34108(5)	0.00810(19)	0.9824(13)[b]
Ga9	8d	0.40930(5)	0.40930(5)	0.18043(5)	0.00632(18)	0.9824(13)[b]

[a]Atoms refined isotropically. [b]These partial occupancies are interpreted in terms of cluster disorder; see note [29].

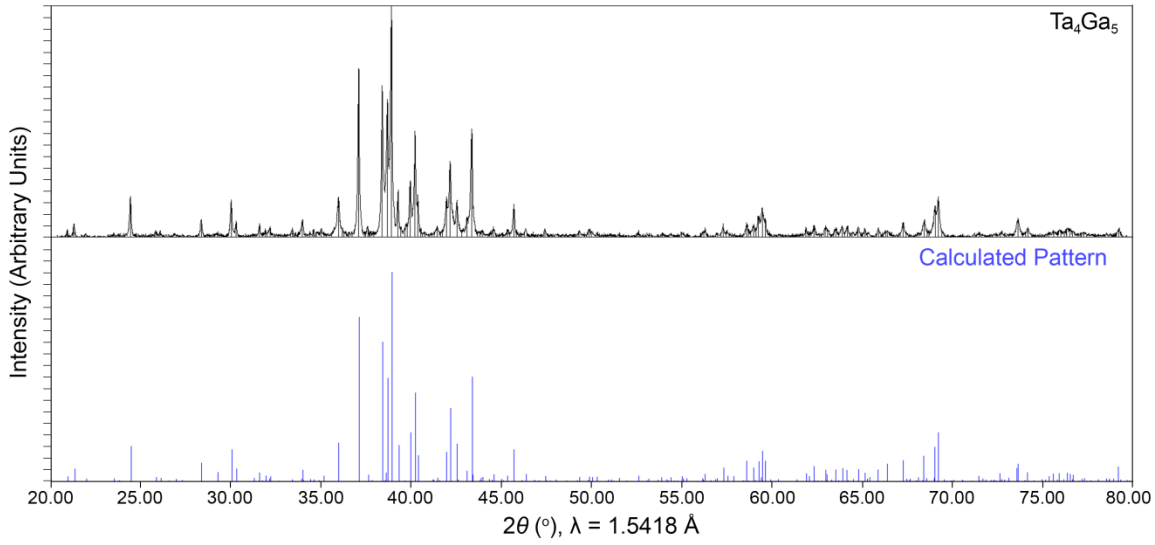

Figure 6.2. Powder X-ray diffraction pattern of Ta_4Ga_5. The top panel gives the experimental pattern for a Ta_4Ga_5 sample, while the bottom panel shows for comparison the intensities calculated from the structure model refined from a single crystal X-ray diffraction data set.

down to produce a smooth flat surface and then polished to reduce the number of surface scratches using a polycrystalline diamond suspension spread on a polishing wheel. As a final step, the sample tube and standards were coated with 250 nm of graphitic carbon and inspected with a Cameca SX-51 electron microprobe using a voltage of 15kV and 30 nA Faraday cup current with a fully focused beam (estimated beam diameter of 500 nm). Ta metal (Sigma Aldrich, >99.9%), Mo metal (provided by the EPMA standard supplier, Tousimis Research Co., 99.97%) and Ga metal (Strem chemicals, 99.99%) were used as standards as the sums of the percentages were close to 100%. The data was processed with the Probe for EPMA software, using the Pouchou and Pichoir model for the matrix correction.[28]

Measurements were taken on a number of random points on the sample materials. Eleven of these showed compositions close to the expected $(Ta/Mo)_4Ga_5$ composition, and gave the averaged composition of $(Ta_{3.92(12)}Mo_{0.12(1)})Ga_{4.97(13)}$ which corresponds well to the $(Ta_{3.86}Mo_{0.14})Ga_5$ composition from the single crystal structure refinement. The remainder of the points corresponded to phases with approximant compositions $Ta_3Ga_2Mo_{x\ (0.05 < x < 0.13)}$ and $TaGaMo_{0.2}$.

6.3.6. Electron Structure Calculations

First principles GGA-DFT calculations were performed on the Ta_4Ga_5-type phases Ta_4Ga_5 and Nb_4Ga_5 using the Vienna Ab Initio Simulation Package (VASP),[30,31] with the ultrasoft pseudopotentials provided with the package.[32] All calculations were carried out in the high precision mode, corresponding to energy cutoffs of 218.21 eV and 218.46 eV for Ta_4Ga_5 and Nb_4Ga_5, respectively, and employed Γ-centered 6×6×4 k-point meshes. Geometrical optimization of the crystal structures was performed by first relaxing the ionic positions, and then releasing all structural parameters. Once the ground state

structures were reached, single point calculations were made to obtain band energies and density of states (DOS) curves.

The output of the GGA-DFT calculations then provided the basis for the parameterization of effective Hückel models using the eHtuner program,[33] which utilizes a modified version of YAeHMOP[34] for the actual Hückel calculations. YAeHMOP was then used to obtain DOS distributions, crystal orbital Hamilton population curves for the structures, as well as for the calculation of the Hamiltonian matrix for the Γ point of a 2×2×2 supercell of Ta_4Ga_5. The Γ point Hamiltonian was then imported into MATLAB, where reversed approximation Molecular Orbital analyses were carried out using in-house functions.

6.4. Results and Discussion

6.4.1. Synthesis and Identification of Ta_4Ga_5-type Phases

Our first crystal exhibiting Ta_4Ga_5-type features was found during a synthetic exploration of the Mo-Ga system using welded Ta tubes as reaction containers. One of the crystals we selected from the synthesis products exhibited an X-ray diffraction pattern consistent with a tetragonal 11.78 Å × 11.78 Å × 16.98 Å unit cell. In a search for similar cells in the transition metal gallide phase diagrams, we found that the Nb_4Ga_5 phase is listed as adopting a tetragonal 8.4 Å × 8.4 Å × 17.1 Å unit cell (but whose structure remained undetermined),[35] which can be approximately transformed to match our crystal's by multiplying the *a*- and *b*- axis lengths by $\sqrt{2}$. Based on this metrical relationship, we suspected that we had obtained Ta_4Ga_5 or a Mo-substituted variant. Our crystal structure solution and refinement supported this hypothesis, yielding a refined composition of $Ta_{3.9}Mo_{0.1}Ga_5$.

After inspecting the Ta-Ga phase diagram in more detail, this synthetic result was somewhat surprising to us. Ta_4Ga_5 appears here as a low-temperature phase which undergoes peritectoid decomposition into $TaGa_3$ and Ta_3Ga_2. At no point does it occur in equilibrium with a melt, making difficult the growth of high quality crystals such as the one obtained in our synthesis. Nevertheless, through experimenting with a variety of synthetic approaches (see the Experimental Section above), we were able to synthesize samples in the Ta-Ga and Nb-Ga binary systems whose powder patterns' major peaks are consistent with binary versions of the $Ta_{3.9}Mo_{0.1}Ga_5$ phase obtained earlier (Figure 6.2). Analysis of crystals selected from these samples revealed that Ta_4Ga_5, Nb_4Ga_5, and $Ta_{3.9}Mo_{0.1}Ga_5$ are closely related. Ta_4Ga_5 and Nb_4Ga_5 are isostructural and represent a new binary structure type.

The strongest reflections for the $Ta_{3.9}Mo_{0.1}Ga_5$ crystal are also consistent with this structure type. A structural refinement with this model leads to reasonable agreement between the calculated and experimental single crystal X-ray diffraction intensities, and yields a Mo content (through partial substitution on the Ta6 and Ta7 sites) that matches that obtained through microprobe measurements. However, close inspection of the diffraction pattern reveals weak superstructure reflections that violate the systematic absence conditions stemming from the *n*-glide of the $P4_2/mnm$ space group. We plan to characterize of this superstructure in conjunction with more systematic studies of Mo-substitution. For now, we include the results of our refinement in a preliminary $P4_2/mnm$ model in Table 6.1 and the Supporting Information.

6.4.2. Structural Description of the Ta_4Ga_5 Type

The basis of all three phases described in this Article is a new structure type. We will refer to this as the Ta_4Ga_5 type, and focus our discussion on this prototype phase. The Ta_4Ga_5 structure is relatively complex, with seven and nine symmetry-distinct Ta and Ga sites, respectively. For Ta_4Ga_5 and $Ta_{3.9}Mo_{0.1}Ga_5$, additional sites with very low occupancy (e.g., ca. 2% for Ta8 and Ta9 in Table 6.2) were uncovered by inspection of the Fourier difference maps. Here, we will restrict ourselves to the sites with full or nearly full occupancy, which encode for a total of 144 atoms per unit cell, while our interpretation of the Ta8 and Ta0 sites in terms of cluster disorder can be found in note 34.

The process of understanding this structure is made considerably simpler by the observation that it is based on an approximately primitive cubic substructure (Figure 6.3). To see this, we begin by noting that the Ta4 site, which occurs at the high symmetry 4*d* positions, forms the center of a small fragment of the *bcc* structure (Figure 6.3a). The Ta4 site is surrounded by a cube of Ta atoms ($Ta4@Ta_8$), whose faces are capped by Ga to create a rhombic dodecahedron, the coordination polyhedron of the *bcc* structure. These $Ta4@Ta_8Ga_6$ clusters pack in a primitive cubic fashion (Figures 6.3b,c), and are linked through Ga-Ga contacts.

The nearly cubic symmetry of this framework is broken by the contents of its void spaces, which are represented in Figures 6.4a,b by ellipsoidal shapes chosen to capture the symmetry relationships among the occupants of the holes. Half of the spaces are filled with distorted icosahedral motifs (yellow ellipsoids in Figures 6.4a,c): flattened Ga_{12} icosahedra center these void spaces, and are enclosed by Ta_{20} pentagonal dodecahedra derived from both additional guest atoms and atoms from the Ta_8 cubes of the host framework.

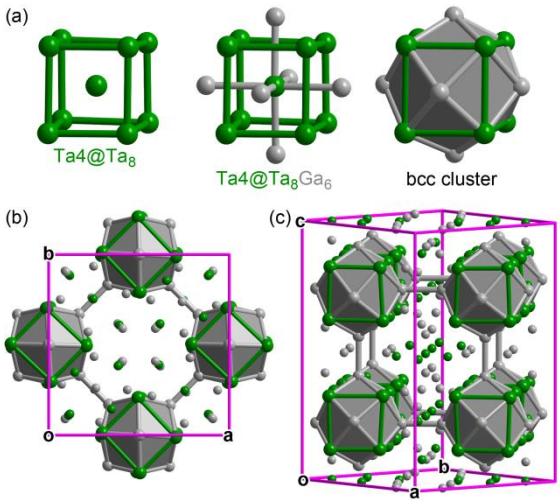

Figure 6.3. The primitive cubic substructure of the Ta_4Ga_5 structure type. (a) The Ta4@Ta_8Ga_6 *bcc* fragment that occurs at the nodes of the primitive cubic framework. (b)-(c) Two views of the cubic substructure shown in the context of the full unit cell.

These icosahedra-stuffed voids alternate with another set of spaces in which the contents form a less recognizable pattern (blue ellipsoids in Figures 6.4a,d). The centers of the cubic holes are occupied by a pair of Ta atoms at a large distance of nearly 4.0 Å, bisected by a square of Ga atoms. The remainder of the space around each Ta atom in the pair resembles a partially successful attempt to create the Ta_8Ga_6 coordination environment of the Ta4 sites.

This arrangement of clusters mirrors the atomic arrangements in a much simpler intermetallic structure type: the $MnAlCu_2$ Heusler type (Figure 6.1). In $MnAlCu_2$, the Cu atoms are arrayed in a primitive cubic network, whose holes are occupied by Mn and Al atoms, similar to the CsCl-type. However, rather than randomly occupying the cubic holes, the Mn and Al atoms are placed in an alternating fashion. The basic features of the Ta_4Ga_5 type are obtained by replacing the Cu atoms of $MnAlCu_2$ with Ta4@Ta_8Ga_6 bcc clusters, the Al atoms with the pseudo-icosahedral units (Figure 6.4c), and the Mn atoms with the bcc fragment dimers (Figure 6.4d).[31]

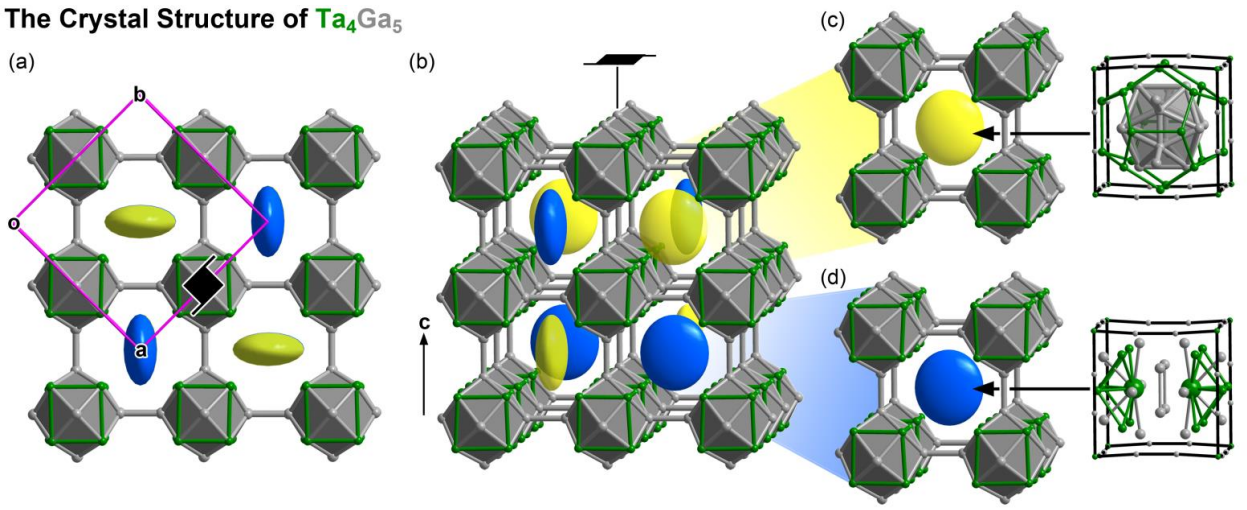

Figure 6.4. The full crystal structure of Ta_4Ga_5, viewed in terms of the filling of a primitive cubic host substructure. The Ta_4Ga_5 structure is first viewed (a) along and (b) approximately perpendicular to the *c*-axis, with yellow and blue ellipsoids indicating the type and orientation of the occupants of each cubic void space. (c) The yellow ellipsoids signify pseudo-icosahedral units centered by flattened Ga_{12} icosahedra which are enclosed in Ta pentagonal dodecahedra. (d) Blue ellipsoids stand for dimers of Ta_7Ga_6 *bcc* fragments separated by Ga squares. See Figure 6.1 for parallels to the $MnAlCu_2$ (Heusler) structure type.

6.4.3. Visualizing Elemental Domains within the Ta_4Ga_5 Structure

In each of these structural features, a surprising theme is encountered: the prominence of homoatomic interactions. For instance, the *bcc* fragments at the vertices of the cubic substructure are centered by clusters of Ta atoms, while the pseudo-icosahedral units are nucleated by Ga_{12} clusters. This trend is also evident in the coordination environments of the individual Ta and Ga sites of the structure. In Figure 6.5, we show the surroundings of the seven symmetry-distinct Ta sites in the structure, with Ta-Ta and Ga-Ga contacts within the coordination shells highlighted. For all but the Ta4 site, the Ta and Ga neighbors to the central atom appear largely aligned toward opposite poles, creating homoatomic domains that seem to clasp each other around the central atom.

The segregation of Ta-Ta and Ga-Ga interactions is more pronounced in the coordination environments of the Ga atoms (Figure 6.6). In these polyhedra, the Ta atoms adopt two basic types of arrangements: pentagonal rings that encircle the central Ga atom (Ga2-Ga4 and Ga6-Ga9) or crowns based on Ta square pyramids with some basal edges capped (Ga1 and Ga5). The Ga neighbors then fill in the remaining spaces.

In both the Ta and Ga coordination environments, a spatial division of the atoms into Ta-rich and Ga-rich domains is observed. How does this apply to the crystal structure as a whole? One way to visualize the presence of such domains in the structure is to attempt to draw interfaces between Ta- and Ga-regions. In Figure 6.7, we illustrate one such surface derived from geometrical considerations.[36] This surface divides the structure into two three-dimensionally-continuous domains, showing that the Ta_4Ga_5 phase can be interpreted in terms of two interpenetrating regions, one Ta-rich, the other Ga-rich. In fact, all of the Ga atoms in the structure lie on the yellow side, while all of the Ta atoms are positioned on the purple side.

This ability to draw surfaces between sublattices of two different elements in a binary structure in itself is not unique, as such could easily be done with, say, the double diamond framework of the NaTl Zintl phase.[37] What is surprising about this surface, however, is the thickness of the domains in many places. For example, at the center of the view in Figure 6.7 is a clustering of Ga tetrahedra on the yellow side of the surface, which is surrounded by Ta bcc fragments on the purple side.

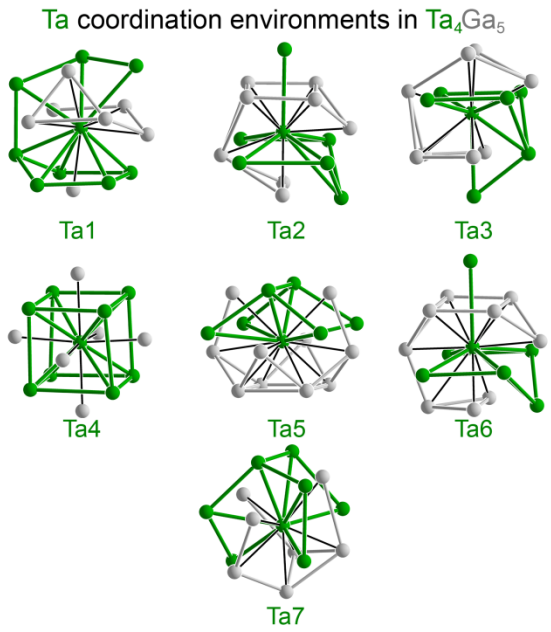

Figure 6.5. Coordination environments for the seven symmetry-distinct Ta sites in Ta_4Ga_5. Ta-Ta and Ga-Ga contacts within the polyhedra are shown to emphasize the prominence of homoatomic interactions.

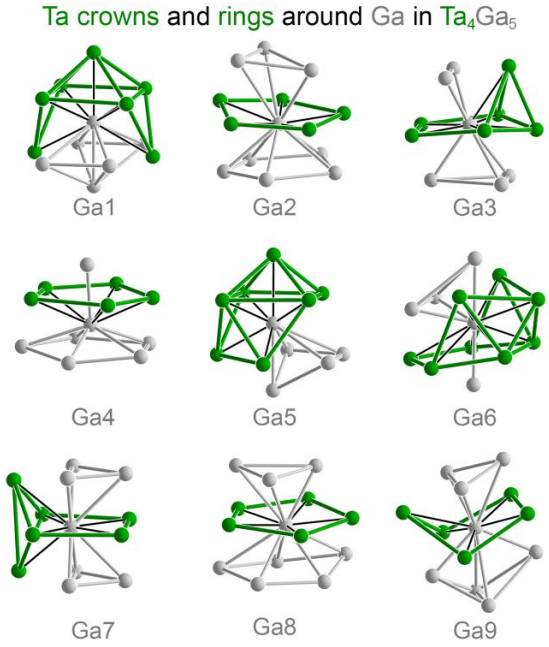

Figure 6.6. Coordination environments of the Ga sites in Ta_4Ga_5, which exhibit clustering of the Ta neighbors into rings and partial cages.

The surface of Figure 6.7 in some ways recalls the use of minimal surfaces or periodic nodal surfaces in interpreting crystal structures. [38-41] A comparison between the current surface and minimal surfaces, in particular, is informative about the nature of the segregation between the Ta and Ga in Ta_4Ga_5. One reason that minimal surfaces are so useful in discussing biphasic phenomena is that they represent the surface-area minimization expected for domains of incompatible bonding types, such as polar and non-polar. However, in the case of Figure 6.7, the surface exhibits bulges of one domain into another; here, the interfacial area is far from being minimized. Based on this observation, we may conclude that Ta-Ga interactions are not simply minimized, but represent an important contributor to the stability of the structure.

For those of us who expect heteroatomic interactions to be the driving force for binary phase formation, this conclusion about the importance of Ta-Ga bonding is comforting. At the same time,

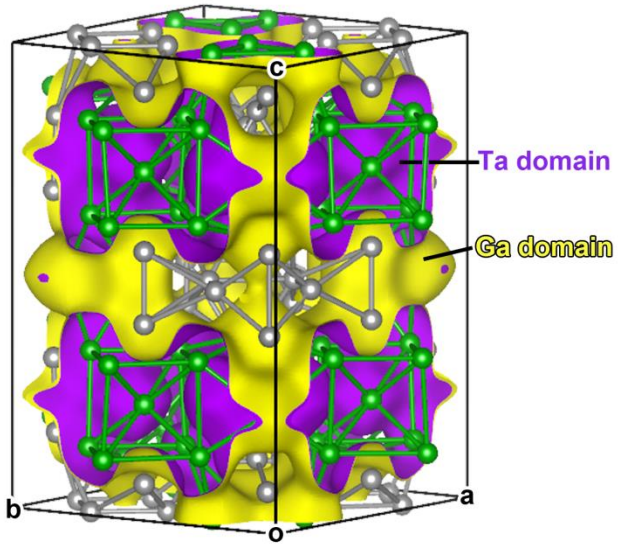

Figure 6.7. Geometrically constructed surface separating the Ta_4Ga_5 structure into Ta and Ga domains. The atoms on the yellow side of the surface are exclusively Ga, while those on the purple side are all Ta. See text for details.

however, it makes the division of the structure into clear Ta and Ga domains more mysterious. In the next section, we will discover that this simultaneous attraction and repulsion between Ta and Ga has origins in multi-center bonding and the nodal properties of the Ga atoms' valence orbitals.

6.4.4. The Electronic Structure of Ta_4Ga_5

In order to understand the origins of the unique host-guest features and homoatomic clustering of the Ta_4Ga_5 type, we carried out GGA-DFT calculations on geometrically optimized structures of Ta_4Ga_5 and Nb_4Ga_5. As in our structural description above, we will focus on the compound Ta_4Ga_5 as a representative of this structure type. For our calculations on this compound, we prepared a slightly idealized structure model, in which the partial occupancies of ca. 98% and 2% for a handful of sites are rounded to 1 or 0, respectively.

The electronic density of states (DOS) curve obtained for Ta_4Ga_5 (the result for Nb_4Ga_5 was very similar; see the Supporting Information) is shown in Figure 6.8a. As with other T-E intermetallics, the DOS distribution can be seen as approximately a superposition of a parabolic nearly-free-electron DOS that stretches to low energies, and a more narrow distribution of T d-orbital based states at an intermediate energy. The Fermi energy (E_F) of the phase lies in a deep well in the DOS that approximately bisects the Ta d block of states. This coincidence of a pseudogap with the transition between filled and empty states strongly indicates that the structure is stabilized by a favorable band-filling.

To gain deeper insights into the origin of this pseudogap, we used the band energies and DOS curves from our DFT calculations as the basis for the parameterization of a simple Hückel model for Ta_4Ga_5.

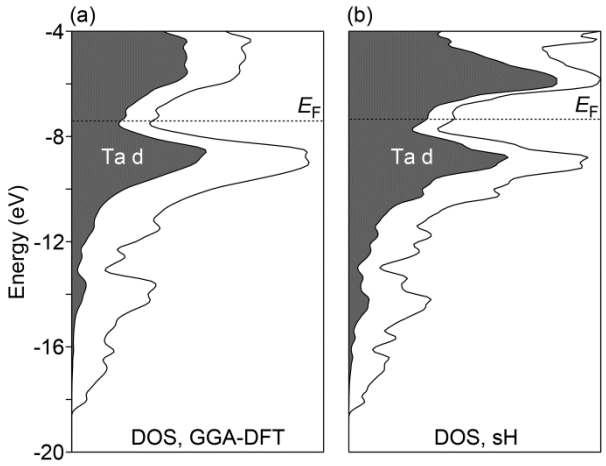

Figure 6.8. Electronic density of states (DOS) distributions calculated for Ta_4Ga_5 using (a) GGA-DFT, and (b) a DFT-calibrated simple Hückel (sH) model. Shaded regions correspond to the contributions from Ta d character. The curves have been treated with Gaussian broadening to make their general features more apparent.

Using our program *eHtuner,*[33] we were able to obtain a simple Hückel model reproducing the DFT band energies with a root-mean-squared deviation of 0.085 eV (for bands up to 1 eV above the E_F).

The DOS distribution calculated using this model is shown alongside the DFT result in Figure 6.8b. While some differences can be noted between the two distributions (particularly above the E_F's), there are important similarities: the Hückel model reproduces the shape of the DOS distribution below the E_F, as well as the energy ranges of its various broad features. Also, the E_F again lies in a deep opening in the DOS distribution, separating two dense mounds of states that are rich in Ta d character. Together these correspondences suggest that the favorability of the phase's electron count should be understandable from the point of view of orbital interactions using this effective Hückel model for the DFT results.

Now that we have established this Hückel model, let us use it to probe deeper into the origins of the DOS pseudogap at the E_F. First, the relative importance of the various interatomic interactions present in the compound can be evaluated through the calculation of crystal orbital Hamilton population (COHP)

curves,[42] in which the DOS distribution is weighted by its component states' energetic contributions to a given interaction. In Figure 6.9, we plot the COHP curves for the Ta-Ta (Figure 6.9b and c), Ga-Ga (Figure 6.9b), and Ta-Ga (Figure 6.9c) interactions in the structure. For all three curves, the COHP function is negative at low energies, corresponding to favorable bonding interactions, and remains negative for all of the occupied states. The transitions to antibonding character occur at various points above the E_F. The first to switch from bonding to antibonding is the Ta-Ta curve, whose transition occurs slightly above the E_F. The Ta-Ga curve displays antibonding character at higher energies (ca -6 eV), while the Ga-Ga curve wobbles about the x=0 axis above the E_F before settling on antibonding character at around -4 eV.

From these COHP curves, it appears that all three interaction types contribute significant bonding to the phase. In terms of the pseudogap, however, the Ta-Ta interactions appear to be especially important: the optimization of Ta-Ta bonding coincides closely to the top of the pseudogap region, suggesting that the gap represents a separation of Ta-Ta bonding and antibonding states. The presence of such Ta-Ta bonding interactions is consistent with the structures' Ta-Ta interatomic distances (2.85 to 3.64 Å in Figure

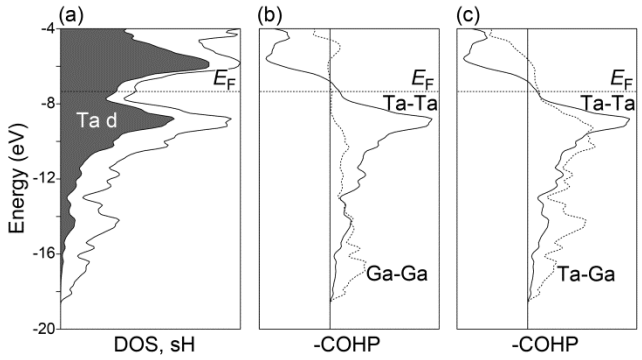

Figure 6.9. Crystal Orbital Hamilton Population (COHP) curves for the homoatomic and heteroatomic interactions in Ta_4Ga_5. (a) The simple Hückel DOS distribution shown for comparison with the COHP curves. (b) COHP curves for the Ta-Ta (solid) and Ga-Ga interactions (dotted). (c) The Ta-Ga COHP curve (dotted) plotted along with the Ta-Ta curve for reference.

6.5), the shortest of which are below the sum of the metallic radii, 2.92 Å).

This transition between Ta-Ta bonding and antibonding character occurs at an electron concentration that is about 0.5 electrons/Ta atom higher than the 8.75 electrons/Ta atom calculated from the formula unit. This small deficiency could explain the ability of the structure to accommodate some substitution with Mo on the Ta sites, as is seen in $Ta_{3.9}Mo_{0.1}Ga_5$, since each Mo atom incorporated increases the number of valence electrons by one.

Based on the position of the DOS pseudogap, it appears that about 9 electrons per Ta atom is a particularly favorable electron count for this phase. What underlies this special electron count? Through bonding analyses on a number of intermetallics formed between transition metals (T) and metalloid elements, we have found that similar pseudogaps could be explained in terms of the 18 electron rule of molecular transition metal complexes. From this point of view, the special stability is obtained when nine electron pairs are associated with a transition metal center, one for each of its nine s, p, and d valence orbitals. For compounds containing T atoms that are isolated from each other, such as $NiSi_2$,[43] $Fe_8Al_{17.4}Si_{7.6}$,[43] and $CrGa_4$,[21] this rule translates into the presence of DOS pseudogaps at 18 electrons/transition metal atom. When T-T contacts are present, as in $Co_3Al_4Si_2$,[44] the sharing of electron pairs between the transition metal atoms allows for 18 electron configurations to be achieved with a smaller number of valence electrons per T: 18-*n*, where *n* is average number of electron pairs.

These considerations lead to a hypothesis for the location of the pseudogap in Ta_4Ga_5 near 9 electrons/Ta atom: this electron count could correspond to 18-*n* electrons with $n = 9$. In other words, each of the Ta atoms' valence s, p, and d atomic orbitals are involved in Ta-Ta bonding interactions, such that they are split across the DOS pseudogap into bonding and antibonding interactions.

6.4.5. Reversed Approximation MO Analysis of Ta_4Ga_5

An approach to testing this idea is given by our recently developed reversed approximation Molecular Orbital (raMO) method.[21] In this technique, one begins by proposing a simple, localized molecular orbital (MO) diagram to explain the bonding interactions in a local part of a larger molecule or solid. One then tests this analogy by using the occupied 1-electron wavefunctions of the full system as a basis set for the calculation of matrix elements for the Hamiltonian operator corresponding to the model MO diagram. Diagonalization of the resulting matrices leads to two classes of eigenvectors: (1) those with nonzero eigenvectors, corresponding to the best approximation to the true eigenstates of the operator possible using the occupied 1-electron wavefunctions of the full compound (while maintaining orthogonality between the eigenstates) and (2) eigenvectors with eigenvalues of zero. The latter set of solutions consists of functions that are orthogonal to the model MO diagram, and thus represent components of a separate bonding system. In this way, isolobal analogies are used to dissect the electronic structure of a complex molecule or solid into a series of orthogonal bonding systems.

Our tentative association of the valence electron concentration of about 9 valence electrons/Ta atom with a half-filling of the 9 valence atom orbitals for the Ta atoms suggests a very simple MO diagram as a starting point: isolated Ta atoms, for which the eigenstates are simply the individual atomic orbitals. If this line of thinking is correct, then raMO analyses using the Ta s, p, and d as target states should lead to eigenvectors centered by each of these orbitals, and each of them should show substantial bonding interactions with neighboring Ta atoms.

A first confirmation of this approach can be found by using the full set of s, p, and d orbitals of all of the Ta atoms as target eigenstates. Upon performing the raMO procedure using this model Hamiltonian,

only eigenvectors with non-zero eigenvectors are obtained. All electrons in the structure are then associated in some way with the Ta atoms, i.e. there are no functions (corresponding, say, to Ga-Ga interactions) that are orthogonal to all of the Ta orbitals. We are to some extent justified, then, in expressing the electron concentration in terms of the electrons per Ta atom.

Let's focus our attention now on what these Ta-based functions look like. In Figure 6.10, we display the raMO functions obtained using the s, p, and d orbitals of a Ta atom on the Ta4 site as target eigenstates. An inspection of the orbital character on the central atom of each of the raMO functions indicates that nine s, p, and d orbitals of the central atom are all represented. However, rather than occurring alone, as would be the case for a nonbonding orbital, all of them exhibit significant in-phase contributions from the surrounding Ga and Ta atoms. This observation is consistent with the results of COHP analysis described above: the Ta atoms are stabilized by substantial Ta-Ta and Ta-Ga bonding.

The ability to use the occupied wavefunctions to create nine functions localized around the Ta4 site with the symmetry properties of its atomic valence orbitals is highly suggestive of the presence of an 18 electron configuration at this atom. Given the low electron concentration of Ta_4Ga_5 (8.75 electrons/Ta), such 18 electron configurations should only be possible with the support of extensive sharing of electrons between Ta atoms. The requisite interactions are readily seen through examination of how the raMO functions spread out from the central Ta4 atom to its neighbors. Its Ta neighbors trace out a slightly distorted cube (green). The central s and p orbitals, as well as the d_{xy}, d_{xz}, and d_{yz}, are well oriented for σ interactions with these neighboring Ta atoms, and indeed each of the raMO functions exhibit hybrid

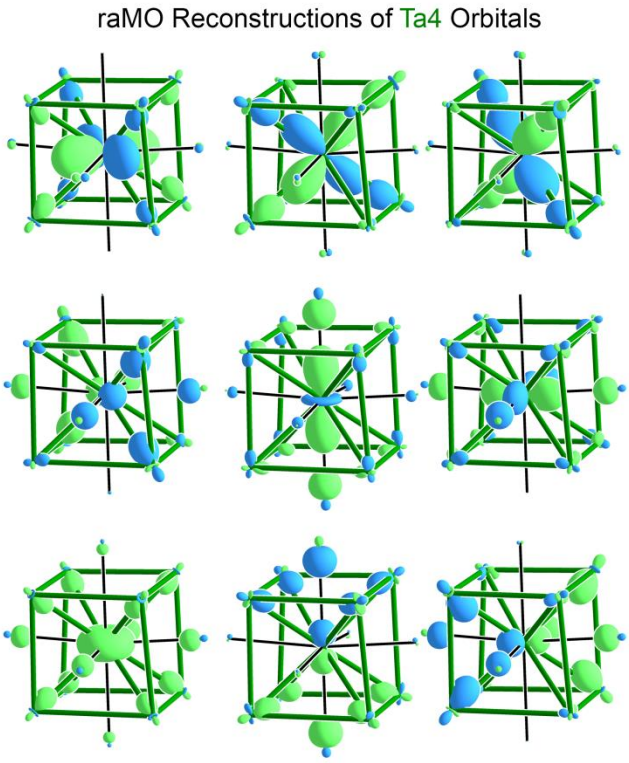

Figure 6.10. raMO reconstructions of the Ta4 site's valence s, p, and d orbitals. See the Supporting Information for a more detailed examination of the degree of localization of these functions.

orbitals on the Ta neighbors (containing s, p, and d character) directed in a bonding fashion toward the central orbital. All seven of these raMO functions represent electron pairs that are involved in significant Ta-Ta bonding. This sharing of electrons between the Ta atoms should be very effective for reducing the necessary electron count for closed-shell electron configurations.

The remaining central orbitals (d_{z2} and d_{x2-y2}) have nodal surfaces that pass through the vertices of a cubic coordination environment, and are thus not well adapted to σ-interactions with the Ta neighbors (but do exhibit strong σ-overlap with lobes on the Ga). Nevertheless, close inspection of the raMO functions reveals contributions from these Ta neighbors: they bear dp hydrids that overlap in a π fashion with the central Ta atom's orbital. The presence of these dp hybrids in the raMOs indicates that the

appearance of the central d_{z2} and d_{x2-y2} functions in the occupied wavefunctions of the system is strongly correlated with in-phase combinations of these π orbitals. Where σ bonding between the Ta atoms is not possible, π bonding takes over.

We have now looked in detail at the raMO functions generated for one Ta site, Ta4. Based on the very different geometrical arrangements of Ta and Ga neighbors for the other six symmetry distinct Ta sites, one might expect that the raMO analysis would lead to different results. However, the raMO functions generated for the remaining Ta sites are in fact remarkably similar, as is illustrated for the Ta2 site in Figure 6.11 (the corresponding diagrams from the remaining Ta sites are provided in the Supporting Information). All nine of the central valence orbitals are well-reproduced in the raMOs. Furthermore, each orbital exhibits Ta-Ta bonding interactions of some sort, which is in many cases supported by bridging interactions with Ga atoms. From this point of view, the clustering of the Ta atoms into their own domain in Ta_4Ga_5 can be seen as supporting the extensive Ta-Ta σ and π interactions needed for the DOS pseudogap at the E_F.

Turning to a raMO analysis of the Ga sites reveals how their placement in the structure helps widen the DOS pseudogap. In Figure 6.12, we present raMO functions which result from the use of the Ga valence orbitals as target eigenstates, using the Ga1 and Ga2 sites as representative examples (the complete set is provided in the Supporting Information). As we saw for the Ta sites earlier, each of the Ga valence orbitals can be seen at the center of a raMO function. All of the functions exhibit bonding interactions with their Ta neighbors, which are mostly of σ-character. The prominence of Ta-Ga overlap in these raMOs is consistent with the strong Ta-Ga interactions appearing in our COHP curves. The close-matching of the nodal properties of the central Ga atomic orbitals and their surrounding Ta lobes

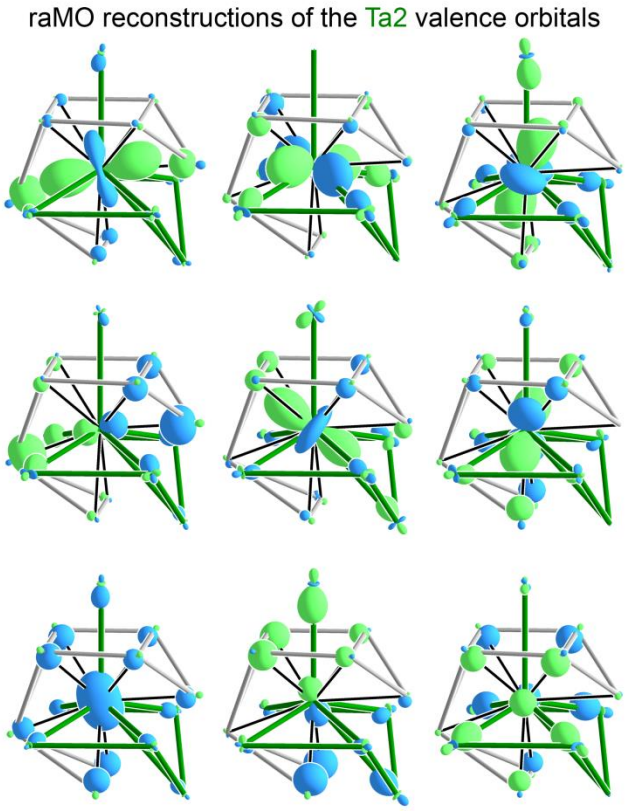

Figure 6.11. raMO functions generated from the occupied crystal orbitals of Ta_4Ga_5 using the valence orbitals of an atom on the Ta2 site as target eigenstates.

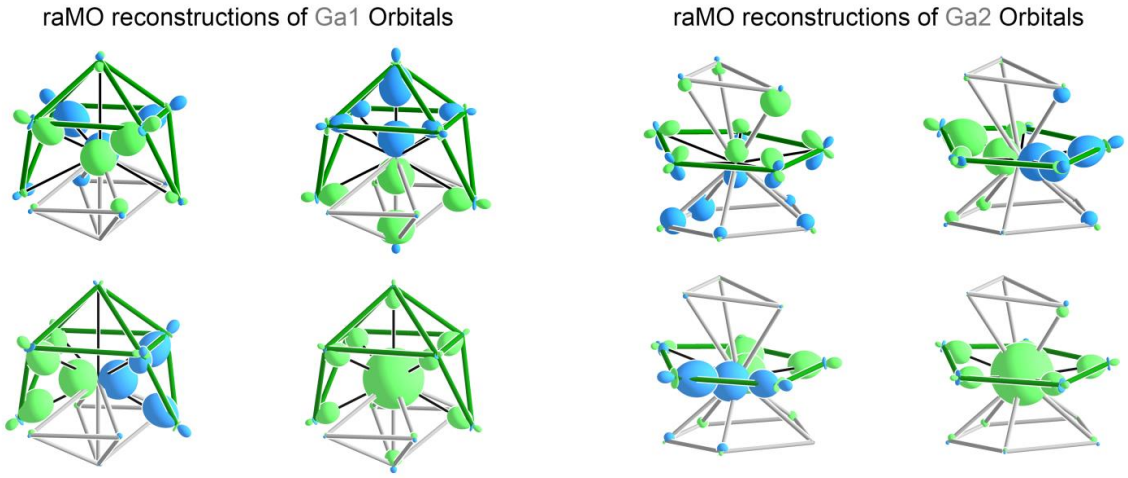

Figure 6.12. raMO functions generated using the valence atomic orbitals of the Ga1 (left) and Ga2 (right) sites in Ta_4Ga_5 as target eigenstates. See the Supporting Information for corresponding analyses of the remaining symmetry-distinct Ga sites.

also helps us understand why Ta-centered raMOs are sufficient to reconstruct the full electronic structure of the compound.

This match in the nodal properties also has implications for the Ta-Ta bonding in the compound. Note that the small number of nodes passing through the Ga center translates into a small number of nodes switching the phases between adjacent Ta atoms in the Ga atoms' coordination environments (Figure 6.13). In this way, the clustering of Ta atoms within these polyhedra naturally leads to Ta-Ta bonding, as the Ta-Ta antibonding functions for a tightly packed ring or cap of Ta atoms would have too many nodes to be effectively stabilized by the Ga s or p orbitals.

The placement of the Ga atoms at the outskirts of the Ta clusters then means that Ta-Ga bonding takes on a multicenter character that correlates with Ta-Ta bonding. A natural result of this is the nearly simultaneous optimization of the Ta-Ta and Ta-Ga interactions in the COHP curves (Figure 6.9).

This multicenter bonding character also plays an important role in the formation of the pseudogap at the E_F. As the pseudogap coincides with the Ta-Ta bonding to antibonding transition in the COHP, the ability of the Ga to preferentially stabilize the Ta-Ta bonding states should deepen the gap. In fact, a Hückel calculation in which the Ga atoms are removed from Ta_4Ga_5 leads to essentially a complete closure of the

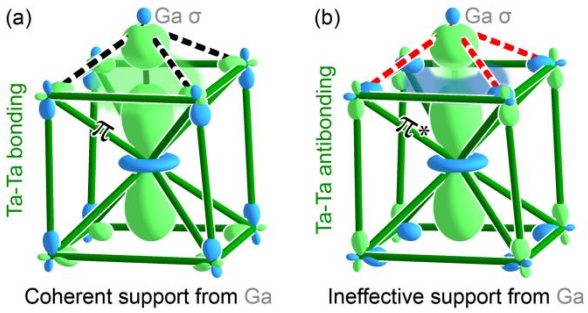

Figure 6.13. Preferential support given by bridging Ga atoms to (a) Ta-Ta bonding orbitals over their (b) Ta-Ta antibonding counterparts.

pseudogap. In this way, the bridging of the Ta-Ta interactions by Ga appears to be essential to the stability of the phase.

In this bonding picture, Ta-Ta and Ta-Ga interactions appear as tightly intertwined, but Ga-Ga interactions have not been assigned a part yet. An examination of the Ga-centered raMOs in Figure 6.12 reveals that the Ga neighbors join the Ta atoms in decorating the central orbital with bonding lobes. In most cases, however, their contributions are smaller than those of the Ta atoms. They also generally share the lobe of the central atom with Ta neighbors. From these observations, we conclude that the Ga-Ga interactions largely serve to support the wavefunctions already templated by Ta-Ta and Ta-Ga interactions. However, the tight packing of Ga atoms and the small number of angular nodes in their valence orbitals allows for Ga-Ga bonding overlap to emerge in this situation. Where contributions from the Ga neighbors to the Ga centers of Figure 6.12 are visible, the interactions are invariably stabilizing.

6.5. Conclusions

This has been a story of reluctant intermetallic phases, which defy the expectation that heteroatomic interactions will dominate the structures of binary compounds. We first described a new binary structure type formed by Ta_4Ga_5 (with and without a little Mo substitution) and Nb_4Ga_5 from several viewpoints. One approach was through a hierarchical relationship to the Heusler structure type, in which atoms are replaced with clusters. A close variation on this view was recognizing that one set of the clusters connect together into a primitive cubic framework which serves as a host matrix for the remaining clusters.

These descriptions are useful in terms of visualizing the structure type, but a deeper connection to the driving forces shaping the structure was made through an inspection of the individual coordination

environments of the atomic sites. Around the majority of the sites, there is a pronounced tendency for the Ga and Ta atoms to collect together into homoatomic clusters. Upon zooming out to see the structure as a whole, we found that the Ta and Ga atoms can be segregated into distinct 3-dimensional domains that interpenetrate each other.

Theoretical analysis of the Ta_4Ga_5 structure using DFT-calibrated Hückel calculations and the reversed approximation MO (raMO) analysis revealed how this segregation helps stabilize the phase. The electronic density of states (DOS) distributions exhibits a deep well at the E_F, a strong indication that a favorable electron configuration has been achieved. This pseudogap can be traced to the clustering of Ta atoms within small angular ranges around the Ga atoms, which allows for correlations between Ta-Ta and Ta-Ga bonding overlap. The multicenter character of the interactions leads to the near simultaneous optimization of Ta-Ta and Ta-Ga bonding (though for both, weaker tails of bonding extend upwards beyond the E_F).

The unexpected structural features of this phase have led us to wonder (from the comfortable perspective of hindsight) whether any of these aspects of this structure type could have been anticipated ahead of time. One emerging principle of transition metal-main group (T-E) intermetallics that is especially useful here is the importance of filled 18 electron configurations on the T atom sites. For a growing series of intermetallic compounds, we have been able to connect DOS pseudogaps or band gaps to an association of electron pairs to each of the nine valence orbitals of the T atoms. Where deficiencies are encountered in the electron count relative to 18 electrons per T atom, filled configurations tend to be achieved through the sharing of electron pairs in E-supported T-T bonds.

From this point of view, the clustering of T atoms together could be expected from the valence electron count of Ta_4Ga_5. The stoichiometry of the phase gives an average number of electrons per Ta atom of only 8.75, which is less than half of that needed for the Ta atoms to achieve closed shells independently of each other. Extensive sharing of electron pairs between the Ta atoms would thus be needed, which would require substantial clustering of the Ta atoms. Our raMO analysis confirms this bonding picture, but falls short of predicting the precise electron count at which the bonding will be optimized. It will be interesting to see whether these correlations between low valence electron count and T/E segregation can be extended to other structures. One example that comes to mind here is the complex rhombohedral structure of MnGa,[45] in which homoatomic clustering similar to that we have seen in this Article can be perceived in the coordination environments of most of the atomic sites.

A way to screen vast numbers of intermetallic structures for this type of homoatomic clustering would be helpful in testing this hypothesis more broadly. The characteristics of the coordination environments in the Ta_4Ga_5 type suggest one approach for such an endeavor. Most of the coordination environments exhibit a polar or quadrupolar distribution of the Ta and Ga atoms. Such distributions could be identified in an automated fashion by assigning a positive or negative number to the two atom types in the coordination shell of each site in a structure, and then projecting these numbers onto spherical harmonics. Structures whose atoms have large magnitudes for the low order functions could then be selected for more detailed structural analysis. We are looking forward to employing this procedure in search of compounds exhibiting chemically-frustrated structures.

6.6. Acknowledgments

This article is dedicated to the memory of Prof. John Corbett, who showed so many of us how the greatest gift that synthesis offers is not validation of our own preconceived notions but the discovery of new possibilities beyond imagining. We thank Dr. John Fournelle for assistance with the EPMA measurements. We gratefully acknowledge the financial support of the US DOE, Office of Science Early Career Program (DE-SC0003947) through the Office of Basic Energy Sciences. BJK thanks the National Science Foundation for a graduate student fellowship (DGE-1256259). This research involved calculations using computer resources supported by National Science Foundation CHE-0840494.

6.7. References

(1) Smithells, C. J.; Gale, W. F.; Totemeier, T. C. *Smithells metals reference book*; 8th ed.; Elsevier Butterworth-Heinemann: Amsterdam ; Boston, 2004.

(2) Fredrickson, D. C.; Lee, S.; Hoffmann, R. *Angew. Chem. Int. Ed.* **2007**, *46*, 1958-1976.

(3) Conrad, M.; Harbrecht, B.; Weber, T.; Jung, D. Y.; Steurer, W. *Acta Crystallogr. B* **2009**, *65*, 318-325.

(4) Weber, T.; Dshemuchadse, J.; Kobas, M.; Conrad, M.; Harbrecht, B.; Steurer, W. *Acta Crystallogr. B* **2009**, *65*, 308-317.

(5) Guo, Y.; Stacey, T. E.; Fredrickson, D. C. *Inorg. Chem.* **2014**, *53*, 5280-5293.

(6) Harris, N. A.; Hadler, A. B.; Fredrickson, D. C. *Z. Anorg. Allg. Chem.* **2011**, *637*, 1961-1974.

(7) Hadler, A. B.; Harris, N. A.; Fredrickson, D. C. *J. Am. Chem. Soc.* **2013**, *135*, 17369-17378.

(8) Solokha, P.; De Negri, S.; Pavlyuk, V.; Saccone, A. *Solid State Sci.* **2009**, *11*, 801-811.

(9) Kovnir, K.; Shatruk, M. *Eur. J. Inorg. Chem.* **2011**, *2011*, 3955-3962.

(10) Yvon, K. *Acta Crystallogr. B* **1974**, *30*, 853-861.

(11) Girgis, K.; Petter, W.; Pupp, G. *Acta Crystallogr. B* **1975**, *31*, 113-116.

(12) Häussermann, U.; Viklund, P.; Svensson, C.; Eriksson, S.; Berastegui, P.; Lidin, S. *Angew. Chem. Int. Ed.* **1999**, *38*, 488-492.

(13) Yvon, K. *Acta Crystallogr. B* **1975**, *31*, 117-120.

(14) Okamoto, H. In *Binary Alloy Phase Diagrams, 2nd Ed.*; Massalski, T. B., Ed. 1990; Vol. 2, p 1861-1862.

(15) Baron, V. V.; Myzenkova, L. F.; Savitskii, E. M.; Gladyshevskii, E. I. *Zh. Neorg. Khim.* **1964**, *9*, 2170-2173.

(16) Carrillo-Cabrera, W.; Caroca-Canales, N.; von Schnering, H. G. *Z. Anorg. Allg. Chem.* **1994**, *620*, 247-257.

(17) Flot, D.; Tillard-Charbonnel, M.; Belin, C. *New J. Chem.* **1998**, *22*, 591-598.

(18) Blatov, V. A.; Shevchenko, A. P.; Proserpio, D. M. *Cryst. Growth Des.* **2014**, *14*, 3576-3586.

(19) Heusler, O. *Ann. Phys.-Berlin* **1934**, *411*, 155-201.

(20) Such a hierarchical relationship to the MnAlCu2 type has also been noted for the Tb117Fe52Ge112 type. See Ref. 9.

(21) Yannello, V. J.; Kilduff, B. J.; Fredrickson, D. C. *Inorg. Chem.* **2014**, *53*, 2730-2741.

(22) Girgis, K. *J. Cryst. Growth* **1975**, *30*, 99-100.

(23) Oszlányi, G.; Sütő, A. *Acta Crystallogr A* **2004**, *60*, 134-141.

(24) Oszlányi, G.; Sütő, A. *Acta Crystallographica, Section A: Foundations of Crystallography* **2005**, *61*, 147-152.

(25) Palatinus, L.; Chapuis, G. *J. Appl. Crystallogr.* **2007**, *40*, 786-790.

(26) Petříček, V.; Dušek, M.; Palatinus, L. *Z. Kristallogr.* **2014**, *229*, 345-352.

(27) Momma, K.; Izumi, F. *J. Appl. Crystallogr.* **2011**, *44*, 1272-1276.

(28) *Probe for EPMA User's Guide and Reference*; Donovan, J. J.; Kremswer, D.; Fournelle, J.; Karsten, G., Eds.; Probe Software, Inc.: Eugene, 2013.

(29) In our discussion of the Ta_4Ga_5 structure, we treat the filling pattern of the voids of the primitive cubic network of Ta@Ta8Ga6 units as perfectly ordered. For the Ta_4Ga_5 and $Ta_{3.9}Mo_{0.1}Ga_5$ crystals that we have examined indicate that this is a slight approximation. Fourier difference maps for this ordered model show noticable peaks which correspond to some of the Ta positions that would arise when replacing one occupant type with the other. These are listed as Ta8 and Ta9 in Table 6.2. Occupation of the Ta8 sites leads to the completion of a Ta pentagonal dodecahedron surrounding the voids containing the bcc fragment dimers. The Ta9 site, meanwhile, corresponds to the placement of a pair of Ta atoms (as occurs at the centers of the bcc fragment dimers) into the center of the distorted Ga12 icosahedra. These sites exhibit unrealistically short distances to some of the Ga sites (Ga4, Ga8, and Ga9), whose occupancies were thus constrained to a model in which these Ga sites are vacant when their nearby Ta8 or Ta9 is occupied. It is likely that the occupation of Ta8 and Ta9 occurs concomitantly with full cluster substitution. However, due to the small values of their refined occupancies (< 2 %), the any remaining disorder has at most a faint signature in the Fourier electron density.

(30) Kresse, G.; Furthmüller, J. *Phys. Rev. B* **1996**, *54*, 11169-11186.

(31) Kresse, G.; Furthmüller, J. *Comput. Mater. Sci.* **1996**, *6*, 15-50.

(32) Vanderbilt, D. *Physical Review B* **1990**, *41*, 7892-7895.

(33) Stacey, T. E.; Fredrickson, D. C. *Dalton Trans.* **2012**, *41*, 7801-7813.

(34) Landrum, G. A.; Glassey, W. V. YAeHMOP: Yet Another extended Hückel Molecular Orbital Package. YAeHMOP is freely available on the WWW at http://sourceforge.net/projects/yaehmop/ Last accessed: 31 Aug. 2014.

(35) Dryś, M. *J. Less Common Met.* **1978**, *58*, 111-113.

(36) The surface in Figure 6.7 was generated by placing exponential decay functions of the form $\pm e^{-\zeta r}$ on each of the atomic centers, where ζ is an adjustable parameter, and the positive and negative signs are used for Ta and Ga respectively. The interface between Ta and Ga domains then emerges when a function f(x,y,z) is constructed from the sums of these atom-centered functions, and the f=0 isosurface is plotted. For the surface in Figure 6.7, ζ was set to 2.0 $Å^{-1}$.

(37) Zintl, E.; Dullenkopf, W. *Z. Phys. Chem. B* **1932**, *16*, 195-205.

(38) von Schnering, H. G.; Nesper, R. *Angew Chem Int Edit* **1987**, *26*, 1059-1080.

(39) Hyde, S.; Andersson, S.; Larsson, K.; Blum, Z.; Landh, T.; Lidin, S.; Ninham, B. W. *The Language of Shape*; Elsevier: Amsterdam, 1997.

(40) Hyde, S. T.; Andersson, S. *Z. Kristallogr.* **1984**, *168*, 221-254.

(41) Hyde, S. T.; Andersson, S. *Z. Kristallogr.* **1985**, *170*, 225-239.

(42) Dronskowski, R.; Blöchl, P. E. *J. Phys. Chem.* **1993**, *97*, 8617-8624.

(43) Fredrickson, R. T.; Fredrickson, D. C. *Inorg. Chem.* **2012**, *51*, 10341-10349.

(44) Fredrickson, R. T.; Fredrickson, D. C. *Inorg. Chem.* **2013**, *52*, 3178-3189.

(45) Gourdon, O.; Miller, G. J. *J. Solid State Chem.* **2003**, *173*, 137-147.

Appendix A.

Supporting Information for Chapter 2:

Progress in Visualizing Atomic Size Effects with DFT-Chemical Pressure Analysis: From Isolated Atoms to Trends in AB_5 Intermetallics

A.1. Detailed Technical Procedures

The geometrical optimization of each structure was carried out in two steps: first the ionic positions were relaxed in a fixed unit cell, and then all structural parameters were released. Energy cutoffs for the planewave basis were set sufficiently high to converge the energy of formation to less than 0.5 meV/atom. Monkhorst-Pack k-point grids[1] were constructed by specifying the ngkpt input parameter or by using the prtkpt utility. Unless otherwise specified, semicore HGH potentials[2] (when available) were used for all atoms, with the exception of Pd, for which the valence-only version is most comparable to the semicore pseudopotentials of Cu, Ag and Au. Further details regarding the calculations are given in Table A.1, while the optimized structural parameters are listed in Tables A.2-A.11.

Once the optimizations were complete, three single-point calculations were performed over a span of 3% about the optimal unit cell volume to prepare the electron densities, potentials, and kinetic energy densities needed for the creation of CP maps. The voxel spacing in the CP maps were derived from the fast Fourier transform grids used in the ABINIT calculations. The DFT-CP software is based on two programs used to calculate the CP maps, as well as integrate and project the CP distribution around each

atom. *CPmap* generates the CP maps from the ABINIT single point calculations, and including the grid unwarping procedure described in the main text. The Hirshfeld-inspired integration scheme is implemented in the *CPintegrate* program, which was used to project the CP map onto real spherical harmonics ($l \leq 5$) centered at the atomic positions.

Table A.1. Computational parameters and total energies

Structure[a]	*Energy cutoff*	*Number of unique k-points*	*FFT grid*	*Total energy*
Isolated Ca (SC)	35 Ha	1	150 × 150 × 150	-36.640997 Ha
Isolated Ca (VO)	35 Ha	1	150 × 150 × 150	-0.668313 Ha
Isolated La	40 Ha	1	150 × 150 × 150	-31.592133 Ha
Isolated Cu	45 Ha	1	120 × 120 × 120	-46.910665 Ha
Isolated Pd	40 Ha	1	150 × 150 × 150	-28.799283 Ha
Isolated Cd	35 Ha	1	150 × 150 × 150	-45.998438 Ha
Isolated Au	80 Ha	1	150 × 150 × 150	-33.160002 Ha
Isolated Ga (SC)	80 Ha	1	150 × 150 × 150	-74.004191 Ha
Isolated Ga (VO)	80 Ha	1	150 × 150 × 150	-2.149122 Ha
$SrAg_5$	50 Ha	15	150 × 150 × 120	-215.769000 Ha
La_5Sn_3	40 Ha	4	108 × 108 × 108	-339.327910 Ha
Ni_3C	80 Ha	60	80 × 80 × 80	-234.948791 Ha
$NbGa_3$	50 Ha	18	75 × 75 × 75	-12.047973 Ha
$CaCu_5$ ($CaCu_5$-type)	85 Ha	15	150 × 150 × 120	-277.195271 Ha
$CaCu_5$ ($AuBe_5$-type)	85 Ha	10	150 × 150 × 150	-1108.722801 Ha
$CaAu_5$ ($CaCu_5$-type)	30 Ha	15	150 × 150 × 120	-203.316309 Ha
$CaAu_5$ ($AuBe_5$-type)	30 Ha	10	120 × 120 × 120	-813.277045 Ha

[a]"Isolated" refers to a single atom placed in the center of a 10 Å cubic unit cell. See Tables A.2 and A.3.

A.2. Structural parameters

Table A.2. Unit cell parameters for DFT-optimized structures (converted to conventional cells for convenience)

Structure	*a*	*b*	*c*	*α*	*β*	*γ*
All isolated atoms	10.00000 Å	10.00000 Å	10.00000 Å	90°	90°	90°
$SrAg_5$	5.55915 Å	5.55915 Å	4.54145 Å	90°	90°	120°
La_5Sn_3	12.59205 Å	12.59205 Å	6.17215 Å	90°	90°	90°
Ni_3C	4.49667 Å	4.49667 Å	12.71836 Å	90°	90°	120°
$NbGa_3$	3.68337 Å	3.68337 Å	8.52030 Å	90°	90°	90°
$CaCu_5$ ($CaCu_5$-type)	4.97267 Å	4.97267 Å	3.97010 Å	90°	90°	120°
$CaCu_5$ ($AuBe_5$-type)	6.88885 Å	6.88885 Å	6.88885 Å	90°	90°	90°
$CaAu_5$ ($CaCu_5$-type)	5.48234 Å	5.48234 Å	4.63381 Å	90°	90°	120°
$CaAu_5$ ($AuBe_5$-type)	7.71309 Å	7.71309 Å	7.71309 Å	90°	90°	90°

Table A.3. Atomic coordinates for all single-atom calculations

Element	*x*	*y*	*z*
Any	0.50000	0.50000	0.50000

Table A.4. Atomic coordinates for ABINIT-optimized $SrAg_5$ structure

Element	*x*	*y*	*z*
Sr	0.00000	0.00000	0.00000
Ag	0.33333	0.66667	0.00000
Ag	0.66667	0.33333	0.00000
Ag	0.50000	0.50000	0.50000
Ag	0.00000	0.50000	0.50000
Ag	0.50000	0.00000	0.50000

Table A.5. Atomic coordinates for ABINIT-optimized La_5Sn_3 structure (converted to conventional cell for convenience)

Element	*x*	*y*	*z*
La	0.08563	0.21856	0.00000
La	0.58563	0.71856	0.50000
La	0.00000	0.50000	0.25000
La	0.50000	0.00000	0.75000
La	0.78144	0.08563	0.00000
La	0.28144	0.58563	0.50000
La	0.50000	0.00000	0.25000
La	0.00000	0.50000	0.75000
La	0.91437	0.21856	0.50000
La	0.41437	0.71856	0.00000
La	0.41437	0.28144	0.50000
La	0.91437	0.78144	0.00000
La	0.28144	0.41437	0.00000
La	0.78144	0.91437	0.50000
La	0.21856	0.08563	0.50000
La	0.71856	0.58563	0.00000
La	0.71856	0.41437	0.50000
La	0.21856	0.91437	0.00000
La	0.58563	0.28144	0.00000
La	0.08563	0.78144	0.50000
Sn	0.15987	0.65987	0.00000
Sn	0.65987	0.15987	0.50000
Sn	0.00000	0.00000	0.25000
Sn	0.50000	0.50000	0.75000
Sn	0.34013	0.15987	0.00000
Sn	0.84013	0.65987	0.50000
Sn	0.34013	0.84013	0.50000
Sn	0.84013	0.34013	0.00000
Sn	0.15987	0.34013	0.50000
Sn	0.65987	0.84013	0.00000
Sn	0.00000	0.00000	0.75000
Sn	0.50000	0.50000	0.25000

Table A.6. Atomic coordinates for ABINIT-optimized $NbGa_3$ structure (converted to conventional cell for convenience)

Element	*x*	*y*	*z*
Nb	0.00000	0.00000	0.00000
Nb	0.50000	0.50000	0.50000
Ga	0.00000	0.00000	0.50000
Ga	0.50000	0.50000	0.00000
Ga	0.00000	0.50000	0.25000
Ga	0.50000	0.00000	0.75000
Ga	0.50000	0.00000	0.25000
Ga	0.00000	0.50000	0.75000

Table A.7. Atomic coordinates for VASP-optimized Ni_3C structure (converted to conventional cell for convenience)

Element	*x*	*y*	*z*
Ni	0.33333	0.00000	0.25000
Ni	0.66667	0.00000	0.75000
Ni	0.00000	0.33333	0.25000
Ni	0.00000	0.66667	0.75000
Ni	0.66667	0.66667	0.25000
Ni	0.33333	0.33333	0.75000
Ni	0.00000	0.33333	0.08333
Ni	0.33333	0.33333	0.58333
Ni	0.66667	0.66667	0.41667
Ni	0.66667	0.00000	0.58333
Ni	0.33333	0.00000	0.41667
Ni	0.00000	0.66667	0.58333
Ni	0.66667	0.66667	0.08333
Ni	0.00000	0.66667	0.91667
Ni	0.33333	0.00000	0.08333
Ni	0.33333	0.33333	0.91667
Ni	0.00000	0.33333	0.41667
Ni	0.66667	0.00000	0.91667
C	0.00000	0.00000	0.00000
C	0.00000	0.00000	0.50000
C	0.66667	0.33333	0.33333
C	0.66667	0.33333	0.83333
C	0.33333	0.66667	0.66667
C	0.33333	0.66667	0.16667

Table A.8. Atomic coordinates for ABINIT-optimized $CaCu_5$ structure ($CaCu_5$-type)

Element	*x*	*y*	*z*
Ca	0.00000	0.00000	0.00000
Cu	0.33333	0.66667	0.00000
Cu	0.66667	0.33333	0.00000
Cu	0.50000	0.50000	0.50000
Cu	0.00000	0.50000	0.50000
Cu	0.50000	0.00000	0.50000

Table A.9. Atomic coordinates for ABINIT-optimized $CaCu_5$ structure ($AuBe_5$-type)

Element	*x*	*y*	*z*
Ca	0.00000	0.00000	0.00000
Ca	0.50000	0.50000	0.00000
Ca	0.00000	0.50000	0.50000
Ca	0.50000	0.00000	0.50000
Cu	0.25000	0.25000	0.25000
Cu	0.62500	0.62500	0.62500
Cu	0.75000	0.75000	0.25000
Cu	0.37500	0.37500	0.62500
Cu	0.75000	0.25000	0.75000
Cu	0.37500	0.62500	0.37500
Cu	0.25000	0.75000	0.75000
Cu	0.62500	0.37500	0.37500
Cu	0.12500	0.12500	0.62500
Cu	0.87500	0.87500	0.62500
Cu	0.87500	0.12500	0.37500
Cu	0.12500	0.87500	0.37500
Cu	0.62500	0.12500	0.12500
Cu	0.37500	0.87500	0.12500
Cu	0.37500	0.12500	0.87500
Cu	0.62500	0.87500	0.87500
Cu	0.12500	0.62500	0.12500
Cu	0.87500	0.37500	0.12500
Cu	0.87500	0.62500	0.87500
Cu	0.12500	0.37500	0.87500

Table A.10. Atomic coordinates for ABINIT-optimized $CaAu_5$ structure ($CaCu_5$-type)

Element	*x*	*y*	*z*
Ca	0.00000	0.00000	0.00000
Au	0.33333	0.66667	0.00000
Au	0.66667	0.33333	0.00000
Au	0.50000	0.50000	0.50000
Au	0.00000	0.50000	0.50000
Au	0.50000	0.00000	0.50000

Table A.11. Atomic coordinates for ABINIT-optimized $CaAu_5$ structure ($AuBe_5$-type)

Element	*x*	*y*	*z*
Ca	0.00000	0.00000	0.00000
Ca	0.50000	0.50000	0.00000
Ca	0.00000	0.50000	0.50000
Ca	0.50000	0.00000	0.50000
Au	0.25000	0.25000	0.25000
Au	0.62500	0.62500	0.62500
Au	0.75000	0.75000	0.25000
Au	0.37500	0.37500	0.62500
Au	0.75000	0.25000	0.75000
Au	0.37500	0.62500	0.37500
Au	0.25000	0.75000	0.75000
Au	0.62500	0.37500	0.37500
Au	0.12500	0.12500	0.62500
Au	0.87500	0.87500	0.62500
Au	0.87500	0.12500	0.37500
Au	0.12500	0.87500	0.37500
Au	0.62500	0.12500	0.12500
Au	0.37500	0.87500	0.12500
Au	0.37500	0.12500	0.87500
Au	0.62500	0.87500	0.87500
Au	0.12500	0.62500	0.12500
Au	0.87500	0.37500	0.12500
Au	0.87500	0.62500	0.87500
Au	0.12500	0.37500	0.87500

A.3. Discussion of the prevalence of highly positive CP features in the atomic core regions that are oriented between internuclear vectors, rather than along them

In Figure 2.4f of the main text, strong chemical pressure features are observed in the core regions of the Ca atoms. The directionality of these features would suggest that they arise from interatomic interactions, but they are awkwardly oriented along the boundaries between contact volumes. This is in fact a specific example of an interesting trend that we have observed for a variety of phases, which we will now explore. In Figure A.1, we show isosurfaces of the CP maps generated for a series of structures, with the isosurface level set to a sufficiently high level that only the most intense, positive pressure features are visible. For all of the structures shown, the isosurfaces reveal lobes that are directed into interstitial spaces rather than along the interatomic contacts.

For $CaPd_2$ (Figure A.1a), the tetrapod of white pressure isosurfaces around each calcium atom point not to the nearest calcium neighbor, but to the centers of the triangular faces of the surrounding Pd truncated tetrahedron. This is echoed in Figure S1b, where similar four-pronged pressures on the elemental silicon point into the interstices. On $CrGa_4$ in the $PtHg_4$ type[3,4] (Figure A.1c), the octahedral arrangement of lobes around the Cr atoms appears to suggest positive pressures along Cr-Cr contacts, but the 5.5 Å bond length suggests this is quite far from a too-close contact ($2 \times d_{Cr} = 2 \times 1.28 = 2.56$ Å). Finally, the niobium atom in $NbGa_3$[5] (Figure A.1d) exhibits these pressure features oriented toward the top and bottom square faces of a cuboctahedron of gallium atoms. These features point out of the *ab* plane of the Nb atom, in which the closest Nb-Ga contacts occur (2.65 Å vs 2.86 Å for out-of-plane contacts). What is the source of these features of the chemical pressure maps?

A straightforward approach to investigating the origins of these features is to plot the contributions to the CP maps from specific terms in the total energy. For simplicity, we will pursue this approach here with

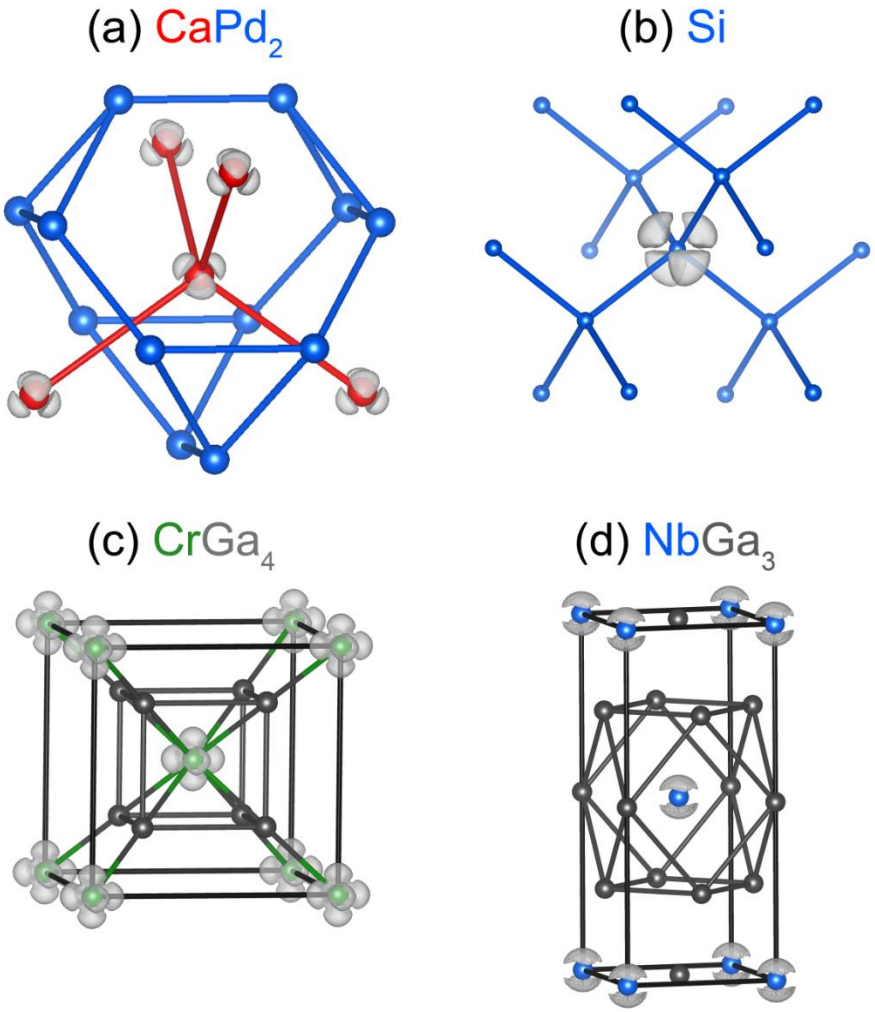

Figure A.1. Positive chemical pressure is shown for a series of solid state structures. (a) $CaPd_2$ in the $MgCu_2$-type Laves phase at an isosurface value of 0.075 a.u. This is a 3-dimensional plot of the strongest positive features seen in Figure 2.4f of the main text. These positive pressure features point not between atomic contacts, but rather to the void spaces in the structure. The same trend can be seen for (b) elemental Si, plotted at an isosurface value of 0.022 a.u., (c) $CrGa_4$ in the $PtHg_4$ type, plotted at 0.083, and (d) $NbGa_3$ in the $TiAl_3$ type, plotted at 0.085.

just for elemental silicon, though the same could be carried out for all of the structures depicted in Figure 2.1.

After examining separately each energetic contribution to the chemical pressure, we found that the major contribution to these positive pressure features was the local potential component of the total

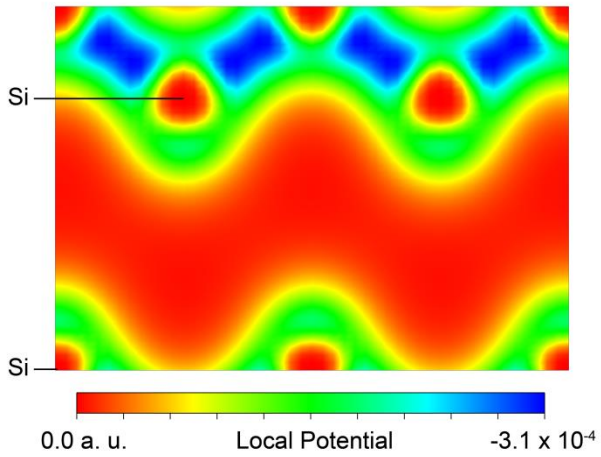

Figure A.2. The difference between the local potential surfaces of elemental silicon from the expanded unit cell volume to the contracted unit cell volume, corrected for distortion using CPmap. The (110) plane of the structure is depicted to capture the interatomic interactions.

energy. In Figure A.2, we see the difference in the local potential on going from a slightly expanded structure to a slightly contracted one. This is akin to computing only the local potential component of the chemical pressure, without multiplying by the electron density and dividing by the change in volume.

We note first that this function is non-positive over the entire unit cell. This implies that the potential becomes universally more negative as the cell contracts, with nearly zero change far from the nuclei. The largest changes are, in fact, between silicon atoms, implying a drastic deepening of the potential on contraction of the unit cell, as is expected for a model of overlapping potential wells. As the atoms are forced closer together, the overlap of the potentials increases, and electrons in the middle ground experience a stronger interaction with both nuclei. This strongly negative component lies directly in line with interatomic contact. When calculating the chemical pressure, the local component depicted in Figure A.2 provides a severe negative component between atoms, which counteracts the strong positive features normally present in the core of the atom. The positive core features remain unopposed in the other

directions around an atomic center, with the net result being the appearance of relatively intense positive pressure features appearing in the core regions away from the interatomic vectors for strong interactions.

Figure A.3 shows the integrated results for the chemical pressure calculation on elemental silicon. Si-Si contacts are nearly optimal, with only small white lobes pointing between them. No longer do we see the high positive pressures observed in Figure A1b; in their place are negative lobes, pointing to interstitial voids within the diamond framework, better reflecting our chemical intuition of this structure.

The integration step correctly disperses the strongly positive features (as seen in Figure 2.4f of the main text), resulting in interatomic pressures that well-represent the full interaction.

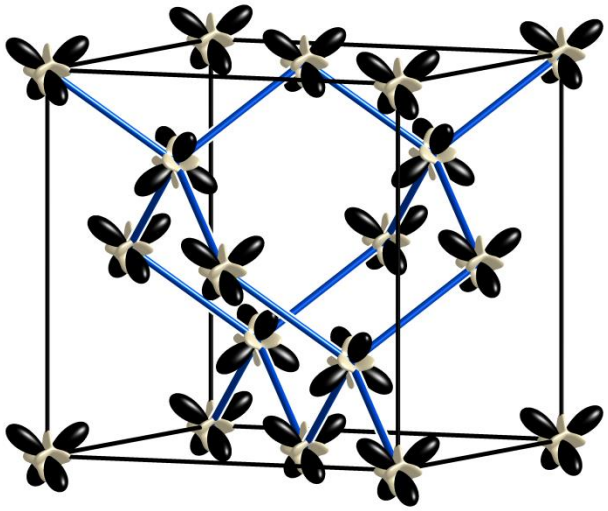

Figure A.3. The DFT-CP anisotropies calculated for elemental silicon. Pressures are near optimal between silicon atoms, as expected. Negative pressure features point towards void spaces in the structure.

A.4. Voxel volume calculation in distorted grid

Since the grid unwarping procedure leads to shifts of grid points relative to a uniform grid, the volume associated with each voxel is no longer constant. The calculation of the corrected voxel volumes is important for subsequent integration over the grids, but the computational cost for an exact calculation of voxel volumes can be prohibitive. Here we present the approximate calculation adopted in the *CPmap* program and demonstrate that it gives satisfyingly accurate results for small distortions of the grid.

In the following discussion, we use $(\boldsymbol{p},\boldsymbol{q},\boldsymbol{r}) \equiv (\boldsymbol{p}\times\boldsymbol{q})\cdot\boldsymbol{r} \equiv \begin{vmatrix} p_x & p_y & p_z \\ q_x & q_y & q_z \\ r_x & r_y & r_z \end{vmatrix}$ to denote the triple product of three-dimensional vectors $\boldsymbol{p},\boldsymbol{q},\boldsymbol{r}$.

For an undistorted grid, each voxel takes the shape of a parallelepiped, so its volume is simply given by

$$V_{voxel} = (\boldsymbol{a}_{voxel}, \boldsymbol{b}_{voxel}, \boldsymbol{c}_{voxel})$$

where $\boldsymbol{a}_{voxel}, \boldsymbol{b}_{voxel}, \boldsymbol{c}_{voxel}$ are the three edge vectors of the undistorted voxel parallelepiped. Here we take voxel 000 to be the voxel of interest, where 000 is its index $n_x n_y n_z$ in the voxel grid. If we consider the coordinates of its six direct neighbors, it can be seen that

$$r_{100} - r_{\bar{1}00} = 2\boldsymbol{a}_{voxel}, r_{010} - r_{0\bar{1}0} = 2\boldsymbol{b}_{voxel}, r_{001} - r_{00\bar{1}} = 2\boldsymbol{c}_{voxel}$$

So we can write its voxel volume as an expression of the coordinates of its neighbors:

$$V_{000} = (\boldsymbol{a}_{voxel}, \boldsymbol{b}_{voxel}, \boldsymbol{c}_{voxel}) = \frac{1}{8}(2\boldsymbol{a}_{voxel}, 2\boldsymbol{b}_{voxel}, 2\boldsymbol{c}_{voxel})$$

$$= \frac{1}{8}(\boldsymbol{r}_{100} - \boldsymbol{r}_{\bar{1}00}, \boldsymbol{r}_{010} - \boldsymbol{r}_{0\bar{1}0}, \boldsymbol{r}_{001} - \boldsymbol{r}_{00\bar{1}}) \quad (A.1)$$

As will be shown in the discussion below, Eq. A.1 can also be applied to approximately to the distorted grid. We will see that this equation captures the essential effect of distortion of neighboring voxels on a voxel's volume, and also preserves (to first order) the sum of all voxel volumes as equal to the total unit cell volume.

Lemma. For a change in the position of any of the six direct neighbor voxels to 000, the first order change to V_{000} (as defined by Eq. D.1) will be $\frac{1}{2}\Delta k \cdot V_{voxel}$, where Δk is the perturbation along the corresponding voxel edge vector away from 000. The other components of the displacement have only higher order effects.

Proof. In a distorted grid, any voxel may experience a perturbation $\Delta\boldsymbol{r}_{n_x n_y n_z}$, so we have

$$V'_{000} = \frac{1}{8}\left((r_{100} - r_{\bar{1}00}) + (\Delta r_{100} - \Delta r_{\bar{1}00}), (r_{010} - r_{0\bar{1}0}) + (\Delta r_{010} - \Delta r_{0\bar{1}0}), (r_{001} - r_{00\bar{1}}) + (\Delta r_{001} - \Delta r_{00\bar{1}})\right)$$

$$= \frac{1}{8}\left(2\boldsymbol{a}_{voxel} + (\Delta r_{100} - \Delta r_{\bar{1}00}), 2\boldsymbol{b}_{voxel} + (\Delta r_{010} - \Delta r_{0\bar{1}0}), 2\boldsymbol{c}_{voxel} + (\Delta r_{001} - \Delta r_{00\bar{1}})\right) \quad (D.2)$$

Since the triple product is linear with respect to each variable, an expansion of Eq. A.2 gives:

$$\Delta V_{000} = V'_{000} - V_{000}$$

$$= \frac{1}{8}[(\Delta r_{100} - \Delta r_{\bar{1}00}, 2\boldsymbol{b}_{voxel}, 2\boldsymbol{c}_{voxel}) + (2\boldsymbol{b}_{voxel}, \Delta r_{010} - \Delta r_{0\bar{1}0}, 2\boldsymbol{c}_{voxel}) + (2\boldsymbol{a}_{voxel}, 2\boldsymbol{b}_{voxel}, \Delta r_{001} - \Delta r_{00\bar{1}})]$$

$$+ 2^{nd} \textit{and higher order terms}$$

$$= \frac{1}{8}[(\Delta r_{100}, 2\boldsymbol{b}_{voxel}, 2\boldsymbol{c}_{voxel}) + (2\boldsymbol{b}_{voxel}, \Delta r_{010}, 2\boldsymbol{c}_{voxel}) + (2\boldsymbol{a}_{voxel}, 2\boldsymbol{b}_{voxel}, \Delta r_{001})]$$

$$- \frac{1}{8}[(\Delta r_{\bar{1}00}, 2\boldsymbol{b}_{voxel}, 2\boldsymbol{c}_{voxel}) + (2\boldsymbol{b}_{voxel}, \Delta r_{0\bar{1}0}, 2\boldsymbol{c}_{voxel}) + (2\boldsymbol{a}_{voxel}, 2\boldsymbol{b}_{voxel}, \Delta r_{00\bar{1}})]$$

$$+ 2^{nd} \textit{and higher order terms} \qquad \text{(A.3)}$$

Here we focus only on the $\Delta \boldsymbol{r}_{100}$ term, since the other five terms can be treated with a similar approach. If we rewrite $\Delta \boldsymbol{r}_{100}$ as a linear combination of the three voxel edge vectors, i.e.

$$\Delta \boldsymbol{r}_{100} = \Delta k_{100a} \boldsymbol{a}_{voxel} + \Delta k_{100b} \boldsymbol{b}_{voxel} + \Delta k_{100c} \boldsymbol{c}_{voxel}$$

the term becomes

$$\frac{1}{8}(\Delta \boldsymbol{r}_{100}, 2\boldsymbol{b}_{voxel}, 2\boldsymbol{c}_{voxel}) = \frac{1}{8}(\Delta k_{100a} \boldsymbol{a}_{voxel} + \Delta k_{100b} \boldsymbol{b}_{voxel} + \Delta k_{100c} \boldsymbol{c}_{voxel}, 2\boldsymbol{b}_{voxel}, 2\boldsymbol{c}_{voxel})$$

$$= \frac{1}{8}(\Delta k_{100a} \boldsymbol{a}_{voxel}, 2\boldsymbol{b}_{voxel}, 2\boldsymbol{c}_{voxel}) = \frac{1}{2} \Delta k_{100a} \cdot V_{voxel}$$

That is, for voxel 100, only a perturbation along the $\boldsymbol{a}_{voxel}$ direction has a first order effect on the voxel volume of $\frac{1}{2} \Delta k_{100a} \cdot V_{voxel}$, while perturbation along $\boldsymbol{b}_{voxel}$ and $\boldsymbol{c}_{voxel}$ has no effect (it only introduces a shearing of the parallelepiped, which does not affect its volume). ■

Proposition. The change in total volume of all voxels as calculated using Eq. A1 in a distorted grid is second order with respect to the distortion.

Proof. We will still focus our discussion on voxel 100. Following from the lemma above, we only need to consider a movement along the $\boldsymbol{a}_{voxel}$ direction. Such a perturbation will change the volume of voxel 000 by $\frac{1}{2}\Delta k_{100a} \cdot V_{voxel}$, but it also changes the volume of voxel 200 by $-\frac{1}{2}\Delta k_{100a} \cdot V_{voxel}$. Therefore the first order perturbations cancel out, so we are left with only the higher order terms in Eq. A.3. It so follows that

$$\sum_{n_x,n_y,n_z} \Delta V_{n_x n_y n_z} = O(|\Delta \boldsymbol{r}_{n_x n_y n_z}|^2)$$

i.e. the change in total volume of all voxels in the unit cell is second order with respect to the distortion.

■

In all calculations carried out in this Article, the volumes of the voxels in the distorted grid add up to the unit cell volume within 0.00001 Å^3. This threshold can be adjusted in the source code if testing to higher precision is desired.

D.5. References

(1) Monkhorst, H.; Pack, J. *Phys. Rev. B* **1976**, *13*, 5188-5192.

(2) Hartwigsen, C.; Goedecker, S.; Hutter, J. *Phys. Rev. B* **1998**, *58*, 3641-3662.

(3) Meissner, H.-G.; Schubert, K. *Z. Metallkd.* **1965**, *56*, 523-530.

(4) Häussermann, U.; Viklund, P.; Boström, M.; Norrestam, R.; Simak, S. *Physical Review B* **2001**, *63*.

(5) Baron, V. V.; Myzenkova, L. F.; Savitskii, E. M.; Gladyshevskii, E. I. *Zh. Neorg. Khim.* **1964**, *9*, 2170-2173.

Appendix B.

Supplemental Information for Chapter 3:

Isolobal Analogies in Intermetallics: The Reversed Approximation MO Approach and Applications to $CrGa_4$ and Ir_3Ge_7-type Phases

B.1. Distinction between the NBO and raMO analyses

The model Hamiltonian operator in equation 3.4 bears some resemblance to the reduced density (γ) matrix subspace operators used in the NBO method for creating natural orbitals for local features of a structure (atoms or bonds). There are several differences, however, of particular relevance for exploring isolobal analogies in delocalized bonding of intermetallics. Perhaps the most important is the difference in the ways that the eigenfunctions of the operators are processed. The NBO analysis reorganizes the γ matrix to Lewis-like structures through a step-wise process. Here, natural orbitals are created by diagonalizing increasingly large blocks of the reduced density matrix. In each step, the eigenvalues of the γ subspace matrix correspond to maximally occupied functions, with the functions with highest occupancy then being considered as the most chemically relevant. In this way, the chemist's view of localized bonding vividly emerges from the immense basis sets of modern calculations.

In the raMO analysis, differences between the eigenvalues of the model Hamiltonian matrix instead indicate correspondences with the different levels of the model MO diagram. In particular, those with energy eigenvalues of zero are sorted as components of the electronic structure that are orthogonal to the

proffered bonding model, and thus belong to other bonding subsystems. Throughout this process, no reference is made to Lewis structures, which can make difficult starting points for perturbative analyses in metals.

Another difference lies in the functions used to create matrix representations of the methods' operators. In the NBO analysis, the basis set of the original electronic structure calculation is used for this task, while in raMO the occupied wavefunctions of the system are used. In this way, raMO is again seen as a reversal of the usual basis set approximation.

Despite these procedural differences, the raMO and NBO analyses are similar in spirit, and we view them as complementary: the raMO analysis provides a simple mechanism for testing bonding ideas and isolobal analogies for compounds, but its success depends greatly on what model is offered, and how the output is interpreted. As such, the method is hypothesis-driven, and lacks the NBO analysis' ability to derive algorithmically a unique bonding description for a compound.

B.2. Computational Details

Table B.1. Details of LDA-DFT calculations on structures serving as basis for parameterization of Hückel models.

Structure[a]	Geo	Pseudopontentials	Energy Cut-	k-point mesh
Benzene	No	Ultrasoft LDA	358.2 eV	4×3×4, Γ-
$CrGa_4$	Yes	Ultrasoft LDA	284.0 eV	13×13×13, Γ-
Os_3Sn_7	Yes[b]	Ultrasoft LDA	285.0 eV	8×8×8, Γ-
Ir_3Sn_7	Yes[b]	Ultrasoft LDA	263.6 eV	8×8×8, Γ-

[a]In anticipation of the supercells needed for the raMO analysis, calculations were carried out on the conventional rather than primitive unit cells (where applicable).

[b]Geometry optimizations were carried out in two steps: first the atomic positions were allowed to relax in a unit cell of fixed size, then energy was minimized with respect to all structural parameters.

Table B.2. DFT-optimized geometry of $CrGa_4$

Cell vectors	*x* (Å)	*y* (Å)	*z* (Å)
a	5.64099986650	0.00000000000	0.00000000000
b	0.00000000000	5.64099986650	0.00000000000
c	0.00000000000	0.00000000000	5.64099986650
Atom	*x* (fractional)	*y* (fractional)	*z* (fractional)
Ga	0.25000000000	0.25000000000	0.25000000000
Ga	0.75000000000	0.75000000000	0.75000000000
Ga	0.75000000000	0.75000000000	0.25000000000
Ga	0.25000000000	0.25000000000	0.75000000000
Ga	0.75000000000	0.25000000000	0.75000000000
Ga	0.25000000000	0.75000000000	0.25000000000
Ga	0.25000000000	0.75000000000	0.75000000000
Ga	0.75000000000	0.25000000000	0.25000000000
Cr	0.00000000000	0.00000000000	0.00000000000
Cr	0.50000000000	0.50000000000	0.50000000000
Total E:	-52.536577 eV		

Table B.3. DFT-optimized geometry of Os_3Sn_7

Cell	*x* (Å)	*y* (Å)	*z* (Å)
a	9.49993563971	0.00000000000	0.00000000000
b	0.00000000000	9.49993563971	0.00000000000
c	0.00000000000	0.00000000000	9.49992829929
Atom	*x* (fractional)	*y* (fractional)	*z* (fractional)
Os	0.34357770364	0.00000000000	0.00000000000
Os	0.84357770364	0.50000000000	0.50000000000
Os	0.00000000000	0.34357770364	0.00000000000
Os	0.50000000000	0.84357770364	0.50000000000
Os	0.65642229636	0.00000000000	0.00000000000
Os	0.15642229636	0.50000000000	0.50000000000
Os	0.00000000000	0.65642229636	0.00000000000
Os	0.50000000000	0.15642229636	0.50000000000
Os	0.00000000000	0.00000000000	0.65642506761
Os	0.50000000000	0.50000000000	0.15642506761
Os	0.00000000000	0.00000000000	0.34357493239
Os	0.50000000000	0.50000000000	0.84357493239
Sn	0.16090112861	0.16090112861	0.16090097296
Sn	0.66090112861	0.66090112861	0.66090097296
Sn	0.83909887139	0.16090112861	0.16090097296
Sn	0.33909887139	0.66090112861	0.66090097296
Sn	0.83909887139	0.83909887139	0.16090097296
Sn	0.33909887139	0.33909887139	0.66090097296
Sn	0.16090112861	0.83909887139	0.16090097296
Sn	0.66090112861	0.33909887139	0.66090097296
Sn	0.16090112861	0.83909887139	0.83909902704
Sn	0.66090112861	0.33909887139	0.33909902704
Sn	0.16090112861	0.16090112861	0.83909902704
Sn	0.66090112861	0.66090112861	0.33909902704
Sn	0.83909887139	0.16090112861	0.83909902704
Sn	0.33909887139	0.66090112861	0.33909902704
Sn	0.83909887139	0.83909887139	0.83909902704
Sn	0.33909887139	0.33909887139	0.33909902704
Sn	0.24999908858	0.00000000000	0.50000000000
Sn	0.74999908858	0.50000000000	0.00000000000
Sn	0.00000000000	0.24999908858	0.50000000000
Sn	0.50000000000	0.74999908858	0.00000000000
Sn	0.75000091142	0.00000000000	0.50000000000
Sn	0.25000091142	0.50000000000	0.00000000000
Sn	0.00000000000	0.75000091142	0.50000000000
Sn	0.50000000000	0.25000091142	0.00000000000
Sn	0.50000000000	0.00000000000	0.75000000000
Sn	0.00000000000	0.50000000000	0.25000000000
Sn	0.50000000000	0.00000000000	0.25000000000
Sn	0.00000000000	0.50000000000	0.75000000000
Total E:	-241.950467 eV		

Table B.4. DFT-optimized geometry of Ir_3Sn_7

Cell	*x* component (Å)	*y* component (Å)	*z* component (Å)
a	9.51621746956	0.00000000000	0.00000000000
b	0.00000000000	9.51621746956	0.00000000000
c	0.00000000000	0.00000000000	9.51620643351
Atom	*x* (fractional)	*y* (fractional)	*z* (fractional)
Ir	0.84191479193	0.50000000000	0.50000000000
Ir	0.15808520807	0.50000000000	0.50000000000
Ir	0.00000000000	0.34191479193	0.00000000000
Ir	0.50000000000	0.84191479193	0.50000000000
Ir	0.34191479193	0.00000000000	0.00000000000
Ir	0.50000000000	0.50000000000	0.84191952683
Ir	0.00000000000	0.00000000000	0.34191952683
Ir	0.50000000000	0.50000000000	0.15808047317
Ir	0.00000000000	0.00000000000	0.65808047317
Ir	0.50000000000	0.15808520807	0.50000000000
Ir	0.00000000000	0.65808520807	0.00000000000
Ir	0.65808520807	0.00000000000	0.00000000000
Sn	0.83509343525	0.83509343525	0.83509081260
Sn	0.16490656475	0.16490656475	0.16490918740
Sn	0.33509343525	0.66490656475	0.33509081260
Sn	0.83509343525	0.16490656475	0.83509081260
Sn	0.66490656475	0.66490656475	0.33509081260
Sn	0.16490656475	0.16490656475	0.83509081260
Sn	0.66490656475	0.33509343525	0.33509081260
Sn	0.16490656475	0.83509343525	0.83509081260
Sn	0.66490656475	0.33509343525	0.66490918740
Sn	0.16490656475	0.83509343525	0.16490918740
Sn	0.33509343525	0.33509343525	0.66490918740
Sn	0.83509343525	0.83509343525	0.16490918740
Sn	0.33509343525	0.66490656475	0.66490918740
Sn	0.83509343525	0.16490656475	0.16490918740
Sn	0.66490656475	0.66490656475	0.66490918740
Sn	0.33509343525	0.33509343525	0.33509081260
Sn	0.50000000000	0.00000000000	0.24999946541
Sn	0.00000000000	0.50000000000	0.24999946541
Sn	0.50000000000	0.00000000000	0.74999946541
Sn	0.50000000000	0.24999720702	0.00000000000
Sn	0.00000000000	0.74999720702	0.50000000000
Sn	0.24999720702	0.50000000000	0.00000000000
Sn	0.74999720702	0.00000000000	0.50000000000
Sn	0.50000000000	0.75000172379	0.00000000000
Sn	0.00000000000	0.25000172379	0.50000000000
Sn	0.75000172379	0.50000000000	0.00000000000
Sn	0.25000172379	0.00000000000	0.50000000000
Sn	0.00000000000	0.50000000000	0.74999946541
Total E:	-224.691401 eV		

Table B.5. DFT-calibrated Hückel parameters used in this work

Compound, RMS deviation[a]	Orbital	H_{ii} (eV)	c_1	$\zeta_1(a_o^{-1})$	c_2	$\zeta_2(a_o^{-1})$
Benzene, 0.24 eV	C 2s	-11.241		2.2477		
	C 2p	-7.857		2.2187		
	H 1s	-7.528		1.4592		
$CrGa_4$, 0.12 eV	Cr 4s	-4.713		2.6238		
	Cr 4p	0.490[c]		1.7809		
	Cr 3d	-7.554	1.0413	5.7500	0.6290	2.7461
	Ga 4s	-9.575		2.4076		
	Ga 4p	-5.244		2.3479		
Os_3Sn_7, 0.12 eV	Os 6s	-2.869		2.5278		
	Os 6p	-1.255		2.5278[b]		
	Os 5d	-7.522	0.6372	5.4453	0.2990	2.0801
	Sn 5s	-10.335		2.7532		
	Sn 5p	-4.990		2.3881		
Ir_3Sn_7, 0.10 eV	Ir 6s	-4.156		2.8220		
	Ir 6p	-2.644		2.8220[b]		
	Ir 5d	-8.056	0.6698	5.7931	0.5823	2.4735
	Sn 5s	-10.509		2.6960		
	Sn 5p	-4.743		2.3618		

[a]Root-mean-squared deviation between the DFT and Hückel band energies up to ca. 1 eV above the E_F.

[b]Constrained to equal the corresponding value for the s orbital on the same element.

[c]For a discussion of our interpretation of such unusually high H_{ii}'s in Huckel parameter sets see Ref. 51.

Appendix C.

Supplemental Information for Chapter 4:

Defusing Complexity in Intermetallics: How Covalently Shared Electron Pairs Stabilize the FCC Variant $Mo_2Cu_xGa_{6-x}$ $(x = 0.9)$

C.1. Crystallographic Tables

In the following, detailed tables are given describing the atomic coordinates, atomic displacement parameters and selected interatomic distances for $Mo_2Cu_{0.9}Ga_{5.1}$.

Table C.1. $Mo_2Cu_{0.9}Ga_{5.1}$ atomic coordinates and displacement parameters.

Site	Wyckoff Position	x	y	z	$U_{equivalent}$	Occupancy
Mo1	2d	0.75	0.75	0.25875(5)	0.00646(13)	1.0
Ga1	2d	1.25	0.75	0.5	0.00690(14)	1.0
Ga2	2d	1.25	1.25	0.22721(9)	0.01066(16)	1.0
Ga3	2d	1.75	1.25	0	0.00821(15)	0.55
Cu3	2d	1.75	1.25	0	0.00821(15)	0.45

Table C.2. $Mo_2Cu_{0.9}Ga_{5.1}$ anisotropic atomic displacement parameters.

Site	U_{11}	U_{22}	U_{33}	U_{12}	U_{13}	U_{23}
Mo1	0.0071(2)	0.0071(2)	0.0052(2)	0	0	0
Ga1	0.0071(2)	0.0071(2)	0.0065(3)	0	0	0
Ga2	0.0090(2)	0.0090(2)	0.0140(3)	0	0	0
Ga3	0.0091(2)	0.0091(2)	0.0065(3)	0	0	0
Cu3	0.0091(2)	0.0091(2)	0.0065(3)	0	0	0

Table C.3. Selected interatomic distances for $Mo_2Cu_{0.9}Ga_{5.1}$.

Site	Neighbor	Distance (Å)
Mo1	Ga1(×4)	2.7822(3)
	Ga2(×4)	2.62918(13)
	Ga3/Cu3(×4)	2.8967(3)
Ga1	Mo1(×4)	2.7822(3)
	Ga1(×4)	2.61509(10)
	Ga2(×4)	2.9908(6)

Site	Neighbor	Distance (Å)
Ga2	Mo1(×4)	2.62918(13)
	Ga1(×4)	2.9908(6)
	Ga3/Cu3(×4)	2.6930(6)
Ga3/Cu3	Mo1(×4)	2.8967(3)
	Ga2(×4)	2.6930(6)
	Ga3/Cu3(×4)	2.61509(10)

C.2. Details of Cu Atom Assignment

In Section 4.2, we determined the space group and lattice parameters of $Mo_2Cu_{0.9}Ga_{5.1}$. From the integrated intensities the structure solution program SUPERFLIP output a structure with the composition Mo_2Ga_6. While it is possible to obtain a reasonable crystal structure solution with this stoichiometry, Energy Dispersive X-ray Spectroscopy (EDS) data on polished cross sections suggested the presence of Cu in the structure. The similar form factors of Cu and Ga for Mo Kα X-ray radiation make them difficult to distinguish using single crystal X-ray diffraction data. However, slightly enlarged isotropic ADP parameters for Ga2 and Ga3 indicated that partial substitution of Cu on these crystallographic sites may be detectable in the diffraction data.

Our first approach to determining the location of the Cu substitution in the $Mo_2Cu_{0.9}Ga_{5.1}$ structure was to attempt to partially substitute Cu at each Ga site in the crystal structure solution separately. In three structural models, a fifty percent occupancy of Cu was placed at each site individually, and then the occupancy was refined using JANA2006. In the cases of Cu substitution on Ga1 and Ga2, the structure refinements resulted in negative Cu occupancies on these sites. For Ga3 however, the refinement converged on a Cu/Ga ratio of about 1:1 with a drop in the $R[I > 3\sigma(I)]$ from 1.99 to 1.43. The placement of Cu on this atomic position agrees with the location of Cu in the $HfCuSi_2$ type, of which $Mo_2Cu_{0.9}Ga_{5.1}$ is a disordered variant. Small changes to the Cu/Ga ratio on this site had little effect on the R or S values for our model, so the occupation was restricted to agree with that of the SEM-EDS data (i.e. a Cu/Ga ratio of 0.9:1.1).

As a check against the possibility of Cu on multiple sites at once, we tried a fourth model in which a fifty percent Cu occupancy was placed on all three Ga sites, and their occupancies were refined simultaneously. In this case, structural refinements lead to occupancies of 16.8%, 1.4%, and 63.7% occupancy of Cu

on Ga1, Ga2, and Ga3 respectively, resulting in a crystallographically refined composition of $Mo_2Cu_{1.7}Ga_{4.3}$. This model led to slightly improved R and S values relative to the Ga3 substituted model (see Table C4), however the improvements were minor, required the addition of 3 extra parameters, and resulted in a refined stoichiometry which disagreed with the SEM-EDS data. The statistical significance of the Cu occupation on Ga1 and Ga2 is also questionable. For Ga2, the standard uncertainty in the Cu occupation is larger than the refined Cu occupation, while for Ga1 the Cu occupancy is within four times the uncertainty. Although we cannot completely discount the Cu occupation of Ga1 and Ga3 sites concurrently as suggested by this model, the minor improvements over the simpler Ga3-only substituted model lead us to propose the most conservative interpretation of the single crystal X-ray diffraction data.

While the Ga3 substituted model leads to a crystal structure solution in agreement with SEM-EDS data, basing this Cu assignment solely on single crystal X-ray diffraction data is tenuous due to the similar form factors of Cu and Ga for Mo, Kα radiation. We therefore looked to GGA-DFT to further support our model. Several ordered models of based on the $Mo_2Cu_{0.9}Ga_{5.1}$ single crystal solution were created and their ionic positions optimized to find which site substitution relaxed to the observed crystal geometry. Models for which Cu had been substituted on a selection of Ga2 positions relaxed to an atomic structure in which the Mo-Cu/Ga layer no longer showed the distortions present in the single crystal solution. On the contrary, models for which Cu were placed on either the Ga1 or Ga3 sites both relaxed to virtually identical structures, the observed geometry of the $Mo_2Cu_{0.9}Ga_{5.1}$ crystal structure with Cu substitution as shown in Figure 1c. As stated above, although we cannot completely rule out partial mixing on multiple Ga sites, this result combination with the single crystal data, SEM-EDS data, and the location of Cu in the $HfCuSi_2$-type structure strongly suggest that the Ga3 site is shared between Ga and Cu in this structure. The slightly enlarged isotropic ADP of the Ga2 site, which neighbors the Cu substituted layer, is likely due to variability

from having a statistical distribution of Cu or Ga neighbors. This agrees with the refined anisotropic ADP of Ga2 which is slightly elongated perpendicular to the Cu3/Ga3 plane, suggesting different ideal interatomic distances depending on the identities of its near Cu/Ga neighbors.

Table C.4. Crystallographic information of several Cu substitution patterns.

site with Cu	refined Cu occupancy	$S[I > 3\sigma(I)]$, S(all)	$R[I > 3\sigma(I)]$, $R_w^2[I > 3\sigma(I)]$	R(all), R_w^2(all)
none	N/A	1.84, 1.78	1.99, 6.06	2.21, 6.14
Ga1	-0.111(58)	1.83, 1.76	2.02, 5.99	2.26, 6.07
Ga2	-0.254(61)	1.74, 1.68	2.06, 5.69	2.30, 5.80
Ga3	0.567(39)	1.20, 1.19	1.43, 3.79	1.71, 3.96
Ga1, Ga2, Ga3	0.168(43), 0.014(46), 0.637(46)	1.10, 1.09	1.36, 3.57	1.65, 3.75

C.3. Powder X-ray Diffraction

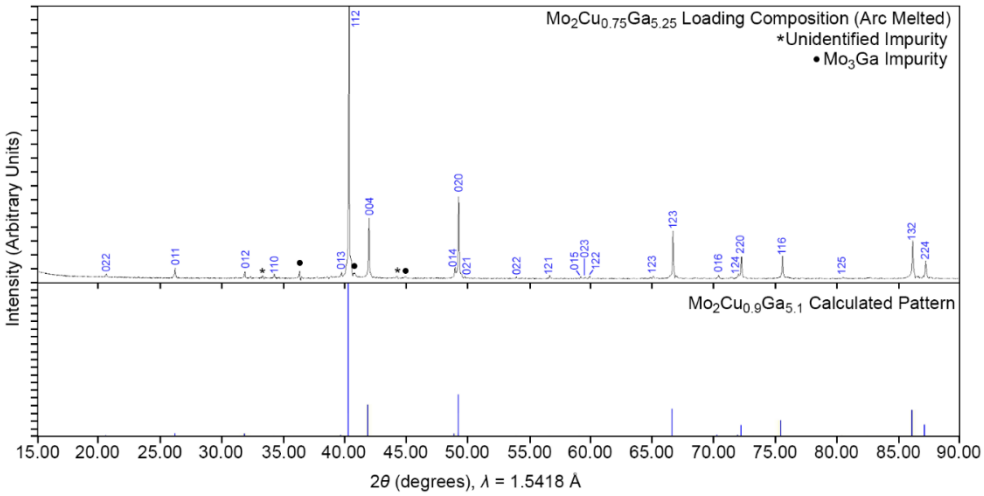

Figure C.1. Powder X-Ray Diffraction Pattern for $Mo_2Cu_{0.9}Ga_{5.1}$

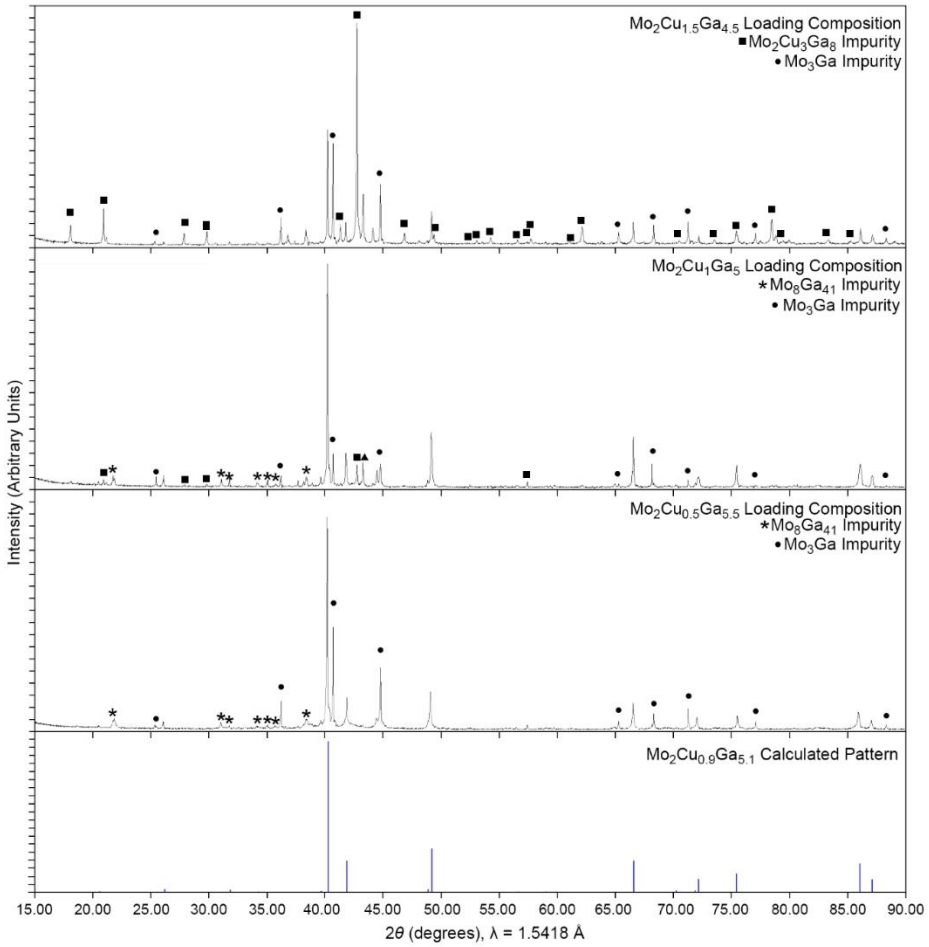

Figure C.2. The powder diffraction patterns for $Mo_2Cu_{0.5}Ga_{5.5}$, $Mo_2Cu_1Ga_5$, and $Mo_2Cu_{1.5}Ga_{4.5}$ loading composition. Loading compositions more Cu-rich than $Mo_2Cu_{1.5}Ga_{4.5}$ displayed no peaks corresponding to the $Mo_2Cu_xGa_{6-x}$ phase. Small shifts in the diffraction peaks between the samples with nominal compositions of $Mo_2Cu_{0.5}Ga_{5.5}$ and $Mo_2Cu_{1.5}Ga_{4.5}$ correspond to a contraction of a = 0.00668 Å and expansion of c = 0.01344 Å with increasing Cu content, suggesting a small phase width. Estimating this phase width from the change in cell parameters is difficult due to the anisotropic nature of the change.

C.4. Computational Details and Optimized Geometries

Table C.5. Details of GGA-DFT calculations on structures serving as basis for parameterization of Hückel models.

Structure[a]	Geo Optimized	Psuedopotentials	Energy Cut-off	k-point mesh
$NbGa_3$	Yes	Ultrasoft GGA	218.5 eV	12×12×5, Γ centered
$MoGa_3$	Yes	Ultrasoft GGA	233.1 eV	12×12×5, Γ centered
Mo_2CuGa_5	Yes[b]	Ultrasoft GGA	292.2 eV	13×13×5, Γ centered[c]

[a]In anticipation of the supercells needed for the raMO analysis, calculations were carried out on the conventional rather than the primitive cells where applicable.

[b]Geometry optimizations were carried out in two steps: first the atomic positions were allows to relax in a unit cell of fixed size, then the energy was minimized with respect to all structural parameters.

[c]The larger c/a ratio of Mo_2CuGa_5 relative to $NbGa_3$ and $MoGa_3$ required a slightly modified k-point grid in order to ensure equal sampling along every axis.

Table C.6. DFT-optimized geometry of $NbGa_3$

Cell vectors	x	y	z
a (Å)	3.7935299977859227	0.0000000000000000	0.0000000000000000
b (Å)	0.0000000000000000	3.7935299977859227	0.0000000000000000
c (Å)	0.0000000000000000	0.0000000000000000	8.7543826834197738
Nb	0.5000000000000000	0.5000000000000000	0.5000000000000000
Nb	0.0000000000000000	0.0000000000000000	0.0000000000000000
Ga	0.5000000000000000	0.0000000000000000	0.7500000000000000
Ga	0.5000000000000000	0.0000000000000000	0.2500000000000000
Ga	0.0000000000000000	0.5000000000000000	0.7500000000000000
Ga	0.0000000000000000	0.5000000000000000	0.2500000000000000
Ga	0.5000000000000000	0.5000000000000000	0.0000000000000000
Ga	0.0000000000000000	0.0000000000000000	0.5000000000000000
Total Energy:	-5.114806589 eV/atom		

Table C.7. DFT-optimized geometry of $MoGa_3$

Cell vectors	x	y	z
a (Å)	3.6790787379546743	0.0000000000000000	0.0000000000000000
b (Å)	0.0000000000000000	3.6790787379546743	0.0000000000000000
c (Å)	0.0000000000000000	0.0000000000000000	8.3421719508189653
Nb	0.5000000000000000	0.5000000000000000	0.5000000000000000
Nb	0.0000000000000000	0.0000000000000000	0.0000000000000000
Ga	0.5000000000000000	0.0000000000000000	0.7500000000000000
Ga	0.5000000000000000	0.0000000000000000	0.2500000000000000
Ga	0.0000000000000000	0.5000000000000000	0.7500000000000000
Ga	0.0000000000000000	0.5000000000000000	0.2500000000000000
Ga	0.5000000000000000	0.5000000000000000	0.0000000000000000
Ga	0.0000000000000000	0.0000000000000000	0.5000000000000000
Total Energy:	-5.954623053 eV/atom		

Table C.8. DFT-optimized geometry of Mo_2CuGa_5

Cell vectors	*x*	*y*	*z*
a (Å)	3.6618809677123725	0.0000000000000000	0.0000000000000000
b (Å)	0.0000000000000000	3.6618809677123725	0.0000000000000000
c (Å)	0.0000000000000000	0.0000000000000000	8.7234548024567768
Mo	0.0000000000000000	0.5000000000000000	0.2375155475210704
Mo	0.5000000000000000	0.0000000000000000	0.7624844824789321
Ga	0.0000000000000000	0.0000000000000000	0.0000000000000000
Ga	0.5000000000000000	0.5000000000000000	0.0000000000000000
Ga	0.5000000000000000	0.0000000000000000	0.2779328017261733
Ga	0.0000000000000000	0.5000000000000000	0.7220671982738267
Ga	0.0000000000000000	0.0000000000000000	0.5000000000000000
Cu	0.5000000000000000	0.5000000000000000	0.5000000000000000
Total Energy:	-5.254192728 eV/atom		

Table C.9. DFT-optimized geometry of Mo_2CuGa_5 with Cu substituted on selection of Ga1 positions

Cell vectors	*x*	*y*	*z*
a (Å)	3.6830981372063731	0.0000000000000000	0.0000000000000000
b (Å)	0.0000000000000000	3.6830981372063731	0.0000000000000000
c (Å)	0.0000000000000000	0.0000000000000000	8.7571485662456858
Mo	0.0000000000000000	0.5000000000000000	0.2627382645235414
Mo	0.5000000000000000	0.0000000000000000	0.7372617654764611
Ga	0.0000000000000000	0.0000000000000000	0.0000000000000000
Ga	0.5000000000000000	0.5000000000000000	0.0000000000000000
Ga	0.5000000000000000	0.0000000000000000	0.2224341611959346
Ga	0.0000000000000000	0.5000000000000000	0.7775658388040654
Ga	0.0000000000000000	0.0000000000000000	0.5000000000000000
Cu	0.5000000000000000	0.5000000000000000	0.5000000000000000
Total Energy:	-5.19385625 eV/atom		

Table C.10. DFT-optimized geometry of Mo_2CuGa_5 with Cu substituted on selection of Ga2 positions

Cell vectors	*x*	*y*	*z*
a (Å)	7.5217014728779654	0.0000000000000000	0.0000000000000000
b (Å)	0.0000000000000000	7.5217014728779654	0.0000000000000000
c (Å)	0.0000000000000000	0.0000000000000000	8.4113536852400301
Mo	0.2500000000000000	0.0000000000000000	0.2501365738542697
Mo	0.2500000000000000	0.5000000000000000	0.2501365738542697
Mo	0.7500000000000000	0.0000000000000000	0.2501365738542697
Mo	0.7500000000000000	0.5000000000000000	0.2501365738542697
Mo	0.0000000000000000	0.2500000000000000	0.7498634261457304
Mo	0.0000000000000000	0.7500000000000000	0.7498634261457304
Mo	0.500000000000000	0.2500000000000000	0.7498634261457304
Mo	0.500000000000000	0.7500000000000000	0.7498634261457304
Ga	-0.0024638762251812	-0.0024638762251812	0.0000000000000000
Ga	0.0024638762251812	0.5024638762251814	0.0000000000000000
Ga	0.5024638762251814	0.0024638762251812	0.0000000000000000
Ga	0.4975361237748188	0.4975361237748188	0.0000000000000000
Ga	0.2524638762251812	0.2524638762251812	0.0000000000000000
Ga	0.2475361237748187	0.7475361237748186	0.0000000000000000
Ga	0.7475361237748186	0.2475361237748188	0.0000000000000000
Ga	0.7524638762251814	0.7524638762251814	0.0000000000000000
Ga	0.0000000000000000	0.2500000000000000	0.2502715308266941
Ga	0.5000000000000000	0.7500000000000000	0.2502715308266941
Ga	0.2500000000000000	0.0000000000000000	0.7497284691733059
Ga	0.7500000000000000	0.5000000000000000	0.7497284691733059
Ga	-0.0026693186106839	-0.0026693186106839	0.5000000000000000
Ga	0.0026693186106839	0.5026693186106835	0.5000000000000000
Ga	0.5026693186106835	0.0026693186106839	0.5000000000000000
Ga	0.4973306813893161	0.4973306813893161	0.5000000000000000
Ga	0.2526693186106839	0.2526693186106839	0.5000000000000000
Ga	0.2473306813893162	0.7473306813893165	0.5000000000000000
Ga	0.7473306813893165	0.2473306813893162	0.5000000000000000
Ga	0.7526693186106835	0.7526693186106835	0.5000000000000000
Cu	0.5000000000000000	0.2500000000000000	0.2476762876407412
Cu	0.2500000000000000	0.5000000000000000	0.7523237123592588
Cu	0.0000000000000000	0.7500000000000000	0.2476762876407412
Cu	0.7500000000000000	0.0000000000000000	0.7523237123592588
Total Energy:	-5.114416688 eV/atom		

C.5. DFT-calibrated Hückel Parameters

Table C.11. DFT-Calibrated Hückel Parameters

Compound, RMS deviation[a]	Orbital	H_{ii} (eV)	c_1	$\xi_1(a_o^{-1})$	c_2	$\xi_2(a_o^{-1})$
$NbGa_3$, 0.17 eV	Nb 5s	-2.885		2.0510		
	Nb 5p	-1.098		2.0510[b]		
	Nb 4d	-7.014	0.5796	7.4150	0.4221	1.8176
	Ga 4s	-10.118		2.6607		
	Ga 4p	-5.293		2.3066		
$MoGa_3$, 0.18 eV	Mo 5s	-2.797		2.1536		
	Mo 5p	-1.308		2.1536[b]		
	Mo 4d	-7.897	0.5698	8.0517	0.4358	1.9443
	Ga 4s	-10.395		2.6831		
	Ga 4p	-5.636		2.3847		
Mo_2CuGa_5, 0.10 eV	Mo 5s	-3.705		2.0627		
	Mo 5p	-1.946		2.0627[b]		
	Mo 4d	-7.566	0.5705	6.1012	0.4345	1.8958
	Cu 4s	-6.928		2.6258		
	Cu 4p	-5.141		2.6258[b]		
	Cu 3d	-10.367	1.1917	6.3252	0.3724	1.8380
	Ga 4s	-9.944		2.7903		
	Ga 5p	-4.765		2.3387		

[a]Root-mean-squared deviation between the DFT and Hückel band energies up to ca. 1 eV above the E_F.

[b]Constrained to equal for the corresponding value for the s orbital on the same element.

C.6. Comparison of GGA-DFT and DFT-Calibrated Hückel DOS Distributions

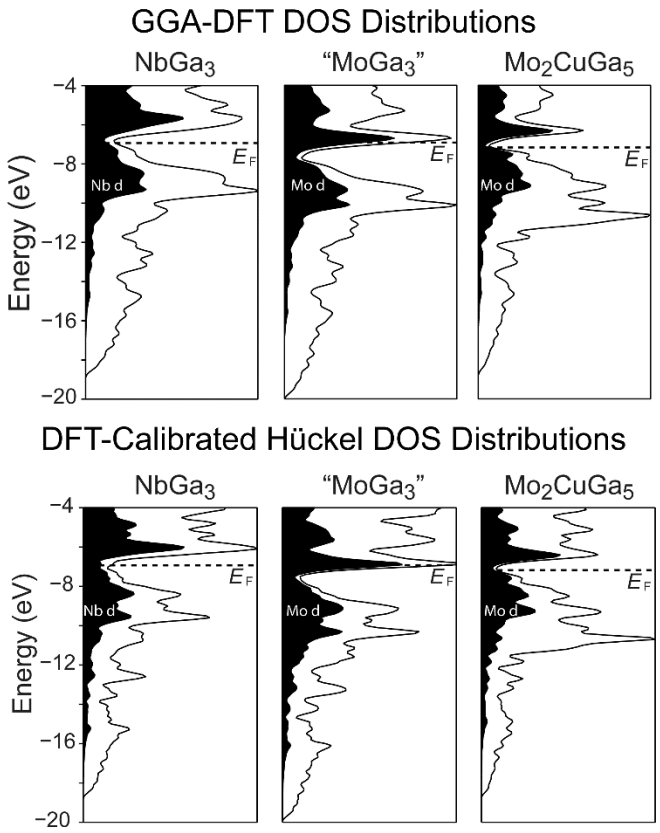

Figure C.3. Electronic DOS curves calculated for $NbGa_3$, a hypothetical $TiAl_3$-type $MoGa_3$ phase, and an ordered model of Mo_2CuGa_5 with GGA-DFT (top) and best-fit Hückel models (bottom).

Appendix D.

Supplemental Information for Chapter 5:

Chemical Pressure-Driven Incommensurability in $CaPd_5$: Clues to High Pressure Chemistry Offered by Complex Intermetallics

D.1. Crystallographic Tables for the Average Structure of $CaPd_{5+q/2}$

In the following, detailed tables are given describing the atomic coordinates and atomic displacement parameters for a model of the average structure of $CaPd_{5+q/2}$ where diffraction intensities attributed to the modulation vector, q, have not been considered (see Sections 5.5.1 and 5.5.2 for discussion).

Table D.1. Refined atomic coordinates for the average $CaPd_{5+q/2}$ structure.[a]

Site	Multi-plicity	x	y	z	$U_{equivalent}$	Occu-pancy
Pd1[a]	8	0.8272(15)	0	0	0.119(5)	0.68
Pd2[a]	16	0.6703(11)	0.8299(8)	0.0007(2)	0.069(2)[a]	0.5195
Pd3	4	0	0.6668(4)	0.75	0.0066(9)	1.0
Pd4	8	0.7504(4)	0.917(3)	0.75	0.0102(8)	1.0
Pd5	8	0	0.8347(4)	0.87914(13)	0.0165(9)	1.0
Pd6	8	0.5	0.0009(4)	0.12112(13)	0.0180(9)	1.0
Ca1	8	0	0.8328(9)	0.1476(4)	0.0131(19)	1.0

[a]The average $CaPd_{5+q/2}$ structure can be indexed in a hexagonal cell with the $P6_3/mmc$ symmetry as discussed in Sections 5.5.1 and 5.5.2 . In order for convenient comparison of the average model with the (3+1)D model, the parameters in this table correspond to a model which has been transformed to the orthorhombic setting and refined in *Cmcm* symmetry with identical cell parameters to those of the (3+1)D model reported Table 5.1.

[b]Pd1 and Pd2 lie in the diffuse electron density atomic positions corresponding most strongly affected by the modulation. It is possible to create a model of this net with more reasonable $U_{equivalent}$ values by splitting the atomic positions of Pd1 and Pd2 into many partially occupied atomic sites tracing out the diffuse honeycomb net of electron density. The atomic positions however are more accurately described by the (3+1)D model.

Table D.2. Refined atomic displacement parameters for the average $CaPd_{5+q/2}$ structure.

Site	U_{11}	U_{22}	U_{33}	U_{12}	U_{13}	U_{23}
Pd1	0.049(4)	0.269(15)	0.012(3)	0	0	-0.023(8)
Pd2	0..026(3)	0.179(9)	0.003(2)	-0.007(3)	0.0013(18)	0.007(6)
Pd3	0.0075(16)	0.0049(16)	0.0073(17)	0	0	0
Pd4	0.0134(13)	0.0101(14)	0.0073(13)	0.0003(8)	0	0
Pd5	0.0258(17)	0.0194(17)	0.0042(14)	0	0	0.0000(13)
Pd6	0.0259(17)	0.0209(17)	0.0071(13)	0	0	-0.0004(13)
Ca1	0.017(3)	0.016(3)	0.006(3)	0	0	0.001(3)

D.2. Powder X-ray Diffraction Pattern of $CaPd_{5+q/2}$

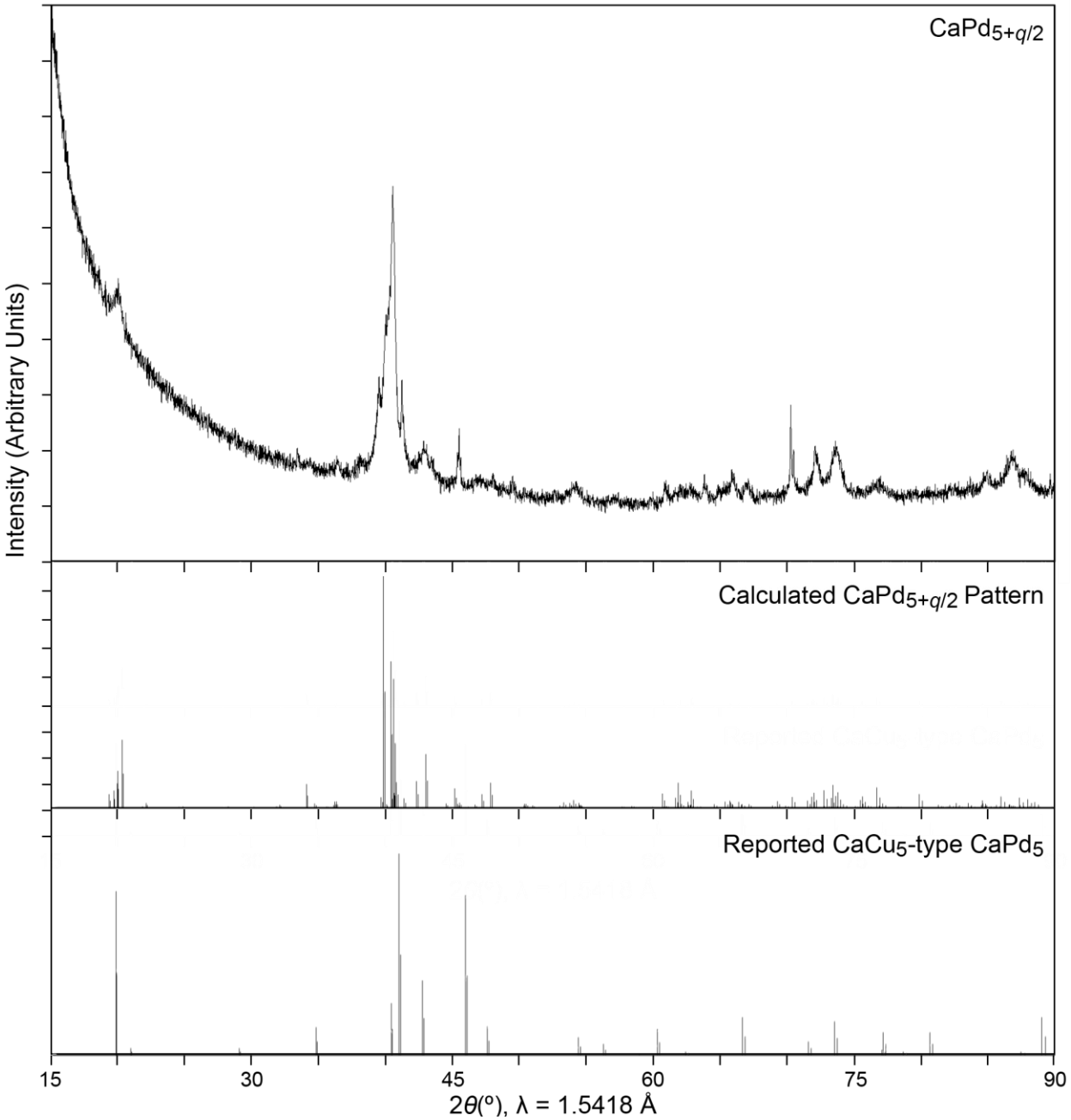

Figure D.1. The powder X-ray diffraction pattern of $CaPd_{5+q/2}$ shown with the calculated diffraction peaks from the average $CaPd_{5+q/2}$ structure and the reported $CaCu_5$-type $CaPd_5$ structure. The broad nature of the peaks and low intensity observed in the experimental diffraction pattern is presumably due to the loss of crystallinity upon grinding this malleable material. The uncertainty in the peak positions caused by the reduced crystallinity make it possible to index the largest peaks using either the calculated $CaPd_{5+q/2}$ or $CaCu_5$-type $CaPd_5$ powder diffraction patterns. Single crystal diffraction experiments on the sample, however, confirm the presence of the incommensurately modulated $CaPd_{5+q/2}$ phase, whereas attempts to isolate a single crystal of the $CaCu_5$-type $CaPd_5$ phase have been unsuccessful.

D.3. Crystallographic Information Tables for the (3+1)D Model of $CaPd_{5+q/2}$

In the following, detailed tables are given describing the atomic coordinates, atomic displacement parameters, and modulation functions refined for the (3+1)D model of $CaPd_{5+q/2}$

Table D.3. Refined atomic coordinates for $CaPd_{5+q/2}$.

Site	Multiplicity	x_1	x_2	x_3	$U_{equivalent}$	Occupancy
Pd1	8	0.8058(2)	0	0	0.0213(3)	0.68[b]
Pd2	16	0.68124(19)	0.82529(9)	0.00077(3)	0.0165(2)[a]	0.5195[b]
Pd3	4	0	0.66697(7)	0.75	0.00798(18)	1.0
Pd4	8	0.75017(9)	0.91686(5)	0.75	0.00784(14)	1.0
Pd5	8	0	0.83442(7)	0.87929(2)	0.00960(15)	1.0
Pd6	8	0.5	0.00086(8)	0.12105(3)	0.01150(15)	1.0
Ca1	8	0	0.83241(17)	0.14608(8)	0.0105(4)	1.0

[a]Pd1 and Pd2 are the atoms whose positions lie in the incommensurate Pd_{net}. While large $U_{equivalent}$ can often indicate an incorrect atomic assignment or partial occupancy of an atomic positions, in this case the relatively large $U_{equivalent}$ values are due to harmonic ADP parameters serving to help model the positional disorder at certain points within this incommensurately modulated net. For more information, see the discussion in Section D6.

[b]Included in model as the Δ parameters of crenel functions.

Table D.4. Refined atomic displacement parameters for $CaPd_{5+q/2}$.

Site	U_{11}	U_{22}	U_{33}	U_{12}	U_{13}	U_{23}
Pd1	0.0337(7)	0.0203(7)	0.0099(4)	0	0	-0.0026(5)
Pd2	0.0236(4)	0.0170(4)	0.0088(3)	-0.0042(3)	0.0032(3)	0.0002(4)
Pd3	0.0082(3)	0.0067(3)	0.0090(3)	0	0	0
Pd4	0.0053(2)	0.0095(3)	0.0087(2)	0.00140(16)	0	0
Pd5	0.0091(2)	0.0136(3)	0.0061(3)	0	0	-0.0001(2)
Pd6	0.0110(2)	0.0154(3)	0.0081(2)	0	0	-0.0003(2)
Ca1	0.0078(6)	0.0103(6)	0.0136(6)	0	0	0.0011(6)

Table D.5. Modulation Parameters for $CaPd_{5+q/2}$.

Crenel Functions	Site	Δ[a]	x_{40}[a]
	Pd1	0.68	0.25
	Pd2	0.5195	0.7734

Legendre Polynomial[a] (xyz)	Site	*N*	$S_{x,n}$(odd)	$S_{y,n}$(odd)	$S_{z,n}$(odd)
	Pd1[b]	1	-0.0912(9)	0	0
		2	-0.0027(13)	0	0
	Pd2[b]	1	0.0619(8)	0	0
		2	0.0116(11)	0.0052(4)	-0.0010(3)
	Site	*N*	$S_{x,n}$(even)	$S_{y,n}$(even)	$S_{z,n}$(even)
	Pd1[b]	1	0	-0.0964(3)	0.00323(16)
		2	0	-0.0099(5)	-0.0013(3)
	Pd2[b]	1	0.0149(5)	-0.0678(2)	-0.0012(2)
		2	-0.0012(10)	-0.0023(5)	0.0004(4)
Harmonic (xyz)	Site	*N*	$A_{x,n}$(cos)	$A_{y,n}$(cos)	$A_{z,n}$(cos)
	Pd3	1	0.00167(11)	0	0
	Pd4[c]	1	0.00169(11)	0.00037(9)	0
	Pd5[c]	1	0.00266(13)	0	0
		2	0	0.00070(18)	0.00012(5)
	Pd6	1	0.00013(13)	0	0
		2	0	0.00020(14)	-0.00030(6)
	Ca1[c]	1	-0.0043(3)	0	0
		2	0	-0.0004(4)	0.00041(12)
	Site	*N*	$A_{x,n}$(sin)	$A_{y,n}$(sin)	$A_{z,n}$(sin)
	Pd3	1	0.01593(15)	0	0
	Pd4[c]	1	0.01624(10)	-0.00001(7)	0
	Pd5[c]	1	0.02465(11)	0	0
		2	0	0.00214(10)	0.00013(9)
	Pd6	1	0.02465(11)	0	0
		2	0	0.00135(12)	0.00019(7)
	Ca1[c]	1	0.0214(3)	0	0
		2	0	0.0008(3)	0.0003(2)

Legendre Polynomial (ADP)	Site	*N*	$S_{U11,n}$(odd)	$S_{U22,n}$(odd)	$S_{U33,n}$(odd)
	Pd1[b]	1	0.0398(17)	0.0053(17)	0.0061(13)
	Pd2[b]	1	0.0165(12)	0.0159(14)	0.0027(11)
	Site	*N*	$S_{U12,n}$(odd)	$S_{U13,n}$(odd)	$S_{U23,n}$(odd)
	Pd1[b]	1	0	0	-0.0018(16)
	Pd2[b]	1	-0.0110(10)	0.0044(8)	-0.0001(12)
	Site	*N*	$S_{U11,n}$(even)	$S_{U22,n}$(even)	$S_{U33,n}$(even)
	Pd1[b]	1	0	0	0
	Pd2[b]	1	0.0075(8)	0.0043(10)	0.0005(7)
	Site	*N*	$S_{U12,n}$(even)	$S_{U13,n}$(even)	$S_{U23,n}$(even)
	Pd1[b]	1	0.0278(10)	0.0004(12)	0
	Pd2[b]	1	-0.0157(7)	-0.0010(9)	-0.0016(5)

[a]The parameters x_{40} for Pd2 and Δ for both Pd1 and Pd2 were locked as their ADP and atomic coordinate parameters were refined (x_{40}[Pd2] lies on a special position in the unit cell and cannot be refined). They were then manually adjusted and the ADP and atomic parameters where refined again in an iterative manner so that the crenel functions defining the occupancies of Pd1 and Pd2 terminated at as similar x_4 values as possible in order to define a piecewise function running almost continuously along each Pd1/Pd2 electron density contour. This ensures that there is one and only Pd1/Pd2 atom for each intersection of the physical *y* axis with the contours of the electron density. The slight Pd deficiency of our crystallographically refined composition, $CaPd_{5.219}$, compared to the ideal composition derived from the length of the *q*-vector, $CaPd_{5.2199}$ (see Section D7), indicate that despite our best efforts, there is a very small interval of x_4 for which no Pd1/Pd2 atom is assigned.

[b]As the occupancies of Pd1 and Pd2 are modelled with a crenel function, their positional and ADP modulations were treated with Legendre polynomials which have been orthogonalized over the crenel interval. Their positions are defined by the equation:

$$\mathbf{r}_v = \mathbf{r}_{v,0} + \sum_n \mathbf{S}^o_{vn} P^o_n[2(x_4 - x_{40})/\Delta] + \mathbf{S}^e_{vn} P^e_n[2(x_4 - x_{40})/\Delta]$$

where $\mathbf{r}_{v,0}$ is the average position ro ADP parameter of atom *v* and **S** is the amplitude of the odd (o) or even (e) members of the Legendre polynomial (*P*) used to create the n^{th} modulation wave for atom *v*. For discussion of the derivation of this equation and the use of Legendre Polynomials in combination with crenel functions in JANA2006 see Dušek, M.; Petříček, V.; Palatinus, L. Journal of Physics: Conference Series **2010**, *226*, 012014.

[c]*N*=2 of Pd3 and Pd4 were not included because their refinement led to no terms for which the magnitude was greater than 3 times the standard deviation. N=2 functions were included on Ca1 because $A_{z,n}$(cos) narrowly surpassed this threshold for this site, but could also be removed without significant detriment to the model.

D.4. Observed Fourier Electron Density Map Cross Sections Centered on Atomic Positions in $CaPd_{5+q/2}$.

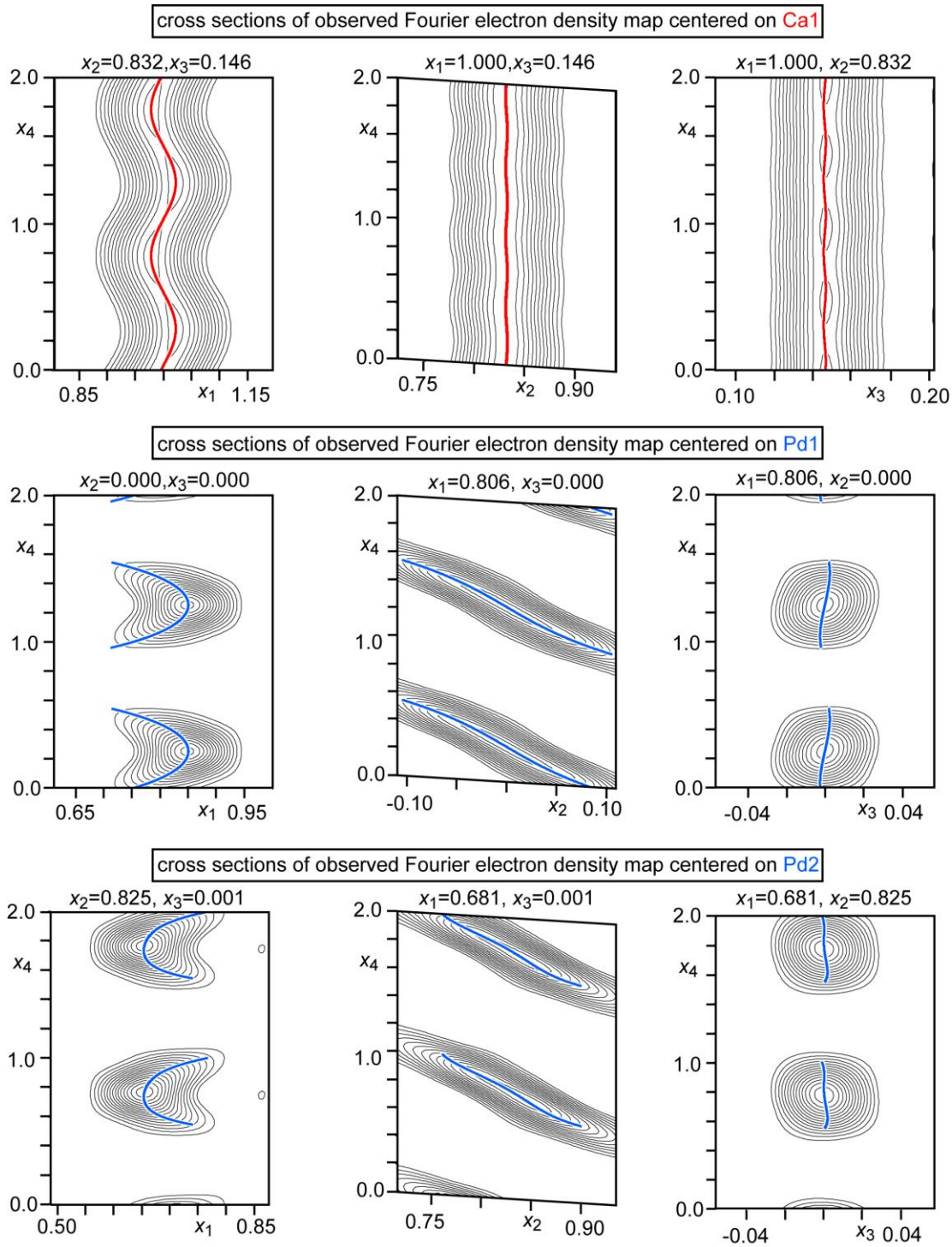

Figure D.2. The functions modelling the atomic positions of Ca1 (red), Pd1 (blue), and Pd2 (blue) overlaid on cross sections of the observed Fourier electron density maps centered on their locations summed over 1 Å in the remaining two dimensions.

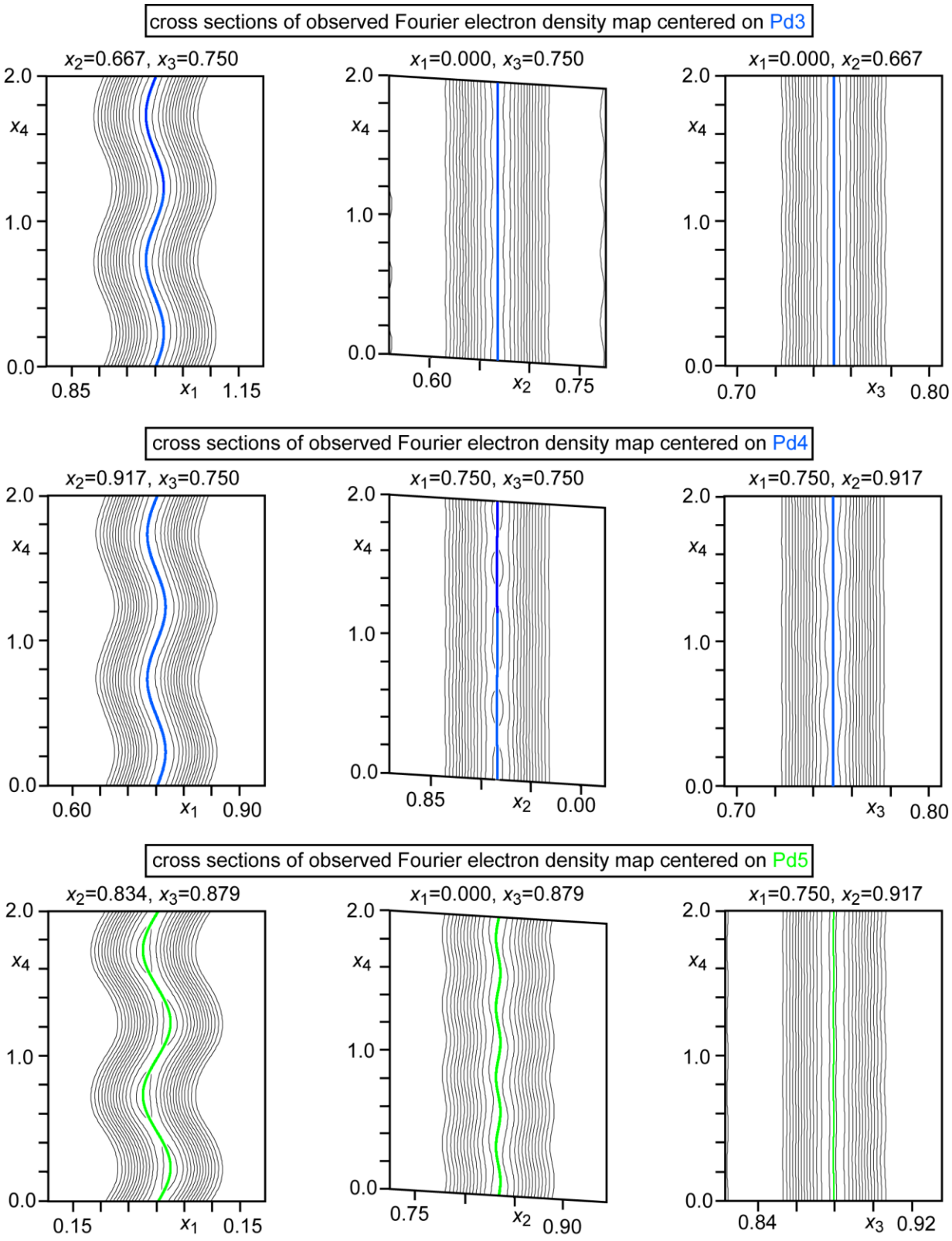

Figure D3. The functions modelling the atomic positions of Pd3 (blue), Pd4 (blue), and Pd5 (green) overlaid on cross sections of the observed Fourier electron density maps centered on their locations summed over 1 Å in the remaining two dimensions.

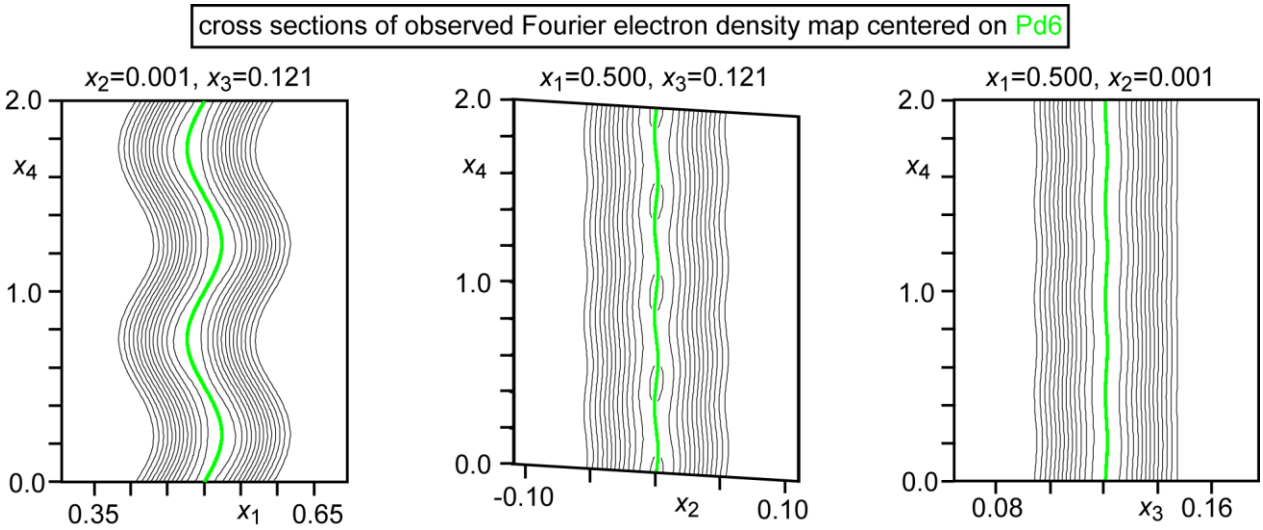

Figure D.4. The functions modelling the atomic position of Pd6 (green) overlaid on cross sections of the observed Fourier electron density maps centered on their locations summed over 1 Å in the remaining two dimensions.

D.5. Interatomic Distances in $CaPd_{5+q/2}$.

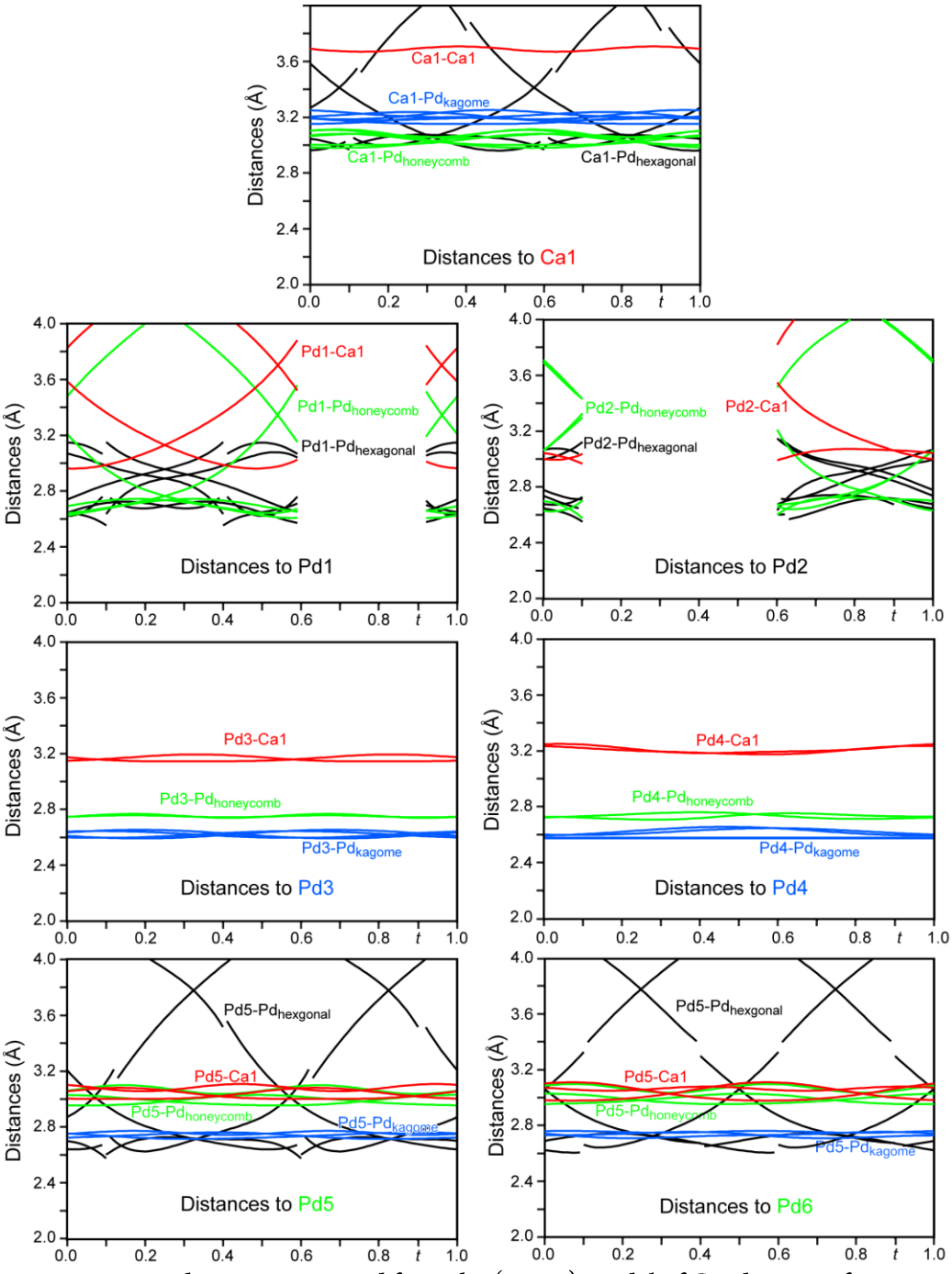

Figure D.5. Interatomic distances extracted from the (3+1D) model of $CaPd_{5+q/2}$ as a function of the x_4-intercept, t, for each of the symmetry-inequivalent atomic domains. Colors are used to distinguish interatomic distances to different geometric features, e.g. in the top panel blue Ca-Pd curves show all distances between Ca1 and the Pd1 and Pd2 atoms in the incommensurate hexagonal net, the black curves show distances between Ca1 and Pd3 and Pd4 atoms in the kagome net, and the green curves show the distances between the Ca1 atom and Pd5 and Pd6 atoms in the honeycomb layer.

D.6. Discussion of Pd1 and Pd2 Atomic Displacement Parameters.

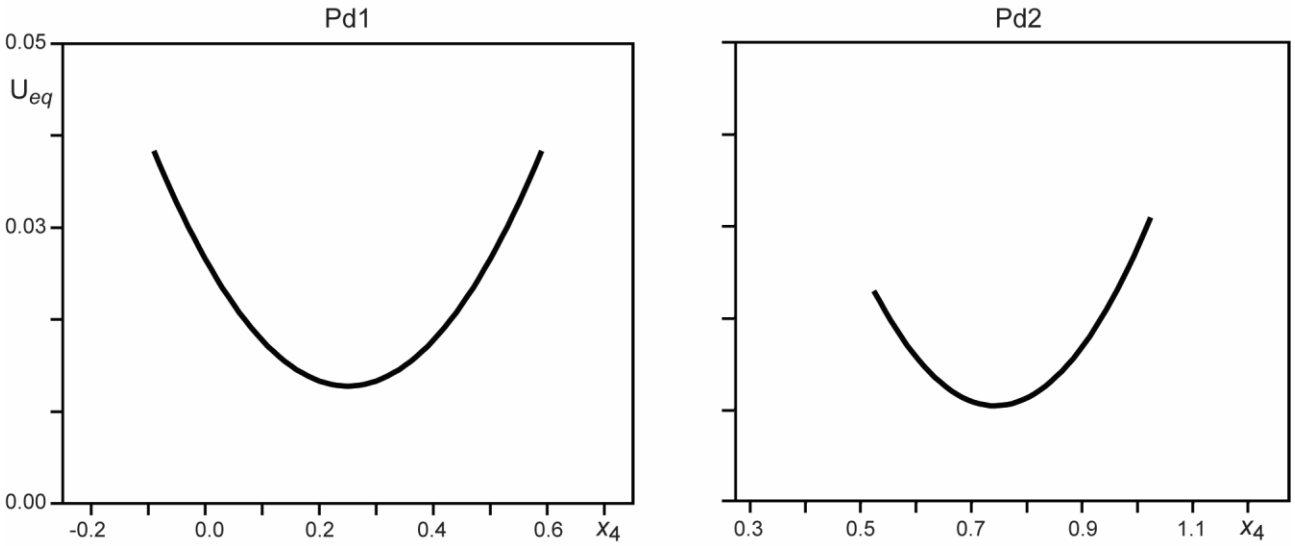

Figure D.6. A plot of $U_{equivalent}$ versus x_4 centered on x_{40} for the atoms Pd1 and Pd2.

From these plots we can see that the $U_{equivalent}$ of Pd1 and Pd2 becomes has a minimum value of over x_{40} (x_4=0.25 and 0.7734 respectively), in good agreement with the $U_{equivalent}$ values of the other Pd atoms in the structure not located in the incommensurate modulated Pd hexagonal net. As we move from x_{40} toward either end of the functions defining the atoms positions of Pd1 or Pd2, the $U_{equivalent}$ for increase substantially. Large values of $U_{equivalent}$ often suggest the assignment of an atom with too much electron density or a relatively diffuse electron density feature. In this case, the locations along x_4 which show the maxima in $U_{equivalent}$ correspond with minima in the Pd1/Pd2 electron density lying over the Ca-Pd and Pd-Pd contact in the layer below (Figure 5.7). We thus interpret the behavior of the Atomic Displacement Parameters as accounting for the positional disorder of the Pd1/Pd2 atoms as they avoid placement directly above the edges of the Ca/Pd triangles in the layer above and below.

Rather than allow the ADP parameter to model the position disorder at specific locations along in this Pd1/Pd2 net, another option would be to add a second occupational modulation function, in addition to the crenel functions, to our model for the Pd1/Pd2 atoms. The use of a harmonic wave in addition to the

crenel functions would allow the use of sine and cosine waves to gradually vary the occupancy of the Pd1/Pd2 atoms along the length of the crenel interval, ideally reaching maxima (representing a fully occupied Pd atomic position) at x_{40} and gradually decreasing to zero toward the ends of the crenel interval where the positional disorder is most prevalent and the functions describing the Pd1 and Pd2 atoms meet. Unfortunately, our attempts to the implement a second occupation modulation into the model led to strong correlations and instability in our refinements.

D.7. Discussion of the Relationship Between the q-Vector and Stoichiometry.

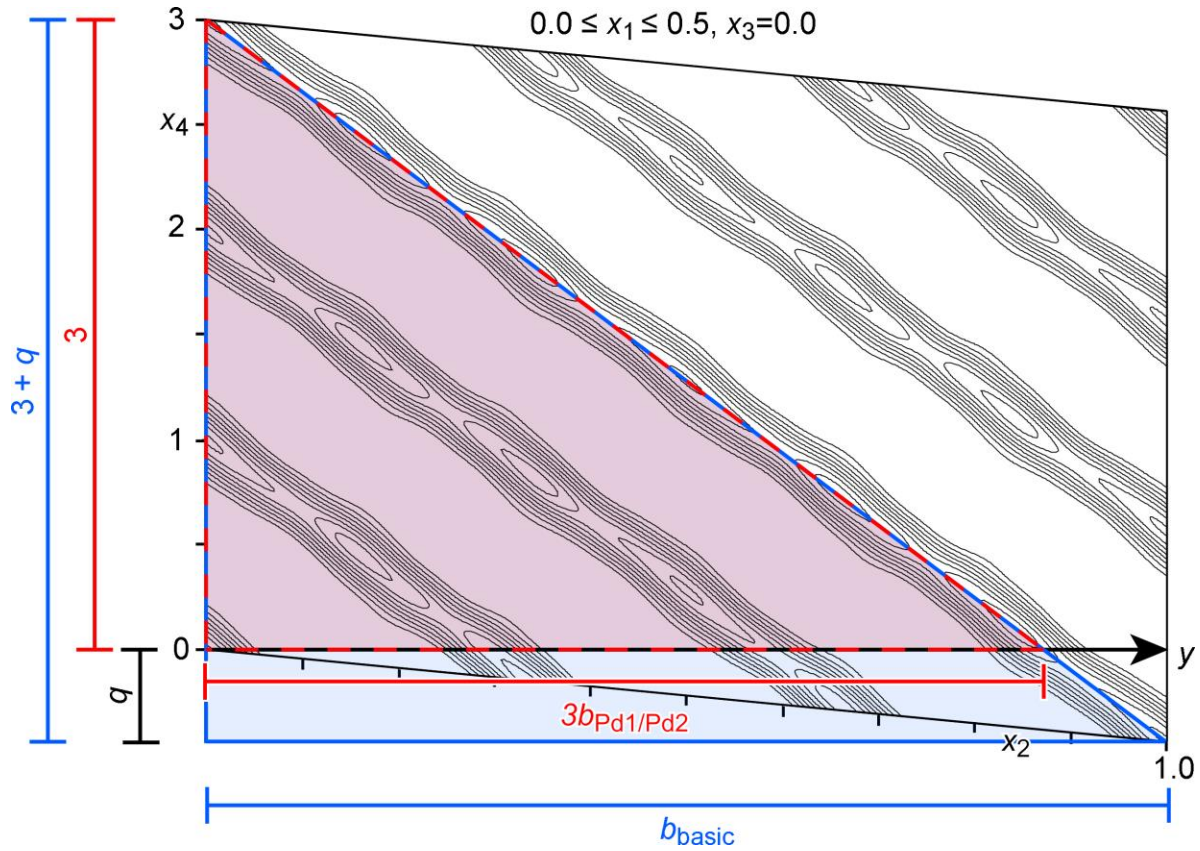

Figure D.7.. A cross section of the electron density at $x_3 = 0$ summed between $0.0 \leq x_1 \leq 0.5$. Overlaid on the electron density cross section are two similar triangles- one defined by intersections of a contour of Pd electron density with x_2 and x_4 (blue) and one defined by intersection of a contour of Pd electron density with y and x_4 (red). From this geometrical construction, the relation of the modulation vector, q, to the number of addition Pd atoms inserted into the structure due to the modulation can be ascertained (see text below).

In Figure D.7 we show a cross section through x_2-x_4 plane of the electron density for one chain of Pd atoms in the incommensurate layer. From this picture we can derive the composition, or the value of x in $CaPd_{5+x}$ as a function of the modulation vector, q. We begin by making some observations about the slope of electron density through x_2-x_4. In order for the structure to maintain translational symmetry, the intersection of the electron density with x_2, or the slope of the electron density through x_2-x_4, must be a positive integer n. In the $CaPd_{5+x}$ structure we can see that for one period of along x_2, n=3. The position of the Pd

atoms in this chain in physical space, however, is controlled by the frequency that the physical axis, *y*, intersects the contours of electron density.

As discussed in Section 5.5.1, the modulation vector, *q*, lies along **b*** in the $CaPd_{5+x}$ structure and consequently directly controls the frequency at which the *y* axis intersects the electron density. From Figure D7, we can see that this frequency is dictated by the ratio of the periodicity of the Pd1/Pd2 chain of atoms, $b_{Pd1/Pd2}$, and the periodicity of the basic unit cell, b_{basic}. Using similar triangles defined by the intersection of the electron density with x_2 and x_4(blue) and the electron density' intersection with *y* and x_4(red), we can see how the ratio $b_{Pd1/Pd2}/b_{basic}$ is dependent upon *q*. For similar triangles, corresponding sides are all in the same proportion, we therefore obtain:

$$\frac{3+q}{b_{\text{basic}}} = \frac{3}{3b_{\text{Pd1/Pd2}}}$$

$$b_{\text{basic}} = (3+q)b_{\text{Pd1/Pd2}}$$

In the case of a commensurate structure defined only by the basic cell, where *q*=0, we can see that:

$$q = 0 \Rightarrow \quad b_{\text{basic}} = 3b_{\text{Pd1/Pd2}}$$

The number of Pd/Pd2 in the basic cell can then calculated in the case of *q*=0 to be:

$$\frac{\text{number of Pd1/Pd2 atoms}}{\text{basic cell}} = \frac{1\ \text{Pd1/Pd2 atom/Pd chain}}{b_{\text{Pd1/Pd2}}} \times \frac{3\ b_{\text{Pd1/Pd2}}}{1\ b_{\text{basic}}} \times b_{\text{basic}} \times \frac{4\ \text{Pd1/Pd2 chains}}{\text{basic cell}}$$

$$= \frac{12\ \text{Pd1/Pd2 atoms}}{\text{basic cell}}$$

There are an addition 8 Ca atoms and 28 Pd atoms in the honeycomb and kagome layers which are relatively unaffected by the modulation leading to an ideal composition for *q* = 0 of:

$$\frac{Ca_8Pd_{28} + Pd_{12}}{\text{basic cell}} \times \frac{\text{basic cell}}{8\ \text{formula units}} = CaPd_5$$

We can therefore see that without modulation the ideal composition of the structure is $CaPd_5$, agreeing with the composition of the hexagonal $CaPd_{5+x}$ used for the Chemical Pressure analysis. How does taking into account the modulation affect the stoichiometry? As modulation is introduced into the Pd1/Pd2 layer, we can calculate the number of Pd1/Pd2 atoms in the basic cell as a function of q:

$$\frac{\text{number of Pd1/Pd2 atoms}}{\text{basic cell}} = \frac{1\ \text{Pd1/Pd2 atom/Pd chain}}{b_{\text{Pd1/Pd2}}} \times \frac{(3+q)b_{\text{Pd1/Pd2}}}{1\ b_{\text{basic}}} \times b_{\text{basic}} \times \frac{4\ \text{Pd1/Pd2 chains}}{\text{basic cell}}$$

$$= \frac{(12+4q)\ \text{Pd1/Pd2 atoms}}{\text{basic cell}}$$

When we take into account the other Ca and Pd atoms in the basic cell, this leads to a composition of:

$$\frac{Ca_8Pd_{28} + Pd_{12+4q}}{\text{basic cell}} \times \frac{\text{basic cell}}{8\ \text{formula units}} = CaPd_{5+q/2}$$

We can see from this that the number of extra Pd atoms added to the composition from the modulation, or the x in $CaPd_{5+x}$, is equal to the half of the length of the modulation vector $(q/2)$. In our case q =0.4398(2), leading to an ideal composition of $CaPd_{5.2199}$, which is in good agreement with our crystallographically refined composition of $CaPd_{5.219}$. The small Pd deficiency in our refined composition reflects the difficulties in ensuring that the discontinuous functions used to define the Pd1 and Pd2 atoms terminate at identical values of t (as seen in Figure 5.7). This indicates that in our model there is a small, nearly imperceptible gap for which when physical space y intersects a Pd1/Pd2 electron density column, no Pd1 or Pd2 atoms are defined in the incommensurately modulated hexagonal net.

D.8. Computational Details and Optimized Geometries for Chemical Pressure Calculations.

Table D.6. Details of LDA-DFT calculations on structures serving as a basis for chemical pressure calculations.

Structure	Psuedopotentials	Energy Cut-off[a]	k-point vectors[b]	k-point shift	FFT mesh	Total Energy (Ha/atom)
$CaPd_5$ ($CaCu_5$-type)	LDA	60 Ha	7 0 0 0 7 0 0 0 8	0.0 0.0 0.5	90 × 90 × 72	-30.27087
$CaPd_5$ (commensurate approx.)	LDA	60 Ha	7 0 0 0 7 0 0 0 2	0.0 0.0 0.5	90 × 90 × 288	-30.27204
Ca_2Pd_7	LDA	60 Ha	5 5 0 -3 3 0 0 0 2	0.5 0.5 0.5	108 × 108 × 288	-30.70869
$CaAg_5$	LDA	120 Ha	7 0 0 0 7 0 0 0 8	0.0 0.0 0.5	144 × 144 × 120	-36.95227
Ca_2Ag_7	LDA	120 Ha	5 5 0 -3 3 0 0 0 2	0.5 0.5 0.5	162 × 162 × 384	-36.94154
$CaCu_5$	LDA	70 Ha	7 0 0 0 7 0 0 0 8	0.0 0.0 0.5	120 × 120 × 96	-37.87103
Ca_2Cu_7	LDA	70 Ha	10 10 0 -6 6 0 0 0 4	0.5 0.5 0.5	126 × 126 × 320	-45.57106

[a]The energy cut-offs were chosen by testing convergence of the CP map against this parameter.
[b]Three vectors that define a real-space supercell whose reciprocal lattice defines the k-point grid.

Table D.7. LDA-DFT optimized cell parameters.[a]

Structure	x (Å)	y (Å)	z (Å)	α(°)	β(°)	γ(°)
$CaPd_5$ ($CaCu_5$-type)	5.23266	5.23266	4.40006	90	90	120
$CaPd_5$ (commensurate approx.)	5.09384	5.09384	17.49488	90	90	120
Ca_2Pd_7	8.93020	5.19168	13.24036	90	90	90
$CaAg_5$	5.46258	5.46258	4.54140	90	90	120
Ca_2Ag_7	9.26178	5.42126	13.73265	90	90	90
$CaCu_5$	4.98557	4.98557	3.94050	90	90	120
Ca_2Cu_7	8.75327	4.84924	12.41638	90	90	90

[a]Geometry optimizations were carried out in two steps: first the atomic positions were allowed to relax in a unit cell of fixed size, then the energy was minimized with respect to all structural parameters.

Table D.8. LDA-DFT optimized atomic positions for the $CaCu_5$-type CaT_5 structure (T=Cu, Ag, or Pd).[a]

Atom Type	x	y	z
Ca	0.00000	0.00000	0.00000
T[b]	0.33333	0.66667	0.00000
T[b]	0.50000	0.00000	0.500000
T[b]	0.66667	0.33333	0.00000
T[b]	0.50000	0.50000	0.50000
T[b]	0.00000	0.50000	0.50000

[a]In the $CaCu_5$-type structure all of the atomic positions lay on high symmetry points in the unit cell. Consequently, there are no free parameters to refine in their atomic positions.

[b]The atomic positions in this table represent the positions for all structures which adopt the $CaCu_5$-type structure.

Table D.9. LDA-DFT-optimized atomic positions for the commensurate approximant of $CaPd_{5+q/2}$ ($q \approx 0.44$)

Atom Type	x	y	z
Ca	0.33333	0.66667	0.85629
Ca	0.66667	0.33333	0.14371
Ca	0.33333	0.66667	0.64371
Ca	0.66667	0.33333	0.35629
Pd	0.17699	0.33301	0.25000
Pd	0.33301	0.17699	0.75000
Pd	0.84398	0.66699	0.75000
Pd	0.15602	0.82301	0.25000
Pd	0.82301	0.15602	0.75000
Pd	0.66699	0.84398	0.25000
Pd	0.66667	0.33333	0.88041
Pd	0.33333	0.66667	0.38041
Pd	0.33333	0.66667	0.11959
Pd	0.66667	0.33333	0.61959
Pd	0.00000	0.00000	0.61854
Pd	0.00000	0.00000	0.11854
Pd	0.00000	0.00000	0.38146
Pd	0.00000	0.00000	0.88146
Pd	0.34071	0.00000	0.00000
Pd	0.00000	0.34071	0.00000
Pd	0.65929	0.65929	0.00000
Pd	0.00000	0.34071	0.50000
Pd	0.34071	0.00000	0.50000
Pd	0.65929	0.65929	0.50000

Table D.10. LDA-DFT-optimized atomic positions of a hypothetical Ca_2Ag_7-type Ca_2Pd_7 phase.

Atom Type	*x*	*y*	*z*
Ca	0.00000	0.32688	0.11510
Ca	0.50000	0.82688	0.11510
Ca	0.00000	0.67312	0.61510
Ca	0.50000	0.17312	0.61510
Ca	0.00000	0.32688	0.38490
Ca	0.50000	0.82688	0.38490
Ca	0.00000	0.67312	0.88490
Ca	0.50000	0.1712	0.88490
Pd	0.00000	0.83862	0.25000
Pd	0.50000	0.33862	0.25000
Pd	0.75205	0.58302	0.25000
Pd	0.25205	0.08302	0.25000
Pd	0.83420	0.83059	0.07666
Pd	0.33420	0.33059	0.07666
Pd	0.00000	0.16138	0.75000
Pd	0.50000	0.66138	0.75000
Pd	0.24795	0.41698	0.75000
Pd	0.74795	0.91698	0.75000
Pd	0.16580	0.16941	0.57666
Pd	0.66580	0.66941	0.57666
Pd	0.24795	0.58302	0.25000
Pd	0.74795	0.08302	0.25000
Pd	0.16580	0.83059	0.42334
Pd	0.66580	0.33059	0.42334
Pd	0.75205	0.41698	0.75000
Pd	0.25205	0.91698	0.75000
Pd	0.83420	0.16941	0.92334
Pd	0.33420	0.66941	0.92334
Pd	0.16580	0.16941	0.92334
Pd	0.66580	0.66941	0.92334
Pd	0.83420	0.83059	0.42334
Pd	0.33420	0.33059	0.42334
Pd	0.83420	0.16941	0.57666
Pd	0.33420	0.66941	0.57666
Pd	0.16580	0.83059	0.07666
Pd	0.66580	0.33059	0.07666

Table D.11. LDA-DFT-optimized atomic positions of Ca_2Ag_7.

Atom Type	x	y	z
Ca	0.00000	0.32130	0.11428
Ca	0.50000	0.82130	0.11428
Ca	0.00000	0.67870	0.61428
Ca	0.50000	0.17870	0.61428
Ca	0.00000	0.32130	0.38572
Ca	0.50000	0.82130	0.38572
Ca	0.00000	0.67870	0.88572
Ca	0.50000	0.17870	0.88572
Ag	0.00000	0.82679	0.25000
Ag	0.50000	0.32679	0.25000
Ag	0.75068	0.57714	0.25000
Ag	0.25068	0.07714	0.25000
Ag	0.83508	0.82927	0.07633
Ag	0.33508	0.32927	0.07633
Ag	0.00000	0.17321	0.75000
Ag	0.50000	0.67321	0.75000
Ag	0.24932	0.42286	0.75000
Ag	0.74932	0.92286	0.75000
Ag	0.16492	0.17073	0.57633
Ag	0.66492	0.67073	0.57633
Ag	0.24932	0.57714	0.25000
Ag	0.74932	0.07714	0.25000
Ag	0.16492	0.82927	0.42367
Ag	0.66492	0.32927	0.42367
Ag	0.75068	0.42286	0.75000
Ag	0.25068	0.92286	0.75000
Ag	0.83508	0.17073	0.92367
Ag	0.33508	0.67073	0.92367
Ag	0.16492	0.17073	0.92367
Ag	0.66492	0.67073	0.92367
Ag	0.83508	0.82927	0.42367
Ag	0.33508	0.32927	0.42367
Ag	0.83508	0.17073	0.57633
Ag	0.33508	0.67073	0.57633
Ag	0.16492	0.82927	0.07633
Ag	0.66492	0.32927	0.07633

Table D.12. LDA-DFT-optimized atomic positions of a hypothetical Ca_2Ag_7-type Ca_2Cu_7 phase.

Atom Type	x	y	z
Ca	0.00000	0.24998	0.11086
Ca	0.50000	0.74998	0.11086
Ca	0.00000	0.75002	0.61086
Ca	0.50000	0.25002	0.61086
Ca	0.00000	0.24998	0.38914
Ca	0.50000	0.74998	0.38914
Ca	0.00000	0.75002	0.88914
Ca	0.50000	0.25002	0.88914
Cu	0.00000	0.74998	0.25000
Cu	0.50000	0.24998	0.25000
Cu	0.75000	0.49998	0.25000
Cu	0.25000	0.99998	0.25000
Cu	0.82014	0.74997	0.08332
Cu	0.32014	0.24997	0.08332
Cu	0.00000	0.25002	0.75000
Cu	0.50000	0.75002	0.75000
Cu	0.25000	0.50002	0.75000
Cu	0.75000	0.00002	0.75000
Cu	0.17986	0.25003	0.58332
Cu	0.67986	0.75003	0.58332
Cu	0.25000	0.49998	0.25000
Cu	0.75000	0.99998	0.25000
Cu	0.17986	0.74997	0.41668
Cu	0.67986	0.24997	0.41667
Cu	0.75000	0.50002	0.75000
Cu	0.25000	0.00002	0.75000
Cu	0.82014	0.25003	0.91668
Cu	0.32014	0.75003	0.91668
Cu	0.17986	0.25003	0.91668
Cu	0.67986	0.75003	0.91668
Cu	0.82014	0.74997	0.41668
Cu	0.32014	0.24997	0.41668
Cu	0.82014	0.25003	0.58332
Cu	0.32014	0.75003	0.58332
Cu	0.17986	0.74997	0.08332
Cu	0.67986	0.24997	0.08332

D.9. Examination of the Role of Ionic Charge in the Integrated Chemical Pressure Schemes.

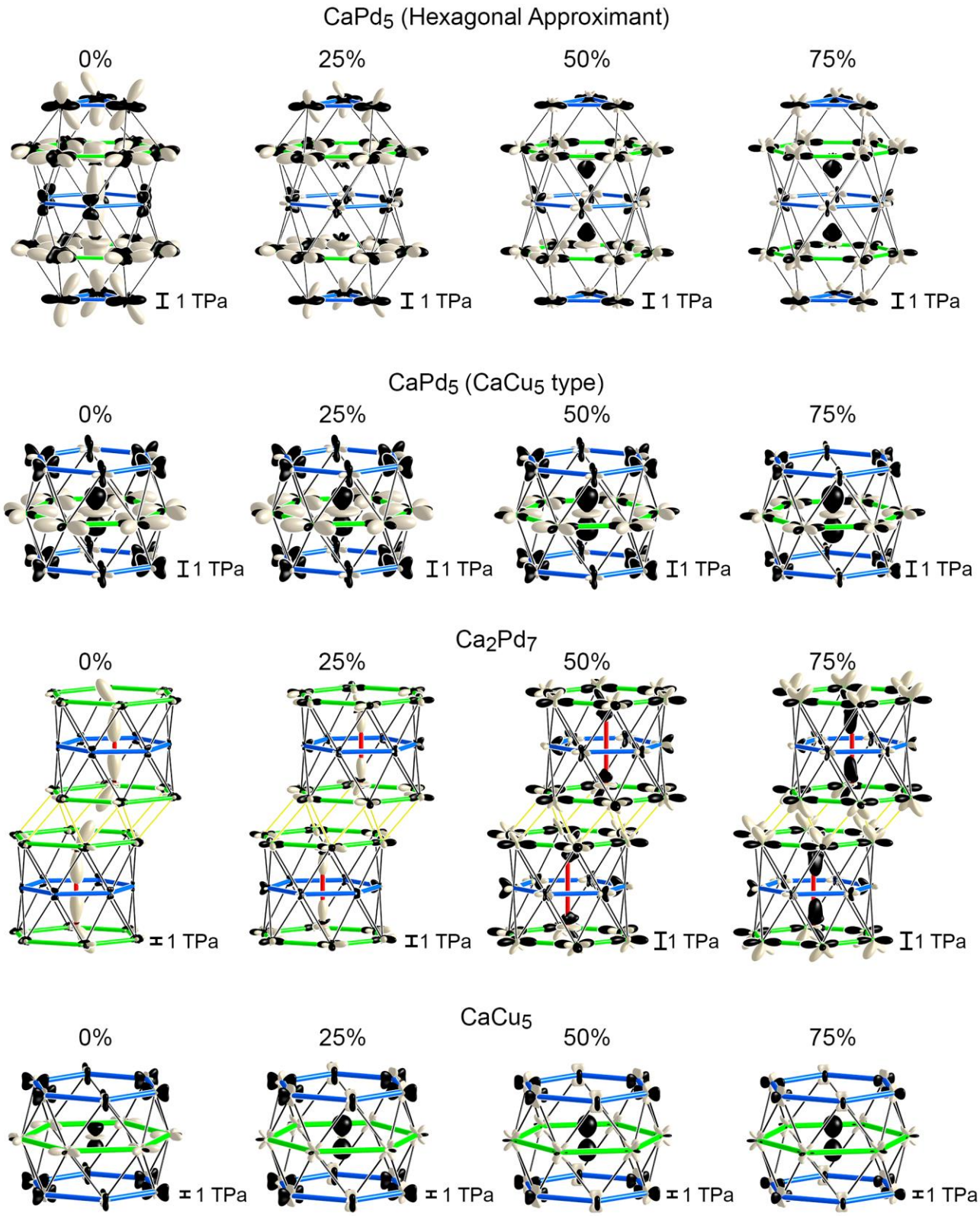

Figure D.8. See caption on next page.

Figure D.8. The role played by ionic charge in the integrated CP schemes of the compounds (real and hypothetical) presented in this paper. The CP schemes have been calculated for each structure using electron density profiles based on 0%, 25%, 50%, and 75% of the charge determined from Bader charger analysis on the phase. The differences in the CP schemes correspond to the differing amounts that the contact volumes reach into the core region of the atoms. Intergration CP schemes using electron density profiles using ~50% of the Bader charge have been shown to accurately represent the Chemical Pressures in the Ca-Pd system and are used for all Ca-Late Transition Metal compounds in this Article. For more information see Engelkemier, J.; Fredrickson, D. C., *Chem. Mater.* **2016**, *ASAP*, DOI:10.1021/acs.chemmater.6b00917.

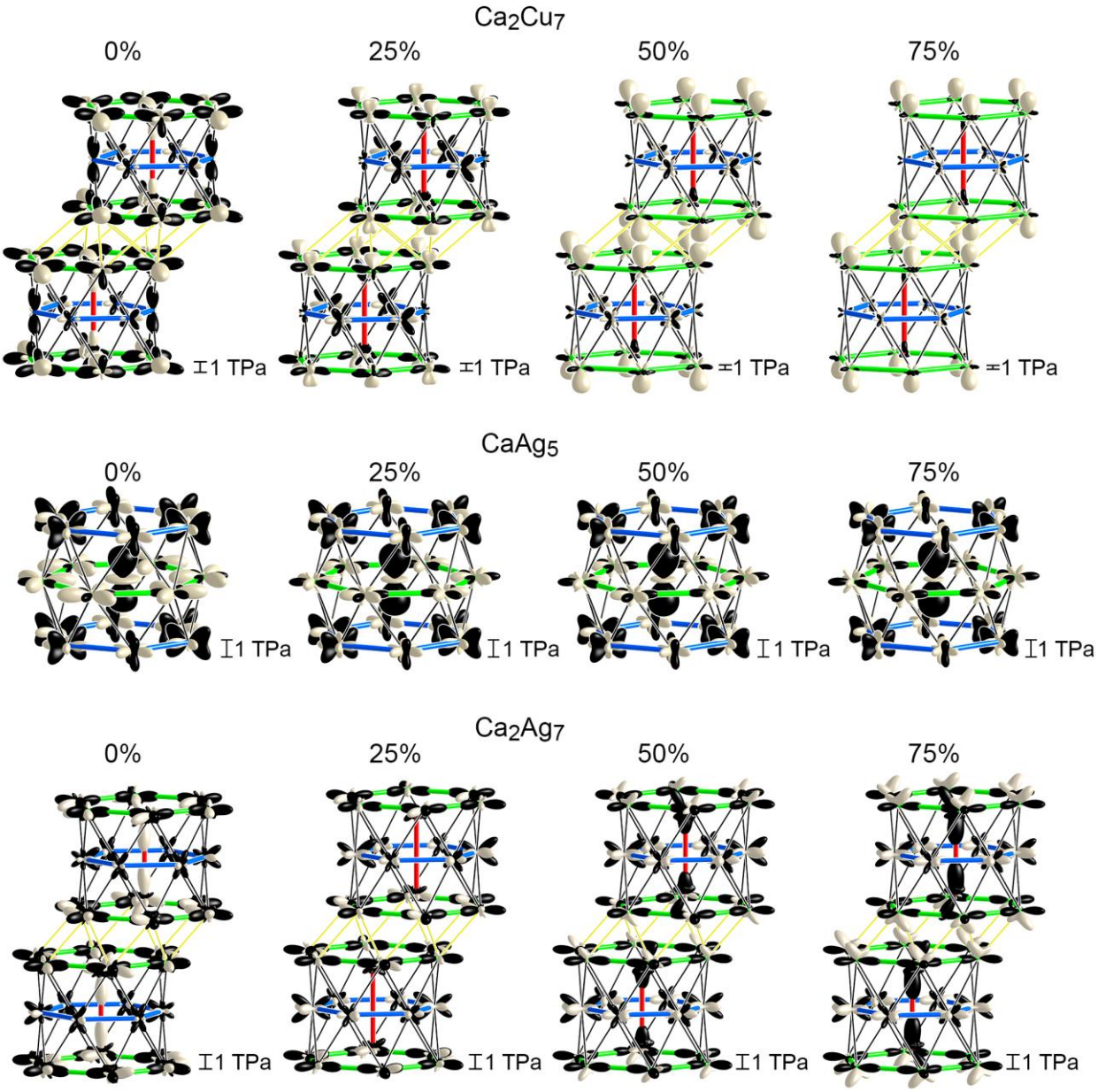

Figure D.8 (cont).

D.10. Computational Details and Optimized Geometries for Variable Pressure Calculations.

Table D.13. Computational parameters and total energies of structures serving as a basis for variable pressure and Bader charge analysis with VASP.

Structure	Potentials	Energy Cut-off	k-point mesh	FFT grid	Fine FFT grid	Total Energy (eV/atom)
$CaPd_5$ ($CaCu_5$-type)	PAW-GGA	313.6 eV	14 × 14 × 17	32 × 32 × 28	48 × 48 × 40	-5.05448
$CaPd_5$ (commensurate approx.)[a]	PAW-GGA	333.4 eV	10 × 10 × 4	30 × 30 × 108	48 × 48 × 160	-6.10505
Ca_2Pd_7	PAW-GGA	313.6 eV	10 × 10 × 4	32 × 32 × 80	48 × 48 × 120	-5.00501
Pd	PAW-GGA	313.6 eV	15 × 15 × 15	11 × 11 × 11	36 × 36 × 36	-5.21754
$CaAg_5$	PAW-GGA	312.3 eV	10 × 10 × 12	32 × 32 × 28	50 × 50 × 42	-2.78271
Ca_2Ag_7	PAW-GGA	312.3 eV	10 × 10 × 4	32 × 32 × 84	50 × 50 × 126	-2.81190
$CaCu_5$	PAW-GGA	341.6 eV	14 × 14 × 17	32 × 32 × 24	50 × 50 × 40	-3.57477
Ca_2Cu_7	PAW-GGA	341.6 eV	10 × 10 × 4	32 × 32 × 80	50 × 50 × 126	-3.44733
Cu	PAW-GGA	341.6 eV	15 × 15 × 15	11 × 11 × 11	36 × 36 × 36	-3.73438

[a]A commensurate approximant to the observed $CaPd_{5+q/2}$ with the composition $CaPd_5$.

Table D.14. GGA-DFT-optimized unit cell parameters[a,b]

Structure	x (Å)	y (Å)	z (Å)	α(°)	β(°)	γ(°)
$CaPd_5$ ($CaCu_5$-type)	5.35130	5.35130	4.47827	90	90	120
$CaPd_5$ (observed)[c]	5.06297	5.06297	17.35399	90	90	120
Ca_2Pd_7	9.15448	5.30923	13.54469	90	90	90
Pd	3.95178	3.95178	3.95178	90	90	90
$CaAg_5$	5.62311	5.62311	4.69087	90	90	120
Ca_2Ag_7	9.58869	5.58707	14.26797	90	90	90
$CaCu_5$	4.96488	4.96488	3.92220	90	90	120
Ca_2Cu_7	8.99941	5.04104	12.71015	90	90	90
Cu	3.63264	3.63264	3.63264	90	90	90

[a]Geometry optimizations were carried out in three steps for the room pressure structures: first, the atomic positions were allowed to relax in a unit cell of fixed size, then the energy was minimized with respect to all structural parameters. Afterwards, the energy was again minimized with respect to all structural parameters to ensure that the basis set was sufficient for the optimized cell volume. For the variable pressure calculations, two more geometry optimizations were performed for each incremental change in the cell volume: first, the atomic positions were allowed to relax in a unit cell of fixed dimensions, then the energy was minimized allowing the atomic positions and the ratios of the cell axes to change while keeping the cell volume constant. Finally, a single point energy calculation was performed with fixed structural parameters for each geometry.

[b]Calculations were performed on primitive cells, however the unit cells and atomic coordinates reported here have been transformed back to the conventional setting (where applicable) for convenience.

[c]A commensurate approximant to the observed $CaPd_{5+q/2}$ with the composition $CaPd_5$.

Table D.15. GGA-DFT-optimized atomic positions for elemental T (T=Pd or Cu)[a]

Atom Type	x	y	z
T[b]	0.00000	0.00000	0.00000
T[b]	0.00000	0.50000	0.50000
T[b]	0.50000	0.00000	0.50000
T[b]	0.50000	0.50000	0.00000

[a] Elemental Pd and Cu both crystallize in a simple face centered cubic packing in which all of the atomic positions lay on high symmetry points in the unit cell. Consequently, there are no free parameters to optimize for atomic positions

[b]The atomic positions in this table represent the positions for all elemental structures which adopt a face centered cubic packing.

Table D.16. GGA-DFT-optimized atomic positions for the $CaCu_5$-type CaT_5 structure (T=Cu, Ag, or Pd)[a]

Atom Type	*x*	*y*	*z*
Ca	0.00000	0.00000	0.00000
T[b]	0.33333	0.66667	0.00000
T[b]	0.50000	0.00000	0.500000
T[b]	0.66667	0.33333	0.00000
T[b]	0.50000	0.50000	0.50000
T[b]	0.00000	0.50000	0.50000

[a]In the $CaCu_5$-type structure all of the atomic positions lay on high symmetry points in the unit cell. Consequently, there are no free parameters to optimize for atomic positions.
[b]The atomic positions in this table represent the positions for all structures which adopt the $CaCu_5$-type structure.

Table D.17. GGA-DFT-optimized atomic positions for the commensurate approximant of $CaPd_{5+q/2}$.

Atom Type	*x*	*y*	*z*
Ca	0.66667	0.33334	0.35565
Ca	0.33334	0.66667	0.64435
Ca	0.33334	0.66667	0.85565
Ca	0.66667	0.33334	0.14435
Pd	0.15894	0.82598	0.25000
Pd	0.82598	0.15894	0.75000
Pd	0.17403	0.33296	0.25000
Pd	0.33296	0.17403	0.75000
Pd	0.66703	0.84105	0.25000
Pd	0.84105	0.66703	0.75000
Pd	0.66667	0.33333	0.61959
Pd	0.33333	0.66667	0.38041
Pd	0.33333	0.66667	0.11959
Pd	0.66667	0.33333	0.88041
Pd	0.00000	0.00000	0.61852
Pd	0.00000	0.00000	0.38148
Pd	0.00000	0.00000	0.11852
Pd	0.00000	0.00000	0.88148
Pd	0.00000	0.34045	0.50000
Pd	0.34045	0.00000	0.50000
Pd	0.34045	0.00000	0.00000
Pd	0.00000	0.34045	0.00000
Pd	0.65955	0.65955	0.00000
Pd	0.65955	0.65955	0.50000

Table D.18. GGA-DFT-optimized atomic positions of a hypothetical Yb_2Ag_7-type Ca_2Pd_7 phase.

Atom Type	x	y	z
Ca	0.00000	0.67187	0.11519
Ca	0.50000	0.17187	0.11519
Ca	0.00000	0.32813	0.88481
Ca	0.50000	0.82813	0.88481
Ca	0.00000	0.32813	0.61519
Ca	0.50000	0.82813	0.61519
Ca	0.00000	0.67187	0.38480
Ca	0.50000	0.17187	0.38480
Pd	0.00000	0.16249	0.25000
Pd	0.50000	0.66249	0.25000
Pd	0.00000	0.83751	0.75000
Pd	0.50000	0.33751	0.75000
Pd	0.24892	0.41463	0.25000
Pd	0.74892	0.91463	0.25000
Pd	0.75108	0.58537	0.75000
Pd	0.25108	0.08537	0.75000
Pd	0.75108	0.41463	0.25000
Pd	0.25108	0.91463	0.25000
Pd	0.24892	0.58537	0.75000
Pd	0.74892	0.08537	0.75000
Pd	0.66774	0.66723	0.07714
Pd	0.16774	0.16723	0.07714
Pd	0.33226	0.33277	0.92286
Pd	0.83226	0.83277	0.92286
Pd	0.66774	0.66723	0.42286
Pd	0.16774	0.16723	0.42286
Pd	0.33226	0.33277	0.57714
Pd	0.83226	0.83277	0.57714
Pd	0.33226	0.66723	0.07714
Pd	0.83226	0.16723	0.07714
Pd	0.66774	0.33277	0.92286
Pd	0.16774	0.83277	0.92286
Pd	0.33226	0.66723	0.42286
Pd	0.83226	0.16723	0.42286
Pd	0.66774	0.33277	0.57714
Pd	0.16774	0.83277	0.57714

Table D.19. GGA-DFT-optimized atomic positions of Ca_2Ag_7.

Atom Type	x	y	z
Ca	0.00000	0.68309	0.11476
Ca	0.50000	0.18309	0.11476
Ca	0.00000	0.31691	0.88524
Ca	0.50000	0.81691	0.88524
Ca	0.00000	0.31691	0.61476
Ca	0.50000	0.81691	0.61476
Ca	0.00000	0.68309	0.38524
Ca	0.50000	0.18309	0.38524
Ag	0.00000	0.17874	0.25000
Ag	0.50000	0.67874	0.25000
Ag	0.00000	0.82126	0.75000
Ag	0.50000	0.32157	0.75000
Ag	0.24910	0.42877	0.25000
Ag	0.74910	0.92877	0.25000
Ag	0.75090	0.57123	0.75000
Ag	0.25090	0.07123	0.75000
Ag	0.75090	0.42877	0.25000
Ag	0.25090	0.92877	0.25000
Ag	0.24910	0.57123	0.75000
Ag	0.74910	0.07123	0.75000
Ag	0.66390	0.67511	0.07597
Ag	0.16390	0.17511	0.07597
Ag	0.33610	0.32489	0.92403
Ag	0.83610	0.82489	0.92403
Ag	0.66390	0.67511	0.42403
Ag	0.16390	0.17511	0.42403
Ag	0.33610	0.32489	0.57597
Ag	0.83610	0.82489	0.57597
Ag	0.33610	0.67511	0.07597
Ag	0.83610	0.17511	0.7597
Ag	0.66390	0.32489	0.92403
Ag	0.16390	0.82489	0.92403
Ag	0.33610	0.67511	0.42403
Ag	0.83610	0.17511	0.42403
Ag	0.66390	0.32489	0.57597
Ag	0.16390	0.82489	0.57596

Table D.20. GGA-DFT-optimized atomic positions a hypothetical Yb_2Ag_7-type of Ca_2Cu_7 phase.

Atom Type	x	y	z
Ca	0.00000	0.67574	0.11219
Ca	0.50000	0.17574	0.11219
Ca	0.00000	0.32426	0.8881
Ca	0.50000	0.82426	0.88781
Ca	0.00000	0.32426	0.61219
Ca	0.50000	0.82426	0.61219
Ca	0.00000	0.67574	0.38781
Ca	0.50000	0.17574	0.38781
Cu	0.00000	0.16784	0.25000
Cu	0.50000	0.66784	0.25000
Cu	0.00000	0.83216	0.75000
Cu	0.50000	0.33216	0.75000
Cu	0.24827	0.41231	0.25000
Cu	0.74827	0.91231	0.25000
Cu	0.75173	0.58769	0.75000
Cu	0.25173	0.08769	0.75000
Cu	0.75173	0.41231	0.25000
Cu	0.25173	0.91231	0.25000
Cu	0.24827	0.58769	0.75000
Cu	0.74827	0.08769	0.75000
Cu	0.68127	0.65824	0.08044
Cu	0.18127	0.15824	0.08044
Cu	0.31873	0.34176	0.91956
Cu	0.81873	0.84176	0.91956
Cu	0.68127	0.65824	0.41956
Cu	0.18127	0.15824	0.41956
Cu	0.31873	0.34176	0.58044
Cu	0.81873	0.84176	0.58044
Cu	0.31873	0.65824	0.08044
Cu	0.81873	0.15824	0.08044
Cu	0.68127	0.34176	0.91956
Cu	0.18127	0.84176	0.91956
Cu	0.31873	0.65824	0.41956
Cu	0.81873	0.15824	0.41956
Cu	0.68127	0.34176	0.58044
Cu	0.18127	0.84176	0.58044

D.11. Energy vs Volume Curves and Vinet Equation of State Parameters.

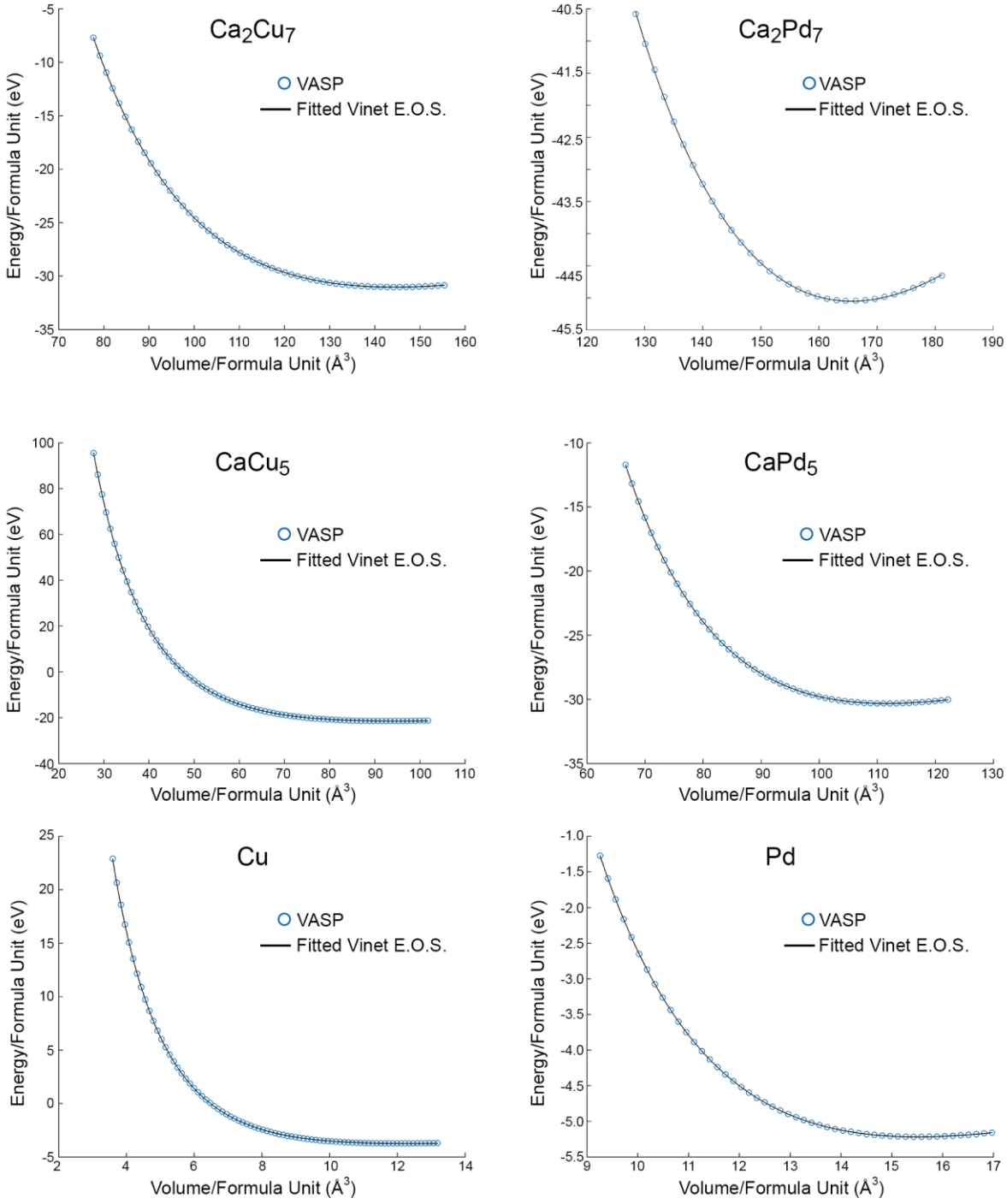

Figure D.9. Energy versus volume curves for $CaCu_5$, Ca_2Cu_7, Cu, $CaPd_5$, Ca_2Pd_7, and Pd calculated using the PAW GGA potentials provided with the Vienna Ab initio Simulation Package (VASP) as described in the main text. Blue circles correspond to the points calculated in VASP while the black line is the Vinet Equation of State (EOS) which was fitted to the energies calculated with VASP using the PHONOPY software package. The fitted parameters to the Vinet EOS can be found in Table D.21.

Table D.21. Vinet Equation of State parameters[a].

Structure	V_0 (Å^3/f.u.)	E_0 (eV/f.u.)	B_0 (GPa)	B'_0
$CaPd_5$ ($CaCu_5$-type)	111.59	-30.32	113.25	5.52
Ca_2Pd_7	165.57	-45.05	107.49	4.80
Pd	15.51	-5.22	163.30	5.84
$CaCu_5$	94.74	-21.46	68.48	5.76
Ca_2Cu_7	144.30	-31.03	73.95	5.14
Cu	12.38	-3.74	99.02	6.17

[a]The Vinet EOS is defined in Vinet, P.; Smith, J. R.; Ferrante, J.; Rose, J. H., *Phys. Rev. B* **1987,** *35*, 1945-1953 as:

$$E(V) = E_0 + \frac{2B_0V_0}{(B'_0-1)^2}\left\{2 - \left[5 + 3\left(\frac{V}{V_0}\right)^{\frac{1}{3}}(B'_0-1) - 3B'_0\right] \times \exp\left[-\frac{3(B'_0-1)}{2}\left[\left(\frac{V}{V_0}\right)^{\frac{1}{3}} - 1\right]\right]\right\}$$

Appendix E.

Supplemental Information for Chapter 6:

Homoatomic Clustering in T_4Ga_5 (T = Ta, Nb, Ta/Mo): A Story of Reluctant Intermetallics Crystallizing in a New Binary Structure Type

E.1. Crystallographic Information

In the following, detailed tables are given describing the atomic coordinates, atomic displacement parameters, and selected interatomic distances for Ta_4Ga_5 and Nb_4Ga_5. For the phase $Ta_{3.9}Mo_{0.1}Ga_5$, our model is still preliminary, as it does not factor in the presence of the reflections violating the systematic absences for the $P4_2/mnm$ space group of the binary phases. As such, rather than tabulating specific geometrical parameters (with the implied assertion of finality), we have provided a crystallographic information file with this model, which can be used as a starting point for further investigations.

Table E.1. Ta_4Ga_5 atomic coordinates and displacement parameters.

Site	Wyckoff Position	*x*	*y*	*z*	U_{eff}	Occupancy
Ta1	16d	0.495017(17)	0.207012(17)	0.146334(13)	0.00404(6)	1.0
Ta2	8d	0.753450(18)	0.246550(18)	0.101243(17)	0.00383(6)	1.0
Ta3	8d	0.34746(2)	0.14424(2)	0	0.00372(7)	1.0
Ta4	4d	1/2	0	1/4	0.00286(8)	1.0
Ta5	4d	0.38351(2)	0.38351(2)	0	0.00529(8)	1.0
Ta6	8d	0.390805(17)	0.609195(17)	0.258047(17)	0.0112(5)	1.0
Ta7	16d	0.29788(12)	0.01161(11)	0.14860(9)	0.00460(6)	1.0
Ta8[a]	8d	0.3900(11)	0.3900(11)	0.2392(11)	0.010(4)	0.0176(13)
Ta9[a]	4d	0.1171(15)	0.1171(15)	0	0.010(4)	0.0176(15)
Ga1	8d	1/2	0	0.07756(5)	0.0050(2)	1.0
Ga2	8d	0.24883(7)	0.93523(7)	0	0.0079(2)	1.0
Ga3	8d	0.57159(7)	0.21779(7)	0	0.0066(2)	1.0
Ga4	8d	0.11666(5)	0.11666(5)	0.07435(5)	0.00631(17)	0.9824(15)
Ga5	16d	0.17015(5)	0.33378(5)	0.25994(3)	0.00451(14)	1.0
Ga6	8d	0.26136(5)	0.26136(5)	0.12618(5)	0.00490(16)	1.0
Ga7	8d	0.59051(5)	0.40949(5)	0.08795(5)	0.00615(17)	1.0
Ga8	8d	0.40429(5)	0.40429(5)	0.34108(5)	0.00810(19)	0.9824(13)
Ga9	8d	0.40930(5)	0.40930(5)	0.18043(5)	0.00632(18)	0.9824(13)

[a]Atoms refined as isotropically.

Table E.2. Ta_4Ga_5 anisotropic parameters.

Site	U_{11}	U_{22}	U_{33}	U_{12}	U_{13}	U_{23}
Ta1	0.00442(9)	0.00390(9)	0.00380(11)	0.00027(6)	0.00052(7)	0.00004(7)
Ta2	0.00421(8)	0.00421(8)	0.00307(13)	0.00022(9)	-0.00026(7)	0.00026(7)
Ta3	0.00438(13)	0.00374(13)	0.00303(13)	0.00024(9)	0	0
Ta4	0.00294(10)	0.00294(10)	0.00271(18)	0	0	0
Ta5	0.00491(11)	0.00491(11)	0.0060(2)	-0.00006(14)	0	0
Ta6	0.00476(8)	0.00476(8)	0.00429(14)	0.00002(10)	0.00044(7)	-0.00044(7)
Ta7	0.00372(9)	0.00424(9)	0.00327(11)	0.00008(7)	-0.00017(7)	0.00027(7)
Ga1	0.0057(4)	0.0051(4)	0.0044(4)	0.0010(3)	0	0
Ga2	0.0144(4)	0.0049(4)	0.0044(4)	-0.0021(3)	0	0
Ga3	0.0053(4)	0.0108(4)	0.0039(4)	-0.0013(3)	0	0
Ga4	0.0070(2)	0.0070(2)	0.0050(4)	0.0016(3)	0.0001(2)	0.0001(2)
Ga5	0.0051(2)	0.0042(2)	0.0042(3)	0.00028(18)	-0.0001(2)	-0.0003(2)
Ga6	0.0056(2)	0.0056(2)	0.0035(4)	0.0017(3)	-0.0005(2)	-0.0005(2)
Ga7	0.0061(2)	0.0061(2)	0.0062(4)	-0.0003(3)	0.0002(2)	-0.0002(2)
Ga8	0.0058(2)	0.0058(2)	0.0126(5)	0.0015(3)	0.0034(2)	0.0034(2)
Ga9	0.0049(2)	0.0049(2)	0.0092(4)	0.0010(3)	-0.0019(2)	-0.0019(2)

Table E.3. Selected interatomic distances for Ta_4Ga_5.

Site	Neighbor	Distance (Å)
Ta1	Ta2	3.1758(3)
	Ta3	3.1223(3)
	Ta4	3.0097(2)
	Ta5	3.4975(3)
	Ta6	3.1789(3)
	Ta7	3.2686(3)
	Ta7	3.5517(3)
	Ta7	3.4881(3)
	Ga1	2.7061(4)
	Ga3	2.6469(4)
	Ga5	2.6509(6)
	Ga5	2.7429(6)
	Ga6	2.8487(6)
	Ga7	2.8193(6)
	Ga9	2.6539(6)
	Ta7 (x2)	2.6730(5)
	Ga1	2.6343(13)
	Ga2(x2)	3.3294(9)
	Ga3(x2)	3.0065(8)
Ga2	Ta2 (x2)	2.7475(7)
	Ta3	2.7246(9)
	Ta7 (x2)	2.7430(4)
	Ga1 (x2)	3.3294(9)
	Ga2	3.0686(12)
	Ga3	2.7813(12)
	Ga4 (x2)	2.9320(10)
	Ga8 (x2)	3.2673(10)
Ga3	Ta1 (x2)	2.6469(4)
	Ta2 (x2)	2.7690(7)
	Ta3	2.7808(8)

Ta2	Ta1 (x2)	3.1758(3)
	Ta2	3.4386(4)
	Ta6	3.5881(4)
	Ta7 (x2)	3.2094(3)
	Ga2 (x2)	2.7475(7)
	Ga3 (x2)	2.7690(7)
	Ga5 (x2)	2.7237(6)
	Ga7	2.7260(6)
	Ga8	2.6988(7)
Ta3	Ta1 (x2)	3.1223(3)
	Ta3	3.3880(4)
	Ta5	2.8524(4)
	Ta7 (x2)	3.0238(3)
	Ga1 (x2)	2.8036(5)
	Ga2	2.7246(9)
	Ga3	2.7808(8)
	Ga4 (x2)	2.7180(10)
	Ga6 (x2)	2.7437(8)
Ta4	Ta1 (x4)	3.0097(2)
	Ta7 (x4)	2.9415(2)
	Ga1 (x2)	2.9283(9)
	Ga5 (x4)	2.8092(5)
Ta5	Ta1 (x4)	3.4975(3)
	Ta3 (x2)	2.8524(4)
	Ta5	3.8843(4)
	Ga3 (x2)	2.9551(9)
	Ga6 (x2)	2.9562(8)
	Ga7 (x4)	2.8774(7)
	Ga9 (x2)	3.0941(9)
Ta6	Ta1 (x2)	3.1789(3)
	Ta2	3.5881(4)
	Ta6	3.6410(3)
	Ta7 (x2)	2.9636(3)
	Ga4	2.8490(9)
	Ga5 (x2)	2.7604(6)
	Ga6	3.2094(7)
	Ga7	2.9054(9)
	Ga8 (x2)	2.8015(7)
	Ga9 (x2)	2.7089(7)
Ta7	Ta1	3.2686(3)
	Ta1	3.5517(3)
	Ta1	3.4881(3)
	Ta2	3.2094(3)
	Ta5	2.9551(9)
	Ga1 (x2)	3.0065(8)
	Ga2	2.7813(12)
	Ga3	3.5115(12)
	Ga7 (x2)	2.7180(10)
Ga4	Ta3 (x2)	2.7180(10)
	Ta6	2.8490(9)
	Ta7 (x2)	2.7727(7)
	Ga2 (x2)	2.9320(10)
	Ga4	2.5251(12)
	Ga6	2.5679(9)
	Ga8 (x2)	2.8969(9)
Ga5	Ta1	2.6509(6)
	Ta1	2.7429(6)
	Ta2	2.7237(6)
	Ta4	2.8092(5)
	Ta6	2.7604(6)
	Ta7	2.6385(6)
	Ta7	2.6890(6)
	Ga5	2.7281(8)
	Ga6	2.6541(10)
	Ga8	3.1950(9)
	Ga9	3.2502(8)
Ga6	Ta1 (x2)	2.8487(6)
	Ta3 (x2)	2.7437(8)
	Ta5	2.9562(8)
	Ta6	3.2094(7)
	Ta7 (x2)	2.9966(6)
	Ga4	2.5679(9)
	Ga5 (x2)	2.6541(10)
	Ga9	2.6330(9)
Ga7	Ta1 (x2)	2.8193(6)
	Ta2	2.7260(6)
	Ta5 (x2)	2.8774(7)
	Ta6	2.9054(9)
	Ga3 (x2)	2.7180(10)
	Ga7	3.0178(8)
	Ga7	2.9870(12)
	Ga9 (x2)	2.6514(10)
Ga8	Ta2	2.6988(7)
	Ta6 (x2)	2.8015(7)
	Ta7 (x2)	2.7073(6)
	Ga2 (x2)	3.2673(10)

	Ta3	3.0238(3)
	Ta4	2.9415(2)
	Ta6	2.9636(3)
	Ga1	2.6730(5)
	Ga2	2.7430(4)
	Ga4	2.7727(7)
	Ga5	2.6385(6)
	Ga5	2.6890(6)
	Ga6	2.9966(6)
	Ga8	2.7073(6)
Ga1	Ta1 (x2)	2.7061(4)
	Ta3 (x2)	2.8036(5)
	Ta4	2.9283(9)

	Ga4 (x2)	2.8969(9)
	Ga5 (x2)	3.1950(9)
	Ga8	3.1914(8)
	Ga9	2.7293(13)
Ga9	Ta1 (x2)	2.6539(6)
	Ta5	3.0941(9)
	Ta6 (x2)	2.7089(7)
	Ga5 (x2)	3.2502(8)
	Ga6	2.6330(9)
	Ga7 (x2)	2.6514(10)
	Ga8	2.7293(13)
	Ga9	3.0242(8)

Table E.4. Nb_4Ga_5 atomic coordinates and atomic displacement parameters.

Site	Wyckoff Position	x	y	z	U_{eff}	Occupancy
Nb1	16d	0.49452(3)	0.20694(3)	0.146212(17)	0.00483(8)	1.0
Nb2	8d	0.75302(3)	0.24698(3)	0.10097(2)	0.00461(8)	1.0
Nb3	8d	0.34666(4)	0.14439(4)	0	0.00456(11)	1.0
Nb4	4d	1/2	0	1/4	0.00365(11)	1.0
Nb5	4d	0.38311(4)	0.38311(4)	0	0.00576(11)	1.0
Nb6	8d	0.39096(3)	0.60904(3)	0.25832(2)	0.00499(8)	1.0
Nb7	16d	0.29827(3)	0.01257(3)	0.148925(17)	0.00459(8)	1.0
Ga1	8d	1/2	0	0.07752(3)	0.00625(14)	1.0
Ga2	8d	0.24964(5)	0.93475(5)	0	0.00986(15)	1.0
Ga3	8d	0.57069(5)	0.21824(5)	0	0.00801(15)	1.0
Ga4	8d	0.11658(3)	0.11658(3)	0.07459(3)	0.00792(11)	1.0
Ga5	16d	0.17012(3)	0.33368(3)	0.26044(2)	0.00558(10)	1.0
Ga6	8d	0.26115(3)	0.26115(3)	0.12647(3)	0.00692(11)	1.0
Ga7	8d	0.59014(3)	0.40986(3)	0.08899(3)	0.00704(11)	1.0
Ga8	8d	0.40360(4)	0.40360(4)	0.34163(4)	0.01052(12)	1.0
Ga9	8d	0.40852(3)	0.40852(3)	0.18173(3)	0.00842(11)	1.0

Table E.5. Nb_4Ga_5 anisotropic atomic displacement parameters.

Site	U_{11}	U_{22}	U_{33}	U_{12}	U_{13}	U_{23}
Nb1	0.00510(14)	0.00459(14)	0.00481(13)	0.00016(10)	0.00043(11)	0.00003(10)
Nb2	0.00481(12)	0.00481(12)	0.00422(16)	0.00010(15)	-0.00029(10)	0.00029(10)
Nb3	0.00482(19)	0.00457(19)	0.00431(16)	-0.00019(15)	0	0
Nb4	0.00353(16)	0.00352(16)	0.0039(2)	0	0	0
Nb5	0.00536(17)	0.00536(17)	0.0065(3)	-0.0008(2)	0	0
Nb6	0.00503(12)	0.00503(12)	0.00492(17)	-0.00010(15)	0.00042(10)	-0.00042(10)
Nb7	0.00444(14)	0.00488(14)	0.00444(13)	0.00009(11)	-0.00023(10)	0.00019(10)
Ga1	0.0070(3)	0.0061(3)	0.0057(2)	0.00121(19)	0	0
Ga2	0.0168(3)	0.0065(3)	0.0063(2)	-0.0017(2)	0	0
Ga3	0.0063(3)	0.0129(3)	0.0049(2)	-0.0014(2)	0	0
Ga4	0.00856(16)	0.00856(16)	0.0066(2)	0.0020(2)	0.00030(14)	0.00030(14)
Ga5	0.00632(17)	0.00543(17)	0.00499(15)	0.00046(13)	-0.00020(13)	-0.00007(13)
Ga6	0.00749(16)	0.00749(16)	0.0059(2)	0.0013(2)	-0.00070(14)	-0.00070(14)
Ga7	0.00653(16)	0.00653(16)	0.0080(2)	-0.0005(2)	-0.00021(14)	0.00021(14)
Ga8	0.00749(17)	0.00749(17)	0.0166(3)	0.0019(2)	0.00422(15)	0.00422(15)
Ga9	0.00618(16)	0.00618(16)	0.0129(3)	0.0014(2)	-0.00253(14)	-0.00253(14)

Table E.6. Selected interatomic distances for Nb_4Ga_5.

Site	Neighbor	Distance (Å)
Nb1	Nb2	3.1870(19)
	Nb3	3.1141(3)
	Nb4	3.0219(18)
	Nb5	3.512(2)
	Nb6	3.1990(18)
	Nb7	3.2643(15)
	Nb7	3.5674(17)
	Nb7	3.5710(4)
	Ga1	2.7144(16)
	Ga3	2.663(3)
	Ga5	2.6614(16)
	Ga5	2.7595(19)
	Ga6	2.8514(18)
	Nb7 (x2)	2.6827(16)
	Ga1	2.653(3)
	Ga2 (x2)	3.3326(19)
	Ga3 (x2)	3.0179(17)
Ga2	Nb2 (x2)	2.7561(18)
	Nb3	2.7297(16)
	Nb7 (x2)	2.769(3)
	Ga1 (x2)	3.3326(19)
	Ga2	3.0815(16)
	Ga3	2.7886(15)
	Ga4 (x2)	2.9525(15)
	Ga8 (x2)	3.279(3)
Ga3	Nb1 (x2)	2.663(3)

	Ga7	2.8263(5)
	Ga9	2.6599(15)
Nb2	Nb1 (x2)	3.1870(19)
	Nb2	3.455(4)
	Nb6	3.611(4)
	Nb7 (x2)	3.2323(19)
	Ga2 (x2)	2.7561(18)
	Ga3 (x2)	2.7823(18)
	Ga5 (x2)	2.737(3)
	Ga7	2.7297(13)
	Ga8	2.7012(13)
Nb3	Nb1 (x2)	3.141(3)
	Nb3	3.3803(17)
	Nb5	2.8536(19)
	Nb7 (x2)	3.041(3)
	Ga1 (x2)	2.8202(13)
	Ga2	2.7297(16)
	Ga3	2.7875(18)
	Ga4 (x2)	3.0213(18)
	Ga6 (x2)	2.7550(3)
Nb4	Nb1 (x4)	3.0219(18)
	Nb7 (x4)	2.9487(18)
	Ga1 (x2)	2.951(4)
	Ga5 (x4)	2.8171(13)
Nb5	Nb1 (x4)	3.512(2)
	Nb3 (x2)	2.8536(19)
	Nb5	3.9070(19)
	Ga3 (x2)	2.9512(15)
	Ga6 (x2)	2.972(2)
	Ga7 (x4)	2.8989(17)
	Ga9 (x2)	3.138(4)
Nb6	Nb1 (x2)	3.1990(18)
	Nb2	3.611(3)
	Nb6	3.6444(17)
	Nb7 (x2)	2.9696(16)
	Ga4	2.861(4)
	Nb2 (x2)	2.7823(18)
	Nb3	2.7823(18)
	Nb5	2.9512(15)
	Ga1 (x2)	3.0179(17)
	Ga2	2.7886(15)
	Ga3	3.5274(18)
	Ga7 (x2)	2.7383(17)
Ga4	Nb3 (x2)	3.0213(18)
	Nb6	2.861(4)
	Nb7 (x2)	2.7817(14)
	Ga2 (x2)	2.9525(15)
	Ga4	2.8965(19)
	Ga6	2.5739(12)
	Ga8 (x2)	2.9061(18)
Ga5	Nb1	2.6614(16)
	Nb1	2.7595(19)
	Nb2	2.737(3)
	Nb4	2.8171(13)
	Nb6	2.7697(17)
	Nb7	2.6481(16)
	Nb7	2.6984(19)
	Ga5	2.7334(14)
	Ga6	2.673(2)
	Ga8	3.1975(18)
	Ga9	3.2452(18)
Ga6	Nb1 (x2)	2.8514(18)
	Nb3 (x2)	2.758(2)
	Nb5	2.972(2)
	Nb6	3.2167(18)
	Nb7 (x2)	2.9948(19)
	Ga4	2.5739(12)
	Ga5 (x2)	2.673(2)
	Ga9	2.6381(13)
Ga7	Nb1 (x2)	2.8263(15)
	Nb2	2.7297(13)
	Nb5 (x2)	2.8989(17)

	Ga5 (x2)	2.7697(17)
	Ga6	3.2167(18)
	Ga7	2.914(4)
	Ga8 (x2)	2.8192(17)
	Ga9 (x2)	2.7156(16)
Nb7	Nb1	3.2643 (15)
	Nb1	3.5674(17)
	Nb1	3.510(4)
	Nb2	2.2323(19)
	Nb3	3.041(3)
	Nb4	2.9487(18)
	Nb6	2.9696(16)
	Ga1	2.6827(16)
	Ga2	2.769(3)
	Ga4	2.7817(14)
	Ga5	2.6481(16)
	Ga5	2.6984(19)
	Ga6	2.9948(19)
	Ga8	2.7156(15)
Ga1	Nb1 (x2)	2.7144(16)
	Nb3 (x2)	2.8202(13)
	Nb4	2.951(4)

	Nb6	2.914(4)
	Ga3 (x2)	2.7383(17)
	Ga7	3.0129(15)
	Ga7	3.045(4)
	Ga9 (x2)	2.6690(17)
Ga8	Nb2	2.7012(13)
	Nb6 (x2)	2.8192(17)
	Nb7 (x2)	2.7156(15)
	Ga2 (x2)	3.3279(3)
	Ga4 (x2)	2.9061(18)
	Ga5 (x2)	3.1975(18)
	Ga8	3.2221(16)
	Ga9	2.737(3)
Ga9	Nb1 (x2)	2.6599(15)
	Nb5	3.138(4)
	Nb6 (x2)	2.7156(16)
	Ga5 (x2)	3.2452(18)
	Ga6	2.6381(13)
	Ga7 (x2)	2.6690(17)
	Ga8	2.737(3)
	Ga9	3.0575(15)

E.2. GGA-DFT Optimized Geometries

Table E.7. GGA-DFT-optimized geometry of Ta_4Ga_5.

Cell vectors	*x* component (Å)	*y* component (Å)	*z* component (Å)
a	11.797036	0.000000	0.000000
b	0.000000	11.797036	0.000000
c	0.000000	0.000000	16.98942
Atom type	*x* (fractional)	*y* (fractional)	*z* (fractional)
Ta	0.753365	0.246635	0.100795
Ta	0.246635	0.753365	0.899205
Ta	0.246635	0.753365	0.100795
Ta	0.753365	0.246635	0.899205
Ta	0.253365	0.253365	0.600795
Ta	0.746635	0.746635	0.399205
Ta	0.746635	0.746635	0.600795
Ta	0.253365	0.253365	0.399205
Ta	0.651745	0.855116	0
Ta	0.348255	0.144884	0
Ta	0.644884	0.151745	0.5
Ta	0.355116	0.848255	0.5
Ta	0.151745	0.644884	0.5
Ta	0.848255	0.355116	0.5
Ta	0.144884	0.348255	0
Ta	0.855116	0.651745	0
Ta	0.702189	0.987419	0.148784
Ta	0.297811	0.012581	0.851216
Ta	0.297811	0.012581	0.148784
Ta	0.702189	0.987419	0.851216
Ta	0.512581	0.202189	0.648784
Ta	0.487419	0.797811	0.351216
Ta	0.487419	0.797811	0.648784
Ta	0.512581	0.202189	0.351216
Ta	0.202189	0.512581	0.351216
Ta	0.797811	0.487419	0.648784
Ta	0.797811	0.487419	0.351216
Ta	0.202189	0.512581	0.648784
Ta	0.012581	0.297811	0.851216
Ta	0.987419	0.702189	0.148784
Ta	0.987419	0.702189	0.851216
Ta	0.012581	0.297811	0.148784
Ta	0.5	0	0.25
Ta	0.5	0	0.75
Ta	0	0.5	0.25

Ta	0	0.5	0.75
Ta	0.494289	0.207361	0.146098
Ta	0.505711	0.792639	0.853902
Ta	0.505711	0.792639	0.146098
Ta	0.494289	0.207361	0.853902
Ta	0.292639	0.994289	0.646098
Ta	0.707361	0.005711	0.353902
Ta	0.707361	0.005711	0.646098
Ta	0.292639	0.994289	0.353902
Ta	0.994289	0.292639	0.353902
Ta	0.005711	0.707361	0.646098
Ta	0.005711	0.707361	0.353902
Ta	0.994289	0.292639	0.646098
Ta	0.792639	0.505711	0.853902
Ta	0.207361	0.494289	0.146098
Ta	0.207361	0.494289	0.853902
Ta	0.792639	0.505711	0.146098
Ta	0.39102	0.60898	0.258162
Ta	0.60898	0.39102	0.741838
Ta	0.60898	0.39102	0.258162
Ta	0.39102	0.60898	0.741838
Ta	0.89102	0.89102	0.758162
Ta	0.10898	0.10898	0.241838
Ta	0.10898	0.10898	0.758162
Ta	0.89102	0.89102	0.241838
Ta	0.38304	0.38304	0
Ta	0.61696	0.61696	0
Ta	0.11696	0.883041	0.5
Ta	0.883041	0.11696	0.5
Ga	0.749111	0.06477	0
Ga	0.250889	0.93523	0
Ga	0.43523	0.249111	0.5
Ga	0.56477	0.750889	0.5
Ga	0.249111	0.43523	0.5
Ga	0.750889	0.56477	0.5
Ga	0.93523	0.250889	0
Ga	0.06477	0.749111	0
Ga	0.261613	0.261613	0.126159
Ga	0.738387	0.738387	0.873841
Ga	0.738387	0.738387	0.126159
Ga	0.261613	0.261613	0.873841
Ga	0.238387	0.761613	0.626159
Ga	0.761613	0.238387	0.373841

Ga	0.761613	0.238387	0.626159
Ga	0.238387	0.761613	0.373841
Ga	0.169296	0.333806	0.260747
Ga	0.830704	0.666194	0.739253
Ga	0.830704	0.666194	0.260747
Ga	0.169296	0.333806	0.739253
Ga	0.166194	0.669296	0.760747
Ga	0.833806	0.330704	0.239253
Ga	0.833806	0.330704	0.760747
Ga	0.166194	0.669296	0.239253
Ga	0.669296	0.166194	0.239253
Ga	0.330704	0.833806	0.760747
Ga	0.330704	0.833806	0.239253
Ga	0.669296	0.166194	0.760747
Ga	0.666194	0.830704	0.739253
Ga	0.333806	0.169296	0.260747
Ga	0.333806	0.169296	0.739253
Ga	0.666194	0.830704	0.260747
Ga	0.409668	0.409668	0.180034
Ga	0.590332	0.590332	0.819966
Ga	0.590332	0.590332	0.180034
Ga	0.409668	0.409668	0.819966
Ga	0.090332	0.909668	0.680034
Ga	0.909668	0.090332	0.319966
Ga	0.909668	0.090332	0.680034
Ga	0.090332	0.909668	0.319966
Ga	0.571127	0.218547	0
Ga	0.428873	0.781453	0
Ga	0.281453	0.071127	0.5
Ga	0.718547	0.928873	0.5
Ga	0.071127	0.281453	0.5
Ga	0.928873	0.718547	0.5
Ga	0.781453	0.428873	0
Ga	0.218547	0.571127	0
Ga	0.5	0	0.078097
Ga	0.5	0	0.921903
Ga	0.5	0	0.578097
Ga	0.5	0	0.421903
Ga	0	0.5	0.421903
Ga	0	0.5	0.578097
Ga	0	0.5	0.921903
Ga	0	0.5	0.078097
Ga	0.882864	0.882864	0.074237

Ga	0.117136	0.117136	0.925763
Ga	0.117136	0.117136	0.074237
Ga	0.882864	0.882864	0.925763
Ga	0.617136	0.382864	0.574237
Ga	0.382864	0.617136	0.425763
Ga	0.382864	0.617136	0.574237
Ga	0.617136	0.382864	0.425763
Ga	0.59074	0.40926	0.088039
Ga	0.40926	0.59074	0.911961
Ga	0.40926	0.59074	0.088039
Ga	0.59074	0.40926	0.911961
Ga	0.09074	0.09074	0.588039
Ga	0.90926	0.90926	0.411961
Ga	0.90926	0.90926	0.588039
Ga	0.09074	0.09074	0.411961
Ga	0.403395	0.403395	0.340519
Ga	0.596605	0.596605	0.659481
Ga	0.596605	0.596605	0.340519
Ga	0.403395	0.403395	0.659481
Ga	0.096605	0.903395	0.840519
Ga	0.903395	0.096605	0.159481
Ga	0.903395	0.096605	0.840519
Ga	0.096605	0.903395	0.159481

Table E.8. GGA-DFT optimized geometry of Nb_4Ga_5.

Cell vectors	*x* component (Å)	*y* component (Å)	*z* component (Å)
a	11.837878	0.000000	0.000000
b	0.000000	11.837878	0.000000
c	0.000000	0.000000	17.062032
Atom type	*x* (fractional)	*y* (fractional)	*z* (fractional)
Nb	0.752824	0.247176	0.100351
Nb	0.247176	0.752824	0.899649
Nb	0.247176	0.752824	0.100351
Nb	0.752824	0.247176	0.899649
Nb	0.252824	0.252824	0.600351
Nb	0.747176	0.747176	0.399649
Nb	0.747176	0.747176	0.600351
Nb	0.252824	0.252824	0.399649
Nb	0.347222	0.145386	0
Nb	0.652778	0.854614	0
Nb	0.354614	0.847222	0.5
Nb	0.645386	0.152778	0.5
Nb	0.152778	0.645386	0.5
Nb	0.847222	0.354614	0.5
Nb	0.145386	0.347222	0
Nb	0.854614	0.652778	0
Nb	0.298049	0.013165	0.148985
Nb	0.701951	0.986835	0.851015
Nb	0.701951	0.986835	0.148985
Nb	0.298049	0.013165	0.851015
Nb	0.486835	0.798049	0.648985
Nb	0.513165	0.201951	0.351015
Nb	0.513165	0.201951	0.648985
Nb	0.486835	0.798049	0.351015
Nb	0.201951	0.513165	0.351015
Nb	0.798049	0.486835	0.648985
Nb	0.798049	0.486835	0.351015
Nb	0.201951	0.513165	0.648985
Nb	0.013165	0.298049	0.851015
Nb	0.986835	0.701951	0.148985
Nb	0.986835	0.701951	0.851015
Nb	0.013165	0.298049	0.148985
Nb	0.5	0	0.25
Nb	0.5	0	0.75
Nb	0	0.5	0.25
Nb	0	0.5	0.75

Nb	0.493511	0.207276	0.146058
Nb	0.506489	0.792724	0.853942
Nb	0.506489	0.792724	0.146058
Nb	0.493511	0.207276	0.853942
Nb	0.292724	0.993511	0.646058
Nb	0.707276	0.006489	0.353942
Nb	0.707276	0.006489	0.646058
Nb	0.292724	0.993511	0.353942
Nb	0.006489	0.707276	0.353942
Nb	0.993511	0.292724	0.646058
Nb	0.993511	0.292724	0.353942
Nb	0.006489	0.707276	0.646058
Nb	0.207276	0.493511	0.853942
Nb	0.792724	0.506489	0.146058
Nb	0.792724	0.506489	0.853942
Nb	0.207276	0.493511	0.146058
Nb	0.391482	0.608518	0.258755
Nb	0.608518	0.391482	0.741245
Nb	0.608518	0.391482	0.258755
Nb	0.391482	0.608518	0.741245
Nb	0.891482	0.891482	0.758755
Nb	0.108518	0.108518	0.241245
Nb	0.108518	0.108518	0.758755
Nb	0.891482	0.891482	0.241245
Nb	0.382851	0.382851	0
Nb	0.617149	0.617149	0
Nb	0.117149	0.882851	0.5
Ga	0.882851	0.117149	0.5
Ga	0.74796	0.06534	0
Ga	0.25204	0.93466	0
Ga	0.43466	0.24796	0.5
Ga	0.56534	0.75204	0.5
Ga	0.75204	0.56534	0.5
Ga	0.24796	0.43466	0.5
Ga	0.06534	0.74796	0
Ga	0.93466	0.25204	0
Ga	0.261136	0.261136	0.126769
Ga	0.738864	0.738864	0.873231
Ga	0.738864	0.738864	0.126769
Ga	0.261136	0.261136	0.873231
Ga	0.238864	0.761136	0.626769
Ga	0.761136	0.238864	0.373231
Ga	0.761136	0.238864	0.626769

Ga	0.238864	0.761136	0.373231
Ga	0.168957	0.333596	0.261379
Ga	0.831043	0.666403	0.738621
Ga	0.831043	0.666403	0.261379
Ga	0.168957	0.333596	0.738621
Ga	0.166404	0.668957	0.761379
Ga	0.833597	0.331043	0.238621
Ga	0.833597	0.331043	0.761379
Ga	0.166404	0.668957	0.238621
Ga	0.331043	0.833597	0.238621
Ga	0.668957	0.166404	0.761379
Ga	0.668957	0.166404	0.238621
Ga	0.331043	0.833597	0.761379
Ga	0.333596	0.168957	0.738621
Ga	0.666403	0.831043	0.261379
Ga	0.666403	0.831043	0.738621
Ga	0.333596	0.168957	0.261379
Ga	0.408707	0.408707	0.181543
Ga	0.591293	0.591293	0.818457
Ga	0.591293	0.591293	0.181543
Ga	0.408707	0.408707	0.818457
Ga	0.091293	0.908707	0.681543
Ga	0.908707	0.091293	0.318457
Ga	0.908707	0.091293	0.681543
Ga	0.091293	0.908707	0.318457
Ga	0.570127	0.218832	0
Ga	0.429873	0.781168	0
Ga	0.281168	0.070127	0.5
Ga	0.718832	0.929873	0.5
Ga	0.929873	0.718832	0.5
Ga	0.070127	0.281168	0.5
Ga	0.218832	0.570127	0
Ga	0.781168	0.429873	0
Ga	0.5	0	0.078231
Ga	0.5	0	0.921769
Ga	0.5	0	0.578231
Ga	0.5	0	0.421769
Ga	0	0.5	0.421769
Ga	0	0.5	0.578231
Ga	0	0.5	0.921769
Ga	0	0.5	0.078231
Ga	0.11696	0.11696	0.074446
Ga	0.88304	0.88304	0.925554

Ga	0.88304	0.88304	0.074446
Ga	0.11696	0.11696	0.925554
Ga	0.38304	0.61696	0.574446
Ga	0.61696	0.38304	0.425554
Ga	0.61696	0.38304	0.574446
Ga	0.38304	0.61696	0.425554
Ga	0.590468	0.409532	0.089086
Ga	0.409532	0.590468	0.910914
Ga	0.409532	0.590468	0.089086
Ga	0.590468	0.409532	0.910914
Ga	0.090468	0.090468	0.589086
Ga	0.909532	0.909532	0.410914
Ga	0.909532	0.909532	0.589086
Ga	0.090468	0.090468	0.410914
Ga	0.402395	0.402395	0.341028
Ga	0.597605	0.597605	0.658972
Ga	0.597605	0.597605	0.341028
Ga	0.402395	0.402395	0.658972
Ga	0.097605	0.902395	0.841028
Ga	0.902395	0.097605	0.158972
Ga	0.902395	0.097605	0.841028
Ga	0.097605	0.902395	0.158972

E.3. DFT-Calibrated Hückel Parameters

Table E.9. DFT-calibrated Hückel parameters used in this work.

Compound, RMS deviation[a]	Orbital	H_{ii} (eV)	c_1	$\zeta_1(a_o^{-1})$	c_2	$\zeta_2(a_o^{-1})$
Ta_4Ga_5, 0.085eV	Ta 6s	-6.034		2.9345		
	Ta 6p	-3.127		2.9345[b]		
	Ta 5d	-6.804	0.6815	4.1266	0.7953	2.3032
	Ga 4s	-9.297				
	Ga 4p	-4.514				
Nb_4Ga_5, 0.091 eV	Nb 5s	-5.876		2.7479		
	Nb 5p	-3.892		2.7479[b]		
	Nb 4d	-7.045	0.1671	6.5594	0.8329	2.2697
	Ga 4s	-10.049		2.4569		
	Ga 4p	-4.466		2.1739		

[a]Root-mean-squared deviation between the DFT and Hückel band energies up to 1 eV above the E_F.

[b]Constrained to equal the corresponding value for the s orbital on the same element.

E.4. Comparison of GGA-DFT and DFT-Calibrated Hückel DOS Curves for Nb_4Ga_5

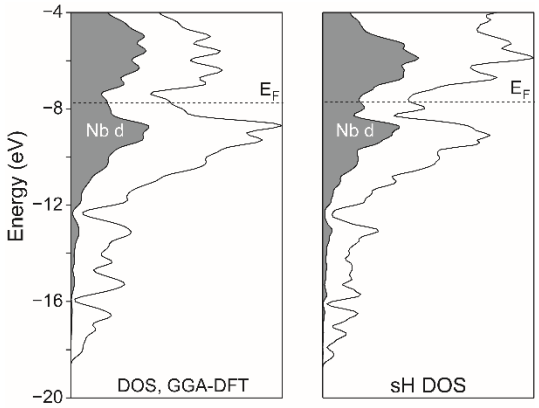

Figure E.1. Electronic DOS curves calculated for Nb_4Ga_5 with GGA-DFT (left) and a best-fit Hückel model (right).

E.5. Additional Results from the raMO Analysis of Ta_4Ga_5

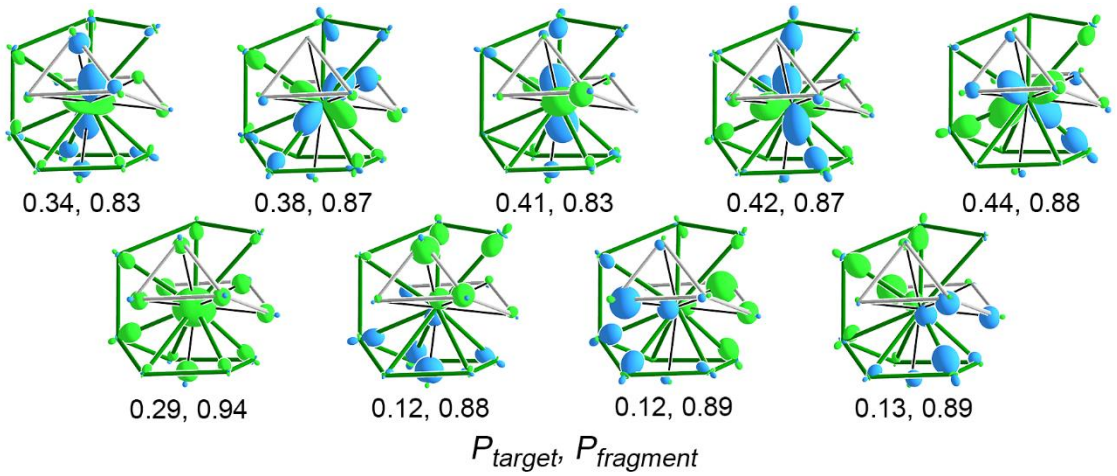

Figure E.2. raMOs resulting from the use of valence atomic orbitals of an atom on Ta_4Ga_5's Ta1 site as target functions. The numbers beneath the functions correspond to the probabilities of finding an electron occupying the raMO on the original target orbital (P_{target}) and the fragment of the structure drawn ($P_{fragment}$).

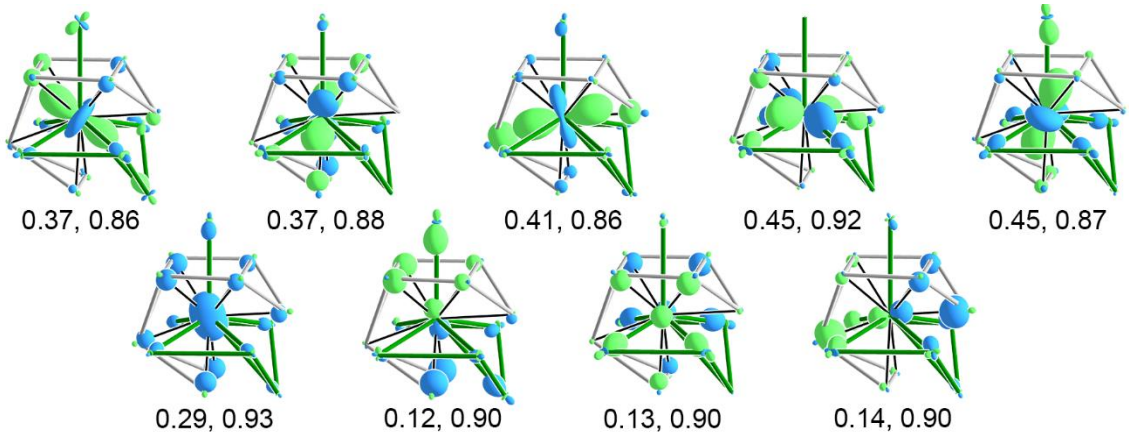

Figure E.3. raMO analysis of the Ta2 site of Ta_4Ga_5. See caption to Figure E.2 for details.

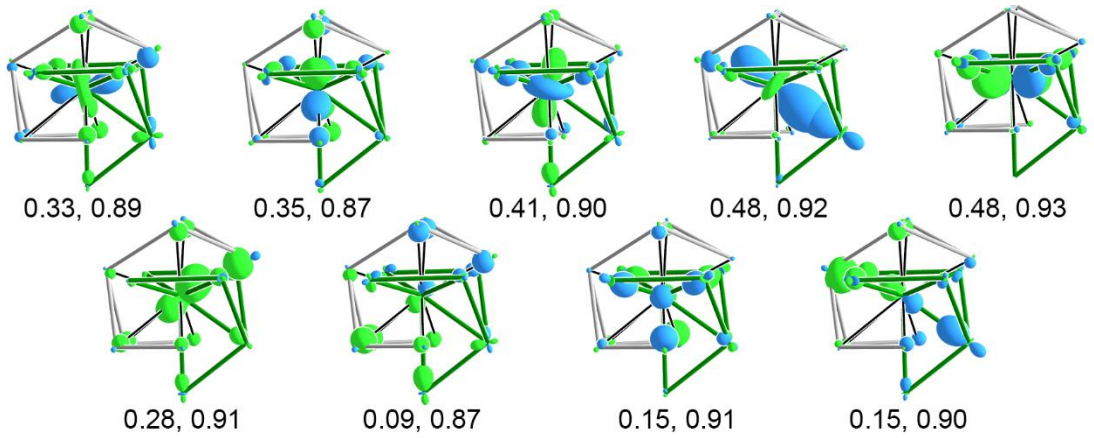

Figure E.4. raMO analysis of the Ta3 site of Ta_4Ga_5, following the conventions of Figure E.2.

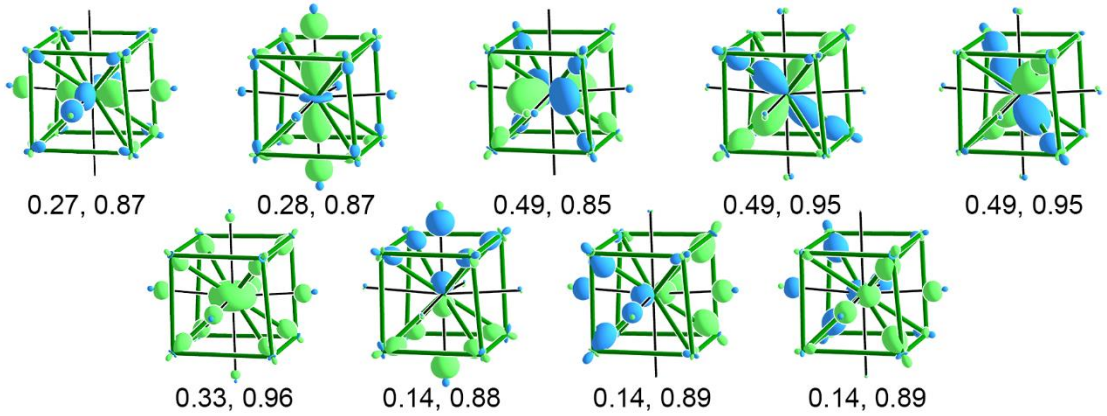

Figure E.5. raMO analysis of the Ta4 site of Ta_4Ga_5 (see caption to Figure E.2).

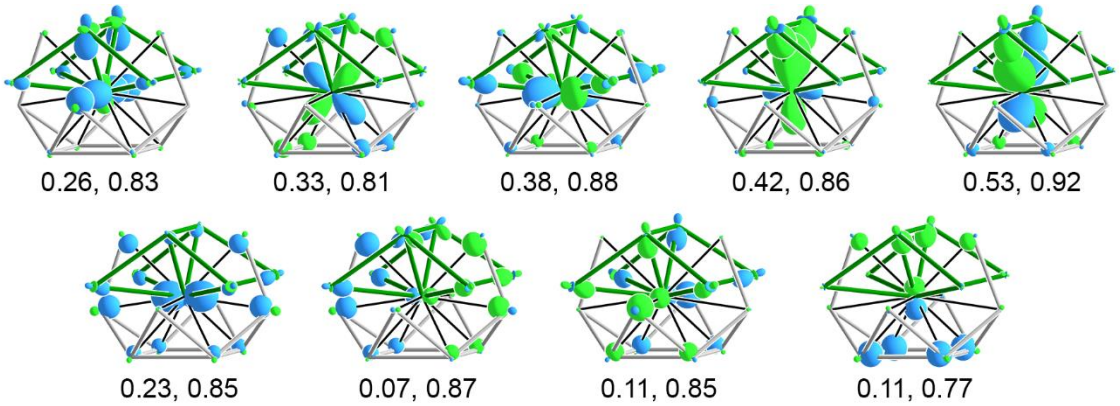

Figure E.6. raMO analysis of the Ta5 site of Ta_4Ga_5 (see caption to Figure E.2).

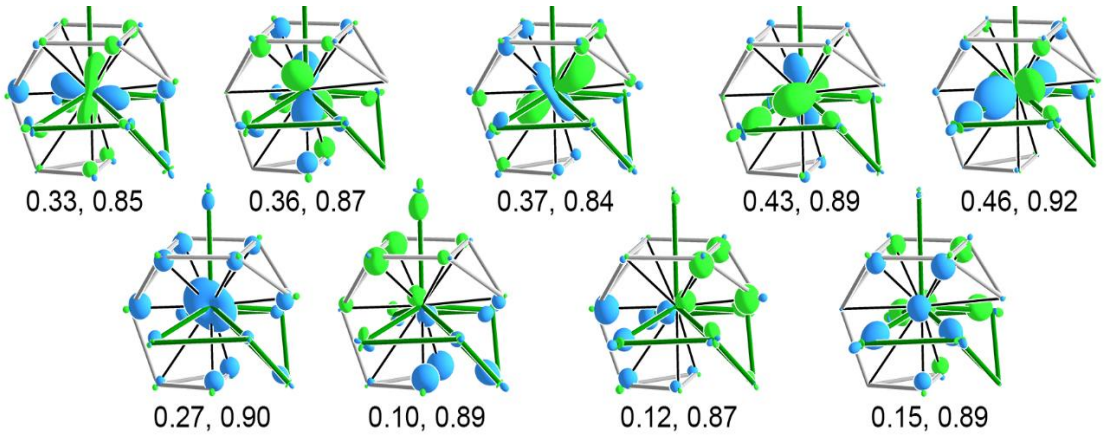

Figure E.7. raMO analysis of the Ta6 site of Ta_4Ga_5 (see caption to Figure E.2).

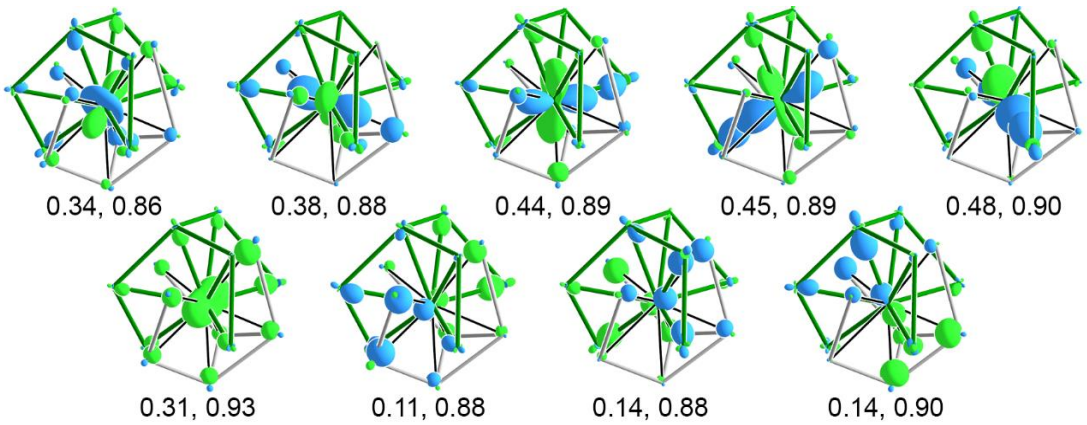

Figure E.8. raMO analysis of the Ta7 site of Ta_4Ga_5 (see caption to Figure E.2).

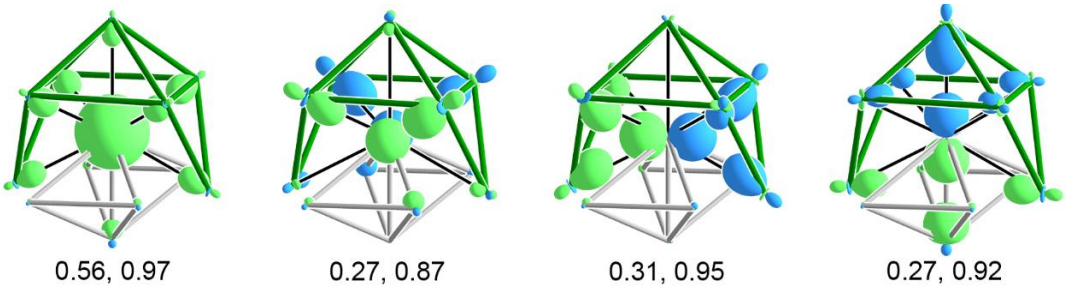

Figure E.9. raMO analysis of the Ga1 site of Ta_4Ga_5 (see caption to Figure E.2).

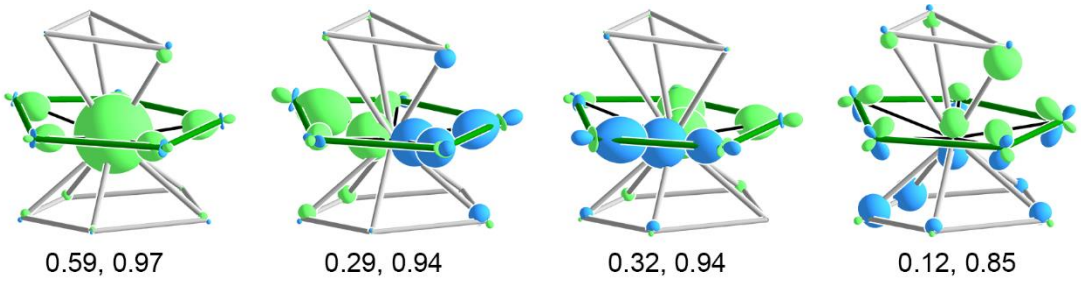

Figure E.10. raMO analysis of the Ga2 site of Ta_4Ga_5 (see caption to Figure E.2).

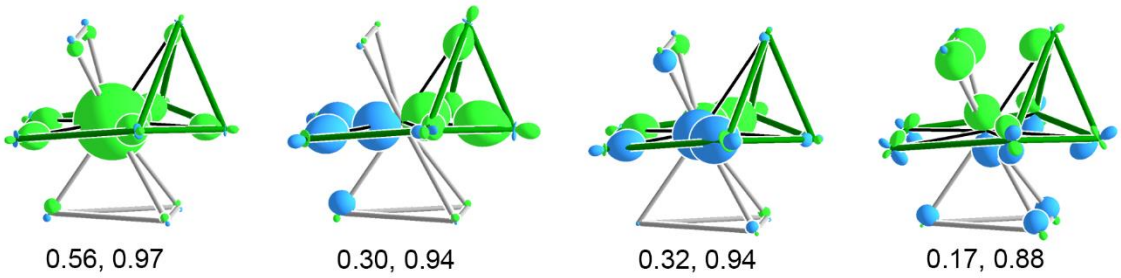

Figure E.11. raMO analysis of the Ga3 site of Ta_4Ga_5 (see caption to Figure E.2).

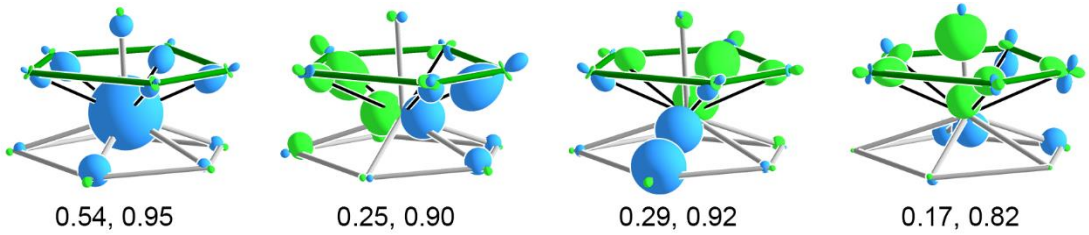

Figure E.12. raMO analysis of the Ga4 site of Ta_4Ga_5 (see caption to Figure E.2).

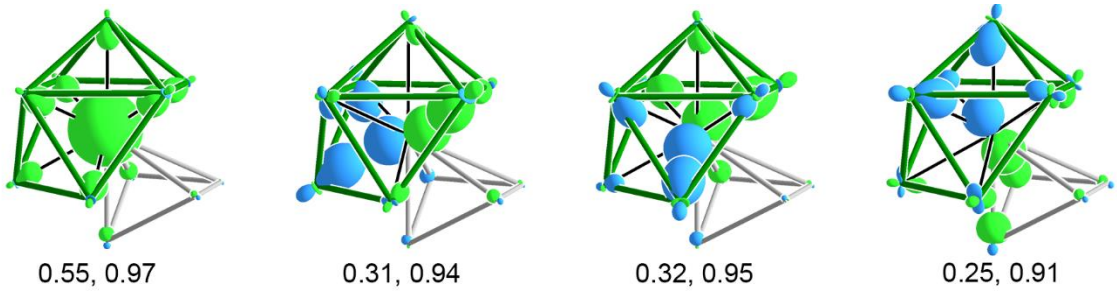

Figure E.13. raMO analysis of the Ga5 site of Ta_4Ga_5 (see caption to Figure E.2).

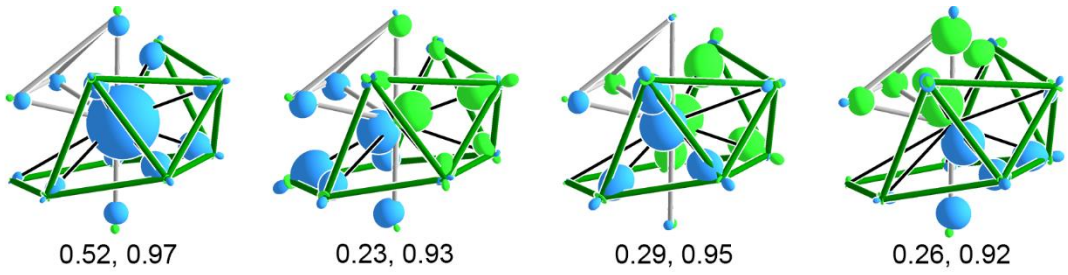

Figure E.14. raMO analysis of the Ga6 site of Ta_4Ga_5 (see caption to Figure E.2).

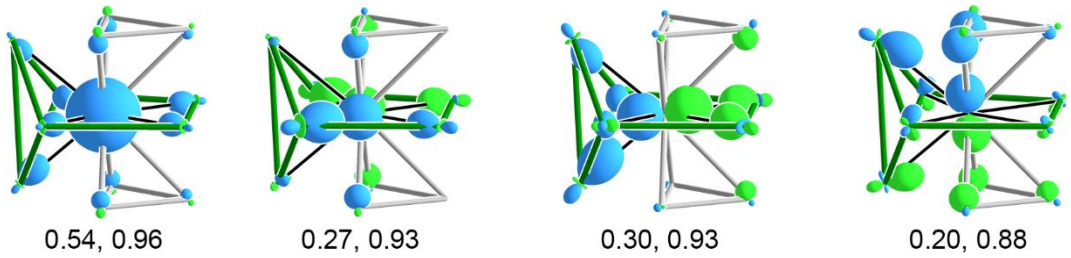

Figure E.15. raMO analysis of the Ga7 site of Ta_4Ga_5 (see caption to Figure E.2).

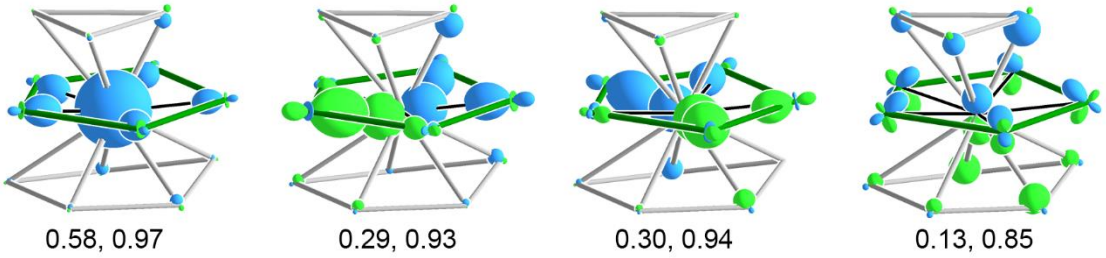

Figure E.16. raMO analysis of the Ga8 site of Ta_4Ga_5 (see caption to Figure E.2).

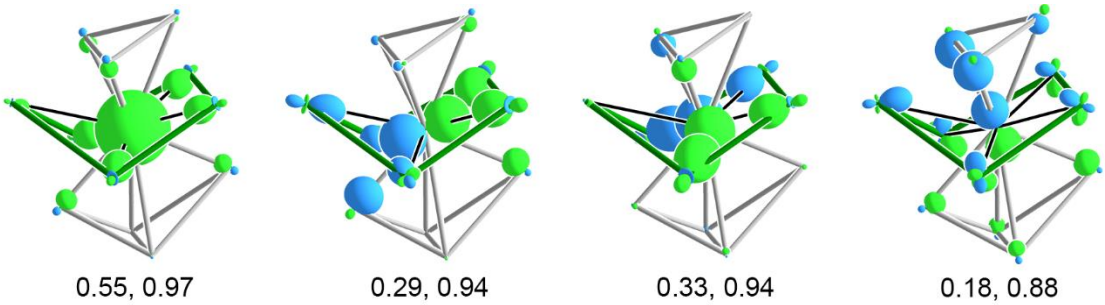

Figure E.17. raMO analysis of the Ga9 site of Ta_4Ga_5 (see caption to Figure E.2).